

# The VLA-COSMOS 3 GHz Large Project

---

**Ceraj, Lana**

**Doctoral thesis / Disertacija**

**2020**

*Degree Grantor / Ustanova koja je dodijelila akademski / stručni stupanj:* **University of Zagreb, Faculty of Science / Sveučilište u Zagrebu, Prirodoslovno-matematički fakultet**

*Permanent link / Trajna poveznica:* <https://um.nsk.hr/um:nbn:hr:217:271070>

*Rights / Prava:* [In copyright](#)/[Zaštićeno autorskim pravom.](#)

*Download date / Datum preuzimanja:* **2024-08-21**



*Repository / Repozitorij:*

[Repository of the Faculty of Science - University of Zagreb](#)





University of Zagreb  
Faculty of Science  
Department of Physics

Lana Ceraj

**The VLA-COSMOS 3 GHz Large Project:  
Origin of radio emission in radiatively  
efficient AGN and their cosmic evolution**

DOCTORAL THESIS

Zagreb, 2020





University of Zagreb  
Faculty of Science  
Department of Physics

Lana Ceraj

**The VLA-COSMOS 3 GHz Large Project:  
Origin of radio emission in radiatively  
efficient AGN and their cosmic evolution**

DOCTORAL THESIS

Supervisor:  
prof. dr. sc. Vernesa Smolčić

Zagreb, 2020







Sveučilište u Zagrebu  
Prirodoslovno-matematički fakultet  
Fizički odsjek

Lana Ceraj

**VLA-COSMOS veliki projekt na 3 GHz:  
Porijeklo zračenja u radio-području kod  
radijativno efikasnih aktivnih galaktičkih  
jezgara i njihov razvoj kroz povijest svemira**

DOKTORSKI RAD

Mentor:  
prof. dr. sc. Vernesa Smolčić

Zagreb, 2020



# Supervisor information

Vernesa Smolčić obtained her Master's degree in physics from the University of Zagreb in 2004. Under the supervision of Dr. Eva Schinnerer and Dr. Hans-Walter Rix, she obtained her doctoral degree in 2007 at the Ruperto-Carola University in Heidelberg (Germany). The title of her doctoral thesis was: *The Faint Radio Population in the VLA-COSMOS Survey: Star-Forming Galaxies and Active Galactic Nuclei*. She continued working in observational astronomy as a CARMA Postdoctoral scholar at the California Institute of Technology in Pasadena (CA, USA) from 2008 to 2010. From 2010 to 2013, she worked as an ESO ALMA COFUND fellow at the Argelander Institute for Astronomy in Bonn (Germany) and the European Southern Observatory in Garching (Germany). Starting in 2010, she became an assistant professor at the Physics department of the Faculty of Science at the University of Zagreb, and in 2015 an associate professor. In 2019, she was awarded tenure at the same institution.

She was awarded several research grants, with the largest ones being the Marie Curie Career Integration Grant and European Research Council Starting Grant, both awarded in 2013. She is a member of several international collaborations and societies, including Cosmic Evolution Survey (COSMOS), Ultimate XMM Extragalactic Survey (XXL), and Croatian Physical Society (HFD). Since 2019, she became a co-leader of the COSMOS survey. Vernesa is a (co-)author of over 120 refereed articles published in Current Content journals and has almost 15,000 citations and H-index of 49 (according to ADS). She also invested a large effort in science outreach by giving outreach talks at schools and museums, participating in TV and radio interviews. She started and maintains the *Astroučionica* website, dedicated to bringing astronomy closer to the general public.

# Acknowledgements

First and foremost, I would like to thank my supervisor Vernesa Smolčić for her excellent scientific guidance, patience, and understanding shown during the last four years. Thank you for showing me that science is much more than just plain analyses and that it is, in fact, human endeavor, which can be a lot of fun when done with the right people.

I am grateful to members of the COSMOS and XXL collaborations, thanks to whose help the work presented in this Thesis has been significantly improved. Special thanks to Dr. Giovanni Zamorani for his always insightful and detailed comments which helped me to advance understanding of my work.

Thank you, Jacinta and Ivan, for being amazing friends, supervisors and office siblings. Nuria, thanks for coming and bringing your unicorn-rare charm into my life. The time spent playing science with all of you was the most fun time I ever had!

PhD would not be the same without Sandra, Olga, Krešimir, Bruno, Dinko and Nikola. Thanks for being great (beverage consuming) buddies. Arigato gozaimasu goes to Mladen, a young friendly sensei of radio astronomy. Cheers to Daniel for being a happy receiver of potatoes and delicious iced teas.

Thanks go to my unscientific friends: Marta, Domagoj, Arijana, Marija, and Mariela whose silliness always makes life more fun, as well as to (the rest of) the Choir. Active galactic core really is the subject of analysis!

Mom and grandma, thank you for your lifelong support and for igniting the first spark of scientific curiosity in me. I must also not forget to thank Krešimir for discussing with me the existence of black holes back when we were just kids (even if I still do not remember that occurrence). I dedicate this Thesis to my ;) Krešo, for always being there, in good times and in bad.

The work presented in this Thesis would not be possible without the founding by the ERC Starting Grant: *Constraining Stellar Mass and Supermassive Black Hole Growth through Cosmic Times: Paving the way for the next generation sky surveys* (ID: 337595).

# Abstract

To study the origin of radio emission and the cosmic evolution of radio detected radiatively efficient active galactic nuclei, I used the radio data of sources detected within the COSMOS and XXL-S sky fields, which were previously cross-correlated with available multiwavelength data. A sample of 1,604 moderate-to-high radiative luminosity AGN (HLAGN) detected within the COSMOS field was selected using criteria sensitive to the X-ray, MIR and optical emissions expected to arise from the efficient accretion onto a supermassive black hole. I developed a statistical method of radio luminosity decomposition, which I used to separate the observed HLAGN radio emission into AGN and star formation-related contributions to the radio luminosity. This was done via the so-called AGN fraction, defined as the fractional contribution of the AGN-related radio emission to the total observed radio emission. I found that the majority of HLAGN ( $\sim 68\%$ ) is dominated by star formation-related radio emission ( $f_{\text{AGN}} < 0.5$ ). However, there are  $\sim 32\%$  of HLAGN whose radio emission is dominated by the AGN-related radio emission ( $0.5 \leq f_{\text{AGN}} \leq 1$ ). The AGN fractions obtained for each source via the decomposition method were used to scale the total radio luminosity down to the radio AGN luminosity. Using the obtained AGN luminosities, the radio AGN luminosity functions were constructed and constrained out to  $z \sim 6$ . The number and luminosity densities of HLAGN were further constrained, with the peak of the evolution found in the cosmic epoch when the universe was 4 billion years old ( $z \sim 1 - 2.5$ ).

Next, by combining the COSMOS HLAGN data-set with the radio-to-X-ray data for a sample of high-excitation radio galaxies within the XXL-S field, I studied a sample of 274 radio and X-ray selected quasars (XQSOs) at  $0.25 < z < 6.1$ . These were selected by a criterion of  $L_{\text{X}}[2 - 10 \text{ keV}] \geq 10^{44} \text{ erg s}^{-1}$  which broadly selects quasars. By calculating the radio loudness of these sources using four different definitions and applying criteria as commonly used in the literature to separate them into radio-quiet and radio-loud AGN, I found that 18 – 73% of XQSOs are selected as radio-loud. This significant disagreement arises both from the different flux density thresholds of the COSMOS and XXL-S radio surveys, as well as because of different criteria that capture different processes related both to star formation and AGN activity. To

---

study further the origin of radio emission in XQSOs, I constructed radio luminosity functions of XQSOs and constrained their shape in six redshift bins at  $0.5 < z < 3.75$ . The lower-1.4 GHz luminosity end shows a higher normalization than expected only from AGN contribution in all studied redshift bins. I found that the so-called ‘bump’ is mostly dominated by emission due to star-forming processes within the host galaxies of XQSOs. As expected, AGN-related radio emission is the dominant contribution at the higher-luminosity end of the RLF.

To test if the environment plays a significant role in the presence of AGN-dominated radio emission in some radiatively efficient AGN, I cross-correlated the HLAGN sample with the X-ray group catalog available within COSMOS finding that 43 HLAGN at  $0.2 < z < 1.3$  are located within the X-ray groups. For these sources, I found a trend of decreasing AGN fractions with increasing distance from the X-ray group center.

Keywords: galaxies, active galactic nuclei, galaxy evolution, radio emission, high-redshift galaxies, star formation, quasars, environments

# Prošireni sažetak

Glavna tema ovog rada je proučavanje porijekla zračenja opaženog u radio području koje dolazi od radijativno efikasnih aktivnih galaktičkih jezgri ili AGN-ova (skraćeno od engl. *active galactic nuclei*) te kako se to zračenje mijenja kroz povijest svemira. Radijativno efikasni AGN-ovi nalaze se u galaksijama domaćinima u kojima se aktivno odvijaju procesi stvaranja zvijezda. Poznato je da i aktivnost galaktičke jezgre, kao i procesi stvaranja zvijezda, mogu proizvesti sinkrotronsko zračenje koje se može opaziti u radio području. Dok je kod galaksija u bliskom svemiru moguće razlučiti pojedine komponente, te na temelju opažanja odrediti odakle dolazi radio zračenje, kod opažanja dalekog svemira većina izvora je nerazlučena i razdioba zračenja na temelju morfologije nije moguća. S tom sam svrhom osmislila statističku metodu razdiobe luminoziteta, detaljno opisanu u daljnjem tekstu. Također, za razumijevanje razvoja galaksija kroz povijest svemira, potrebno je znati kako se pojedine komponente galaksija mijenjaju kroz vrijeme. S tom svrhom, određujem funkcije luminoziteta i pomoću njih računam krivulje razvoja broja i luminoziteta u ovisnosti o crvenom pomaku (engl. *redshift*). Potom razmatram porijeklo radio zračenja u najekstremnijim aktivnim galaktičkim jezgrama - kvazarima - koji su opaženi u području radio i rendgenskog zračenja. U zadnjem dijelu teze, proučavam ima li lokalno galaktičko okruženje utjecaj na prisutnost radio zračenja kod radijativno efikasnih AGN-ova. U daljnjem tekstu radim kratak uvod u područje astrofizike znano kao razvoj galaksija, u sklopu kojeg je napravljen rad predstavljen u ovoj disertaciji.

Ključne riječi: galaksije, aktivne galaktičke jezgre, razvoj galaksija, zračenje u radio području, daleke galaksije, stvaranje zvijezda, kvazari, okruženja

## Razvoj svemira i galaksija u njemu

### Standardni model svemira

Trenutno prihvaćen model svemira -  $\Lambda$ CDM (engl. *Lambda cold dark matter*) - opisuje razvoj svemira i njegovih sastavnica, barionske i tamne tvari te tamne energije, od najranijih trenutaka



do danas (Carroll & Ostlie 2007). Ovaj, tzv. standardni, model svemira počiva na kozmološkom principu i Einsteinovoj teoriji opće relativnosti te opisuje razvoj prostorno izotropnog i homogenog svemira čija geometrija ima Friedman-Robertson-Walkerovu metriku (Frieman et al. 2008). Svemir prema  $\Lambda$ CDM modelu je prostorno ravan te, uz barionsku tvar, sadrži hladnu tamnu tvar (engl. *cold dark matter - CDM*) i tamnu energiju koja pokreće ubrzanu kozmičku ekspanziju. Prema posljednjim rezultatima kolaboracije Planck, naš svemir je ravan i star oko 13.8 milijardi godina, a sadrži 4.95 % bariona, 26.55 % tamne tvari i 68.53 % tamne energije (Planck Collaboration et al. 2018).

Prema standardnom modelu, svemir je nastao velikim praskom, nakon kojeg se sastojao od vruće plazme tvari i fotona, u čijoj su raspodjeli postojale male kvantne fluktuacije. Te fluktuacije bile su preteča svih struktura koje danas opažamo u svemiru. U fazi inflacije, koja je trajala manje od 1 s, dimenzije svemira povećale su se od mikroskopskih do dimenzija većih od trenutno opazivog svemira (npr. Peebles & Ratra 2003, Baumann 2009). Upravo su tijekom inflacije kvantne fluktuacije bile povećane i postale dijelovi svemira u kojima je započelo stvaranje prvih zvijezda i galaksija. Širenje svemira nastavilo se i nakon inflacije, no sporije nego tijekom inflacije. Količina tvari u svemiru nakon velikog praska je konstantna, no njegov volumen se mijenja. Širenjem svemira gustoća energije se smanjuje te se svemir pri ekspanziji hladi. Od početne plazme kvarkova i gluona, stvorili su se protoni i neutroni te se vezali u jezgre prvih elemenata: vodika, helija i malo litija. Tijekom rekombinacije, elektroni su se vezali uz jezgre prvih elemenata tvoreći prve neutralne atome. Preostali fotoni nastavili su se slobodno širiti svemirom sve do danas. Zbog širenja i hlađenja svemira, danas te fotone opažamo kao kozmičko pozadinsko zračenje na 2.7 K (engl. *cosmic microwave background radiation*; Penzias & Wilson 1965).

Struktura u svemiru raste hijerarhijski galaktičkim interakcijama više haloa tamne tvari; mali halo stvoreni su prvi, a potom su veći nastali spajanjima manjih haloa ili prirastom difuzne tamne tvari (npr. Frenk & White 2012). Barionska tvar, u ranom svemiru uglavnom neutralni vodik, slijedi raspodjelu tamne tvari na velikim skalama. Barioni u haloima tamne tvari kraću se prema njihovim gravitacijskim središtima, hlade i kondenziraju, čime započinje stvaranje prvih zvijezda i galaksija.

## Razvoj galaksija

Naša galaksija Mliječna staza tek je jedna od mnogo milijardi galaksija u našem svemiru (npr. Carroll & Ostlie 2007). Područje astronomije poznato kao razvoj galaksija bavi se proučavanjem svojstava galaksija opaženih u različitim trenucima kozmičke povijesti i kako se ta svojstva mijenjaju kroz vrijeme.

Tijekom 20. stoljeća, Edwin Hubble bio je pionir u istraživanju galaksija te je pomoću opažanja teleskopom "Hooker" u sklopu opservatorija "Mount Wilson" pokazao da tzv. galaktičke maglice nisu oblaci plina u našoj Galaksiji, već zasebne galaksije (Hubble 1926, Hubble 1929). Hubble je opažene galaksije grupirao s obzirom na njihove oblike i posložio u tzv. Hubbleovu vilicu. U Hubbleovoj vilici, galaksije su bile poredane od sferičnih, preko eliptičnih i lećastih, do izraženih spiralnih oblika. Spiralne galaksije bile su podijeljene u dvije skupine, ovisno o prisutnost tzv. prečke koja prolazi kroz središte galaksije. Galaksije sferičnog, eliptičnog i lećastog oblika često su bile nazivane galaksijama "ranog tipa", a one spiralnog oblika galaksijama "kasnog tipa". Iako ovakav naziv sugerira da u kozmičkoj povijesti prvo nastaju galaksije ranog, a potom galaksije kasnog tipa, takav smjer razvoja galaksija je pogrešan (npr. Binney & Merrifield 1998, Baldry 2008).

Analize lokalnih uzoraka galaksija otkrile su da postoji bimodalnost u bojama i zvjezdanim masama galaksija (Strateva et al. 2001, Bell et al. 2004, Faber et al. 2007, Conselice 2014). Ta bimodalnost ukazuje na postojanje dvije glavne populacije galaksija, čije je postojanje posljedica toga da se u njima nalaze različite zvjezdane populacije i količine hladnog plina. Tzv. plave galaksije sadrže mnogo hladnog plina i u njima se aktivno odvijaju procesi stvaranja novih zvijezda. Zbog toga plave galaksije sadrže mnogo mladih zvijezda velikih masa koje zrače većinom ultraljubičastu svjetlost, a u vidljivom dijelu elektromagnetskog spektra izgledaju plavo. Statistički gledano, plave galaksije uglavnom imaju spiralne oblike ili oblike u kojima je dominantan galaktički disk te se te galaksije, prema originalnoj Hubbleovoj klasifikaciji, često naziva jednostavno galaksijama kasnog tipa. S druge strane, crvene galaksije imaju male količine hladnog plina, koji je "gorivo" za stvaranje novih zvijezda. Dominantna populacija zvijezda u crvenim galaksijama su stare zvijezde koje većinu svog zračenja zrače u infracrvenim i crvenim bojama vidljivog dijela elektromagnetskog spektra. Crvene galaksije uglavnom su eliptičnog oblika i često ih se naziva galaksijama ranog tipa. U dijagramu boja i zvjezdanih masa (engl. *color-stellar mass diagram*), plave i crvena galaksije zauzimaju različita područja tog dijagrama: plave galaksije tvore tzv. plavi oblak (engl. *blue cloud*), a crvene se nalaze na tzv. crvenom nizu (engl. *red sequence*). Ta dva područja odvojena su tzv. zelenom dolinom (engl. *green valley*) u kojoj je gustoća galaksija znatno manja nego u plavom oblaku i na crvenom nizu. Prema jednostavnom scenariju iz Faber et al. (2007), razvoj galaksija odvija se tako da mlade galaksije, pune hladnog plina, aktivno stvaraju nove zvijezde i nalaze se u plavom oblaku dijagrama boja i zvjezdanih masa. Kako se smanjuje količina hladnog plina u galaksiji, započinje proces gašenja (engl. *quenching*), te se stvara sve manje zvijezda čime galaksija prolazi kroz zelenu dolinu i završava na crvenom nizu.

Koristeći noviji uzorak lokalnih galaksija na  $0.02 < z < 0.05$ , dobiven kombinacijom poda-

taka iz pregleda neba SDSS, od satelita GALEX i iz projekta Galaxy Zoo, [Schawinski et al. \(2014\)](#) su pokazali da situacija nije tako jednostavna. Galaksije u zelenoj dolini sadrže crvene galaksije s tipičnim oblicima kasnog tipa, kao i plave galaksije oblika ranog tipa. To je ukazalo na to uzrok gašenja stvaranja novih zvijezda nije jednak u galaksijama ranog i kasnog tipa. Prema scenariju iz [Schawinski et al.](#), razvoj galaksija kasnog tipa izrazito ovisi o količini dostupnog hladnog plina i njegovom prirastu iz međugalaktičkog prostora. U slučaju da plin prestane pristizati, započinje sporo gašenje stvaranja zvijezda tzv. sekularnim procesima koji se odvijaju unutar galaksije. S druge strane, brzo gašenje stvaranja novih zvijezda kod galaksija ranog tipa posljedica je naglog uništavanja rezervoara plina unutar i oko galaksije procesima spajanja galaksija koje na taj način mijenjaju i boje i oblik iz spiralnog u eliptični. Osim sekularnih procesa i spajanja galaksija, smatra se da velik utjecaj na razvoj galaksija može imati i povratna sprega procesa stvaranja zvijezda i aktivne galaktičke jezgre (npr. [Silverman et al. 2008](#), [Peng et al. 2010](#)). U daljnjem tekstu opisat ću što su aktivne galaktičke jezgre i na koji način mogu utjecati na galaksiju domaćina, njezinu okolinu i njezin razvoj.

## Aktivne galaktičke jezgre

Danas se vjeruje da se u središtu svake masivnije galaksije nalazi supermasivna crna rupa ([Soltan 1982](#)). Ukoliko dolazi do prirasta plina na tu crnu rupu, okolni prostor može emitirati svjetlost valnih duljina duž cijelog elektromagnetskog spektra, od gama zračenja do zračenja u radio području (npr. [Lynden-Bell 1969](#)). U tom slučaju se središnje područje galaksije naziva aktivna galaktička jezgra ili AGN.

## Dva tipa AGN-a i njihov razvoj

Opažanja lokalnog svemira pokazala su da postoje dva glavna tipa AGN-a (npr. [Abazajian et al. 2009](#)). S obzirom na način na koji se energija AGN-a prenosi na njegovu okolinu, razlikujemo radijativno efikasne i neefikasne AGN-ove. Kod radijativno efikasnih AGN-ova većina energije otpuštena je u obliku elektromagnetskog zračenja. Radijativno neefikasni AGN-ovi proizvode relativno malo energije u obliku zračenja, a većinu energije na okolinu prenose u kinetičkom obliku putem mlazova čestica. Ova dva tipa AGN-a razlikuju se u osnovnim svojstvima i s obzirom na galaksije domaćine u kojima se nalaze.

Za radijativno efikasne AGN-ove se smatra da je brzina prirasta tvari na crnu rupu velika te se pretpostavlja se da vrijedi  $\lambda > 0.01$ , gdje je  $\lambda$  Eddingtonov omjer<sup>1</sup> ([Heckman & Best 2014](#)).

---

<sup>1</sup>Eddingtonov omjer bitan je parametar koji opisuje mehanizam prirasta tvari na crnu rupu. Definiran je kao

Oko supermasivne crne rupe postoji tvar koja orbitira u obliku geometrijski tankog, a optički gustog diska prirasta (engl. *accretion disk*). U disku postoji radijalni gradijent temperature zbog čega disk proizvodi kontinuirano zračenje opazivo od vidljivog do ultraljubičastog dijela elektromagnetskog spektra (Shakura & Sunyaev 1973). Oko diska se nalaze oblaci vrućih elektrona koji komptonovski raspršuju fotone emitirane iz diska prirasta, tvoreći rendgensko zračenje sa spektrom koji ima oblik zakona potencije. Područje širokih linija (engl. *broad line region*) nalazi se udaljeno od nekoliko svjetlosnih dana do nekoliko svjetlosnih godina od supermasivne crne rupe. U tom području nalaze se oblaci plina koji su fotoionizirani ionizirajućim zračenjem diska prirasta i njegove okoline, o čemu svjedoče emisijske linije u ultraljubičastom, vidljivom i bliskom infracrvenom području spektra. Na još većim udaljenostima od crne rupe nalazi se neprozirna struktura (engl. *obscuring structure*) sastavljena od prašine i molekularnog plina koji apsorbiraju fotone koji dolaze iz unutarnjih komponenti AGN-a i reemitiraju tu energiju kao termalno infracrveno zračenje. Zbog te strukture pod nekim kutovima gledanja nije moguće vidjeti disk prirasta. U smjeru polarne osi neprozirne strukture, u području uskih linija (engl. *narrow line region*), nalaze se oblaci plina manje gustoće koji stvaraju dozvoljene i zabranjene uske emisijske linije u infracrvenom, optičkom i ultraljubičastom području elektromagnetskog spektra. Također, u nekim slučajevima su kod radijativno efikasnih AGN-ova prisutni i radio mlazovi (engl. *radio jets*) čiji mehanizam nastajanja još uvijek nije u potpunosti razjašnjen. U ovu skupinu AGN-ova pripadaju Seyfertove galaksije i kvazari. Različite podvrste radijativno efikasnih AGN-ova objedinjene su Ujedinjenim modelom AGN-ova prema kojem je orijentacija opažačice u odnosu na središnji dio AGN-a glavni razlog za opažanje velikog broja različitih AGN-ova (Antonucci & Miller 1985, Antonucci 1993). Ukoliko opažačica gleda izravno prema supermasivnoj crnoj rupi i disku prirasta, AGN nazivamo Tip 1, a ukoliko izravnom pogledu smeta neprozirna struktura nazivamo ga Tip 2.

Prirast mase na supermasivnu crnu rupu kod radijativno neefikasnih AGN-ova odvija se manjim brzinama te vrijedi  $\lambda < 0.01$ . Prirast se odvija kroz tzv. tok prirasta dominiran advekcijom (engl. *advection-dominated accretion flow*) koji je geometrijski gust i može usmjeriti električki nabijene čestice u dva mlaza te ih ubrzati do relativističkih brzina (Narayan & Yi 1994, Abramowicz et al. 1995). Te čestice tvore sinkrotronsko zračenje koje je najlakše opaziti u radio području elektromagnetskog spektra. U usporedbi s radijativno efikasnim AGN-ovima, relativno malo energije ovog tipa AGN-ova odlazi na zračenje; većina energije na okolinu se prenosi u kinetičkom obliku preko mlazova čestica.

Pronađeno je da se dva tipa AGN-a nalaze u različitim galaksijama domaćinima (npr. Ka-

---

omjer bolometrijskog i Eddingtonovog luminoziteta AGN-a te kao takav daje mjeru količine energije koju AGN može generirati.

uffmann et al. 2003). Radijativno efikasni AGN-ovi nalaze se uglavnom u galaksijama plavih boja, dok je izglednije da su galaksije domaćini radijativno neefikasnih AGN-ova crvene galaksije s morfologijom ranog tipa. Razlog za ovu razdiobu vjerojatno je blisko povezan uz količinu hladnog plina koji je dostupan galaksiji za stvaranje novih zvijezda i aktivnost galaktičke jezgre. Prirast hladnog plina većim brzinama (tipično većim od 1% Eddingtonove brzine prirasta) radijativno je efikasan i proizvodi obilježja koja se mogu opaziti kao emisijske linije. Zbog toga se AGN-ove koji sadrže takva svojstva često naziva i radijativnim tipom ili tipom kvazara AGN-ova. Ukoliko su radijativno efikasni AGN-ovi opaženi i u radio području, tada ih se također naziva i jako pobuđenim radio galaksijama (engl. *high-excitation radio galaxies*), neke od kojih mogu imati i snažne radio mlazove. U slučaju radijativno neefikasnih AGN-ova, prirast vrućeg plina odvija se malim brzinama (manjim od 1% Eddingtonove brzine prirasta), a glavna energija se prenosi u kinetičkom obliku putem snažnih radio mlazova koji mogu nadjačati sjaj galaksije domaćina u radio području. Budući da ove vrste AGN-ova proizvode relativno malo zračenja često ih se naziva i slabo pobuđenim radio galaksijama (engl. *low-excitation radio galaxies*) ili mlaznim tipom AGN-ova (npr. Best & Heckman 2012, Best et al. 2014, Pracy et al. 2016, Butler et al. 2019).

Otkriće korelacija između svojstava središnje supermasivne crne rupe i svojstava galaksije domaćina ukazuje na to je njihov razvoj kroz povijest svemira međuovisan (Magorrian et al. 1998, King 2014). Također, nađeno je da krivulje razvoja kozmičke gustoće stvaranja zvijezda (engl. *cosmic star formation rate density*) i brzine prirasta supermasivnih crnih rupa (engl. *SMBH accretion rate*) imaju sličan oblik i maksimum na crvenom pomaku  $z \sim 2$  (Madau & Dickinson 2014). Budući da različite tipove AGN-ova nalazimo u različitim galaksijama domaćinima, za očekivati je da će se dva tipa AGN-ova mijenjati različito kroz povijest svemira. To je potvrđeno istraživanjima razvoja spektroskopski selektiranih AGN-ova opaženih u radio području (npr. Best & Heckman 2012, Best et al. 2014, Padovani et al. 2015, Pracy et al. 2016). Dok se radijativno efikasni AGN-ovi opaženi u radio području značajno mijenjaju kroz vrijeme, radijativno neefikasni AGN-ovi opaženi u radio području mijenjaju se vrlo malo.

Unatoč gore navedenim indikatorima povezanosti između razvoja galaksija i rasta supermasivne crne rupe, točni procesi koji ih vežu još nisu u potpunosti jasni. Jedan od kandidata koji bi mogao objasniti tu vezu je povratna sprega AGN-ova.

## Povratna sprega AGN-ova i njihova okruženja

Povratna sprega koja povezuje razvoj AGN-a i galaksije domaćina javlja se u dva oblika: povratna sprega mlaznog tipa (engl. *radio mode feedback*) i povratna sprega tipa kvazara (engl. *quasar mode feedback*, npr. Alexander & Hickox 2012, Croton et al. 2016). Povratna sprega

mlaznog tipa uvedena je kako bi se riješio problem toka hlađenja (engl. *cooling flow problem*) koji se javljao u najranijim poluanalitičkim modelima i numeričkim simulacijama stvaranja strukture u svemiru (npr. [Bower et al. 2006](#), [Croton et al. 2006, 2016](#)). Ta vrsta povratne sprege javlja se u masivnim galaksijama kod kojih radio mlazovi AGN-a prenose kinetičku energiju na svoju okolinu, čime griju plin i zaustavljaju stvaranje novih zvijezda. S druge strane, povratna sprega tipa kvazara povezana je uz periode brzog rasta crne rupe velikim brzinama prirasta u uvjetima spajanja galaksija ili nestabilnosti u disku galaksije. Ti periodi brzog prirasta uzrokuju tzv. vjetrove kvazara (engl. *quasar winds*) koji mogu utjecati na plin u galaksiji tako da ga otpušu iz galaksije, čime efektivno također zaustavljaju ili smanjuju stvaranje novih zvijezda (npr. [Croton et al. 2016](#)).

Istraživanja povratna sprege mlaznog tipa otkrila su da postoji veza između kinetičke energije prenesene na okolinu i monokromatskog radio luminoziteta opaženog radio mlaza AGN-a (npr. [Willott et al. 1999](#), [Merloni & Heinz 2007](#), [Cavagnolo et al. 2010](#), [Godfrey & Shabala 2016](#)). Doduše, u literaturi su prisutne mnoge relacije između kinetičkog i radio luminoziteta, neke od kojih međusobno odstupaju i nekoliko redova veličine (za više informacija, pogledati Prilog A u [Smolčić et al. 2017c](#)). Imajući to u obziru, procjene kinetičkog luminoziteta na temelju opaženog radio luminoziteta mogu se koristiti za procjenu gustoće kinetičkog luminoziteta koja je dalje izravno usporediva s predviđanjima koja daju modeli razvoja galaksija (npr. [Bower et al. 2006](#), [Croton et al. 2006, 2016](#), [Merloni & Heinz 2008](#)).

Proučavanja galaksija u različitim okruženjima dovela su do otkrića da se galaksije različitih oblika nalaze u različitim okruženjima (npr. [Conselice 2014](#)). Tako primjerice masivne galaksije ranog tipa, u kojima su dominantna populacija zvijezda one starije, nalazimo u gušćim okruženjima, dok manje masivne galaksije kasnog tipa nalazimo u okruženjima manje gustoće (npr. [Dressler 1980](#), [Hashimoto et al. 1998](#)). Sličan trend pronađen je i za AGN-ove: radijativno neefikasne AGN-ove često nalazimo u znatno gušćim okruženjima, kao što su jata i grupe galaksija, nego radijativno efikasne AGN-ove, koje najčešće nalazimo u područjima manje gustoće galaksija (npr. [Best et al. 2005b](#), [Heckman & Best 2014](#)).

## Pregledi neba na više valnih duljina

Za proučavanje svojstava AGN-ova, njihovih galaksija domaćina te kako se oni mijenjaju kroz povijest svemira, potrebno je napraviti opažanja na što je više moguće valnih duljina. Pregledi neba fokusirani na određeni dio, tzv. polje (engl. *field*), nebeske sfere osmišljeni su kako bi napravili velik broj opažanja galaksija unutar tih polja kako bi mogli odgovoriti na aktualna astrofizička pitanja svog vremena. U ovoj disertaciji koristim podatke iz dva takva pregleda



neba, opisana u daljnjem tekstu.

## Podaci u nebeskom polju COSMOS

COSMOS (skraćena od engl. *Cosmic Evolution Survey*) je pregled neba na više valnih duljina osmišljen za istraživanje stvaranja i razvoja galaksija u svemiru od najranijih trenutaka do danas (Scoville 2007). U sklopu ovog pregleda neba proučava se dio nebeske sfere površine dva kvadratna stupnja zvan polje COSMOS. COSMOS je opažen na valnim duljinama od radio valova do rendgenskih zraka koristeći vrhunske teleskope poput svemirskih teleskopa Hubble, Spitzer, XMM-Newton, Chandra i Herschel te zemaljskih teleskopa VLA<sup>2</sup>, Subaru, VLT<sup>3</sup>, itd. Zahvaljujući brojnim opažanjima, preko 2 milijuna galaksija su pronađena u kozmičkim epohama od najranijeg svemira pa sve do danas.

## Podaci na više valnih duljina unutar polja COSMOS

Kompilacija fotometrijskih podataka sakupljenih za izvore u polju COSMOS objavljena je u obliku kataloga COSMOS2015 (Laigle et al. 2016). U katalogu su sabrani podaci u rasponu od ultraljubičastog do infracrvenog dijela elektromagnetskog spektra za preko milijun izvora. Ti podaci prikupljeni su svemirskim teleskopima GALEX<sup>4</sup>, Spitzer i Herschel, te zemaljskim teleskopima CFHT<sup>5</sup> i Subaru. Usporedbom kataloga COSMOS2015 i kataloga rendgenski opaženih izvora u sklopu pregleda neba Chandra COSMOS-Legacy, pronađeno je ukupno 4016 izvora (Civano et al. 2016, Marchesi et al. 2016).

## Veliki projekt VLA-COSMOS na 3 GHz

U sklopu Velikog projekta VLA-COSMOS na 3 GHz COSMOS polje bilo je opažano 384 sati teleskopom VLA (Smolčić et al. 2017a). Opažanja dijela nebeske sfere površine  $2.6 \text{ deg}^2$ , centrirane na polju COSMOS, na 3 GHz (10 cm) dosegla su  $1\sigma$  osjetljivost od  $2.3 \mu\text{Jy}/\text{beam}$  preko unutarnja  $2 \text{ deg}^2$  s kutnom razlučivošću od  $0.75''$ . Ukupan broj izvora opaženih preko cijelog polja COSMOS s omjerom signala i šuma (engl. *signal-to-noise ratio*) većim ili jednakim pet iznosi 10,830.

Radio podaci izvora opaženih na 3 GHz kombinirani su s katalogom COSMOS2015, čime je pronađeno podudaranje za 7,729 radio izvora (Smolčić et al. 2017b). Za  $\sim 31\%$  tih izvora

---

<sup>2</sup>VLA - Very Large Array

<sup>3</sup>VLT - Very Large Telescope

<sup>4</sup>GALEX - Galaxy Evolution Explorer

<sup>5</sup>CFHT - Canada-France-Hawaii Telescope

dostupni su pouzdani spektroskopski crveni pomaci, dok su za ostale ( $\sim 69\%$ ) dostupni fotometrijski crveni pomaci. Za 33% izvora opaženih na 3 GHz unutar polja COSMOS, dostupni su i radio podaci na 1.4 GHz (Schinnerer et al. 2007, 2010). Oni omogućuju određivanje spektralnog indeksa za izvore opažene na 1.4 i 3 GHz. Za ostale izvore se pretpostavlja da je spektralni indeks  $-0.7$ , što je vrijednost koja se očekuje za radio zračenje koje nije termičko (Condon 1992) te se slaže sa srednjim spektralnim indeksom pronađenim za sve izvore opažene na 3 GHz (Smolčić et al. 2017a).

### Populacije galaksija

Radio izvori opaženi u sklopu Velikog projekta VLA-COSMOS na 3 GHz, koji su opaženi i na ostalim valnim duljinama, podijeljeni su u sljedeće populacije galaksija: AGN-ove malog do srednjeg radijativnog luminoziteta (MLAGN), AGN-ove srednjeg do visokog radijativnog luminoziteta (HLAGN) i zvjezdorodne galaksije (SFG). Klasifikacija izvora na te populacije opisana je detaljno u članku Smolčić et al. (2017b). Ukratko, HLAGN-i su odabrani s obzirom obilježja koja se očekuju od radijativno efikasnog prirasta na supermasivnu crnu rupu: veliki luminozitet u rendgenskom području ( $L_X \geq 10^{42} \text{ erg s}^{-1}$ ) i značajna količina infracrvenog zračenja od neprozirnog područja identificirana preko dijagrama boja (engl. *color-color diagram*) i spektralnih energijskih raspodjela tih izvora. Izvori koji ne zadovoljavaju te kriterije klasificirani su kao MLAGN-i ili SFG-ovi.

Na temelju prilagodbe spektralnih energijskih raspodjela fotometrijskim podacima, za svaki izvor određen je i luminozitet u infracrvenom području koji dolazi od procesa stvaranja zvijezda, ispravljen za eventualni doprinos od aktivnosti galaktičke jezgre (Delvecchio et al. 2017). Brzine stvaranja zvijezda (engl. *star formation rates*) izračunate su koristeći te luminozitete i jednadžbu iz Kennicutt 1998, uz pretpostavku početne funkcije mase iz Chabrier 2003.

U konačnici, 1,604 HLAGN-a, 1,619 MLAGN-a i 4,506 SFG-a klasificirano je među izvorima koji su opaženi na 3 GHz i za koje postoje podaci u katalogu COSMOS2015. U dijelu analize koristim skup svih tih izvora te ih oslovljavam kao "cijeli uzorak".

### Katalog rendgenskih grupa galaksija

Gozaliasl et al. (2019) su identificirali 247 grupa opaženih u rendgenskom području unutar  $2 \text{ deg}^2$  polja COSMOS. Za identifikaciju su koristili opažanja u rendgenskom području prikupljena svemirskim teleskopima XMM-Newton i Chandra. Tzv. X grupe opažene su do granične gustoće toka zračenja  $S_X[0.5 - 2 \text{ keV}] = 3 \times 10^{-16} \text{ erg cm}^{-2} \text{ s}^{-1}$  i nalaze se na crvenim pomacima  $0.08 < z < 1.53$ . Slijedeći metodu opisanu u Finoguenov et al. (2009), koristeći kombi-



naciju osjetljivijih podataka u rendgenskom području, [Gozaliasl et al.](#) su identificirali središta X grupa. Masa grupa  $M_{200C}$  određena je unutar radijusa  $R_{200}$ , definiranog tako da opisuje površinu oko središta grupe unutar koje je gustoća haloa 200 puta veća od kritične gustoće svemira. U njihovom katalogu<sup>6</sup> sabrane su informacije o položaju središta grupa,  $R_{200}$  i crveni pomaci.

## Podaci u nebeskom polju XXL-S

Pregled neba XXL projekt je usmjeren na opažanja AGN-ova i jata galaksija s ciljem određivanja parametara bitnih za bolje određivanje kozmoloških modela i razumijevanja fizikalne pozadine supermasivnih crnih rupa i njihovog razvoja kroz povijest svemira u različitim okolinama ([Pierre et al. 2016](#)). Bazira se na rendgenskim opažanjima dva nebeska polja, XXL-N (skraćenog od engl. *XXL-North*) i XXL-S (skraćeno od engl. *XXL-South*), ukupne površine  $50 \text{ deg}^2$  teleskopom XMM-Newton. Osim rendgenskih opažanja, polja su opažena teleskopima GALEX, VISTA<sup>7</sup>, Spitzer, WISE<sup>8</sup>, GMRT<sup>9</sup> i ATCA<sup>10</sup>, čime je sakupljeno obilje podataka diljem elektromagnetskog spektra.

## Podaci na više valnih duljina unutar polja XXL-S

Obilje fotometrijskih i spektroskopskih podataka na više valnih duljina za izvore opažene u polju XXL-S sakupljeno je u katalogu opisanom detaljno u [Fotopoulou et al. \(2016\)](#). Katalog sadrži podatke na valnim duljinama u ultraljubičastom, vidljivom i infracrvenom području elektromagnetskog spektra za nekoliko milijuna galaksija opaženih teleskopima GALEX, Vista, Spitzer i WISE ([Morrissey et al. 2005](#), [McMahon et al. 2013](#), [Wright et al. 2010](#), [Ashby et al. 2013](#)). Rendgenska opažanja polja XXL-S teleskopom XMM-Newton dosegla su granične vrijednosti toka zračenja  $S_X[0.5 - 2 \text{ keV}] = 6 \times 10^{-15} \text{ erg s}^{-1}$  i  $S_X[2 - 10 \text{ keV}] = 2 \times 10^{-14} \text{ erg s}^{-1}$  ([Pierre et al. 2016](#)). Rendgenski tokovi zračenja dodani su katalogu izvora opaženih na više valnih duljina ([Fotopoulou et al. 2016](#)) te su pomoću njih izračunati rendgenski luminoziteti  $L_X[2 - 10 \text{ keV}]$ .

## Pregled polja XXL-S na 2.1 GHz teleskopom ATCA

Polje XXL-S, čija je površina  $25 \text{ deg}^2$ , opaženo je na 2.1 GHz teleskopom ATCA, što je detaljno opisano u [Butler et al. \(2018a\)](#). Osjetljivost od  $1\sigma = 41 \mu\text{Jy}/\text{beam}$  dosegnuta je uz kutnu

<sup>6</sup><https://academic.oup.com/mnras/article/483/3/3545/5211093#supplementary-data>

<sup>7</sup>VISTA - Visible and Infrared Survey Telescope for Astronomy

<sup>8</sup>WISE - Wide-field Infrared Survey Explorer

<sup>9</sup>GMRT - Giant Metrewave Radio Telescope

<sup>10</sup>ATCA - Australia Telescope Compact Array

rezoluciju 4.8". Broj opaženih izvora s omjerom signala i šuma većim ili jednakim pet je 6,287. Za podskup nerazlučenih izvora, radio opažanja na 2.1 GHz podijeljena su u podpojaseve (engl. *sub-bands*) centrirane na 1,417 MHz, 2,100 MHz i 2,783 MHz kako bi se odredili spektralni indeksi tih izvora na temelju njihove gustoće toka zračenja unutar tih podpojaseva (Butler et al. 2018b). Tom metodom određeni su spektralni izvori za ~61% (3,827/6,287) izvora.

Katalog optičkih izvora (Fotopoulou et al. in prep) uspoređen je s radio podacima, čime je pronađeno podudaranje za 4,770 izvora (Ciliegi et al. 2018). Nakon što je 12 izvora u tom skupu klasificirano kao zvijezde te odbačeno, broj izvora opaženih u radio području s podacima na više valnih duljina je 4,758. Ti izvori klasificirani su u Butler et al. (2018b) kao SFG-ovi i AGN-ovi. 23% izvora ima pouzdana mjerenja spektroskopskih crvenih pomaka, dok ostali izvori (77%) imaju dostupna mjerenja fotometrijskih crvenih pomaka ( $\sigma_{\Delta z/1+z} = 0.062$ ).

### Kozmologija i izračun radio luminoziteta

Kroz ovu disertaciju pretpostavljam da vrijedi kozmološki model  $\Lambda$ CDM s  $H_0 = 70 \text{ km s}^{-1} \text{ Mpc}^{-1}$ ,  $\Omega_m = 0.3$  i  $\Omega_\Lambda = 0.7$ . Pretpostavljam da spektar sinkrotronskog zračenja slijedi zakon potencije  $S_\nu \propto \nu^\alpha$ , gdje je  $S_\nu$  gustoća toka zračenja opaženog na frekvenciji  $\nu$ , a  $\alpha$  spektralni indeks. Radio luminoziteti na 1.4 GHz izračunati su iz gustoće toka zračenja  $S_{\nu_0}$  preko formule:

$$L_{1.4\text{GHz}} = \frac{4\pi D_L^2(z)}{(1+z)^{1+\alpha}} \left( \frac{1.4\text{GHz}}{\nu_0} \right)^\alpha S_{\nu_0},$$

gdje je  $z$  crveni pomak,  $\nu_0$  frekvencija opažanja (3 GHz za COSMOS, 2.1 GHz za XXL-S, a  $D_L$  luminozitetna udaljenost.

### Porijeklo zračenja u radio području kod dalekih galaksija

Najnoviji pregledi neba u radio području daju nam jedinstveni uvid u daleki svemir i vrijeme nastanka prvih galaksija i AGN-ova. Budući da kozmička prašina ne utječe na radio valove, njihovo opažanje omogućuje izravan pogled na stvaranje zvijezda i aktivnost AGN-ova u galaksijama sve do najranijih trenutaka svemira. Za preglede neba u radio području koriste se radio interferometri, teleskopi koji se sastoje od nekoliko međusobno povezanih antena. Koristeći metodu radio interferometrije, interferometar ostvaruje veću osjetljivost i kutnu rezoluciju nego li bi to mogli njegovi zasebni teleskopi. Podaci u radio području korišteni u ovom istraživanju opaženi su radio interferometrima VLA i ATCA.

Sinkrotronsko radio zračenje, opaženo u sklopu vangalaktičkih opažanja neba, uzrokovano je procesima koji su posljedica aktivnosti AGN-ova (radio mlazovi; Blandford & Rees 1974) ili

procesima vezanim uz stvaranje zvijezda (ostaci supernovae eksplozija; [Kennicutt 1998](#)). Radijativno neefikasni AGN-ovi nalaze se u domaćinima galaksijama u kojima se stvara relativno malo novih zvijezda te se za njih očekuje da većina opaženog radio zračenja dolazi od aktivnosti AGN-ova. To zračenje može doći od jezgara, mlazova ili mjehura AGN-ova, koji u ekstremnim slučajevima mogu prodrijeti do skala van galaksije gdje se nalazi tvar u jatima galaksija te se može opaziti do velikih udaljenosti. S druge strane, radijativno efikasni AGN-ovi često imaju galaksije domaćine u kojima su aktivni procesi stvaranja zvijezda te je ukupno radio zračenje koje opažamo kombinacija radio zračenja koje dolazi od procesa stvaranja zvijezda i aktivnosti AGN-a. Većina izvora opaženih u radio području do velikih crvenih pomaka nije razlučena i morfološka razdioba opaženog radio luminoziteta nije moguća (npr. [Bonzini et al. 2013](#), [Smolčić et al. 2017a](#), [Butler et al. 2018a](#)). No, uz pretpostavku da su galaksije domaćini radijativno efikasni AGN-ova slične SFG-ovima koji su opaženi u istoj kozmičkoj epohi, ukupni radio luminozitet može se razdvojiti na doprinos od procesa stvaranja zvijezda i aktivnosti AGN-a putem korelacije pronađene između infracrvenog i radio zračenja (IRRC; engl. *infrared-radio correlation*) u SFG-ovima.

IRRC, koji povezuje ukupno infracrveno i radio zračenje, prvi put je otkriven za uzorak lokalnih galaksija 1990-ih godina, od kada je provjeravan na mnogim uzorcima u lokalnom i dalekom svemiru (npr. [Helou et al. 1985](#), [Condon 1992](#), [Yun et al. 2001](#), [Calistro Rivera et al. 2017](#), [Delhaize et al. 2017](#)). Porijeklo korelacije su procesi stvaranja zvijezda unutar galaksija u kojima se stvaraju velike količine mladih masivnih zvijezda i koje su bogate plinom i prašinom koji su gorivo za stvaranje zvijezda. Mlade i masivne zvijezde zrače velike količine energije u međuzvjezdani prostor ispunjen prašinom. Ta prašina apsorbira zračenje zvijezda i emitira ga kao zračenje u dalekom infracrvenom području. Mlade, masivne zvijezde imaju relativno kratak životni vijek ( $\sim 10^{6-7}$  godina) koji završavaju u eksplozijama supernovae, čiji ostaci ubrzavaju elektrone kozmičkih zraka do relativističkih brzina koji potom proizvode sinkrotronsko zračenje koje se opaža u radio području. Životni vijek tih relativističkih elektrona je oko 10 puta dulji od životnog vijeka masivnih zvijezda, čime je uzrokovan IRRC, koji vrijedi preko nekoliko redova veličina infracrvenog i radio luminoziteta ([Condon et al. 1991](#)). IRRC je tipično izražen preko parametra  $q \propto \log(L_{\text{IR,SF}}/L_{\text{radio}})$ , koji povezuje luminozitet u infracrvenom području,  $L_{\text{IR,SF}}$ , koji dolazi od procesa stvaranja zvijezda i luminozitet u radio području,  $L_{\text{radio}}$ .

## Porijeklo zračenja u radio području i kozmički razvoj AGN-ova srednjeg do jakog radijativnog luminoziteta

U ovoj disertaciji predstavljam statističku metodu razdiobe radio luminoziteta kojom, putem IRRC-a, procjenjujem količinu radio zračenja koja dolazi od procesa stvaranja zvijezda i računam radio luminozitet AGN-a. Radio luminozitate AGN-ova koristim za određivanje funkcija luminoziteta u radio području te na temelju njih određujem krivulje razvoja radijativno efikasnih AGN-ova opaženih u radio području.

Uzorak 1,604 radijativno efikasnih AGN-ova opaženih u radio području u sklopu VLA-COSMOS velikog projekta na 3 GHz (Smolčić et al. 2017b), tzv. HLAGN-i, odabran je na temelju obilježja detektiranih u rendgenskom i srednjem infracrvenom području (Smolčić et al. 2017b, Delvecchio et al. 2017). Analizom svojstava galaksija domaćina HLAGN-a, Delvecchio et al. (2017) su pokazali da su te galaksije slične SFG-ovima. To potvrđuje ideju da radio zračenje ovih izvora sadrži dvije komponente, doprinos od procesa stvaranja zvijezda i aktivnosti AGN-a, te je razdioba luminoziteta nužna kako bi se mogao odrediti razvoj radijativno efikasnih AGN-ova opaženih u radio području.

### Statistička metoda razdiobe radio luminoziteta

Ukupni luminozitet opažen u radio području ( $L_{1.4 \text{ GHz, TOT}}$ ) sadrži dva doprinosa: luminozitet procesa stvaranja zvijezda ( $L_{1.4 \text{ GHz, SF}}$ ) i aktivnosti AGN-a ( $L_{1.4 \text{ GHz, AGN}}$ ). Kako bih provela metodu razdiobe luminoziteta, koristim IRRC kalibriran na *cijelom uzorku*, odnosno na uzorku svih izvora opaženih na 3 GHz za koje postoje podaci u katalogu COSMOS2015 i u kojima su dominantni procesi stvaranja zvijezda. Ta korelacija prikladnija je za naš uzorak HLAGN-a, jer nije izvedena na uzorku koji sadrži granične vrijednosti luminoziteta, kao što su primjerice napravili Delhaize et al. (2017). Koristeći IRRC kalibriran u devet intervala crvenog pomaka i luminozitate u infracrvenom području koji dolaze od procesa stvaranja zvijezda, procjenjujem iznos luminoziteta u radio području koji dolazi od procesa stvaranja zvijezda. To mi omogućuje određivanje radio luminoziteta AGN-a za svaki izvor te računanje parametra  $f_{\text{AGN}}$  definiranog kao udio radio zračenja AGN-a u ukupnom radio luminozitetu. Neodređenosti svih izračunatih vrijednosti,  $L_{1.4 \text{ GHz, SF}}$ ,  $L_{1.4 \text{ GHz, AGN}}$  i  $f_{\text{AGN}}$ , procijenjene su Monte Carlo simulacijama, uzimajući u obzir pogreške mjerenja ukupnog radio luminoziteta i luminoziteta u infracrvenom području koji dolazi od procesa stvaranja zvijezda.

Dekompozicijom radio luminoziteta nalazim da  $68.0 \pm 1.5\%$  HLAGN-a ima radio luminozitet u kojem dominantan udio čine procesi stvaranja zvijezda ( $0 \leq f_{\text{AGN}} \leq 0.5$ ). Kod ostatka

HLAGN-a, njih  $32.0 \pm 1.5\%$ , dominantan doprinos radio zračenju dolazi od aktivnosti AGN-a ( $0.5 < f_{\text{AGN}} \leq 1.0$ ). Ovi rezultati slažu se s onima temeljenim na sličnim uzorcima iz literature (npr. [Hickox et al. 2009](#), [Delvecchio et al. 2017](#)).

## Funkcija luminoziteta AGN-ova u radio području

Kako bih odredila radio funkcije luminoziteta AGN-ova, dalje koristim samo podskup izvora kod kojih postoji doprinos radio zračenju koji dolazi od AGN-a ( $f_{\text{AGN}} > 0$ ). Za pravilan odabir izvora za konstrukciju funkcije luminoziteta, potrebno je uzeti u obzir nekompletnosti koje bi mogle nastati kao posljedica granične gustoće toka zračenja danog opažanja neba ( $S_{3\text{GHz,lim}}$ ), kao i posljedice korištenja metode dekompozicije luminoziteta. Zbog toga, nakon što za svaki izvor izračunam gustoću toka zračenja AGN-a kao  $S_{3\text{GHz,AGN}} = f_{\text{AGN}} \times S_{3\text{GHz,TOT}}$ , za odabir uzorka koristim i kriterij  $S_{3\text{GHz,AGN}} \geq S_{3\text{GHz,lim}}$ , čime se osigurava da u izračun funkcije luminoziteta ulaze svi izvori koji imaju gustoću toka zračenja AGN-a iznad granične vrijednosti radio opažanja. Time dobivam uzorak od 575 HLAGN-a s crvenim pomacima  $0.1 \leq z \leq 6.1$  čije AGN radio luminozitate koristim u izračunu funkcija luminoziteta AGN-ova u radio području.

Funkcije luminoziteta, definirane kao broj izvora po intervalu luminoziteta proučavan u određenoj kozmičkoj epohi, koriste se da bi se odredila razvojna krivulja brojčane i luminozitetne gustoće za neku populaciju izvora (npr. [Best & Heckman 2012](#), [Pracy et al. 2016](#)). Uzorak HLAGN-a podijeljen je u devet intervala crvenog pomaka te su za svaki interval izračunate funkcije luminoziteta. U izračunu funkcija luminoziteta koristim tzv. metodu  $V_{\text{max}}$  ([Schmidt 1968](#)), kojom se procjenjuje maksimalan volumen unutar kojeg je moguće opaziti svaki od AGN-ova u uzorku, uzimajući u obzir površinu nebeske sfere pokrivenu radio opažanjima, kao i kompletnost radio kataloga. Procijenjene su Poissonove pogreške ([Marshall 1985](#)) te, u slučaju da je broj izvora po intervalu luminoziteta bio manji ili jednak deset, korigirane za statistiku malih brojeva ([Gehrels 1986](#)). Ovakav izračun funkcija luminoziteta konzistentan je izračunu iz [Smolčić et al. \(2017c\)](#) i [Novak et al. \(2017\)](#).

Dobivene vrijednosti funkcija luminoziteta AGN-ova usporedive su s onima konstruiranim na sličnim uzorcima (npr. [Best et al. 2014](#), [Pracy et al. 2016](#)). Usporedba s rezultatima iz [Padovani et al. \(2015\)](#), temeljenih na uzorku radio tih AGN-ova, pokazuje neslaganje na nižim radio luminozitetima zbog doprinosa procesa stvaranja zvijezda koji u njihovom uzorku nije uzet u obzir.

Kako bih odredila kako se HLAGN-i mijenjaju kroz povijest svemira, koristim analitički oblik lokalne funkcije luminoziteta iz [Pracy et al. \(2016\)](#). Pronašla sam da je taj oblik lokalne funkcije luminoziteta prikladan za prilagodbu na AGN funkcije luminozitate HLAGN-a, budući

da je radio zračenje uzorka na kojem je određen taj analitički oblik dominirano radio luminozitetom AGN-a. Prilagodбом analitičkog oblika lokalne funkcije luminoziteta iz [Pracy et al. \(2016\)](#), koji ima oblik zakona dvostruke potencije, na AGN funkcije luminoziteta u devet intervala crvenog pomaka testirala sam dva modela razvoja: razvoj luminoziteta (engl. *pure luminosity evolution*) i razvoj gustoće izvora (engl. *pure density evolution*). Vrijednosti parametara razvoja, dobivene u sklopu oba modela, smanjuju se s povećanjem crvenih pomaka.

Koristeći analitičke oblike funkcija luminoziteta određene u devet intervala crvenog pomaka, određujem krivulje razvoja brojčane i luminozitetne gustoće. Obje krivulje ukazuju na to su se i brojčana i luminozitetna gustoća povećavale od viših crvenih pomaka ( $z \sim 6$ ) do trenutka kada je svemir bio star oko 4 milijarde godina ( $z \sim 1.5$ ), nakon čega su se smanjile na vrijednost opaženu u lokalnom ( $z \sim 0$ ) svemiru.

Postojanje radio luminoziteta koji dolazi od aktivnosti AGN-a u uzorku nerazlučenih HLAGN-a ukazuje na to da je moguće da to zračenje, barem kod dijela uzorka, dolazi od radio mlazova. Radio mlazovi, prolazeći kroz okolni medij, mogu prenijeti energiju na svoju okolinu, grijući je, što može za posljedicu imati zaustavljanje stvaranja novih zvijezda (npr. [Fabian 2012](#)). Ta povratna sprega mlaznog tipa moguće je objašnjenje za vezu između razvoja galaksija domaćina i AGN-a. Kako bih procijenila gustoću kinetičkog luminoziteta na temelju radio zračenja AGN-a, koristim korelaciju između kinetičkog luminoziteta i monokromatskog radio luminoziteta iz [Wiltott et al. \(1999\)](#). Krivulja razvoja gustoće kinetičkog luminoziteta pokazuje da se ta gustoća povećavala od većih crvenih pomaka sve do maksimuma na crvenim pomacima  $1 < z < 2.5$ , nakon čega se smanjila do vrijednosti opažene u lokalnom svemiru. Usporedba te krivulje s rezultatima poluanalitičkog modela stvaranja galaksija GALFORM ([Lacey et al. 2016](#), [Griffin et al. 2019](#)) pokazuje slaganje na crvenim pomacima manjim od  $z \sim 3$ , no neslaganje postoji na većim crvenim pomacima.

## Porijeklo zračenja u radio području kod rendgenski selektivnih kvazara

Podskup radijativno efikasnih AGN-ova su kvazari, AGN-i jako velikog luminoziteta. Iako je prvi kvazar ikad otkriven bio otkriven kao izvor snažnog radio zračenja ([Schmidt 1963](#)), većina kvazara zapravo ne emitira snažno radio zračenje. Istraživanja provedena na uzorcima nezatamljenih (engl. *unobscured*) tzv. tip 1 kvazara, čije su jedno od obilježja široke emisijske spektralne linije, ukazuju na postojanje dvije populacije, tzv. radio tihih i radio glasnih kvazara (npr. [Ivezić et al. 2002](#)). Niti nakon nekoliko desetljeća istraživanja ne zna se postoji li fizi-



kalni razlog za postojanje te dvije populacije (npr. [Kellermann et al. 1989](#), [White et al. 2000](#)). Standardan pristup ovom problemu je proučavanje tzv. parametra radio glasnoće (engl. *radio loudness*) koji je najčešće definira kao omjer luminoziteta u radio području i luminoziteta u optičkom području (npr. [Kellermann et al. 1989](#)). Luminozitet u radio području posljedica je radio zračenja mlaza relativističkih čestica, dok zračenje u vidljivom području dolazi od zračenja čestica u disku prirasta koji se nalazi oko crne rupe ([Heckman & Best 2014](#)). Bimodalnost u raspodjeli parametra radio glasnoće nađena je u istraživanjima uzoraka kvazara selektiranih na temelju obilježja u vidljivom području ([Kellermann et al. 1989](#), [Ivezić et al. 2002](#)) i ukazuje na to da je postojanje radio glasne i radio tihe populacije posljedica različitih fizikalnih svojstava, kao što su različite mase, brzine prirasta ili različiti spinovi supermasivnih crnih rupa ([Heckman & Best 2014](#)).

Kako bih pristupila problemu porijekla radio zračenja kvazara, kombiniram uzorke izvora opaženih u radio području s podacima na više valnih duljina opaženih u nebeskim poljima COSMOS i XXL-S. Kako bih odabrala samo najsjajnije izvore koji su sigurno kvazari ([Pado-vani et al. 2017](#)), postavljam prag u rendgenskom luminozitetu  $L_X[2 - 10 \text{ keV}] \geq 10^{44} \text{ erg s}^{-1}$ , čime dobivam uzorak od 274 kvazara na crvenim pomacima  $0.1 < z < 6.1$  koje dalje nazivam XQSO-ima.

Koristim četiri različite definicije radio glasnoće koje međusobno povezuju radio luminozitet AGN-a te optički luminozitet AGN-a, rendgensko zračenje AGN-a, kao i infracrveno zračenje galaksije domaćina. Uporabom prikladnih pragova u tim raspodjelama radio glasnoće na temelju vrijednosti iz literature ([Kellermann et al. 1989](#), [Miller et al. 1990](#), [Goldschmidt et al. 1999](#), [Pierce et al. 2011](#), [Delvecchio et al. 2017](#)) nalazim da različite definicije odabiru različite uzorke u kojima postotak radio glasnih XQSO-a varira od  $\sim 18\%$  do  $\sim 73\%$  i kao takve nisu precizna metoda proučavanja porijekla zračenja kvazara u radio području.

Alternativni pristup proučavanja porijekla radio zračenja je putem oblika funkcije luminoziteta ([Kimball et al. 2011](#), [Condon et al. 2013](#)). Svojim istraživanjima na temelju uzoraka optički selektiranih kvazara, [Kimball et al. \(2011\)](#) i [Condon et al. \(2013\)](#) su ukazali na to da procesi u pozadini opaženog radio zračenja ostavljaju otisak na obliku funkcije luminoziteta. Rezultati [Kimball et al. \(2011\)](#) ukazuju da viša normalizacija funkcije luminoziteta u radio području od one očekivane samo od doprinosa aktivnosti AGN-a dolazi od procesa stvaranja zvijezda u galaksiji domaćinu kvazara. Koristeći njihov pristup, koristim podskup od 267 XQSO-a na crvenim pomacima  $0.5 < z < 3.75$  i određujem radio funkcije luminoziteta u šest intervala crvenog pomaka. Za prilagodbu na podatke funkcija luminoziteta, koristim analitičke oblike lokalne funkcije luminoziteta iz istraživanja [Kimball et al. \(2011\)](#) i [Condon et al. \(2013\)](#), gdje funkcija luminoziteta [Kimball et al. \(2011\)](#) služi za određivanje oblika u području nižih radio lu-

minoziteta, a [Condon et al. \(2013\)](#) za određivanje oblika u području visokih radio luminoziteta. Nalazim da se XQSO-i mijenjaju značajno u brojčanoj gustoći kroz povijest svemira.

Koristeći funkcije luminoziteta određene u različitim intervalima crvenog pomaka, definiram pragove u radio luminozitetu na 1.4 GHz ispod i iznad kojeg više od 80% izvora koji doprinose funkciji luminoziteta imaju radio zračenje dominirano procesima stvaranja zvijezda, odnosno aktivnošću AGN-a. Uspoređujući te rezultate s vrijednosti parametra  $q_{TOT}$ <sup>11</sup>, potvrđujem da povećana normalizacija funkcije luminoziteta XQSO-a u području nižih radio luminoziteta dolazi od toga da je radio zračenje izvora u tom režimu dominirano zračenjem od procesa stvaranja zvijezda. S druge strane, izvori koji doprinose funkciji luminoziteta u području visokih radio luminoziteta imaju radio zračenje kojem je glavni doprinos aktivnost galaktičke jezgre. Ovi rezultati potvrđuju dihotomiju procesa koji leže u pozadini opaženog radio zračenja kod XQSO-a.

## Okruženja AGN-ova opaženih u radio području

Lokalno okruženje galaksije domaćina može imati učinak na razvoj same galaksije, kao i njezinog AGN-a ([Conselice 2014](#)). Istraživanja su pronašla da su svojstva galaksija korelirana s njezinom morfologijom: galaksije koje nalazimo u lokalnim okruženjima veće gustoće često imaju morfologiju ranog tipa galaksija te stvaraju relativno male količine novih zvijezda ([Blanton & Moustakas 2009](#), [Conselice 2014](#)). S druge strane, brzina stvaranja zvijezda u galaksijama povećava se sa smanjenjem gustoće lokalnog okruženja. Sličan trend pronađen je i za AGN-ove u lokalnom svemiru: radijativno neefikasni AGN-ovi najčešće se nalaze u središtima grupa i jata galaksija, dok su radijativno efikasni AGN-ovi češći u područjima niže gustoće galaksija (npr. [Best et al. 2005b](#), [Heckman & Best 2014](#)). S obzirom na prisustvo radio zračenja, izglednije je da radijativno efikasni AGN-ovi pronađeni u gušćim okruženjima budu radio glasni, što vjerojatno ukazuje na to da se ti AGN-ovi nalaze u galaksijama veće mase nego je to slučaj za radio tihe AGN-ove ([Shen et al. 2009](#)).

Kako bih proučavala okruženja AGN-ova opaženih u radio području, na temelju položaja uspoređujem katalog X grupa ([Gozaliasl et al. 2019](#)) i AGN-ove opažene u radio području za koje postoje podaci na više frekvencija (HLAGN i MLAGN). Pronalazim 43 HLAGN-a i 72 MLAGN-a u X grupama na crvenim pomacima  $0.2 < z < 1.3$ . Rezultati ukazuju da se  $f_{AGN}$ <sup>12</sup> HLAGN-a i MLAGN-a u X grupama smanjuju s povećanom udaljenošću od središta grupe.

<sup>11</sup>Kao i u slučaju HLAGN-a, parametar  $q_{TOT}$  proporcionalan je omjeru luminoziteta u infracrvenom području koji dolazi od procesa stvaranja zvijezda i ukupnog opaženog radio luminoziteta.

<sup>12</sup>Parametar  $f_{AGN}$  definiran je kao i u metodi razdiobe radio luminoziteta, tj. kao omjer radio luminoziteta koji dolazi od aktivnosti AGN-a i ukupnog opaženog radio luminoziteta.



# Contents

|          |  |           |
|----------|--|-----------|
| <b>1</b> | <b>Introduction</b>                                    | <b>1</b>  |
| 1.1      | The universe we live in . . . . .                      | 1         |
| 1.1.1    | $\Lambda$ CDM universe . . . . .                       | 2         |
| 1.1.2    | Expansion and the first stars . . . . .                | 3         |
| 1.1.3    | Hierarchical growth of structures . . . . .            | 4         |
| 1.2      | Galaxy evolution . . . . .                             | 5         |
| 1.2.1    | Hubble tuning fork . . . . .                           | 5         |
| 1.2.2    | Color and stellar mass evolution of galaxies . . . . . | 6         |
| 1.3      | Active galactic nuclei . . . . .                       | 8         |
| 1.3.1    | AGN dichotomy . . . . .                                | 11        |
| 1.3.2    | AGN evolution . . . . .                                | 14        |
| 1.3.3    | AGN feedback . . . . .                                 | 16        |
| 1.3.4    | Environments . . . . .                                 | 17        |
| 1.4      | Panchromatic surveys . . . . .                         | 18        |
| 1.4.1    | The COSMOS survey . . . . .                            | 18        |
| 1.4.2    | The XXL survey . . . . .                               | 19        |
| 1.5      | Radio view of the sky . . . . .                        | 20        |
| 1.5.1    | Radio interferometry . . . . .                         | 20        |
| 1.5.2    | Origin of radio emission in distant galaxies . . . . . | 23        |
| 1.5.3    | Radio luminosity functions . . . . .                   | 26        |
| 1.6      | Thesis outline . . . . .                               | 29        |
| <b>2</b> | <b>Data</b>  | <b>30</b> |
| 2.1      | COSMOS data-sets . . . . .                             | 30        |
| 2.1.1    | Multiwavelength data . . . . .                         | 30        |
| 2.1.2    | The VLA-COSMOS 3 GHz Large Project . . . . .           | 31        |
| 2.1.3    | Galaxy populations . . . . .                           | 31        |
| 2.1.4    | X-ray group catalog . . . . .                          | 33        |
| 2.2      | XXL-S data-set . . . . .                               | 33        |
| 2.2.1    | The XXL-S multiwavelength data . . . . .               | 34        |
| 2.2.2    | The 2.1 GHz ATCA XXL-S Survey . . . . .                | 34        |

|          |  |           |
|----------|--|-----------|
| <b>3</b> | <b>Methods</b>   | <b>35</b> |
| 3.1      | 1.4 GHz radio luminosity . . . . .   | 35        |
| 3.2      | Statistical method of the radio luminosity decomposition . . . . .   | 36        |
| 3.2.1    | Star formation in HLAGN host galaxies . . . . .  | 36        |
| 3.2.2    | Decomposition of the 1.4 GHz radio luminosity . . . . .  | 38        |
| 3.3      | Radio luminosity function . . . . .  | 41        |
| 3.3.1    | Maximum observable volume ( $V_{\max}$ ) method . . . . .  | 41        |
| 3.3.2    | Constructing radio luminosity functions . . . . .  | 42        |
| 3.3.3    | Evolution of the radio luminosity function . . . . .   | 42        |
| <b>4</b> | <b>Star formation properties and radio luminosity functions of radio-detected AGN in the COSMOS field out to <math>z \sim 6</math></b>     | <b>44</b> |
| 4.1      | Decomposition of the radio luminosity . . . . .  | 45        |
| 4.1.1    | HLAGN . . . . .  | 45        |
| 4.1.2    | The full sample . . . . .  | 46        |
| 4.2      | Radio AGN luminosity functions . . . . .   | 47        |
| 4.2.1    | HLAGN AGN radio luminosity functions and their cosmic evolution out to $\sim 6$ . . . . .  | 47        |
| 4.2.2    | Radio AGN luminosity functions and the cosmic evolution of AGN within the full 3 GHz sample . . . . .                                      | 58        |
| 4.3      | Discussion . . . . .   | 61        |
| 4.3.1    | Origin of radio emission in HLAGN . . . . .  | 62        |
| 4.3.2    | Cosmic evolution of radio AGN . . . . .  | 65        |
| 4.3.3    | Kinetic feedback of radio AGN and comparison with semi-analytic models . . . . .   | 66        |
| 4.4      | Chapter summary and conclusions . . . . .  | 71        |
| <b>5</b> | <b>The quasar radio loudness dichotomy exposed via radio luminosity functions by combining the COSMOS and XXL-S X-ray selected quasars</b> | <b>73</b> |
| 5.1      | Chapter introduction . . . . .   | 73        |
| 5.2      | X-ray and radio selected quasars . . . . .   | 75        |
| 5.2.1    | Sample selection . . . . .   | 75        |
| 5.2.2    | Infrared and B-band luminosities . . . . .   | 75        |
| 5.2.3    | Radio spectral indices . . . . .   | 76        |
| 5.3      | Radio loudness . . . . .   | 77        |
| 5.4      | Cosmic evolution of XQSO RLFs . . . . .  | 82        |
| 5.4.1    | Local luminosity function . . . . .  | 85        |
| 5.4.2    | Cosmic evolution of XQSOs . . . . .  | 86        |
| 5.5      | Discussion . . . . .   | 88        |
| 5.5.1    | Host galaxies of XQSOs . . . . .   | 89        |
| 5.5.2    | AGN-related radio emission in XQSOs . . . . .  | 92        |
| 5.5.3    | Origin of XQSO radio emission . . . . .  | 92        |
| 5.6      | Chapter summary and conclusions . . . . .  | 95        |

---

|          |   |            |
|----------|---|------------|
| <b>6</b> | <b>Environments of radio-detected AGN within the COSMOS field</b> | <b>96</b>  |
| 6.1      | Chapter introduction . . . . .                                    | 96         |
| 6.2      | Radio-detected AGN in X-ray groups . . . . .                      | 98         |
| 6.3      | Results . . . . .   | 98         |
| 6.4      | Discussion . . . . .  | 99         |
| 6.5      | Chapter summary and conclusions . . . . .                         | 101        |
| <b>7</b> | <b>Thesis summary and outlook</b>                                 | <b>103</b> |
| 7.1      | Summary of this Thesis . . . . .                                  | 103        |
| 7.2      | Future work . . . . .   | 107        |
|          | <b>References</b>   | <b>109</b> |
|          | <b>Curriculum vitae</b>   | <b>117</b> |

# List of Figures

|      |  |    |
|------|--|----|
| 1.1  | The Cosmic Microwave Background radiation. . . . .   | 2  |
| 1.2  | The expansion of the universe. . . . .   | 3  |
| 1.3  | Hubble tuning fork diagram. . . . .  | 6  |
| 1.4  | The color-mass diagram of SDSS galaxies. . . . .   | 7  |
| 1.5  | Image of the shadow of a SMBH. . . . .   | 9  |
| 1.6  | The central engines of two types of AGN. . . . .   | 12 |
| 1.7  | The schematic representation of the broad-band spectral energy distribution of AGN. . . . .  | 14 |
| 1.8  | Comparison of star formation history and SMBH accretion history. . . . .   | 15 |
| 1.9  | Two main modes of AGN feedback in galaxies. . . . .  | 16 |
| 1.10 | Examples of AGN feedback observed in local galaxies. . . . .   | 17 |
| 1.11 | Density field of the dark matter distribution simulated with Millenium run. . . . .  | 18 |
| 1.12 | The 2deg <sup>2</sup> COSMOS field. . . . .  | 19 |
| 1.13 | XXL-North and XXL-South fields. . . . .  | 20 |
| 1.14 | The basic element of radio interferometer. . . . .   | 21 |
| 1.15 | The VLA and ATCA. . . . .  | 23 |
| 1.16 | Redshift evolution of the infrared-radio correlation. . . . .  | 25 |
| 1.17 | Radio luminosity functions of AGN. . . . .   | 28 |
| 2.1  | The classification scheme of the VLA-COSMOS 3 GHz sources with COSMOS2015 multiwavelength counterparts. . . . .  | 32 |
| 3.1  | Infrared-to-1.4 GHz radio luminosity ratio vs. $L_{1.4 \text{ GHz}}$ for HLAGN. . . . .  | 37 |
| 3.2  | Example of one iteration of the $q_{\text{TOT}}$ distribution for the HLAGN. . . . .   | 39 |
| 4.1  | Infrared-to-1.4 GHz radio luminosity ratio vs. redshift for the full sample and HLAGN. . . . .   | 45 |
| 4.2  | Histogram of median AGN fractions of the HLAGN and full samples. . . . .   | 46 |
| 4.3  | Radio AGN luminosity function at 1.4 GHz at redshifts $0.1 < z < 6.1$ of HLAGN. . . . .  | 48 |
| 4.4  | Distribution of the ratio of 1.4 GHz radio luminosity to SFR as a function of the 1.4 GHz radio luminosity for HERGs and SFGs drawn from the LARGESS sample. . . . . | 53 |
| 4.5  | Local HERG luminosity function. . . . .  | 54 |

|      |  |     |
|------|--|-----|
| 4.6  | Parameters obtained from fitting two different redshift evolution models to the HLAGN luminosity functions. . . . .                        | 55  |
| 4.7  | 1.4 GHz AGN luminosity function of the full VLA-COSMOS 3 GHz Large Project sample with COSMOS2015 counterparts out to $z \sim 6$ . . . . . | 57  |
| 4.8  | Fitting parameters obtained to model the redshift evolution of the full AGN sample. . . . .  | 61  |
| 4.9  | VLBA-to-VLA AGN flux density ratio vs. 1.4 GHz AGN luminosity. . . . .   | 63  |
| 4.10 | Redshift evolution of the number and luminosity density of AGN in COSMOS field. . . . .  | 67  |
| 4.11 | Cosmic evolution of the kinetic luminosity density. . . . .  | 69  |
| 5.1  | Distributions of redshifts and spectral indices of XQSOs. . . . .  | 76  |
| 5.2  | Radio loudness vs. redshift of XQSOs from COSMOS and XXL-S. . . . .  | 78  |
| 5.3  | Venn diagram of COSMOS and XXL-S XQSOs classified as radio-loud based on three criteria. . . . .   | 80  |
| 5.4  | $R_X$ vs. 1.4 GHz luminosity color-coded by the AGN fraction of XQSOs. . . . .   | 82  |
| 5.5  | Radio luminosity function at 1.4 GHz of the radio and X-ray selected quasars at redshifts $0.50 < z < 3.75$ . . . . .                      | 83  |
| 5.6  | Parameters of evolution obtained from fitting Model 1 and Model 2. . . . .   | 87  |
| 5.7  | $L_{\text{IR,SF}}$ vs. $L_X[2 - 10 \text{ keV}]$ of XQSOs. . . . .   | 89  |
| 5.8  | An example of how luminosity thresholds $L_{\text{t,SF}}$ and $L_{\text{t,AGN}}$ were defined. . . . .                                     | 91  |
| 5.9  | $q_{\text{TOT}}$ vs. redshift of COSMOS (upper panel) and XXL-S (lower panel) XQSOs. . . . .   | 94  |
| 6.1  | Distributions of AGN fractions and ratio of AGN fractions of the AGN within X-ray groups and of the parent population. . . . .             | 99  |
| 6.2  | AGN fractions vs. the distances from the centers of the X-ray groups of HLAGN and MLAGN. . . . .   | 100 |
| 6.3  | The number of HLAGN and MLAGN at different distances from the X-ray group center. . . . .  | 101 |
| 6.4  | The number of sources vs. the distance from the center of the X-ray groups. . . . .  | 102 |

# List of Tables

|     |   |    |
|-----|---|----|
| 4.1 | AGN luminosity functions for the HLAGN population. . . . .  | 50 |
| 4.2 | Best-fit redshift evolution parameters for HLAGN. . . . .   | 56 |
| 4.3 | AGN luminosity functions for the full VLA-COSMOS 3 GHz Large Project sample with COSMOS2015 multiwavelength counterparts. . . . .                                     | 59 |
| 4.4 | Best-fit evolution parameters obtained for the full sample. . . . .   | 62 |
| 5.1 | Number of XQSOs defined as RL or RQ based on different criteria of radio loudness. . . . .  | 81 |
| 5.2 | Radio luminosity functions of the radio and X-ray selected quasars. . . . .   | 84 |
| 5.3 | Evolution parameters of XQSOs derived for the two evolution models. . . . .   | 88 |
| 5.4 | Number of COSMOS and XXL-S XQSOs divided in ranges of $L_{1.4 \text{ GHz}}$ defined on the basis of the thresholds $L_{t,\text{SF}}$ and $L_{t,\text{AGN}}$ . . . . . | 93 |

# Chapter 1

## Introduction

In this Thesis, I present the work which concerns the origin of radio emission of a special kind of radio-detected AGN which are hosted by galaxies in which there are ongoing processes of star formation. In the following sections, I will introduce the cosmological framework within which the analysis presented in this Thesis is done. The field of galaxy evolution will be introduced, along with its currently open questions, especially those related to the role of the active galactic nucleus (AGN) in the evolution of galaxies. To study properties of AGN and their host galaxies I exploit the multiwavelength data-sets available within the COSMOS and XXL-S sky fields. Both the AGN activity and star formation can produce radio emission so, to study its origin and how it evolves over time, it is important to know the relative contribution of both of these processes to the total observed radio emission. This is especially important in the case of sources that are unresolved in our surveys. I use the new high-quality radio data obtained with the radio interferometers Karl G. Jansky Very Large Array and Australia Telescope Compact Array. These data enable us to study the origin of radio emission within our sample of AGN out to the earliest times when the universe was only at 10% of its current age.

### 1.1 The universe we live in

Due to the finite value of the speed of light in a vacuum ( $299,792,458 \text{ m s}^{-1}$ ), the further away an object is away from us, the longer it takes for its light to reach us. In other words, the further away the object is from us, we see it earlier in cosmic history. The theoretical and observational discovery of the cosmic expansion changed our understanding of the universe and has provided us with tools for studying distant stars, galaxies and the very first light to ever shine upon us - the cosmic microwave background (CMB) radiation. In this section, I describe the basic principles of the currently accepted cosmological model - the Lambda Cold Dark Matter ( $\Lambda$ CDM) model

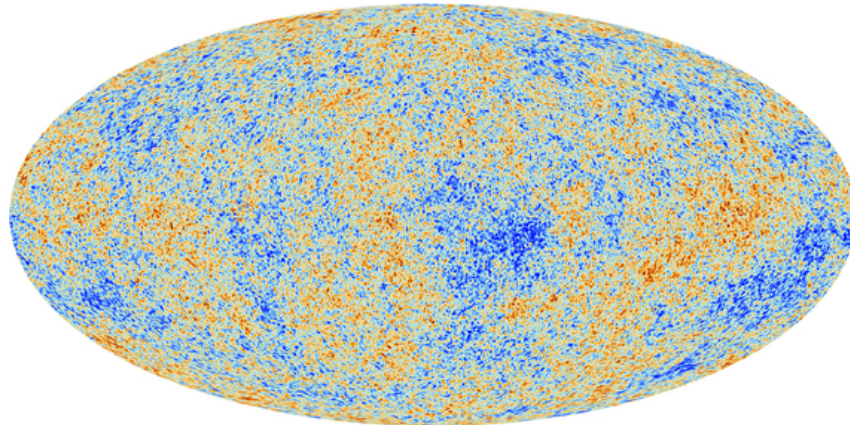


Figure 1.1: The cosmic microwave background radiation. This faint relic radiation, originating from the era of recombination, shows the fluctuations in the density of the primordial universe. Credit: ESA and the Planck Collaboration.

and its basic principles.

### 1.1.1 $\Lambda$ CDM universe

The  $\Lambda$ CDM model, also known as the *standard model* of Big Bang cosmology, is the most successful set of recipes for building a universe like the one we live in. It describes the evolution of the universe and its components, baryonic matter, dark matter, and dark energy, from the earliest times to today (e.g., [Carroll & Ostlie 2007](#)). Its building blocks are the *Cosmological Principle* and Einstein's theory of *General Relativity*. Together they govern the evolution of the spatially isotropic and homogeneous universe whose geometry is described by the Friedman-Robertson-Walker metric (e.g., [Frieman et al. 2008](#)). The  $\Lambda$ CDM predicts that the universe is spatially flat and composed of matter and the mysterious dark energy, which is assumed to be the driving force of the accelerating cosmic expansion. Only around one-sixth of the total matter is regular baryonic matter<sup>1</sup>, while the rest is the elusive dark matter hidden from our standard observing methods as it does not emit any light. The dark matter in  $\Lambda$ CDM is assumed to be cold, which means that it moves slowly compared to the speed of light and is hence called *cold dark matter* (CDM). Based on the latest results from the Planck collaboration ([Planck Collaboration et al. 2018](#)), our universe is  $\sim 13.8$  Gyr old, flat and contains roughly 68.53 % dark energy and 26.55 % dark matter, while only 4.95 % of the universe is baryonic matter.

<sup>1</sup>The strict physical definition of baryonic matter is that it is composed purely of baryons: protons, neutrons and all matter composed of them. In astronomy, baryonic matter is considered to be all objects composed of atomic matter, since protons and neutrons are always accompanied by electrons. The presence of electrons is usually ignored, as they are only a small fraction of the total mass. Neutrinos are non-baryonic matter.



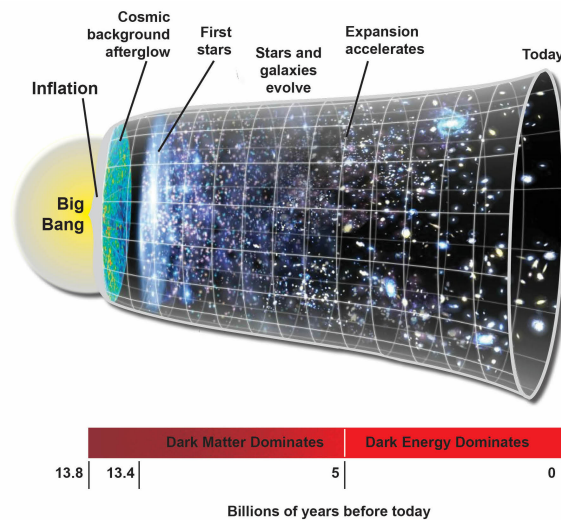


Figure 1.2: The expansion of the universe according to the current  $\Lambda$ CDM model. Credit: NASA, SKA

These results were obtained from observations of the relic CMB radiation, first discovered by Arno Penzias and Robert Wilson using a 6 m horn antenna at Bell Labs (Penzias & Wilson 1965). This radiation provides a unique map (see Fig. 1.1) that tells us what the universe looked like when it was only 366000 yr old. The nearly isotropic spatial distribution of the CMB in the sky carries information about the distribution of mass in the young universe, from which the first stars and galaxies started to grow.

### 1.1.2 Expansion and the first stars

The standard hot Big Bang model assumes that the universe at its beginning was in a state of extremely hot plasma composed of a nearly homogeneous distribution of photons and matter. However, small quantum fluctuations existed, which were the seeds of all the structures seen in the universe today. During the era of rapid accelerated superluminal expansion called *inflation*, which lasted less than 1 s, the universe has grown from a microscopic size to a size larger than the currently visible universe (e.g., Peebles & Ratra 2003, Baumann 2009). During this period, the small quantum fluctuations ‘inflated’ into the sites where the first stars and galaxies were to form. After the inflation, expansion continued, but at a slower pace. The energy density decreased during expansion (the same amount of energy is contained within the increasing volume) and the universe cooled over time. From the original plasma of quarks and gluons, protons and neutrons assembled, later forming the nuclei of the first elements: hydrogen, helium, and lithium. In the epoch of *recombination*, electrons became bound with the nuclei forming the first neutral atoms. The remaining photons continued traveling freely through the universe until

the present day. Due to cosmic expansion, they cooled over time and are today observable in the microwave range of the electromagnetic spectrum as the CMB radiation. After the formation of the first neutral atoms, the universe was filled mostly with neutral hydrogen gas which was slowly gravitationally influenced by the first dark matter halos. During this epoch, the first stars were slowly forming in the potential wells of dark matter halos (White & Rees 1978). As there were yet no sources of light, this epoch in cosmic history is known as the *dark ages*. However, the neutral hydrogen gas can be detected via its 21 cm emission line even before the time the first stars formed. Mapping of the spatial distribution of hydrogen gas in the early universe and how it condenses into first stars will be one of the missions of the Square Kilometre Array<sup>2</sup> (SKA) telescope, currently under construction. The first stars formed within the first billion years after the Big Bang and were most likely very massive ( $\geq 100M_{\odot}$ ), hot and short-lived (e.g. Abel et al. 2002). During this time, called the *epoch of reionization*, mostly neutral interstellar and intracluster medium became once again ionized by the very energetic radiation of massive stars. These first stars have never yet been detected and will be the subject of studies planned with the upcoming James Webb Space Telescope<sup>3</sup> (JWST).

### 1.1.3 Hierarchical growth of structures

The structure in the universe grows hierarchically: smaller dark matter halos form first, while the larger halos form by mergers of pre-existing halos and accretion of the diffuse dark matter (e.g., Frenk & White 2012). Baryonic matter appears to follow the distribution of the dark matter on larger scales, as found through observational studies of the Lyman- $\alpha$  forest<sup>4</sup> (e.g., McDonald et al. 2005). As primordial small mass halos ( $\sim 10^6 M_{\odot}$ ) collapse, the baryons within these halos collapse with them, cooling and condensing at the centers of the halos to form the first stars and galaxies. The distribution of dark matter is fairly well understood based on N-body numerical simulations (e.g., Springel et al. 2005b, Klypin et al. 2011). However, several processes involving baryon physics that govern the (magneto)hydrodynamics of the formation of stars and galaxies, as well as the role of different kinds of energetic feedback, are still not well understood (Madau & Dickinson 2014). These processes are tested within the semi-analytic (e.g., Croton et al. 2006, 2016, Fanidakis et al. 2011, Lacey et al. 2016) and hydrodynamic

---

<sup>2</sup><https://www.skatelescope.org/>

<sup>3</sup><http://www.jwst.nasa.gov>

<sup>4</sup>The Lyman- $\alpha$  forest is the part of the spectrum of distant quasars or galaxies in which a ‘forest’ of absorption lines appear. These absorption lines are observational evidence of the existence of the intergalactic medium, mostly composed of neutral hydrogen clouds. As the light of the distant source passes through these clouds, the hydrogen gas absorbs the light of wavelength 1215.67 Å which corresponds to a Lyman- $\alpha$  atomic transition of the hydrogen atom. Since the gas clouds are located at different distances from us, the absorption lines are redshifted by different amounts, leading to the appearance of a forest of hundreds of absorption lines in the spectra of distant sources.

simulations of galaxy formation (e.g., [Katz et al. 1992](#), [Springel et al. 2005a](#), [Crain et al. 2009](#), [Vogelsberger et al. 2014](#), [Weinberger et al. 2017](#)). Despite the success of these simulations in reproducing the global properties of galaxies, we are still far from a complete understanding of the way structure in the universe grows and evolves. In the following section, I summarize the current understanding of galaxy evolution.

## 1.2 Galaxy evolution

At the beginning of the 20<sup>th</sup> century, astronomers thought we lived in a unique galaxy which was the largest part of our universe, full of bright stars, none of which seemed to have planets around them (e.g., [Carroll & Ostlie 2007](#)). However, the next 100 years of exploration changed everything. In this short time of the universe, scientists and engineers developed technology and gathered knowledge about the stars in our Galaxy, most of which have planets around them. Furthermore, it was found that our galaxy is just one in many billions of galaxies being pushed and pulled in the universe by the interplay of cosmic expansion and gravity ([Penzias & Wilson 1965](#), [Peebles & Ratra 2003](#), [Frieman et al. 2008](#)). With an ever-increasing number of galaxies being detected, astronomers discovered that the galaxies change over time in their colors, shapes, and sizes (e.g., [Stoughton et al. 2002](#), [Lintott et al. 2008](#), [Abazajian et al. 2009](#), [Schawinski et al. 2014](#)) - opening a chapter of astronomy known as galaxy evolution.

### 1.2.1 Hubble tuning fork

Based on observations at the Mount Wilson Observatory, Edwin Hubble showed that galactic nebulae were not just gas clouds within our galaxy but separate neighboring galaxies ([Hubble 1929](#)). With the discovery of more and more galaxies, came the need to sort them based on their basic properties. Hubble ([Hubble 1926](#)) used a classification scheme based on rotational symmetry about the centers of galaxies, splitting them into two main morphological classes - the elliptical and spiral galaxies. In the so-called Hubble sequence or Hubble tuning fork diagram (see [Fig. 1.3](#)), the local elliptical galaxies were separated from those with the most spheroidal shape to those with selongated elliptical shapes. The galaxies of transitional shape, between the elliptical and spiral galaxies, were thought to be those of lenticular shape, which have the central bulge and disk, but no spiral arms. Spiral galaxies were separated into two classes, depending on the presence of the bar structure, in both of which the shape changed from a bulge dominated with tightly wound spiral arms toward that with smaller bulges and widely open spiral arms. The elliptical and lenticular galaxies are often referred to as ‘*early-type*’ galaxies,

while the spiral galaxies are referred to as ‘*late-type*’ galaxies. This nomenclature originates from the incorrectly assumed direction of galaxy evolution within the Hubble diagram, where the galaxies of spiral shape evolve later in cosmic time from the elliptical galaxies present at earlier times of the universe (e.g., [Binney & Merrifield 1998](#), [Baldry 2008](#)).

## 1.2.2 Color and stellar mass evolution of galaxies

Based on the studies of local samples of galaxies, a bimodality in galaxy colors has been found, revealing the existence of two main galaxy populations ([Strateva et al. 2001](#), [Bell et al. 2004](#), [Faber et al. 2007](#), [Conselice 2014](#)). The difference in their colors and stellar masses reflects the difference in their stellar and gas content. The so-called ‘blue’ galaxies are dust rich systems with active processes of star formation which produce a significant number of young massive stars. These young stars radiate ultraviolet (UV) light and appear blue in optical light. In a statistical sense, these galaxies are mostly found to have spiral and disk-dominated morphologies and are sometimes referred to simply as late-type galaxies (after the original Hubble classification). On the other hand, ‘red’ galaxies are dominated by older stellar populations which radiate most of their light in the visible red and infrared ranges of the electromagnetic spectrum. These galaxies typically have less cold gas available for the formation of new stars and hence

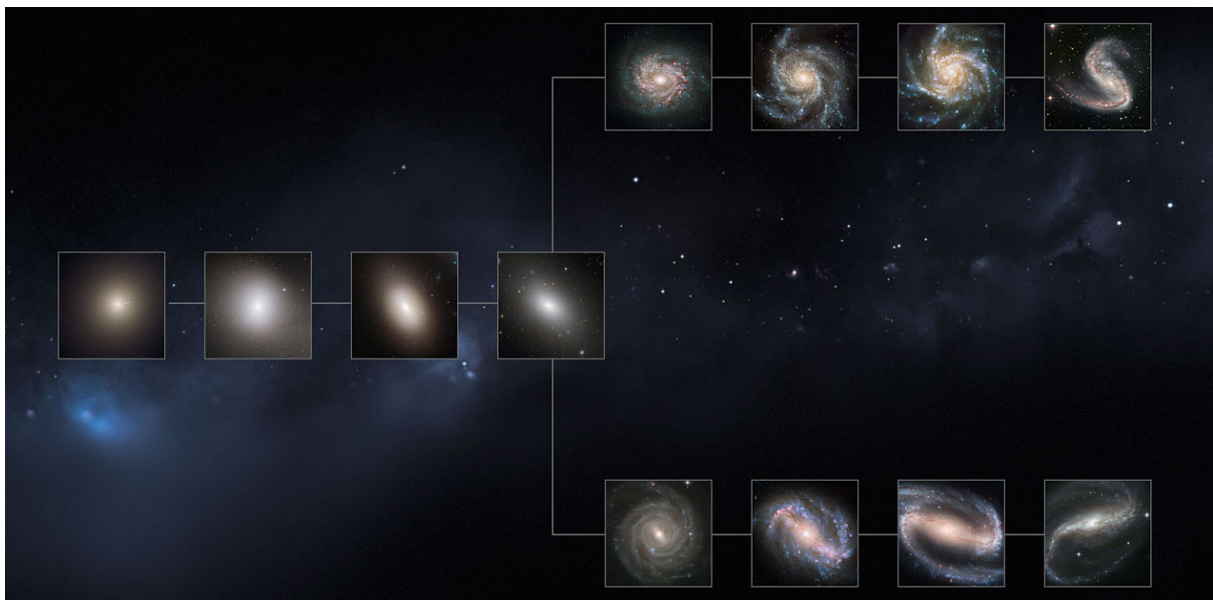


Figure 1.3: Hubble tuning fork diagram. Galaxies are sorted from the most spherical on the left to the transitional lenticular shape in the middle. Spiral galaxies are divided into those having a bar feature (lower branch) and those without it (upper branch), with the ones on the right having the least tightly wound spiral arms. Image credit: NASA, ESA, M. Kornmesser.

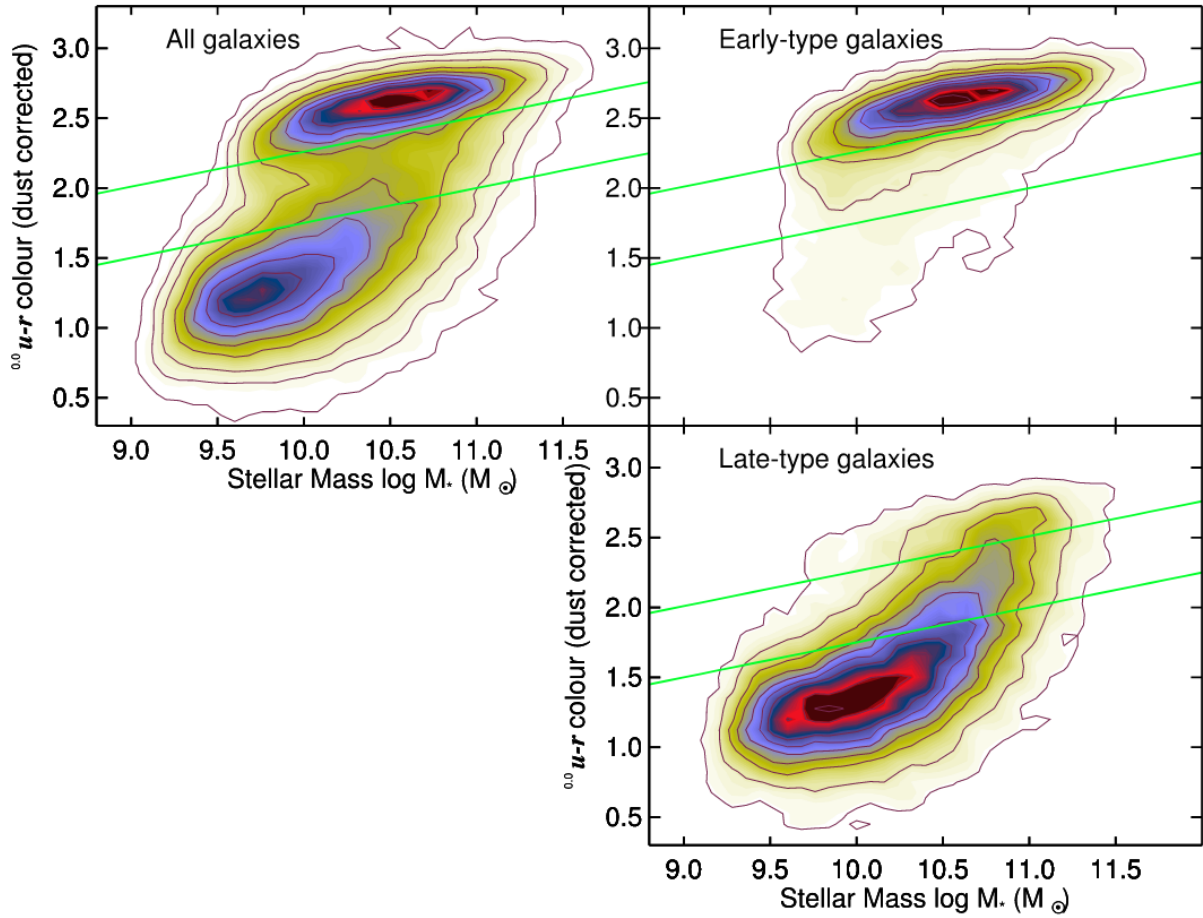


Figure 1.4: The color-mass diagram of SDSS galaxies, morphologically classified within the Galaxy Zoo project. The contours in each panel show the linear density of galaxies. The left upper panel shows all the galaxies in the sample, while the right panels show the sample split by galaxy morphology: early- and late-type galaxies in the upper and lower right panels, respectively. Green lines show the green valley. The image is taken from [Schawinski et al. \(2014\)](#).

appear ‘red and dead’. They mostly have elliptical morphologies and are hence referred to as early-type galaxies. Blue and red galaxies have been found to occupy different regions of the color-stellar mass diagram - the so-called *blue cloud* and *red sequence*. These two regions are separated by the ‘*green valley*’ in which the density of galaxies is significantly lower than on the red sequence and the blue cloud. As proposed in a relatively simple scenario by [Faber et al. \(2007\)](#), galaxy evolution is a result of the quenching of star formation within the galaxies. In this scenario, galaxies start their life as star-forming systems with blue colors within the blue cloud. As the quenching starts, star formation slowly declines over time and the galaxies move through a green valley finally settling on the red sequence.

A similar conclusion was reached by [Schawinski et al. \(2014\)](#) who studied colors of local



galaxies at  $0.02 < z < 0.05$  using data from the Sloan Digital Sky Survey (SDSS), GALEX satellite and a citizen science project Galaxy Zoo<sup>5</sup>. As shown in the upper left panel of Fig. 1.4, a clear bimodality in galaxy colors is seen for these local galaxies, with red and blue regions of the plot containing a high density of galaxies, separated by the region of the lower galaxy density - the green valley. Star-forming galaxies (SFGs) follow a tight correlation between their star formation rates (SFRs) and galaxy stellar mass, hereafter referred to as the ‘*main sequence*’ which changes only in normalization with redshift (e.g., Whitaker et al. 2012). However, when the sample is split with respect to galaxy morphologies (right panels of Fig. 1.4), some red galaxies have late-type morphologies, while some blue galaxies have early-type morphologies. The green valley galaxies contain both late- and early-type morphologies and are offset from the main sequence of star formation, with early-type galaxies showing larger offset than the late-type ones. Schawinski et al. suggest that there are two mechanisms behind quenching in late- and early-type galaxies. According to their scenario, the evolution of late-type galaxies is governed by the cosmic gas supply which, when shut off, causes slow exhaustion of the remaining gas over several billions of years during which secular processes<sup>6</sup> and the galactic environment play a key role in changing the colors and the shape of these galaxies. On the other hand, the rapid quenching in early-type galaxies may be explained by a scenario in which the gas supply and gas reservoirs are destroyed almost instantaneously as a consequence of a major merger<sup>7</sup> which then transforms the galaxy from a disk to an elliptical morphology. The quenching of star formation in local blue galaxies is assumed to be related to major mergers between several blue galaxies or feedback processes from star formation or AGN activity (e.g., Silverman et al. 2008, Peng et al. 2010). In the following section, I will focus on AGN, their cosmic evolution and the influence they might have on the evolution of their host galaxies.

### 1.3 Active galactic nuclei

Active galactic nuclei are powerful extragalactic sources visible across the entire electromagnetic spectrum, from the gamma-rays to the radio. The current paradigm for AGN fueling is that the central engine consists of a supermassive black hole (SMBH) surrounded by an accretion

---

<sup>5</sup><http://zoo1.galaxyzoo.org/>

<sup>6</sup>Secular processes are those behind the slow and steady evolution of the galaxy. It is thought that these processes are internal to the galaxy and include the action of spiral arms or bars on the evolution of galaxy via the formation of new stars, hence being more important in the late- than in the early-type galaxies.

<sup>7</sup>A galaxy merger is the result of a collision between two or more galaxies. If the mass of the colliding galaxies is being considered, they can be divided into minor and major mergers. Minor mergers are those in which one galaxy is significantly more massive than the other(s), while during the major merger colliding galaxies have similar masses.

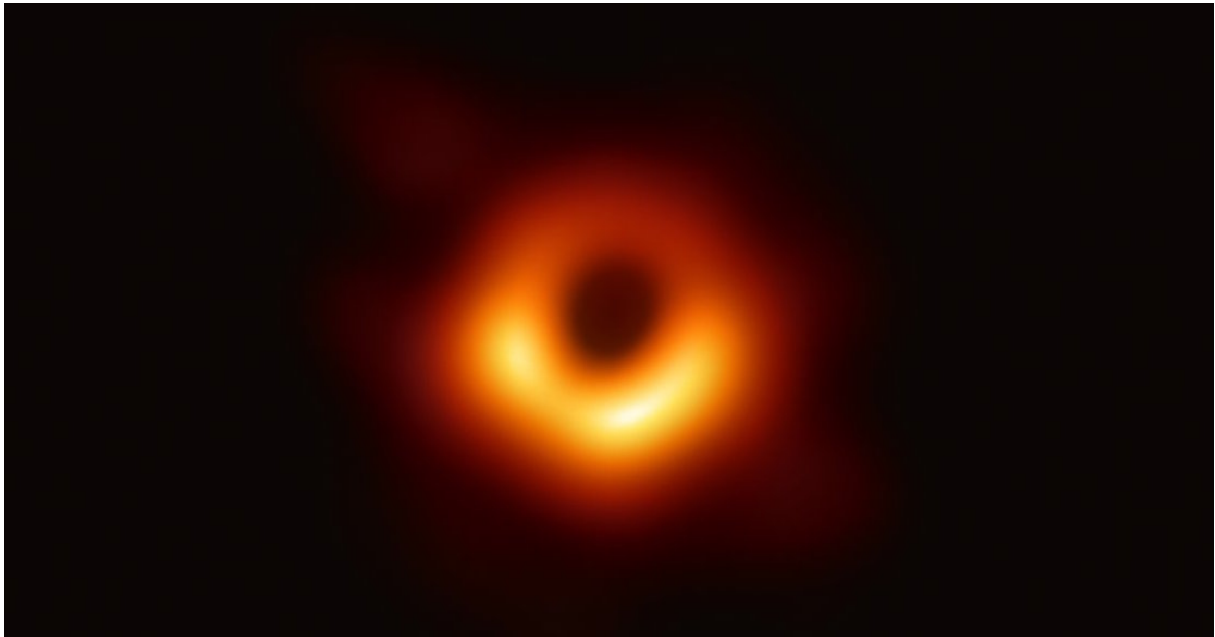


Figure 1.5: The first image of the shadow of a supermassive black hole obtained using the Event Horizon Telescope. The image shows the SMBH M87\* in the heart of the active center of galaxy M87. Credit: EHT collaboration.

disk. The energy is released in a process of accretion of matter from the accretion disk onto the SMBH.

The first imaging of the shadow of a SMBH was performed within the central area of the giant elliptical galaxy Messier 87, which was known to harbor a low-luminosity AGN (Di Matteo et al. 2000). This galaxy, central to the Virgo cluster, has been well studied over the entire electromagnetic spectrum ever since it was first classified as a galaxy at the beginning of the 20<sup>th</sup> century (e.g., Di Matteo et al. 2000, Ferrarese et al. 2006). Based on the observations with the Event Horizon Telescope (EHT, Goddi et al. 2019), the EHT collaboration published the first image of a supermassive black hole using the method of aperture synthesis. As shown in Fig. 1.5, the light rays, curved by a truly supermassive central object of mass  $\sim 6 \times 10^9 M_{\odot}$ , create a shadow around the supermassive black hole. This image presents yet another strong confirmation of Einstein's theory of General Relativity and supports our current understanding of the central engines lying within the heart of AGN in the universe. In this section, I shortly describe the observational signatures of AGN and the engine powering them.

### The AGN zoo

The first detected AGN were Seyfert galaxies, identified by Carl Seyfert in 1943 (Seyfert 1943). These galaxies were characterized by their optical spectra containing high-excitation broad emission lines. Due to their unresolved nuclei, the sizes were estimated to be very small ( $< 100$  pc) and with high mass ( $> 10^9 M_{\odot}$ ). The first extragalactic radio sources identified with individual optically resolved galaxies appeared star-like and were first called quasi-stellar radio sources, shortened to the term ‘quasars’ by Hong-Yee Chiu in 1964 (Kellermann 2014). Maarten Schmidt (Schmidt 1963) measured the distance to one of the brightest quasars ever detected (3C 273) which led to the conclusion that these quasi-stellar sources are usually found at very high redshifts and have extreme luminosities ( $\sim 100$  times higher than normal spiral galaxies). These extreme luminosities implied that the physical nature of these sources is different from those of stars and may be related to the supermassive black holes, with the possibility to influence galaxy formation and evolution (Lynden-Bell 1969, Rees 1984). Seyfert galaxies and quasars are only two of many classes of AGN found in the universe. With the development of radio interferometers, the extended radio sources were found to be identified with giant elliptical galaxies, finding a new class of AGN - radio galaxies. Some of the other AGN classes are low-ionization nuclear emission-line region galaxies (LINERs), BL-Lacs, blazars, although many others are present in the literature (see, e.g., Muckaelian 2015, Padovani et al. 2017) giving rise to a true ‘AGN zoo’. Even though all of these AGN classes differ either in spectral signatures or morphological properties, it is believed that the central engine is similar in all of them and is related to the gravitational accretion of matter onto the SMBH (Heckman & Best 2014).

### Engine powered by accretion onto SMBH

The gravitational infall of matter generates energy through an accretion process of conversion of mass  $M$  to energy  $E$  with the efficiency  $\eta$ :

$$E = \eta Mc^2. \quad (1.1)$$

The galaxy nucleus emits the energy per unit time, the so-called accretion luminosity,  $L_{\text{acc}}$ :

$$L_{\text{acc}} = \frac{dE}{dt} = \eta \dot{M} c^2, \quad (1.2)$$

where  $\dot{M} = \frac{dM}{dt}$  is the mass accretion rate. The mass-energy efficiency conversion  $\eta$  is typically assumed to be of the order of 0.1, but can assume values in range 0.05 – 0.42, depending on



the SMBH spin (Kerr 1963, Thorne 1974). To sustain the maximum luminosity of the source of mass  $M$  powered by the spherical accretion, called the Eddington luminosity  $L_{\text{Edd}}$ , the Eddington mass accretion rate,  $\dot{M}_{\text{Edd}}$ , is needed:

$$\dot{M}_{\text{Edd}} \approx 2.2 \frac{M}{10^8 M_{\odot}} \frac{0.1}{\eta}, \quad (1.3)$$

where  $\dot{M}_{\text{Edd}}$  is in units of  $M_{\odot} \text{ yr}^{-1}$ .

The accretion disk through which matter accretes onto the black hole is assumed to depend upon several parameters, some of which are the accretion rate and magnetic field strength. The local emission within the accretion disk can be approximated with a blackbody spectrum, under the assumption that the energy of the particle at the distance  $r$  from the central source is dissipated locally through viscosity and that the medium is optically thin. The radial gas temperature profile of the accretion disk,  $T(r)$ , can then be written as (Shakura & Sunyaev 1973):

$$T(r) \approx 6.3 \cdot 10^5 \left( \frac{\dot{M}}{\dot{M}_{\text{Edd}}} \right)^{1/4} M_8^{-1/4} \left( \frac{r}{R_S} \right)^{-3/4} \text{ K}, \quad (1.4)$$

where  $R_S$  is the lower limit on the radius of the inner edge of the accretion disk. These inner edges of the accretion disk surrounding a  $\sim 10^8 M_{\odot}$  black hole accreting at the Eddington rate produce radiation in the UV part of the electromagnetic spectrum. The temperature decreases toward the outer edges of the accretion disk, producing a blackbody emission that switches the peak from the UV to optical light from the innermost to the outermost radii of the accretion disk.

Another important parameter that describes the accretion mechanism is the Eddington ratio  $\lambda$ , which relates the Eddington luminosity and the bolometric luminosity of an AGN:

$$\lambda = \frac{L_{\text{bol}}}{L_{\text{Edd}}}. \quad (1.5)$$

The Eddington ratio is a measure of the energy output of an AGN and the physical limit of that energetic output. As described in the following section, it can be used to divide the AGN into two physically different subpopulations.

### 1.3.1 AGN dichotomy

Based on the studies of the local universe, it is now believed that there exist two main types of AGN (e.g., see review by Heckman & Best 2014). The main difference between the two AGN types is the efficiency of the mechanism that governs the accretion onto the central SMBH,

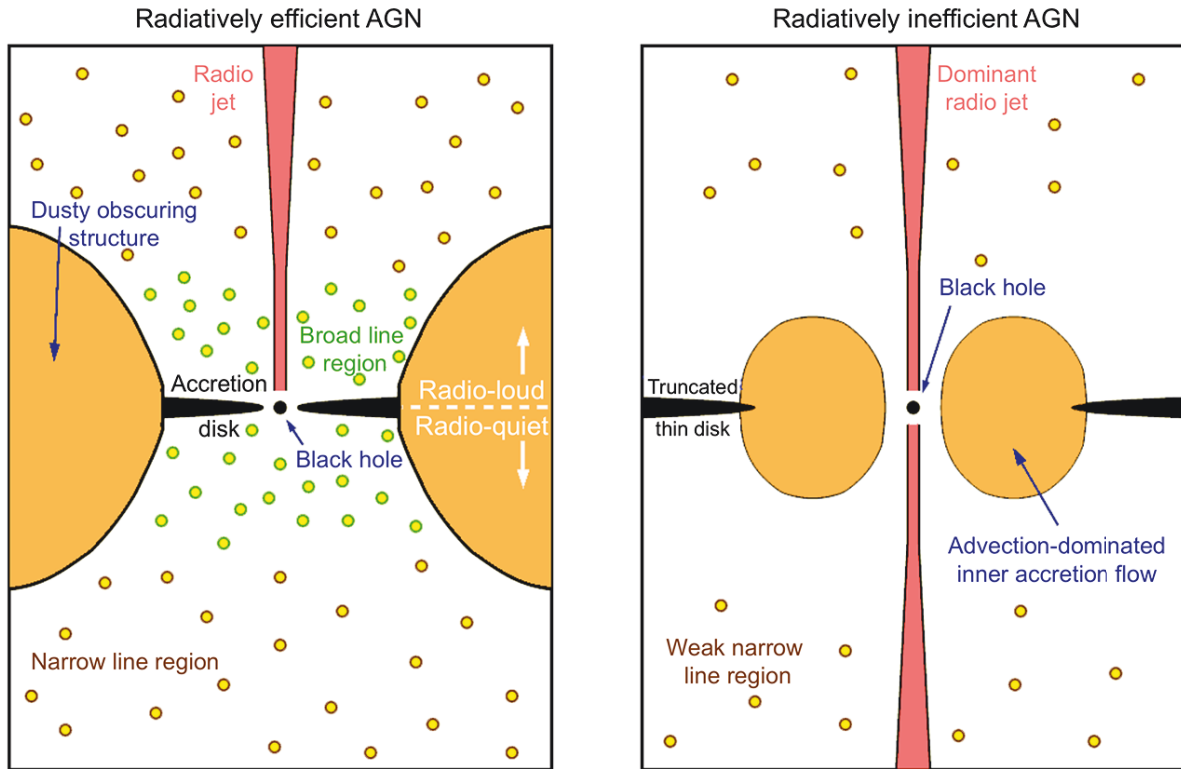


Figure 1.6: The central engines of two types of AGN. Modified from Heckman & Best (2014). *Left:* Radiatively efficient AGN contain a SMBH surrounded by a geometrically-thin, optically-thick accretion disk. The obscuring structure is present at larger distances from the SMBH and prevents a direct view of the accretion disk along lines of sight in the case of Type 2 AGN. In some radiatively efficient AGN radio jets are also present. *Right:* The central engine of radiatively inefficient AGN contains SMBH surrounded by a geometrically-thick advection-dominated accretion flow. The bulk of energy in this type of AGN is transported in a kinetic form via radio light-emitting jets.

which ultimately leads to the difference in the main energetic output.

In the first type, the so-called *radiatively efficient AGN*, the accretion of matter onto the SMBH occurs at high accretion rates, typically assumed to be at  $\lambda > 0.01$ . The schematic representation of these AGN is shown in the left panel of Fig. 1.6. The SMBH is surrounded by the geometrically-thin, optically-thick accretion disk with a radial temperature gradient (Shakura & Sunyaev 1973). The *accretion disk* produces continuum emission detectable from the visible to UV portion of this electromagnetic spectrum. The disk is surrounded by *clouds of hot electrons* which Compton up-scatter optical-to-UV photons emitted by the accretion disk, producing a power-law spectrum of X-ray emission. This X-ray emission, alongside the ionizing radiation of the accretion disk, photo-ionizes dense gas clouds located on the scales of a few light-days to several light-years from the SMBH. Due to a high-velocity dispersion of these gas clouds,

the emission-lines produced in the UV, optical and near-IR are broad and this region is hence called the *broad line region*. At even larger distances from the SMBH the *obscuring structure* of dusty molecular gas absorbs photons from the accretion disk and corona and re-emits them as thermal infrared emission. Due to the presence of this obscuring structure, the accretion disk is hidden along some lines of sight. In the direction of the polar axis of the obscuring structure reside clouds of lower density, called the *narrow line region*, which produce infrared, optical and UV forbidden and permitted narrow emission lines. In some cases, the *radio jets* are also present in this type of AGN, although the exact mechanism is not yet well understood.

The combined emission of all the components described above produces spectral signatures observable from infrared to X-ray wavelengths, with occasional radio emission present, as shown in Fig. 1.7. This type of AGN fits into the so-called *Unified model of AGN*<sup>8</sup>. According to this model, if the viewing angle is such that the observer can see the central engine (black hole and the accretion disk), the AGN is called Type 1 or unobscured, while in case of an obscured view of the central engine it is labeled as Type 2.

The second type of AGN, the so-called *radiatively inefficient AGN*, is associated with low accretion rates,  $\lambda < 0.01$ . The accretion occurs via a geometrically thick structure called *advection-dominated accretion flow* (ADAF) which is capable of launching two-sided *jets* (Narayan & Yi 1994, Abramowicz et al. 1995). These jets produce synchrotron emission which is most easily detectable in the radio range of wavelengths. Compared to the radiative-mode AGN, these AGN produce a relatively small amount of radiation, while the bulk of the energy is transported in *kinetic form* via collimated jets.

The above described two types of AGN have been found to reside in different host galaxies: radiatively efficient AGN tend to be hosted by galaxies with bluer colors, while the radiatively inefficient AGN are more likely to be found in early-type red galaxies (e.g., Kauffmann et al. 2003). The most likely origin of this AGN dichotomy is the difference in the modes of accretion which reflect the different available gas supply. Cold gas accretion at high rates (above 1% of Eddington) onto the central SMBH is radiatively efficient and can produce signatures that can be detected as optical emission lines. For this reason, objects which contain this type of signature are referred to as radiative-mode AGN, quasar-mode AGN and, in the case of

---

<sup>8</sup>To explain the wide variety of observed AGN, unified models were developed. Antonucci & Miller (1985) observed galaxy NGC 1068 in polarized light, which was previously classified as a Seyfert 2 galaxy. Given the classification, they were surprised to find a Seyfert 1 spectrum with broad emission lines. This was the first indication that objects which are divided based on the presence of broad emission lines might be physically the same, but are observed to be different due to the presence of some absorber. In the following years, the Unified Model of AGN (e.g. Antonucci 1993) has been developed according to which the difference in observed properties might be only due to the angle between the rotational axis of the AGN and the direction from which we observe an AGN. According to this unification, the accretion disk is surrounded by a thick torus containing dust which then obscures the view to the center of an AGN.

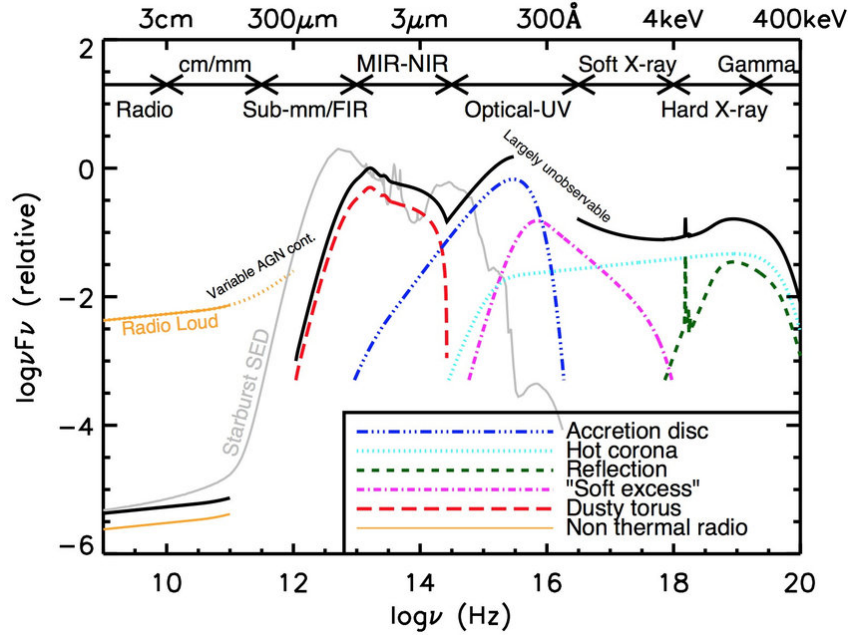


Figure 1.7: The schematic representation of the broad-band spectral energy distribution of AGN based on observations of radiatively efficient AGN. The black solid line shows the total SED, while different colors show various components of an AGN, as indicated in the legend. Depending on the AGN type, the relative contribution of each component may vary. For comparison, there is also shown the SED of starburst galaxy M82. The image is taken from [Harrison \(2014\)](#).

radio-detected sources, high-excitation radio galaxies (HERGs), some of which are found to have strong radio jets. In the case of inefficient accretion fueled by the inflow of hot gas at low accretion rates (below 1% of Eddington), the main energetic output is the kinetic energy transported by powerful radio jets, which can outshine the radio emission from the host galaxy. These AGN produce a relatively small amount of radiation across the rest of the electromagnetic spectrum and are hence called low-excitation radio galaxies (LERGs) or jet-mode AGN (e.g., [Best & Heckman 2012](#), [Best et al. 2014](#), [Pracy et al. 2016](#)).

### 1.3.2 AGN evolution

The co-evolution of host galaxies and the SMBHs within them has been accepted after the discovery of scaling relations between the SMBH mass and host galaxy properties (e.g., [Magorrian et al. 1998](#), [Ferrarese & Merritt 2000](#)). This idea was further strengthened by the cosmic star formation rate density history and SMBH accretion rate history (see Fig. 1.8) curves, both of which show similar shapes, peaking at  $z \sim 2$ . However, despite these pieces of evidence, the exact mechanisms through which the co-evolution occurs are still not clear. One of the possible

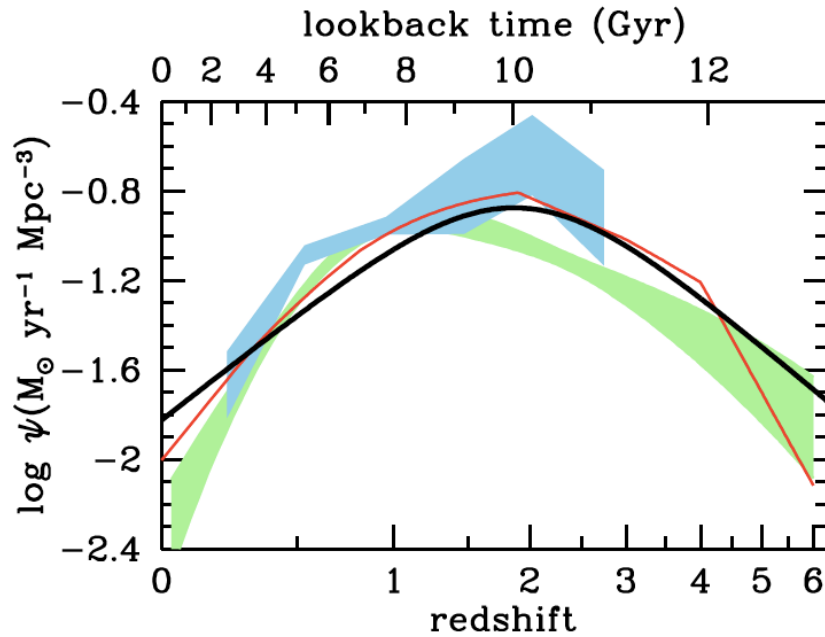


Figure 1.8: Comparison of star formation history (black solid line) and SMBH accretion history (red curve, light green, and light blue shadings) from the literature. For a visual comparison, SMBH accretion rates have been scaled by a factor of 3300. The image is taken from [Madau & Dickinson \(2014\)](#).

candidate mechanisms is AGN feedback, discussed in more detail in Sect. 1.3.3.

In Sect. 1.2.2, I described the bimodality in galaxy colors and discussed it in the context of evolutionary scenarios according to which blue star-forming galaxies evolve over time into red quiescent galaxies. Since the host galaxies of radiatively efficient and inefficient AGN are respectively on average star-forming and quiescent galaxies, it is reasonable to expect two AGN types to show different evolutionary trends. This was confirmed by studies of the evolution of spectroscopically selected radio detected AGN; while LERGs were found to show little or no evolution, HERGs seem to be a strongly evolving population (e.g., [Best & Heckman 2012](#), [Pracy et al. 2016](#)). The same conclusion was reached using somewhat different classification schemes (e.g., [Best et al. 2014](#), [Padovani et al. 2015](#)), confirming that radiatively efficient AGN are a strongly evolving population, while their inefficient counterparts show little or no evolution with redshift.

In the context of this Thesis, it is interesting to examine the evolution of radio detected radiatively efficient AGN. As described in detail in Chapter 4, after the decomposition of the total observed radio luminosity arising from both the AGN activity and star formation, the evolution of radio AGN emission is constrained out to a high redshift ( $z \sim 6$ ).

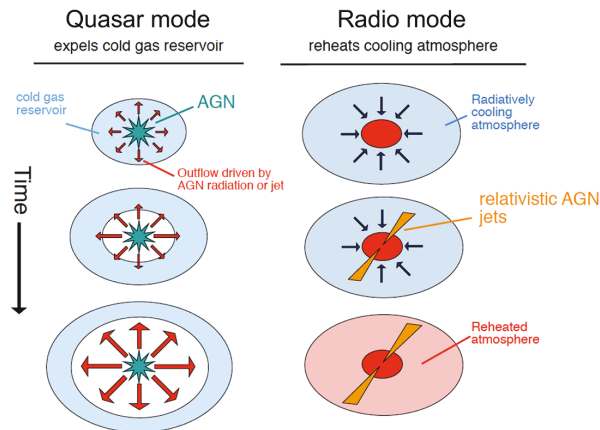


Figure 1.9: Two main modes of AGN feedback in galaxies. The quasar mode feedback operates over wide angles by creating sub-relativistic outflows which are most likely radiatively driven. Radio mode feedback occurs via relativistic collimated jets launched from the accretion flow. Modified from Alexander & Hickox (2012).

### 1.3.3 AGN feedback

The feedback mechanism that governs the co-evolution of AGN and their host galaxy is thought to occur in two flavors, namely radio and quasar mode feedback (e.g., Alexander & Hickox 2012, Croton et al. 2016). *Radio mode feedback* was first introduced to solve the cooling flow problem arising in the earliest semi-analytic models and numerical simulations of structure formation (e.g., Bower et al. 2006, Croton et al. 2006, 2016). As depicted in Fig. 1.9, it operates in massive galaxies where powerful radio jets inject energy in kinetic form into the surrounding environment, effectively heating the gas and preventing star formation. On the other hand, *quasar mode feedback* is associated with periods of rapid black hole growth due to the high accretion rates triggered by galaxy mergers or disk instabilities. These episodes of rapid accretion produce quasar winds that can affect the surrounding gas blowing it out of the galaxy and hence also terminating the formation of new stars (e.g., Croton et al. 2016). Examples of local galaxies in which AGN feedback operates are shown in Fig. 1.10.

The kinetic energy injected into the environment can be estimated using one of many scaling relations between monochromatic radio luminosity and kinetic luminosity (e.g., Willott et al. 1999, Merloni & Heinz 2007, Cavagnolo et al. 2010, Godfrey & Shabala 2016). However, the different scaling relations can result in estimates of kinetic luminosity which differ by several orders of magnitude (see Appendix A in Smolčić et al. 2017c for details). Keeping this in mind, estimates of the kinetic luminosity density can be further compared to models of galaxy evolution (e.g., Bower et al. 2006, Croton et al. 2006, 2016, Merloni & Heinz 2008).



### 1.3.4 Environments

The  $\Lambda$ CDM model is currently the most accurate cosmological model that describes the universe we live in fairly accurately. As discussed in Sect. 1.1, it is based on the cosmological principle which states that the universe is isotropic and homogeneous, which is true only on average and on scales larger than 100 Mpc. On smaller scales, the universe is composed of galaxies, gas and dark matter which together make the cosmic web - a complex universal network combined of dense clusters and groups of galaxies, connected by filaments and surrounded by voids (Bond et al. 1996). The cosmic web is the birthplace of galaxies and, alongside internal processes, it has the potential to significantly influence how galaxies evolve through cosmic time.

Observations of galaxies in different environments led to the discovery that galaxies with different morphologies reside in different environments (e.g., Conselice 2014). The more massive galaxies with early-type morphology populated with older stellar populations tend to reside in denser environments (e.g., Dressler 1980) than lower-mass late-type galaxies in which there is ongoing star formation (e.g., Hashimoto et al. 1998).

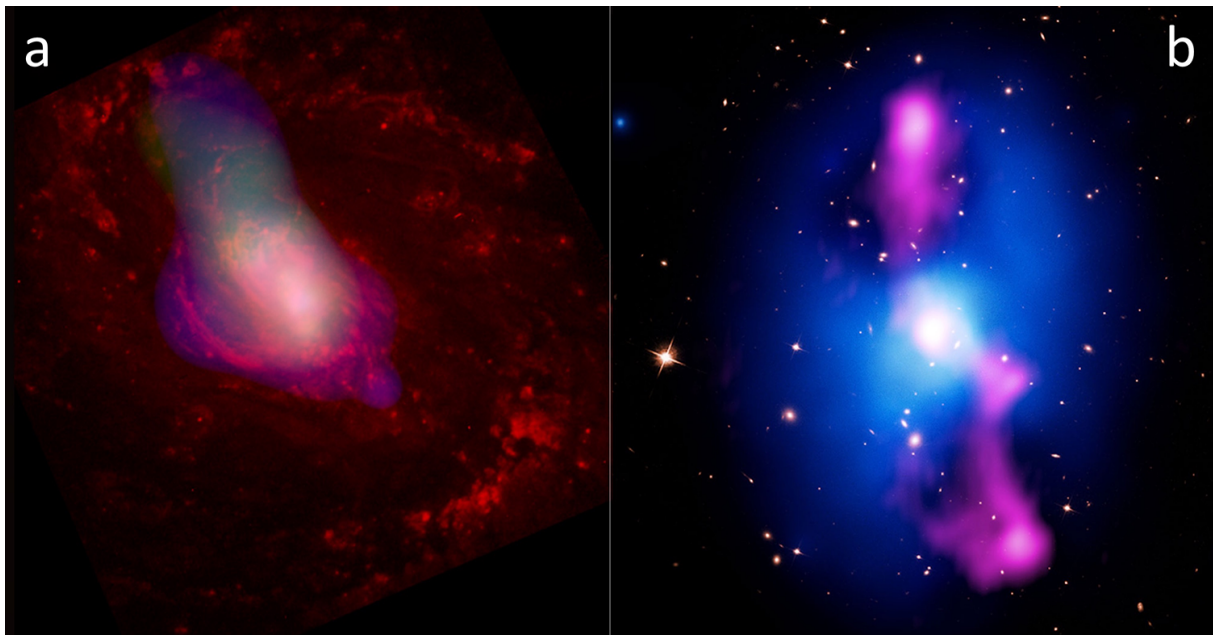


Figure 1.10: Examples of AGN feedback observed in local galaxies. *Left:* Composite image of NGC 1068 (X-rays - blue and green, optical - red) shows the high-speed wind powered by quasar activity within the nucleus of the galaxy. Credit: NASA/CXC/MIT/UCSB/STScI. *Right:* In the center of the galaxy cluster MS 0735.6+7421 lies a huge elliptical galaxy (optical - white) whose active nucleus launches one of the most powerful relativistic jets (radio - purple) ever observed in the local universe. These jets create cavities in the hot gas (X-rays - blue) in the intracluster medium. Credit: Hubble and Chandra: NASA, ESA, CXC, STScI, B. McNamara, VLA: NRAO, L. Birzan and team.

A similar trend is followed by AGN: while the radiatively inefficient AGN are preferentially found in centers of groups and clusters (e.g., Best et al. 2005b), radiatively efficient AGN are found to be more common in the field (e.g. Heckman & Best 2014). Depending on the presence of strong radio emission, radiatively efficient AGN that are found in denser environments are more likely to be radio-loud, which likely reflects the trend that these sources are hosted by more massive galaxies relative to their radio-quiet counterparts (Shen et al. 2009).

## 1.4 Panchromatic surveys

Studying the properties of AGN, their host galaxies, and their co-evolution requires an approach in which multiwavelength observations are combined. To achieve this, *panchromatic surveys* are designed to allow collaboration between international research groups to focus their efforts on particular patches of the sky to answer the most challenging astrophysical questions of their time. In the following text, I describe two such surveys from which the data are taken to perform the analysis presented in this Thesis.

### 1.4.1 The COSMOS survey

The Cosmic Evolution Survey<sup>9</sup> (COSMOS) is a panchromatic survey designed to study how galaxies form and evolve in the universe over time (Scoville 2007). The survey is focused on a  $2 \text{ deg}^2$  patch of sky called the COSMOS field, located in the direction of the constellation of

<sup>9</sup><http://cosmos.astro.caltech.edu/>

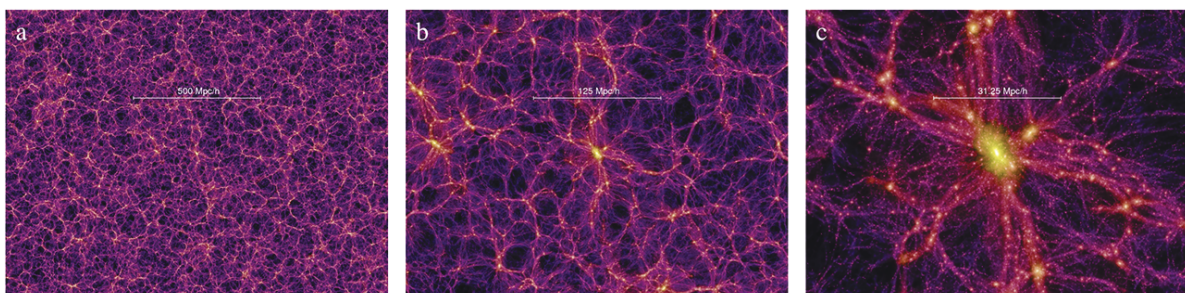


Figure 1.11: Density field of the dark matter distribution at  $z = 0$  simulated with Millenium run. Subsequent panels show the fourfold zoomed-in area of the simulated universe. The universe at large scales looks homogeneous and isotropic. However, ‘zooming in’ on it reveals the rich structure of the cosmic web. The images were taken from the official website of the Millennium Simulation: <https://wwwmpa.mpa-garching.mpg.de/galform/virgo/millennium/>.



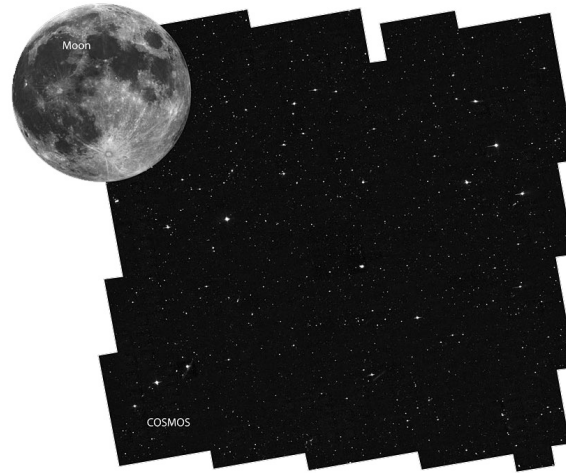


Figure 1.12: The  $2 \text{ deg}^2$  COSMOS field. The image is taken and modified from the official COSMOS website: <http://cosmos.astro.caltech.edu/>.

Sextans, centered at the coordinates (J2000)  $RA = 10^{\text{h}}00^{\text{m}}28.6^{\text{s}}$  and  $Dec = +02^{\circ}12'21''$ . The COSMOS field has been observed from X-ray to radio wavelengths with most of the major space and ground-based telescopes, such as the Hubble Space Telescope, Spitzer Space Telescope, XMM-Newton, Chandra X-ray Observatory, Herschel Space Observatory, Very Large Telescope, Subaru, Very Large Array, and others. Over 2 million galaxies were detected from the local universe, all the way to the early universe. The multiwavelength data-set containing 30-band photometry (optical-to-NIR) and precise photometric redshifts for over half a million objects within the COSMOS field is presented in the COSMOS2015 catalog (Laigle et al. 2016). The combination of this exquisite photometric data-set with the catalogs of sources detected in the X-ray (Civano et al. 2016, Marchesi et al. 2016) and radio bandwidths (Schinnerer et al. 2007, 2010, Smolčić et al. 2017a) enables astronomers to study the evolution of galaxies and their AGN out to the earliest cosmic epochs at  $z \sim 6$ .

### 1.4.2 The XXL survey

The XXL Survey is a project with the aim of detecting AGN and clusters of galaxies to support precise cosmological studies and to capture the nature and evolution of SMBHs over cosmic time and different environments (Pierre et al. 2016). It is based on X-ray observations with the XMM-Newton observatory which cover two celestial fields called the XXL-North and XXL-South field (see Fig. 1.13), encompassing  $\sim 50 \text{ deg}^2$  of the sky in total. The two fields have been covered by the observations over the full electromagnetic spectrum with the Galaxy Evolution Explorer (GALEX), Visible and Infrared Survey Telescope for Astronomy (VISTA), Spitzer

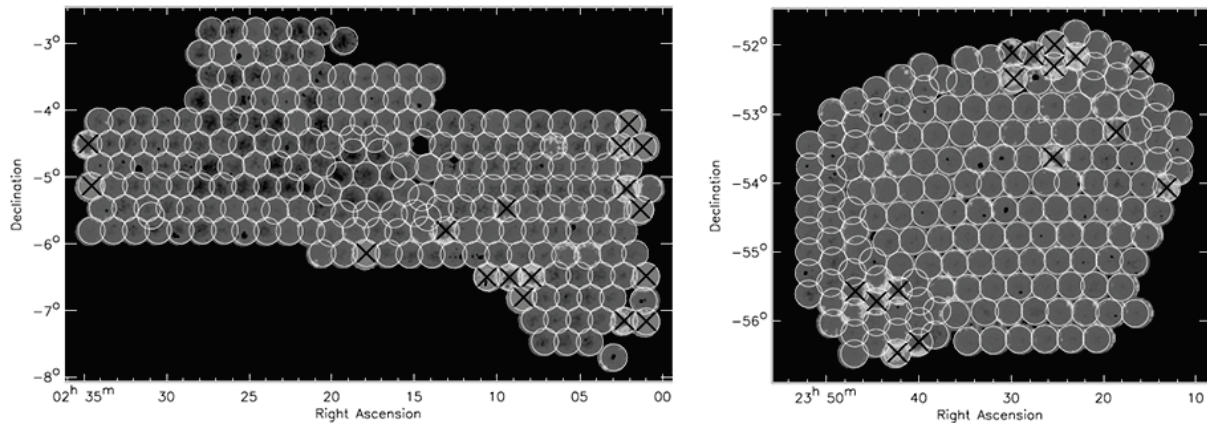


Figure 1.13: XXL fields: XXL-North field is shown in the left panel, while the XXL-South field is shown in the right panel. The image is modified from [Pierre et al. 2016](#).

Space Telescope, the Wide-field Infrared Survey Explorer (WISE), Giant Metrewave Radio Telescope (GMRT), Australia Telescope Compact Array (ATCA), and others.

## 1.5 Radio view of the sky

Current radio surveys give us a first-class view into the earliest universe in which the first galaxies and AGN have formed. The reason for this exclusivity is the fact that radio waves are not affected by cosmic dust and can directly probe star formation and AGN activity in galaxies out to the earliest times of the universe.

### 1.5.1 Radio interferometry

The beginning of radio astronomy was marked by the detection of radio signals originating from the Galactic center by Karl G. Jansky ([Jansky 1933](#)). Ever since then, radio telescopes have grown both in size and capabilities, differing in their shapes depending on the range of radio wavelengths they are designed to capture. Dipole antennas, such as those of the Low-Frequency Array (LOFAR; [Falcke et al. 2007](#)), are designed to detect long radio wavelengths, while to capture shorter radio wavelengths parabolic dishes are used (e.g., Parkes radio telescope in Australia). The main restriction on radio observations with single-dish antennas is the angular resolution, which is limited by the Rayleigh criterion:

$$\sin\theta_R = 1.22 \frac{\lambda}{D}, \quad (1.6)$$

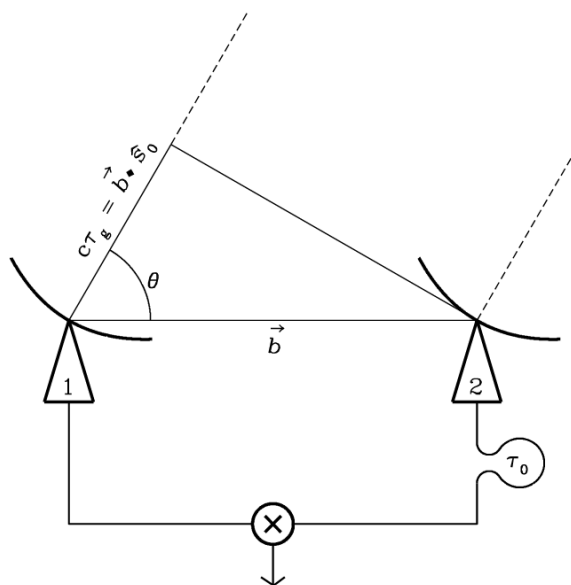


Figure 1.14: The basic element of radio interferometer is one pair of antennas. The image is taken from [www.cv.nrao.edu](http://www.cv.nrao.edu).

where  $\lambda$  is the wavelength of the radio wave and  $D$  is the diameter of the circular aperture of the dish. To obtain a good angular resolution of the detected radio emission, large aperture diameters are needed. However, it is technically difficult to build single dish telescopes of sufficient size and maneuverability. A solution to this problem is radio interferometry - a technique which connects multiple radio telescopes into an interferometric array and, thus, can achieve a better angular resolution than the individual radio telescopes.

As shown in Fig. 1.14, the smallest element of the radio interferometer is a pair of two antennas, separated by distance  $B$  called the *baseline*. The radio signal from the distant object is a plane wave and due to the separation of the antennas it arrives with a geometric delay  $\tau_g$  to the slightly more distant antenna. This time delay is proportional to the scalar product of the baseline vector  $\vec{b}$  and the unit vector  $\vec{s}$  pointing in the direction of the radio source. The two signals received at each antenna are combined and interference is achieved in a special computer called the *correlator*, producing a 2D image of the sky. To gain better coverage, a combination of multiple antennas and the Earth's rotation are used, while baselines can be varied to get better resolution. Observations with a radio interferometer are characterized by the coverage of the so-called *uv* plane onto which all the baselines of the observations are projected. The  $u$  and  $v$  coordinates are measured in the Earth's east-west and north-south directions. If the number of the radio interferometer's antennas is  $N$ , then the number of baselines is  $N(N - 1)/2$ . Increasing the number of baselines, the *uv* plane is better sampled providing the better *uv* coverage needed

for a good image of the sources. However, unlike the image generated by a single-dish telescope, a radio interferometer samples the Fourier transform of the sky brightness distribution. Each baseline can be understood as one spatial frequency or one component of the image of the observed source. The problem is that a finite number of baselines cannot sample all Fourier components, which produces artifacts in the final image. To obtain the best possible  $uv$  coverage, the Earth's rotation is used to cover as much of the  $uv$  plane as possible when baselines change their position with respect to the sky.

After performing observations with the radio interferometer, the raw radio data need to be processed and calibrated using special software packages. The final radio map is a 2D surface brightness image characterized by the angular resolution quantified by the so-called synthesized beam. All the sources or the components of a single source detected within the one synthesized beam cannot be resolved. For example, if two objects of the same flux density have different sizes, the one which is more likely to be detected is that of the smaller size if the larger one extends over several synthesized beams. In the following text, I describe the two radio interferometers used to collect the radio data analyzed and presented in this Thesis.

### **Karl G. Jansky Very Large Array**

Ever since it was built in the 1980s on the Plains of San Agustin near Socorro in New Mexico, the Very Large Array (VLA) observes the radio skies. It consists of 27 radio antennas each 25 m in diameter, together positioned in a Y-shape configuration, as shown in the left panel of Fig. 1.15. The sensitivity of this radio interferometer is equivalent to a 130 m diameter dish. The VLA antennas are placed on rails, which allows for the change of configuration of the array by stretching or shrinking the three arms of its Y-shape. The best resolution is achieved in its A-array configuration when the telescopes are at the largest mutual distances, with the longest baseline within the array being 36 km long. However, some observations are designed to capture diffused radio emission, in which case an array can be placed in its most compact D-array configuration with the largest baseline of 1 km in length.

The VLA is operated by the National Radio Astronomy Observatory<sup>10</sup> (NRAO) and has undergone a major technological upgrade which expanded its technical capacities significantly. In honor of the founder of radio astronomy, it was renamed into the "Karl G. Jansky Very Large Array". It completely covers the frequency range from 1 to 50 GHz ( $\sim 6$  mm – 30 cm) and the additional frequency band from 50-450 MHz ( $\sim 66$  cm – 6 m; van Moorsel 2014). Depending on the frequency of the observed radio waves and the array configuration, the VLA can achieve an angular resolution between 0.04'' and 0.2''.

---

<sup>10</sup><https://public.nrao.edu/>



Figure 1.15: *Left*: The Very Large Array. Credit: NRAO. *Right*: The Australia Telescope Compact Array. Credit: David Smyth, CSIRO.

### Australia Telescope Compact Array

The Australia Telescope Compact Array (ATCA) is an array of six antennas located near Narrabri in New South Wales in Australia. It is operated by the Commonwealth Scientific and Industrial Research Organisation<sup>11</sup> (CSIRO). Each of the six antennas have a diameter of 22 m. Five antennas are placed on a 3 km long east-west track along which they can move to change configurations. The sixth antenna is at a fixed position 3 km west of these tracks, making the longest baseline 6 km. The ATCA observes at frequencies 1.1 – 105 GHz (3 mm – 27 cm). Depending on the observing frequency band and the configuration, the ATCA can reach an angular resolution of 0.2 – 9”.

## 1.5.2 Origin of radio emission in distant galaxies

As previously discussed in Sect. 1.3.1, the two types of AGN, radiatively efficient and radiatively inefficient AGN, are hosted by galaxies with different stellar populations (e.g., [Kauffmann et al. 2003](#)). This dichotomy has been observed also in samples of radio galaxies out to  $z \sim 1$ , where it has been found that HERGs tend to have bluer colors associated with ongoing star formation, while LERGs are mostly red quiescent galaxies (e.g., [Smolčić et al. 2009](#), [Best & Heckman 2012](#), [Ching et al. 2017](#)). A similar conclusion was also reached (albeit for a small covered area, not sampling a significant number of the brightest sources) for RQ and RL AGN at redshifts  $0.1 < z < 4$ , where they were found to be hosted mainly by late- and early-type galaxies, respectively ([Bonzini et al. 2013](#)).

<sup>11</sup><https://www.csiro.au/>

Radio emission, observed in extragalactic surveys, that arises either from AGN or star-forming processes is of non-thermal synchrotron origin (e.g., [Condon 1992](#), [Miller et al. 1993](#)). Due to low levels of star-forming activity in host galaxies of radiatively inefficient AGN, the main contribution to the detected radio emission is expected to originate in AGN cores, jets or lobes which, in the most extreme cases, penetrate the intracluster medium and can be resolved even at the largest distances. On the other hand, radiatively efficient AGN are often found in highly star-forming host galaxies. The total non-thermal radio emission observed from these sources can hence be a combination of the AGN activity and star-forming processes. Most radio-detected sources in high-redshift samples are unresolved (e.g., [Bonzini et al. 2013](#), [Smolčić et al. 2017a](#), [Butler et al. 2018a](#)) and a morphological study of the origin of radio emission cannot be performed. However, under the assumption that the host galaxies of radiatively efficient AGN are similar to the star-forming galaxy population observed at a given redshift, the total radio emission can be decomposed into AGN and star-forming contributions using the infrared-radio correlation. This has not been previously achieved and it is the main focus of this Thesis.

### The infrared-radio correlation

The infrared-radio correlation (IRRC) is the tight correlation between the total infrared and 1.4 GHz radio emission, first observed in local galaxy samples in the 1990s and has been actively studied until today (e.g., [Helou et al. 1985](#), [Condon 1992](#), [Yun et al. 2001](#), [Calistro Rivera et al. 2017](#), [Delhaize et al. 2017](#)). Star-forming processes, which operate within galaxies with high levels of star formation, are believed to be the physical origin of this almost linear correlation. These galaxies contain large dust reservoirs which are heated by young and massive stars. Dust absorbs their radiation and re-emits it as far-infrared (FIR) radiation. These stars have relatively short lifetimes ( $\sim 10^{6-7}$  yr) and explode as supernovae, leaving remnants that accelerate the relativistic cosmic-ray electrons and produce the non-thermal diffuse radio emission. The lifetime of relativistic electrons is by a factor of  $\sim 10$  larger than the lifetime of massive stars ([Condon et al. 1991](#)) and hence the tight correlation persists over time, spanning several orders of magnitude in luminosity. The well-constrained IRRC can hence be used to estimate the star-formation rate (SFR) directly from the radio emission out to a high redshift, as demonstrated by, e.g., [Delhaize et al. 2017](#). The IRRC can be quantified via the parameter  $q_{\text{TIR}}$  defined as:

$$q_{\text{TIR}} = \log \left( \frac{L_{\text{TIR}}}{3.75 \times 10^{12} \text{ Hz}} \right) - \log \left( \frac{L_{1.4\text{GHz}}}{\text{W Hz}^{-1}} \right), \quad (1.7)$$



where  $L_{\text{TIR}}$  is the total infrared ( $8 - 1000\mu\text{m}$ ) luminosity, divided by the central frequency of  $3.75 \times 10^{12}$  Hz, and  $L_{1.4\text{GHz}}$  is the 1.4 GHz radio luminosity. Fig. 1.16 shows the redshift evolution of the  $q_{\text{TIR}}$  parameter from the literature. The IRRC from high redshift samples of SFGs shows a decreasing trend of the parameter  $q_{\text{TIR}}$  with redshift (e.g., Magnelli et al. 2015, Calistro Rivera et al. 2017, Delhaize et al. 2017). However, the origin of this trend is still not well understood and may be a result of unknown biases, such as the poor knowledge of the SEDs of high redshift SFGs (e.g., Delhaize et al. 2017, but see also Tisanić et al. 2019).

In the case of galaxies which host radiatively efficient AGN, the well-constrained  $q_{\text{TIR}}$  may be used to infer the amount of radio emission due to star-forming processes (if the infrared luminosity is independently determined). For a sample of radio-detected radiatively efficient AGN with good photometric coverage, broad-band optical-to-millimeter spectral energy distribution (SED) fitting can be used to decompose the contributions of the host galaxy and AGN

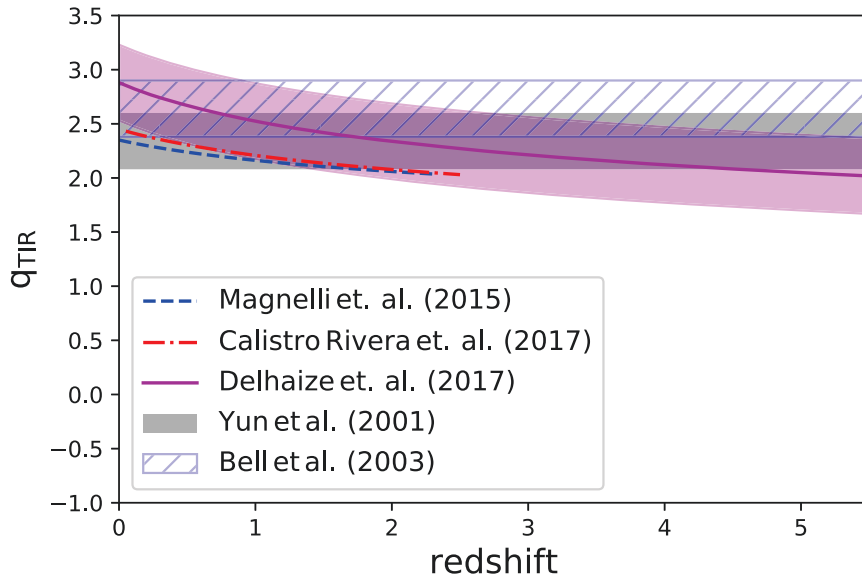


Figure 1.16: Redshift evolution of the infrared-radio correlation. Gray shaded area shows the local value of the IRRC centered at the value of  $2.34 \pm 0.01$  with a spread  $\pm 0.26$  derived by Yun et al. (2001). The local value of IRRC  $2.64 \pm 0.02$  by Bell (2003) with  $\pm 0.26$  is shown with the blue hatched area. In a study of the IRRC of  $0 < z < 2.3$  SFGs by Magnelli et al. (2015), they found a value of the  $q_{\text{TIR}}$  which decreases with redshift as  $(2.35 \pm 0.08)(1+z)^{-0.12 \pm 0.04}$ , shown with the blue dashed line. A similar result was obtained by Calistro Rivera et al. (2017), who obtained  $q_{\text{TIR}} = (2.45^{+0.045}_{-0.04})(1+z)^{-0.15^{+0.032}_{-0.032}}$  for a  $0.05 < z < 2.5$  sample of SFGs in the Boötes field, shown with the red dash-dotted line. The magenta line and area show the Delhaize et al. (2017) value of  $q_{\text{TIR}} = (2.88 \pm 0.03)(1+z)^{-0.19 \pm 0.01}$  with  $\pm 0.35$  spread, obtained using a sample of SFGs at  $0.05 < z < 5.65$  within the COSMOS field.

to the total SED (Delvecchio et al. 2017). Information about the SFR within a galaxy can be obtained from the FIR luminosity, which can further be used to estimate the radio emission due to star-forming processes via  $q_{\text{TIR}}$ . This approach is used in this Thesis to decompose the radio luminosity of the sample of radio-detected radiatively efficient AGN into AGN and star-forming contributions, as described in detail in Chapter. 3.

### Quasar radio loudness

The most powerful radiatively efficient AGN are quasars. Their emission dominates the observed galaxy spectrum from gamma to infrared frequencies. However, in only 5 – 10% of quasars the strong radio emission is present and these are usually referred to as radio-loud quasars (Condon et al. 1980). The remaining quasars are quiet, with only low levels of radio emission detected, or silent in the radio regime with current radio interferometers. Two main questions puzzling astronomers are: (i) what is the origin of radio emission in quasars, and (ii) what is the physical difference between radio-loud and radio-quiet quasars?

To answer these questions, the most common approach used in the literature is to define radio loudness via the radio-to-optical flux density or luminosity ratio (e.g., Kellermann et al. 1989, Ivezić et al. 2002, White et al. 2007, Baloković et al. 2012). Such a definition relates the two mechanisms associated with the accretion onto the SMBH: the thermal emission from the accretion disk, which can be observed as the optical emission, and the synchrotron radiation from the core, jets or lobes traced via radio emission. Bimodality in the radio loudness distribution, if found, would point toward subpopulations of quasars which differ in some of their basic properties such as the dominant radiative output, difference in the SMBH spin, different origin of radio emission (star formation and AGN), as well as many others. However, results in the literature differ widely: while some evidence points to a bimodality (e.g., Ivezić et al. 2002, White et al. 2007), others show no statistical significance of its existence (e.g., Cirasuolo et al. 2003). As discussed in detail by Baloković et al. (2012), the disagreement may be explained by selection biases not fully accounted for in the various analyses and low number statistics. Another approach in studying the origin of radio emission in quasars is by using the radio luminosity function, as described below and utilized in this Thesis.

### 1.5.3 Radio luminosity functions

The luminosity function is a measure of the number of sources per cosmic volume per logarithm of luminosity. In the case of a radio luminosity function (RLF), sources are detected at some radio frequency and ‘sorted’ per interval of the radio luminosity. Some of the first ra-



radio luminosity functions, constructed on local samples of galaxies spectroscopically selected as AGN or SFGs, found that the SFGs are the dominant population at the lower luminosity end of RLF, while AGN start to dominate at 1.4 GHz luminosities above  $L_{1.4\text{GHz}} \sim 10^{23} \text{ W Hz}^{-1}$  (e.g., Condon et al. 2002, Sadler et al. 2002, Mauch & Sadler 2007).

With the advent of deeper multiwavelength surveys it was found that both the SFG and AGN RLFs evolve with redshift (e.g., Best & Heckman 2012, Best et al. 2005a, Novak et al. 2017). The next step was to examine if the two radio AGN subpopulations show different evolutionary trends.

### HERG and LERG RLFs

The difference between the two AGN populations is reflected in the shape of the RLF constructed using the local samples of radio galaxies (Filho et al. 2006, Best & Heckman 2012, Gendre et al. 2013, Best et al. 2014, Pracy et al. 2016). As shown in the left panel of Fig. 1.17, radiatively inefficient AGN and LERGs dominate at lower radio luminosities, while radiatively efficient AGN and HERGs become dominant at radio luminosities above  $L_{1.4\text{GHz}} \sim 10^{26} \text{ W Hz}^{-1}$ .

However, the RLFs derived from various radio surveys of the local universe, such as FIRST, NVSS, SDSS, Palomar Sky Survey (Becker et al. 1994, Condon et al. 1998, York et al. 2000, Ho et al. 1997, respectively), show a substantial disagreement at  $L_{1.4\text{GHz}} < 10^{25} \text{ W Hz}^{-1}$ . While Filho et al. (2006; based on the Palomar Sky Survey) and Pracy et al. (2016; based on the LARGESS) find substantial volume densities at luminosities  $L_{1.4\text{GHz}} \lesssim 10^{25} \text{ W Hz}^{-1}$ , Best & Heckman (2012; based on the SDSS survey) find up to about an order of magnitude lower volume densities at these luminosities (see Fig. 7 in Pracy et al. 2016). As argued by Pracy et al., this disagreement may be due to the different approaches they used to eliminate SFGs from the HERG sample. Best & Heckman (2012) choose a conservative approach, removing all radio galaxies where the radio emission was suspected to arise from star formation, and this may have led to an underestimation of the volume densities of their HERG population (particularly at the low-luminosity end). On the other hand, the contribution from star-forming processes may bias the low luminosity end of the luminosity functions as derived by Filho et al. (2006) and Pracy et al. (2016).

In the case where the evolution of only AGN-related radio emission needs to be examined in radiatively efficient AGN, which are found to be hosted by galaxies exhibiting high levels of star formation, their radio luminosity needs to be decomposed into the AGN and star-forming contributions. While a morphological decomposition may be possible for samples of local radio sources, most radio sources detected in surveys such as FIRST, SDSS, COSMOS and the E-CDFS are unresolved and morphological decomposition cannot be performed. To study the

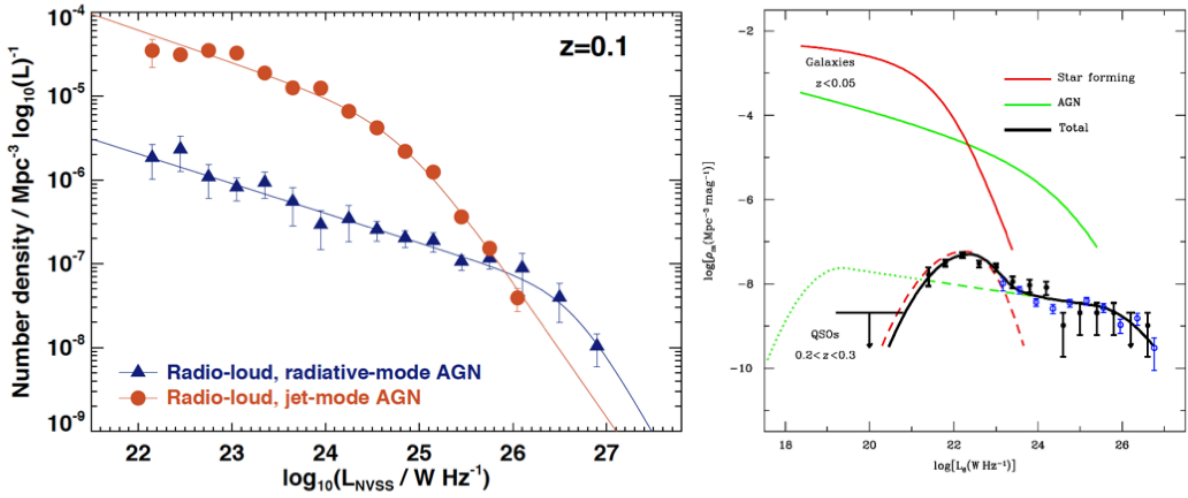


Figure 1.17: Radio luminosity functions of AGN. *Left*: The radio luminosity functions of the local radiatively efficient and inefficient AGN are shown with blue and red symbols and lines, respectively. The image is taken from Heckman & Best (2014). *Right*: The radio luminosity function of spectroscopically selected quasars is shown with the black solid line, while the star-forming ‘bump’ is shown with the red dashed line, while the AGN-related RLF part is shown with the green dotted line. For comparison, red and green lines show the radio luminosity functions of the total SFGs and AGN populations, respectively. The image is taken from Kimball et al. (2011).

evolution of these components separately, another approach is needed, as taken in this Thesis and described in detail in Chapter 3.

### Quasar RLFs

In the case of evolutionary studies of AGN-related radio emission, the star-forming contribution may be considered contamination. However, it can also be useful to study the origin of radio emission as it imprints its presence on the shape of the RLF, especially at the lower-luminosity end.

An alternative approach to the problem of the quasar radio loudness dichotomy is to study the quasar RLF (e.g., Kimball et al. 2011, Condon et al. 2013). Based on the studies by Condon et al. (2013) and Kimball et al. (2011), the RLF of spectroscopically selected quasars at  $0.2 < z < 0.3$  displays a ‘bump’ at radio luminosities below  $L_{6 \text{ GHz}} = 10^{23.5} \text{ W Hz}^{-1}$ , which they attribute to the sources in which most of the radio emission is due to star-forming processes within the quasar host galaxies, rather than AGN-related radio emission. In Chapter 5 I use a similar approach to study the origin of radio and X-ray detected quasars out to a redshift of  $\sim 4$ .

## 1.6 Thesis outline

In this Thesis, I explore the origin of radio emission in radiatively efficient AGN detected in the COSMOS and XXL-S fields. Their radio emission can originate both from AGN activity and from the star-forming processes within the host galaxies. To conduct the investigation, I exploit the multi-wavelength data-sets within the COSMOS and XXL-S fields described in Chapter 2. To study the origin of radio emission, I develop a novel statistical method of radio luminosity decomposition and use radio luminosity functions to trace the evolution of the AGN over cosmic times. These methods are described in Chapter 3. Results are presented in Chapter 4 and Chapter 5. In Chapter 6, I explore what effect environments of radiatively efficient AGN have on the presence of the radio emission in them. In Chapter 7 I summarize and conclude this Thesis.

The main results which are presented in this Thesis have been published in one paper, while one paper is submitted to A&A and in the phase of being reviewed. These two papers are:

1. **Ceraj, L.**, Smolčić, V., Delvecchio, I., Novak, M., Zamorani, G., Delhaize, J., Schinnerer, E., Vardoulaki, E., Herrera Ruiz, N., 2018, *A&A*, 620, A192, *The VLA-COSMOS 3 GHz Large Project: Star formation properties and radio luminosity functions of AGN with moderate-to-high radiative luminosities out to  $z \sim 6$ ,*

2. **Ceraj, L.**, Smolčić, V., Delvecchio, I., Novak, M., Butler, A., Tisanić, K., Delhaize, J., Zamorani, G., Horellou, K., Marchesi, S., Kolokythas, K., Vardoulaki, E., Kartaltepe, J., Leslie, S., Plionis, M., Pierre, M., submitted to *A&A*, *The XXL Survey: XLIII. The quasar radio loudness dichotomy exposed via radio luminosity functions by combining the COSMOS and XXL-S X-ray selected quasars,*

# Chapter 2

## Data

In this Chapter, I describe the data-sets used in this Thesis. These data-sets contain information about extragalactic sources detected with multiwavelength observations in the COSMOS and XXL-S sky fields. In Section 2.1 and 2.2 I describe the multiwavelength catalogs and the radio data of the COSMOS and XXL-s fields, respectively.

### 2.1 COSMOS data-sets

In this Section, I describe the multiwavelength and radio data-sets of galaxies detected in the COSMOS field. The data described in this Section are used in the analyses presented in Chapters 4, 5, and 6.

#### 2.1.1 Multiwavelength data

The latest compilation of the photometric data of the sources detected in the COSMOS field has been published as the COSMOS2015 catalog by [Laigle et al. \(2016\)](#). The catalog lists optical-to-near infrared (NIR) data for 1,182,108 sources identified via combination of over 30 band photometry, covering in total  $\sim 2.3 \text{ deg}^2$  of the COSMOS field. Optical-to-NUV data were collected with GALEX ([Zamojski et al. 2007](#)), Canada-France-Hawaii Telescope’s MegaCam (CFHT; [Capak et al. 2007](#)) and with Subaru Suprime-Cam and Hyper-Suprime-Cam ([Taniguchi et al. 2007, 2015, Miyazaki et al. 2012](#)). The NIR photometry combines data from WIRCam at CFHT ([McCracken et al. 2010](#)) and UltraVISTA ([McCracken et al. 2012](#)). MIR and FIR data were collected from observations with the Spitzer (IRAC, [Sanders et al. 2007](#); MIPS, [Le Flocc’h et al. 2009](#)) and Herschel (PACS, [Poglitsch et al. 2010](#); SPIRE, [Griffin et al. 2010](#)) space telescopes. These data are described in more detail in [Laigle et al. \(2016\)](#). There are 4,016

X-ray sources detected down to a flux limit of  $S_X[0.2 - 2 \text{ keV}] = 2 \times 10^{-16} \text{ erg s}^{-1} \text{ cm}^{-2}$  within the Chandra COSMOS-Legacy Survey (Civano et al. 2016). Those were matched with their optical-NIR counterparts by Marchesi et al. (2016) via maximum likelihood algorithm.

### 2.1.2 The VLA-COSMOS 3 GHz Large Project

The VLA-COSMOS 3 GHz Large Project provides radio data from 384 hours of observations with the Karl G. Jansky Very Large Array (VLA). The 3 GHz (10 cm) observations were carried out over  $2.6 \text{ deg}^2$  centered in the COSMOS field, reaching a median  $1\sigma$  sensitivity of  $2.3 \mu\text{Jy}/\text{beam}$  over the inner  $2 \text{ deg}^2$  at an angular resolution of  $0.75''$ . The total number of radio detected sources with signal-to-noise ratios (S/N) of five or more across the entire  $2 \text{ deg}^2$  COSMOS field is 10,830. All details of the observations and the extraction of radio sources can be found in Smolčić et al. (2017a).

Smolčić et al. (2017b) cross-matched the VLA-COSMOS 3 GHz Large Project radio data with the multiwavelength COSMOS2015 catalog (Laigle et al. 2016), identifying a sample of 7,729 radio sources with optical-NIR counterparts. This is 89% of all radio sources in the effective area considered ( $1.77 \text{ deg}^2$ ). For  $\sim 31\%$  ( $\sim 69\%$ ) of these sources, reliable spectroscopic (photometric) redshifts are available. 33% of radio sources have also been detected in the 1.4 GHz VLA-COSMOS Large Survey (Schinnerer et al. 2007, 2010). For these sources, the spectral index is calculated from the observed slope between 1.4 and 3 GHz. Otherwise, the spectral index is set to be -0.7 which is the expected value for non-thermal synchrotron radiation (e.g., Condon 1992) and corresponds to the average spectral index found for 3 GHz sources in this survey (Smolčić et al. 2017a).

### 2.1.3 Galaxy populations

The radio sources detected in the VLA-COSMOS 3 GHz Large Project were separated into the following classes by Smolčić et al. (2017b): low-to-moderate radiative luminosity AGN (MLAGN), moderate-to-high radiative luminosity AGN<sup>1</sup> (HLAGN) and star-forming galaxies (SFGs). I briefly summarize the classification method here.

Firstly, HLAGN were identified using a combination of X-ray<sup>2</sup> ( $L_X > 10^{42} \text{ erg s}^{-1}$ ) and

<sup>1</sup>A justification for the use of the HLAGN nomenclature is provided in Smolčić et al. (2017b) and Delvecchio et al. (2017). They find that, despite the overlap between two classes, HLAGN sources classified as such on the basis of X-ray and MIR criteria, as well as SED fitting, tend to have higher ( $\sim 1 \text{ dex}$ ) radiative luminosities than MLAGN. This trend is present at all redshifts they studied ( $0.01 \leq z \leq 5.70$ ), confirming that this naming convention is justified in a statistical sense.

<sup>2</sup>The X-ray data used to classify HLAGN are taken from the COSMOS Legacy/Chandra COSMOS surveys (see Civano et al. 2016, Marchesi et al. 2016).

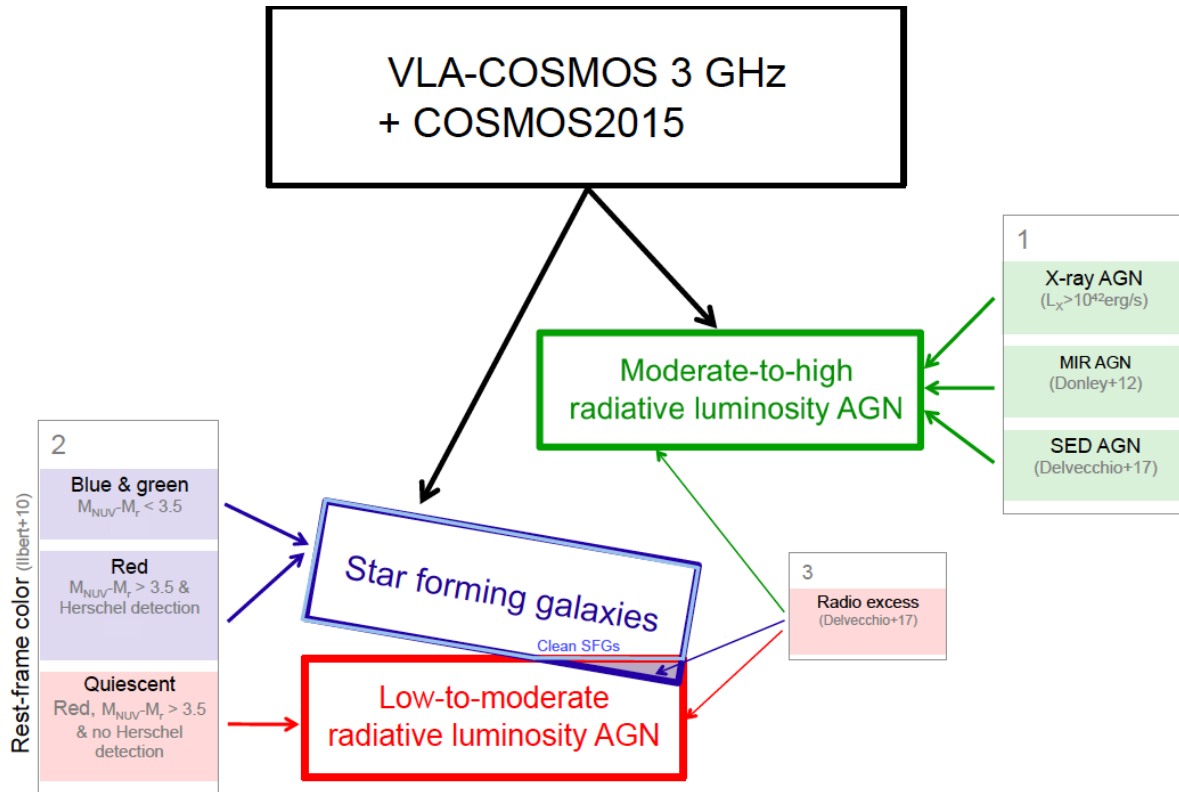


Figure 2.1: The classification scheme of the VLA-COSMOS 3 GHz sources with COSMOS2015 multi-wavelength counterparts. The image is modified from [Smolčić et al. \(2017b\)](#).

MIR<sup>3</sup> (color-color diagram; see [Donley et al. 2012](#)) criteria and via template fitting to the optical-to-millimeter spectral energy distributions (SED; see [Delvecchio et al. 2017](#)). The union of these three criteria yielded a sample of 1604 sources classified as HLAGN. The remaining radio sources were classified further based on their rest-frame NUV minus  $r^+$  colors corrected for dust extinction ( $M_{\text{NUV}} - M_{r^+}$ ), using the method based on UV/optical colors developed by [Ilbert et al. \(2010\)](#). This method identifies all sources that have  $M_{\text{NUV}} - M_{r^+} > 3.5$  and are not detected in Herschel bands as red quiescent galaxies, with colors consistent with those expected from host galaxies of radio AGN. The remainder ( $M_{\text{NUV}} - M_{r^+} < 3.5$  or  $M_{\text{NUV}} - M_{r^+} > 3.5$  with Herschel detection) is considered to be galaxies with intermediate and high levels of star formation - the star-forming galaxies.

For every radio source, IR luminosities arising from star-forming processes were obtained from the best-fit galaxy SED, after correcting for possible AGN-related emission (for more details see [Delvecchio et al. 2017](#)). Star formation rates (SFRs) were calculated from these

<sup>3</sup>The MIR data used to select HLAGN are taken from the SPLASH project (IRAC/Spitzer space telescope; see [Steinhardt et al. 2014](#)).

luminosities, by assuming a Kennicutt (1998) scaling relation and a Chabrier (2003) initial mass function. Using an appropriate IRRC, IR-based SFRs can be used to estimate the radio luminosity due to star-forming processes. In the case of AGN host galaxies, radio excess from the expected levels of radio emission due to star formation can be used to identify radio AGN (Smolčić et al. 2017b, Delvecchio et al. 2017). Delvecchio et al. (2017) defined a  $> 3\sigma$  radio excess threshold to select sources in which more than 80% of radio emission originates from AGN-related activity. Some of these sources were previously classified as HLAGN. However, the largest fraction of radio excess AGN have quiescent host galaxies and are classified as MLAGN. The data products as described by Smolčić et al. (2017a) and Delvecchio et al. (2017) are available at the COSMOS IPAC/IRSA archive<sup>4</sup>.

The final sample of the radio sources detected at 3 GHz with COSMOS2015 counterparts contains 1604 HLAGN, 1619 MLAGN and 4506 SFGs. In Chapter 4, I refer to the union of HLAGN, MLAGN and SFGs as the *full sample*.

### 2.1.4 X-ray group catalog

Using the combined X-ray observations with the XMM-Newton and Chandra X-ray observatories, Gozaliasl et al. (2019) identified a sample of 247 X-ray groups within the  $2 \text{ deg}^2$  of the COSMOS field. This sample contains X-ray groups at redshifts  $0.08 \leq z \leq 1.53$  detected down to a X-ray flux limit of  $S_X[0.5 - 2 \text{ keV}] = 3 \times 10^{-16} \text{ erg cm}^{-2} \text{ s}^{-1}$ . Following Finoguenov et al. (2009), centers of groups were revised by using the combined X-ray data-set with increased sensitivity, after rejecting possible contamination of point sources. The mass of the X-ray groups  $M_{200c}$  has been estimated within the  $R_{200}$ , which defines the area around the group center within which the internal density of haloes is 200 times larger than the critical density of the universe. For each X-ray group within their sample, the position of the group center,  $R_{200}$  and redshift are provided within the catalog<sup>5</sup>.

## 2.2 XXL-S data-set

In this Section, I describe the data-sets available for the galaxies detected in the XXL-S field. The described data are used in the analysis presented in Ch. 5.

<sup>4</sup><http://irsa.ipac.caltech.edu/data/COSMOS/tables/vla/>

<sup>5</sup><https://academic.oup.com/mnras/article/483/3/3545/5211093#supplementary-data>



### 2.2.1 The XXL-S multiwavelength data

A wealth of photometric and spectroscopic data have been collected in a multiwavelength catalog, described in detail by Fotopoulou et al. (2016, XXL Paper VI). The catalog contains the data for several million galaxies detected in UV GALEX bands (Morrissey et al. 2005), optical bands by the Blanco Cosmological Survey (BCS, Desai et al. 2012), NIR bands with Vista Hemisphere Survey (VHS, McMahon et al. 2013) and MIR bands as observed with Spitzer and WISE (Wright et al. 2010, Ashby et al. 2013).

The observations of the XXL-S with the XMM-Newton X-ray telescope (Pierre et al. 2016, XXL Paper I) achieved depths of  $6 \times 10^{-15} \text{ erg s}^{-1}$  and  $2 \times 10^{-14} \text{ erg s}^{-1}$  in the  $[0.5 - 2 \text{ keV}]$  and  $[2 - 10 \text{ keV}]$  bands, respectively. The X-ray fluxes were added to the optical counterpart catalog, as described in Paper VI. These fluxes were used to estimate the hard  $[2-10 \text{ keV}]$  band X-ray luminosity.

### 2.2.2 The 2.1 GHz ATCA XXL-S Survey

The 2.1 GHz observations of the  $25 \text{ deg}^2$  XXL-S field were carried out with the Australia Telescope Compact Array (ATCA) within the 2.1 GHz ATCA XXL-S survey, as described in Butler et al. (2018a, hereafter XXL Paper XVIII). The  $1\sigma$  level sensitivity achieved from the analysis of the radio mosaic is  $\sim 41 \mu\text{Jy}/\text{beam}$  at a resolution of  $\sim 4.8''$ . The number of sources detected with S/N of five or more is 6287. For a subsample of sources which were unresolved in the full 2 GHz ATCA bandwidth, Butler et al. (2018b, hereafter XXL Paper XXXI) constructed radio mosaics of three ATCA sub-bands (centered at 1417 MHz, 2100 MHz, and 2783 MHz) to estimate radio spectral indices of these sources based on their sub-band flux densities. This procedure yielded estimates of spectral indices for 3827/6287 ( $\sim 61\%$ ) sources.

By cross-matching the radio data and the XXL-S catalog of optical counterparts (Fotopoulou et al., in prep.), Ciliegi et al. (2018, XXL Paper XXVI) produced a sample of 4770 sources with multiwavelength coverage. After removing 12 sources classified as stars, the sample of 4758 sources was used in Paper XXXI to study star-forming galaxies and AGN found in high-excitation and low-excitation radio galaxies. Out of these,  $\sim 23\%$  have reliable spectroscopic redshifts, while for the rest ( $\sim 77\%$ ) photometric redshift estimates ( $\sigma_{\Delta z/1+z} = 0.062$ ) are available.



# Chapter 3

## Methods

In this Chapter I describe the methods used in this Thesis. Non-thermal radio emission in extragalactic surveys arises either from AGN or star-forming processes (e.g., [Condon 1992](#), [Miller et al. 1993](#)). As most of the sources detected within radio surveys described in Chapter 2 are unresolved, I developed a statistical method of the radio luminosity decomposition to study the origin of radio emission in these sources. This method is described in Section 3.2. Using decomposition, I split the total observed radio luminosity of the sources into an AGN and star forming contributions to the radio emission. Using only the AGN-related radio luminosity, I construct the AGN radio luminosity functions and study how they evolve over cosmic time. The construction of radio luminosity function is described in Section 3.3.

Throughout this Thesis, I assume a  $\Lambda$ CDM cosmology with  $H_0 = 70 \text{ kms}^{-1}\text{Mpc}^{-1}$ ,  $\Omega_m = 0.3$  and  $\Omega_\Lambda = 0.7$ . I assume that the synchrotron radio emission follows a simple power law spectrum of the form  $S_\nu \propto \nu^\alpha$ , where  $S_\nu$  is the flux density at frequency  $\nu$  and  $\alpha$  is the spectral index.

### 3.1 1.4 GHz radio luminosity

Most of the previous studies of radio luminosity functions have been conducted using surveys at 1.4 GHz (e.g., [Best & Heckman 2012](#), [Condon et al. 2013](#), [Padovani et al. 2015](#), [Pracy et al. 2016](#), [Butler et al. 2019](#)). To compare to and complement those studies, I calculate 1.4 GHz radio luminosities. Observed flux densities  $S_{\nu_{\text{obs}}}$  ( $\text{WHz}^{-1} \text{m}^{-2}$ ) and spectral indices are used to derive 1.4 GHz radio luminosity ( $L_{1.4 \text{ GHz}}$ ) defined as:

$$L_{1.4 \text{ GHz, TOT}} = \frac{4\pi D_L^2(z)}{(1+z)^{1+\alpha}} \left( \frac{1.4 \text{ GHz}}{\nu_{\text{obs}}} \right)^\alpha S_{\nu_{\text{obs, TOT}}}, \quad (3.1)$$

where  $D_L$  [m] is the luminosity distance,  $z$  is the redshift and  $\nu_{\text{obs}}$  is the observed frequency (3 GHz for COSMOS, 2.1 GHz for XXL-S, see Ch. 2). The index TOT, if present, refers to the total 1.4 GHz radio luminosity and the observed flux density prior to the luminosity decomposition.

## 3.2 Statistical method of the radio luminosity decomposition

### 3.2.1 Star formation in HLAGN host galaxies

[Delvecchio et al. \(2017\)](#) analyzed the properties of MLAGN and HLAGN, finding that MLAGN at redshifts  $z \leq 1$  show SFRs and stellar masses consistent with those of passive galaxies with little or no ongoing star formation. For the HLAGN population they find that the majority lies on the main sequence for star formation ([Whitaker et al. 2012](#)). They also argue that about 70% of HLAGN exhibit no ‘significant’ ( $> 3\sigma$ ) radio excess relative to their IR-based SFRs, suggesting that a large fraction of radio emission in HLAGN is of star formation origin.

Both the infrared and radio emissions can be used to trace the recent star formation in SFGs, which leads to a tight correlation between them, the so-called infrared-radio correlation (IRRC; e.g., [Yun et al. 2001](#), [Bell 2003](#), [Magnelli et al. 2015](#)). [Delhaize et al. \(2017\)](#) examined the cosmic evolution of the IRRC in the COSMOS field using a sample of 9,575 SFGs. This sample was jointly selected in the far-infrared (based on Herschel fluxes) and in the radio (objects in the VLA-COSMOS 3 GHz sample) after removing HLAGN and quiescent MLAGN (as described by [Smolčić et al. 2017b](#)). They found a redshift-dependent infrared-to-1.4 GHz radio luminosity ratio,  $q_{\text{TIR}}(z)$ , with a  $1\sigma$  spread of 0.35 dex. The spread around the IRRC shows the part of the IRRC parameter space in which we expect most of the radio emission to be produced in star-forming processes (e.g., [Yun et al. 2001](#), [Bell 2003](#)).

In Fig. 3.1 I show the redshift evolution of the logarithm of infrared-to-total 1.4 GHz luminosity ( $q_{\text{TOT}}$ ) vs. the total 1.4 GHz luminosity ( $L_{1.4 \text{ GHz, TOT}}$ ) of the HLAGN sample, overlaid with the [Delhaize et al.  \$q\_{\text{TIR}}\(z\)\$](#)  result. A significant number of HLAGN is found within and above the  $1\sigma$  envelope around the IRRC at all redshifts, which is qualitatively consistent with the results by [Delvecchio et al. \(2017\)](#) and [Smolčić et al. \(2017b\)](#). This implies that star-forming processes contribute considerably to the radio emission of these HLAGN, while the excess of the radio emission in HLAGN below the IRRC envelope is mainly powered by the AGN activity. To quantify the extent to which star-forming processes and AGN activity contribute to the total 1.4 GHz luminosity, I perform a decomposition analysis as described in the next section.

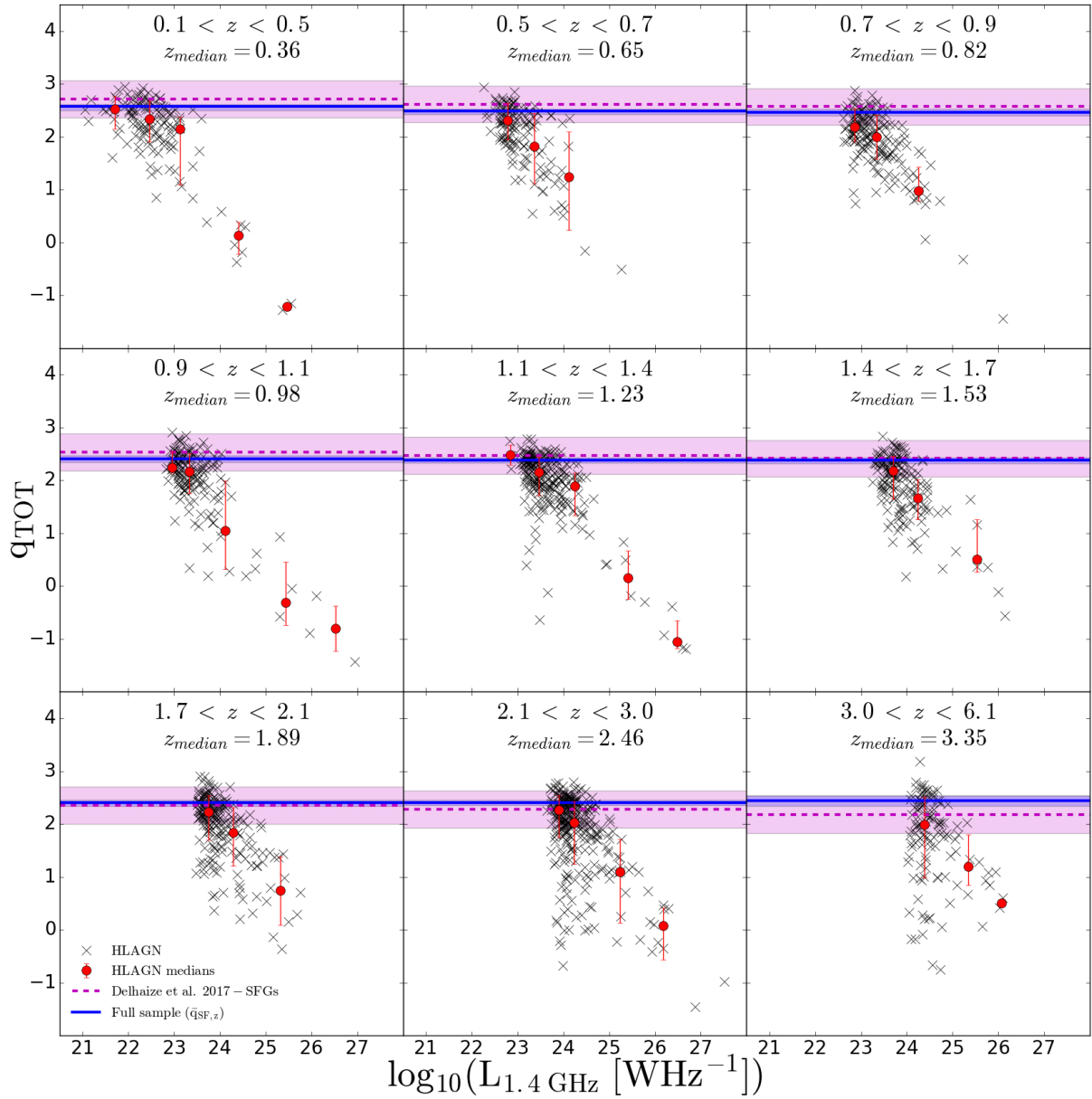


Figure 3.1: Infrared-to-1.4 GHz radio luminosity ratio ( $q_{\text{TOT}}$ ) vs.  $L_{1.4 \text{ GHz}}$  for HLAGN (black crosses). Radio luminosity binned median values of the ratio are shown with red circles with error bars showing 16th and 84th percentiles of the distribution. The dashed magenta line corresponds to the IRRC derived by Delhaize et al. (2017) at the median redshift of the underlying HLAGN sample, along with its  $1\sigma$  spread of  $\pm 0.35$  dex. Blue solid lines and area show the median of the star-forming peak  $\bar{q}_{\text{SF},z}$  and  $1\sigma_{\text{qSF},z}$  uncertainties calibrated on the full radio detected sample of the VLA-COSMOS 3 GHz Large Project sources with the COSMOS2015 counterparts.

### 3.2.2 Decomposition of the 1.4 GHz radio luminosity

As previously discussed, the radio emission in extragalactic sources (full sample, HLAGN and/or XQSOs in the analyses presented in Chapters 4 and 5) is expected to originate from both star-forming processes in the host galaxy and AGN activity. The total 1.4 GHz radio luminosity ( $L_{1.4 \text{ GHz, TOT}}$ ) is hence the sum of star forming ( $L_{1.4 \text{ GHz, SF}}$ ) and AGN ( $L_{1.4 \text{ GHz, AGN}}$ ) contributions. To quantify these contributions, I perform the decomposition analysis described here.

I calculated the infrared-to-total 1.4 GHz luminosity ratio:

$$q_{\text{TOT}} = \log \left( \frac{L_{\text{IR, SF}}}{3.75 \times 10^{12} \text{ Hz}} \right) - \log \left( \frac{L_{1.4 \text{ GHz, TOT}}}{\text{W Hz}^{-1}} \right), \quad (3.2)$$

where  $L_{\text{IR, SF}}$  [in unit W] is the infrared luminosity only due to star-forming processes (see Chapter 2), divided by the central frequency of  $3.75 \times 10^{12} \text{ Hz}$  making the first term on the right-hand side of the equation dimensionless. Uncertainties on  $q_{\text{TOT}}$ ,  $\sigma_{q_{\text{TOT}}}$ , are estimated by propagating the uncertainties on the luminosities.

#### Calibration of the infrared-to-1.4 GHz luminosity ratio of the host galaxies

The full sample of the radio detected sources from the VLA-COSMOS 3 GHz Large Project with COSMOS2015 counterparts contains 7,729 sources, classified as HLAGN, MLAGN or SFGs (see Sect. 2.1). Since the aim is to isolate the AGN-related radio emission, here I have used the decomposition technique to derive AGN fractions for all sources which display radio excess, assuming this excess arises from AGN activity.

As discussed in Sect. 3.2.1, [Delhaize et al. \(2017\)](#) found a redshift dependent IRRC. Their SFG sample contained both direct radio and far-infrared measurements and limits. On the other hand, the full sample considered here contains only radio (3 GHz) detections. For this reason, I derived a separate IRRC by binning this radio detected sample in nine redshift bins (defined as in the analysis of the HLAGN sample, described in the next Chapter).

For each source, I calculated the infrared-to-total 1.4 GHz luminosity ratio ( $q_{\text{TOT}}$ ) using Eq. 3.2. To find the median and corresponding  $1\sigma$  confidence range originating from the star-forming processes I locate the peak ( $\bar{q}_{\text{SF}, z}$ ) of the  $q_{\text{TOT}}$  distribution in each redshift bin. I then mirror the part of the  $q_{\text{TOT}}$  distribution above the location of its peak where we are certain that all radio emission originates from the star formation (e.g., [Bell 2003](#), [Magnelli et al. 2015](#)). By fitting a Gaussian functional form to the mirrored distribution, I find the dispersion. To account for the uncertainties on the luminosities used in the calculation of the  $q_{\text{TOT}}$ , a Monte Carlo

method is used. An example of the derived  $\bar{q}_{\text{SF},z}$  peak values for one of the redshift bins used in the analysis in Chapter 4 is shown in Fig. 3.2.

Derived in this way, the IRRC has slightly lower values below  $z \sim 1.5$  than the correlation derived by Delhaize et al. (2017) and increases toward higher redshifts. The observed trend is not in agreement with result by Delhaize et al. and most likely occurs due to differently selected samples (e.g., Sargent et al. 2010).

### Decomposition

To perform the radio luminosity decomposition, a sample needs to be split into redshift bins to account for the evolution of the star formation within host galaxies. In the case of analyses of the HLAGN and full samples (see Chapter 4), samples are split into nine redshift bins, each with a roughly equal number of sources, in the redshift range  $0.1 < z < 6.1$ .

Assuming for each source a normal distribution of  $q_{\text{TOT}}$  with root mean square scatter  $\sigma_{q_{\text{TOT}}}$ , and drawing  $q_{\text{TOT}}$  from this distribution, in Fig. 3.2 I show one representation of the  $q_{\text{TOT}}$  distribution for the HLAGN sample ( $2.1 < z < 3.0$ ; gray histogram in Fig. 3.2).

I next computed the median  $q_{\text{SF}}$  calibrated on the full radio-detected sample in each redshift bin ( $\bar{q}_{\text{SF},z_i}$ ), as described above. I have assumed that for HLAGN, the star formation contribution

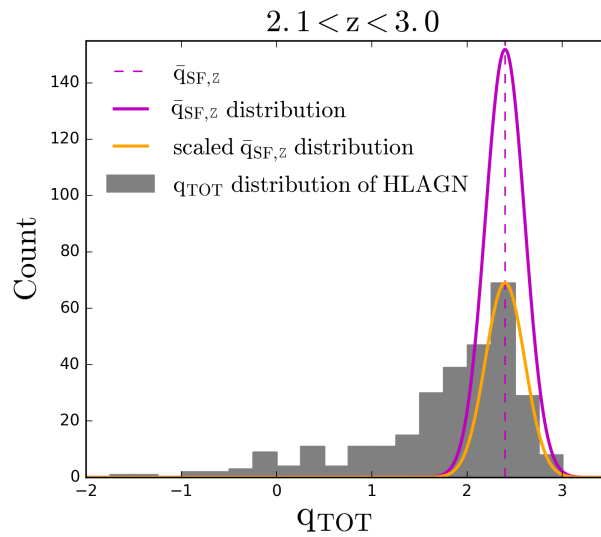


Figure 3.2: Example of one iteration of the  $q_{\text{TOT}}$  distribution for the HLAGN (gray histogram) overlaid with the Gaussian functional forms showing the contribution of star-forming processes in the redshift bin  $2.1 < z < 3.0$ . Gaussian functional forms show the contribution from the star formation as derived from the full sample and after scaling it to the normalization of the HLAGN distribution at the  $\bar{q}_{\text{SF},z}$  (shown with magenta and orange lines, respectively).

to the radio emission follows the same Gaussian functional form expected for the star-forming galaxy sample of radio detected sources; in other words, that it is peaked at  $\bar{q}_{\text{SF},z}$  with the corresponding dispersion  $\sigma_{\text{qSF},z}$ . I set the normalization of the Gaussian to the value of the HLAGN  $q_{\text{TOT}}$  distribution at the position of the  $\bar{q}_{\text{SF},z}$  (see purple and orange lines in Fig. 3.2).

Then I find the difference in the number count between the observed  $q_{\text{TOT}}$  distribution of HLAGN (gray filled histogram in Fig. 3.2) and the normalized  $\bar{q}_{\text{SF}}$  distribution (orange line in Fig. 3.2) in bins of  $q_{\text{TOT}}$ <sup>1</sup>. This gives an estimate of the number of sources ( $N_{\text{AGN}}$ ) expected to have AGN emission contributing to the total radio emission. I randomly select  $N_{\text{AGN}}$  sources within each  $q_{\text{TOT}}$  bin and calculate their AGN fractions at 1.4 GHz,  $f_{\text{AGN}}$ , defined as

$$f_{\text{AGN}} = 1 - 10^{(q_{\text{TOT}} - \bar{q}_{\text{SF},z})}. \quad (3.3)$$

If a source within a particular  $q_{\text{TOT}}$  bin is not selected in this process, it is given a  $f_{\text{AGN}} = 0$  value in this particular iteration. To account for the uncertainties, this entire procedure is repeated 1,000 times using Monte Carlo simulations, constructing a new  $q_{\text{TOT}}$  distribution each time. The result is a distribution of  $f_{\text{AGN}}$  values for each source, which accounts for the distribution of  $q_{\text{SF},z}$  and the uncertainty on  $q_{\text{TOT}}$ .

AGN fractions range from 0 to 1, where the two extreme values correspond to situations where all radio emission is due to the star-forming processes ( $f_{\text{AGN}} = 0$ ) or AGN activity ( $f_{\text{AGN}} = 1$ ). Given the definition of  $f_{\text{AGN}}$  in Eq. 3.3, AGN fractions can assume unphysical (negative) values if the source has randomly extracted  $q_{\text{TOT}}$  value greater than the average  $q_{\text{SF},z}$  value calibrated on the full radio sample. In these cases we set  $f_{\text{AGN}} = 0$  which is equivalent to assuming that radio emission arises entirely from star formation.

I scale the total 1.4 GHz radio luminosity and the observed 3 GHz flux density down to the AGN-related contributions:

$$L_{1.4 \text{ GHz,AGN}} = L_{1.4 \text{ GHz,TOT}} f_{\text{AGN}}, \quad (3.4)$$

$$S_{3 \text{ GHz,AGN}} = S_{3 \text{ GHz,TOT}} f_{\text{AGN}}. \quad (3.5)$$

<sup>1</sup>To minimize the effect binning might have on our results, I used Freedman-Diaconis rule (Freedman & Diaconis 1981) to choose  $q_{\text{TOT}}$  bin widths:

$$\text{Bin size} = 2 \text{ IQR}(x) n^{-1/3},$$

where  $\text{IQR}(x)$  is the interquartile range of the data within the bin and  $n$  is the number of sources within that bin.

### 3.3 Radio luminosity function

In this section I describe the derivation of radio luminosity functions. In Chapter 4, this method is used to derive both the total and AGN radio luminosity functions of the full and HLAGN samples. The radio luminosity functions of X-ray selected quasars in Chapter 5 are also derived using the described procedure.

#### 3.3.1 Maximum observable volume (V<sub>max</sub>) method

To constrain the redshift evolution of the radio luminosity function, first I calculate the co-moving space density of radio sources per logarithm of luminosity in  $N$  redshift bins ( $N = 9$  in Ch. 4,  $N = 6$  in Ch. 5). To find the maximum observable volume in which each of the galaxies in the sample could be observed, the  $V_{\text{max}}$  method (Schmidt 1968) is used:

$$V_{\text{max},i} = \int_{z_{\text{min}}}^{z_{\text{max}}} C(S_V) \frac{dV}{dz} dz, \quad (3.6)$$

where  $V_{\text{max},i}$  is the maximum observable volume of the  $i$ -th galaxy in the sample,  $z_{\text{min}}$  is the minimum redshift of the redshift bin under study, and  $z_{\text{max}}$  is the maximum redshift where the source can still be part of the sample given its radio luminosity. To take into account the area covered by the radio data and the variation of completeness of the radio catalog as a function of the observed flux, we define the completeness factor ( $C$ ) as:

$$C(S_{3 \text{ GHz, AGN}}) = \frac{A_{\text{obs}}}{A_{\text{sky}}} \times C_{\text{comp}}(S_V), \quad (3.7)$$

where  $A_{\text{obs}} = 1.77 \text{ deg}^2$  is the effective unmasked area of the fields considered ( $1.77 \text{ deg}^2$  in COSMOS,  $23.32 \text{ deg}^2$  in XXL-S) and  $A_{\text{sky}} \approx 41253 \text{ deg}^2$  is the area of the sky sphere. The completeness of the radio catalogs,  $C_{\text{comp}}(S_{V_{\text{obs}}})$ , is taken from Smolčić et al. (2017a; see their Table 2) for the 3 GHz COSMOS and Butler et al. (2018a; see their Fig. 11) for the 2.1 GHz XXL-S radio data. This calculation of  $V_{\text{max}}$  is consistent with those by Novak et al. (2017) and Smolčić et al. (2017c).

### 3.3.2 Constructing radio luminosity functions

The radio luminosity functions,  $\Phi(L)$ , meaning the number of sources per comoving volume element per interval of luminosity logarithm, are calculated using:

$$\Phi(L) = \frac{1}{\Delta \log(L)} \sum_{i=1}^N \frac{1}{V_{\max,i}}, \quad (3.8)$$

where  $V_{\max,i}$  is the maximum observable volume of the  $i$ -th galaxy,  $\Delta \log(L)$  is the interval of logarithm of luminosity (in Chapters 4 and 5 taken to be 0.8 dex), and the sum is taken over all sources within the redshift and luminosity bin under consideration. Following [Marshall \(1985\)](#), I calculated the errors on  $\Phi(L)$  as

$$\sigma_{\Phi(L)} = \frac{1}{\Delta \log(L)} \sqrt{\sum_{i=1}^N \frac{1}{V_{\max,i}^2}}. \quad (3.9)$$

In the case where the number of sources used to calculate  $\Phi(L)$  in a bin is less or equal to ten, the values of  $\sigma_{\Phi(L)}$  given by Eq. 3.9 are corrected by using the tabulated values of Poissonian uncertainty for small number statistics as given by [Gehrels \(1986\)](#).

To compute the AGN luminosity functions in Chapter 4, I had to properly take into account the uncertainties on the AGN fractions (and therefore luminosities), which in some cases are significant. To do this, I used the Monte Carlo approach described in Sect. 3.2 which provides the distribution of the AGN fraction for each object. For each Monte Carlo iteration, I split the sample into luminosity bins and calculated luminosity functions using Eq. 3.8. This procedure results in a distribution of luminosity functions per luminosity bin, from which I find the median and the corresponding 16th and 84th percentiles.

### 3.3.3 Evolution of the radio luminosity function

One of the purposes of deriving the radio (AGN) luminosity functions of the samples described in Chapters 4 and 5 is to study their evolution over cosmic time. The analytic representation of the local radio luminosity function is needed to constrain this evolution. However, in radio samples of COSMOS and XXL-S fields, the area of the fields is not large enough to sample a large enough volume at low redshift needed to constrain shape of the local radio luminosity function over a wide range of radio luminosity. For this reason, I considered local luminosity functions of appropriate samples derived on the basis of larger area surveys, such as FIRST, NVSS, LARGESS ([Becker et al. 1994](#), [Condon et al. 1998](#), [Ching et al. 2017](#)), which are in the



local universe comparable to the samples analyzed in this Thesis. The local luminosity functions used to constrain the evolution of different samples are described in the Sections alongside the results of the analyses (see Sections 4.2.1, 4.2.1 and 5.4.1).

The cosmic evolution of the galaxies is usually tested with the pure density evolution (PDE) and pure luminosity evolution (PLE) models. The analytic form of the local luminosity function is then fitted to the radio luminosity function data (calculated via procedure described in Sect. 3.3.2):

$$\Phi(L, z) = (1 + z)^{\alpha_D} \Phi_0 \left[ \frac{L}{(1 + z)^{\alpha_L}} \right], \quad (3.10)$$

where  $\alpha_D$  and  $\alpha_L$  are pure density and pure luminosity evolution parameters, respectively, and  $\Phi_0$  is the local luminosity function. More details on the evolution analyses are provided in Chapters 4 and 5.

## Chapter 4

# Star formation properties and radio luminosity functions of radio-detected AGN in the COSMOS field out to $z \sim 6$

The co-evolution of the host galaxies and the AGN within them has been widely accepted after the discovery of scaling relations between SMBH mass and host galaxy properties (e.g., [Magorrian et al. 1998](#), [Ferrarese & Merritt 2000](#)). To better understand this co-evolution we need to examine how AGN and their host galaxies change through cosmic time.

In this Chapter, I study the cosmic evolution of a population of AGN in the COSMOS field, detected in the VLA-COSMOS 3 GHz Large Project out to  $z \sim 6$ . Selection of the, so-called, HLAGN is based on a combination of X-ray and mid-infrared (MIR) criteria and broadband spectral energy distribution fitting, as described in Chapter 2. Using the applied selection, the aim is to trace the analogs of HERGs, as these criteria are sensitive to the excess of emission likely to arise due to radiatively efficient accretion onto SMBH. A statistical method of radio luminosity decomposition, described in detail in Section 3.2, allows the study of star forming and AGN contributions to the radio emissions separately. Using the radio luminosity functions, I study the evolution of AGN-related radio emission out to redshift  $z \sim 6$ . I also compare HLAGN evolutionary trends to the full sample of the radio detected AGN within the COSMOS field. The results presented here were published in:

Ceraj, L., Smolčić, V., Delvecchio, I., Novak, M., et al., [2018, A&A, 620, A192](#), *The VLA-COSMOS 3 GHz Large Project: Star formation properties and radio luminosity functions of AGN with moderate-to-high radiative luminosities out to  $z \sim 6$*

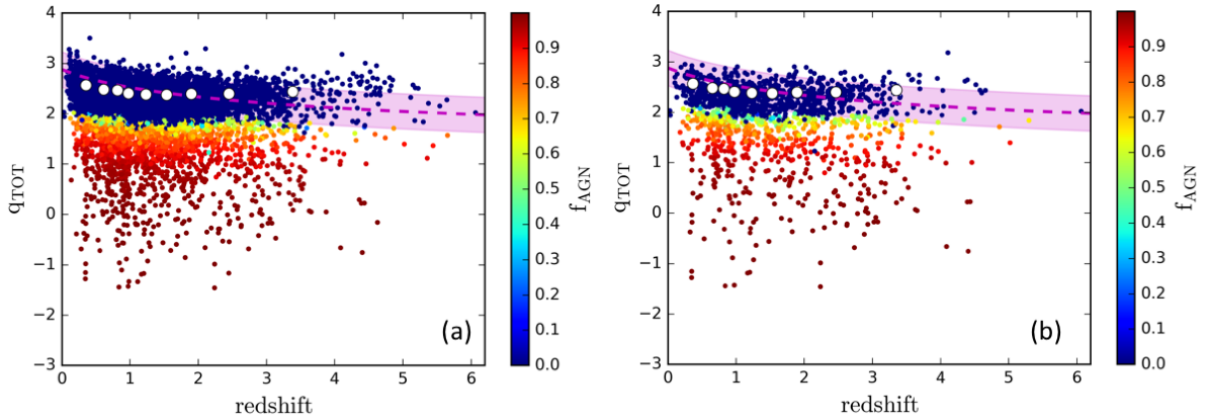


Figure 4.1: Infrared-to-1.4 GHz radio luminosity ratio ( $q_{\text{TOT}}$ ) vs. redshift for the (a) full sample and (b) HLAGN. The data are color-coded by their median values of AGN fractions. The magenta dashed line is the redshift dependent analytic form calibrated by [Delhaize et al. \(2017\)](#) on a sample of SFGs, with  $\pm 1\sigma$  spread (magenta area). White dots show the peaks ( $\bar{q}_{\text{SF},z}$ ) of the underlying  $q_{\text{TOT}}$  distribution calibrated on the star-forming galaxies in the full radio detected sample, as described in Section 3.2.

## 4.1 Decomposition of the radio luminosity

The decomposition of the radio luminosity is performed following the procedure described in Section 3.2. Using the infrared-to-1.4 GHz luminosity ratio of the AGN host galaxies, calibrated on the full radio detected sample, radio luminosities of sources within the full and HLAGN samples are decomposed. Figure 4.1 shows the distribution of  $q_{\text{TOT}}$  as a function of redshift for the full (panel a) and HLAGN (panel b) samples, color-coded by the derived AGN fractions. The AGN fraction can range from 0 to 1, with extremes being sources in which all radio emission is due to star formation and AGN have  $f_{\text{AGN}} = 0$  and  $f_{\text{AGN}} = 1$ , respectively. The distribution of the median AGN fractions is shown in Fig. 4.2.

### 4.1.1 HLAGN

My results show that the majority of HLAGN,  $(68.0 \pm 1.5)\%$ , have their total radio emission dominated by star-forming processes ( $0 \leq f_{\text{AGN}} \leq 0.5$ ), which is consistent with results by [Smolčić et al. \(2017b\)](#) and [Delvecchio et al. \(2017\)](#). On the other hand, a subsample of HLAGN is dominated by the AGN-related radio emission. I find that  $(9.9 \pm 0.9)\%$  of HLAGN have 1.4 GHz AGN fractions in the range  $0.5 < f_{\text{AGN}} \leq 0.75$ , while  $(22.1 \pm 0.9)\%$  have these fractions of  $0.75 < f_{\text{AGN}} \leq 1$ .

Using Eq. 3.4, I scale the total 1.4 GHz radio luminosity to the AGN-related contribution. For the  $(37.5 \pm 2.2)\%$  of HLAGN that show evidence for AGN-related radio emission

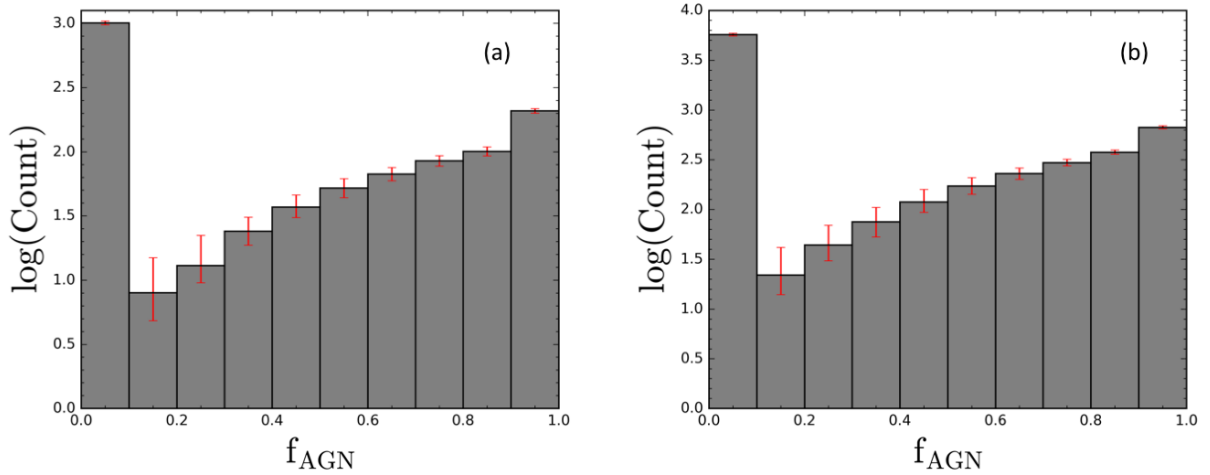


Figure 4.2: Histogram of median AGN fractions across all redshifts of the (a) HLAGN and (b) full samples, computed using Eq.3.3 (see Sect. 3.2 for details). Error bars show the 16th and 84th percentile values.

( $f_{\text{AGN}} > 0$ ), the 1.4 GHz AGN luminosities are estimated via the decomposition method. To test whether AGN fractions derived for this subsample evolve with redshift, I derive the median and  $1\sigma$  values per redshift bin, but find no significant evidence of evolution. The median of the AGN fraction of the HLAGN sample with  $f_{\text{AGN}} \neq 0$  is  $0.83^{+0.15}_{-0.23}$ .

### 4.1.2 The full sample

By following the procedure described in Sect. 3.2, I derived AGN fractions for all sources within the full sample. For  $(77.4 \pm 1.4)\%$  of these sources I found radio emission to be dominated by star-forming processes in the radio ( $0 \leq f_{\text{AGN}} \leq 0.5$ ), while the rest,  $(22.6 \pm 1.4)\%$ , are dominated by the AGN-related radio emission ( $0.5 < f_{\text{AGN}} \leq 1.0$ ).

By imposing a redshift dependent threshold, [Delvecchio et al. \(2017\)](#) found that  $\sim 23\%$  of the sources in the full sample display radio excess due to the presence of AGN-related radio emission. For comparison, with the method of statistical decomposition I effectively imposed a "lower" threshold and found evidence of AGN-related emission in  $\sim 26\%$  of the sample. This method enables me to retrieve information on the AGN contribution to the total radio luminosity also in sources which are not dominated by AGN activity in the radio part of the electromagnetic spectrum.

## 4.2 Radio AGN luminosity functions

Only the radio luminosity component due to AGN ( $L_{1.4 \text{ GHz, AGN}}$ ) is further used to calculate the radio AGN luminosity functions. This effectively allows us to exclude "contamination" of the AGN luminosity functions by star formation-related emission and thus derive the genuine radio AGN luminosity function. To ensure a complete sample of sources with fully observable AGN radio emission by the VLA-COSMOS 3 GHz Large Project survey, I imposed a cut in the AGN flux densities  $S_{3 \text{ GHz, AGN}} \geq S_{\text{lim}, 3 \text{ GHz}}$ , where  $S_{\text{lim}, 3 \text{ GHz}}$  is the detection limit of the survey ( $S_{\text{lim}, 3 \text{ GHz}} = 5\sigma = 11.5 \mu\text{Jy}$ ). Sources within the HLAGN and full samples are split into nine redshift bins, each with roughly equal number of sources, in the redshift range  $0.1 < z < 6.1$ . To show how the decomposition affects the shape of the luminosity functions, I also calculated the total luminosity functions for the HLAGN and full samples containing all the sources ( $0 \leq f_{\text{AGN}} \leq 1.0$ ), using the total 1.4 GHz luminosity which includes emission of both AGN and star-formation origin. Finally, I compared the results with those in the literature.

### 4.2.1 HLAGN AGN radio luminosity functions and their cosmic evolution out to $\sim 6$

#### HLAGN RLFs

Following the procedure described in Sect. 3.3, I constructed AGN luminosity functions using AGN luminosities of the sample of 575 HLAGN that satisfy the condition  $S_{3 \text{ GHz, AGN}} \geq S_{\text{lim}, 3 \text{ GHz}}$ . The AGN luminosity functions are tabulated in Table 4.1 and shown in Fig. 4.3. The median values of redshift quoted per redshift bin represent the median values of redshift of HLAGN that satisfy the flux density condition  $S_{3 \text{ GHz, AGN}} \geq S_{\text{lim}, 3 \text{ GHz}}$ .

As expected, based on comparison with the literature (e.g., Best et al. 2014, Pracy et al. 2016), the total radio luminosity functions (without any decomposition applied), shown in Fig. 4.3, are dominated by AGN emission at the high-luminosity end. At lower luminosities we can see the effect of the decomposition technique as the normalization of the AGN luminosity function is lower than that of the total luminosity function. This is expected given that at these luminosities the SFG luminosity function starts to significantly contribute to the total luminosity function (Novak et al. 2018).

#### Comparison with the literature

In Fig. 4.3 I compare our results with literature values of radio AGN luminosity functions at 1.4 GHz. Best & Heckman (2012) used a combined SDSS, NVSS and FIRST sample of

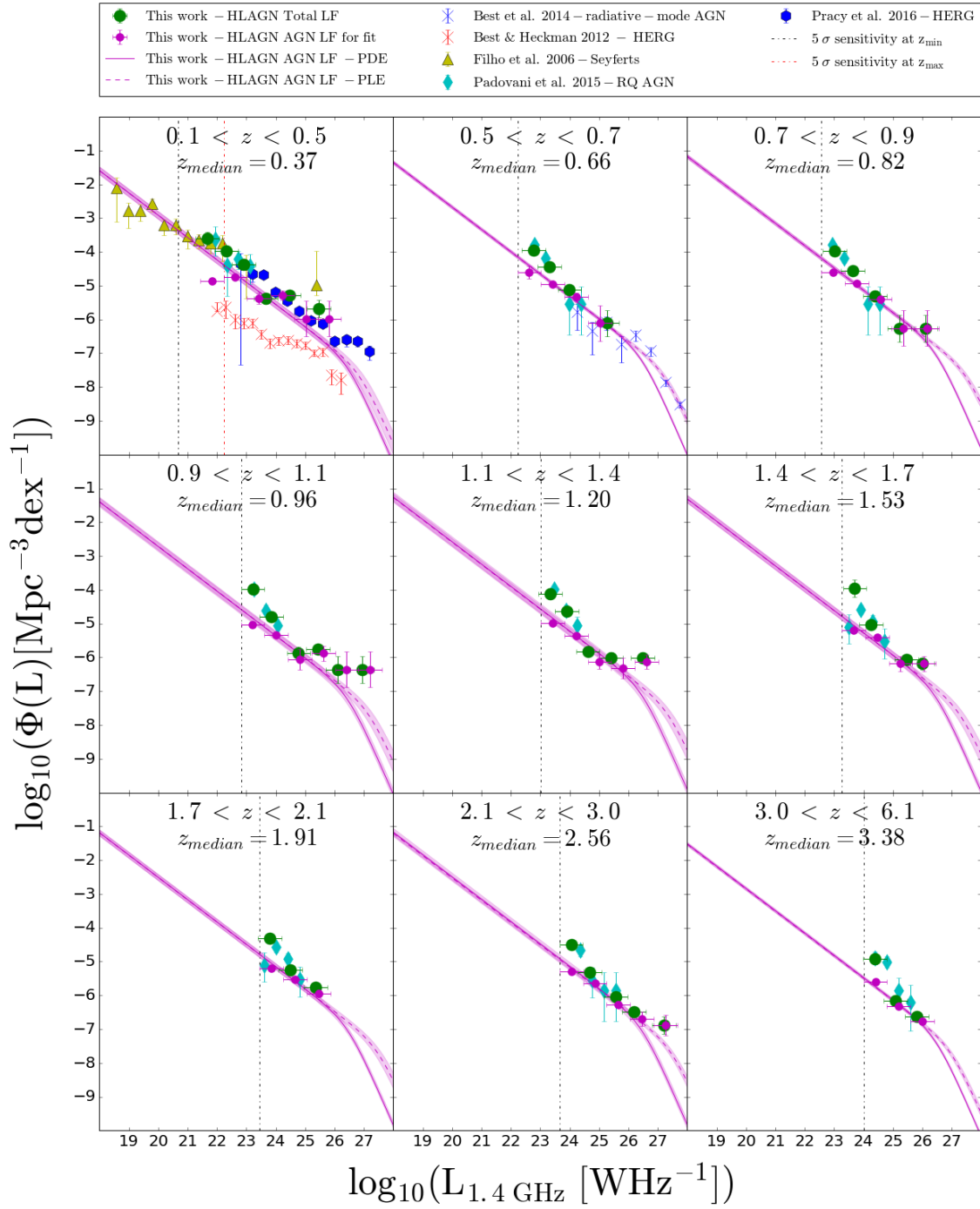


Figure 4.3: Radio AGN luminosity function at 1.4 GHz at redshifts  $0.1 < z < 6.1$ . AGN and total luminosity functions of HLAGN are plotted as magenta and green points, respectively. Solid and dashed magenta lines show the fit of the analytic form of the local luminosity function to the AGN luminosity function data for the pure density and pure luminosity evolutions, respectively, with shaded areas indicating  $1\sigma$  confidence range. The black and red vertical dashed lines show the luminosity corresponding to the  $5\sigma$  sensitivity at  $z_{\text{min}}$  and  $z_{\text{max}}$  of the redshift bin, respectively. Results from the literature are also shown, as detailed in the legend.

RL AGN at redshifts  $z < 0.3$  to study the difference between LERGs and HERGs. For both classes they constructed local luminosity functions. Their local luminosity function of HERGs is systematically lower in comparison to our data. As previously discussed by [Pracy et al. \(2016\)](#), this disagreement reflects the difference in the classification criteria, where [Best & Heckman](#) conservatively removed from their HERG sample all sources which showed evidence of star formation and classified them as SFGs (see also Sect. 4.2.1).

[Pracy et al. \(2016\)](#) use a sample of radio galaxies identified by matching FIRST sources with SDSS images. Based on their optical spectra, sources were classified into LERG and HERG classes ([Ching et al. 2017](#)). In Fig. 4.3 I show their HERG luminosity functions. As will be discussed in more detail in Sect. 4.2.1, 1.4 GHz luminosity functions derived by [Pracy et al.](#) for the HERG sample are dominated by the AGN emission and are in excellent agreement with the values of AGN luminosity functions calculated in this Chapter.

Based on the Palomar sample of bright nearby galaxies ([Ho et al. 1997](#)) [Filho et al. \(2006\)](#) constructed 5 GHz radio luminosity functions of low-luminosity AGN at a median distance of 17 Mpc. The luminosity function of 37 Seyfert galaxies, scaled to 1.4 GHz luminosities, is in good agreement with our data and constrains the low-luminosity end of the local luminosity function.

[Best et al. \(2014\)](#) combine eight radio surveys to obtain a large source sample covering a broad range of radio luminosities. They further separated these sources into radiative-mode or jet-mode AGN based on optical emission line strengths and line flux ratios. Here I have compared our data with their luminosity functions of 123 radiative-mode AGN at redshifts  $0.5 < z < 1.0$ . Their results are in agreement with my luminosity functions, with the [Best et al.](#) luminosity functions constraining the high-luminosity end.

Using the VLA sample of sources within the  $\sim 0.3 \text{ deg}^2$  of the Extended Chandra Deep Field South (E-CDFS), [Padovani et al. \(2015\)](#) studied the evolution out to  $z \sim 4$  of two radio faint populations down to the sensitivity of  $5\sigma \sim 32.5 \mu\text{Jy}$  at 1.4 GHz. To minimize the effect of missing redshift estimation, they have applied a cut in  $3.6 \mu\text{m}$  flux density,  $f_{3.6 \mu\text{m}} > 1 \mu\text{Jy}$ , yielding a sample of 680 radio detected sources. Using the scheme described in detail in [Bonzini et al. \(2013\)](#), these sources were classified as RL AGN, RQ AGN, or SFGs. This classification was based on the logarithm of the ratio between the observed  $24 \mu\text{m}$  and 1.4 GHz flux densities,  $q_{24 \text{ obs}}$ . They define the "SFGs locus" using the SED of M82 chosen to represent the entire population of SFGs across all studied redshifts. All sources which displayed an excess of radio emission with respect to this locus were classified as RL AGN. Sources within the SFGs locus, for which X-ray and MIR diagnostics showed evidence of AGN activity, were classified as RQ AGN. The remaining sources were classified as SFGs.

Table 4.1: AGN luminosity functions for the HLAGN population.

| Redshift          | $\log\left(\frac{L_{1.4\text{GHz}}}{\text{WHz}^{-1}}\right)$ | $\log\left(\frac{\Phi}{\text{Mpc}^{-3}\text{dex}^{-1}}\right)$ |
|-------------------|--|--|
| $0.10 < z < 0.50$ | 21.82  | $-4.86 \pm 0.05$   |
| $Med(z) = 0.37$   | 22.62  | $-4.74 \pm 0.07$   |
|                   | 23.42  | $-5.37 \pm 0.17$   |
|                   | 24.22  | $-5.28 \pm 0.14$   |
|                   | 25.02  | $-5.98 \pm 0.53$   |
|                   | 25.82  | $-5.98 \pm 0.53$   |
| $0.50 < z < 0.70$ | 22.62  | $-4.61 \pm 0.19$   |
| $Med(z) = 0.66$   | 23.42  | $-4.94 \pm 0.07$   |
|                   | 24.22  | $-5.33 \pm 0.12$   |
|                   | 25.02  | $-6.11 \pm 0.53$   |
| $0.70 < z < 0.90$ | 22.96  | $-4.61 \pm 0.09$   |
| $Med(z) = 0.82$   | 23.76  | $-4.93 \pm 0.07$   |
|                   | 24.56  | $-5.41 \pm 0.11$   |
|                   | 25.36  | $-6.26 \pm 0.53$   |
|                   | 26.16  | $-6.26 \pm 0.53$   |
| $0.90 < z < 1.10$ | 23.21  | $-5.04 \pm 0.09$   |
| $Med(z) = 0.96$   | 24.01  | $-5.34 \pm 0.08$   |
|                   | 24.81  | $-6.06 \pm 0.30$   |
|                   | 25.61  | $-5.88 \pm 0.22$   |
|                   | 26.41  | $-6.36 \pm 0.53$   |
|                   | 27.21  | $-6.36 \pm 0.53$   |
| $1.10 < z < 1.40$ | 23.42  | $-4.98 \pm 0.08$   |
| $Med(z) = 1.20$   | 24.22  | $-5.35 \pm 0.07$   |
|                   | 25.02  | $-6.13 \pm 0.22$   |
|                   | 25.82  | $-6.31 \pm 0.30$   |
|                   | 26.62  | $-6.13 \pm 0.22$   |



Table 4.1: Continued.

| Redshift          | $\log\left(\frac{L_{1.4\text{GHz}}}{\text{WHz}^{-1}}\right)$ | $\log\left(\frac{\Phi}{\text{Mpc}^{-3}\text{dex}^{-1}}\right)$ |
|-------------------|--|--|
| $1.40 < z < 1.70$ | 23.66  | $-5.19 \pm 0.07$   |
| $Med(z) = 1.53$   | 24.46  | $-5.41 \pm 0.09$   |
|                   | 25.26  | $-6.19 \pm 0.22$   |
|                   | 26.06  | $-6.19 \pm 0.22$   |
| $1.70 < z < 2.10$ | 23.85  | $-5.20 \pm 0.07$   |
| $Med(z) = 1.91$   | 24.65  | $-5.53 \pm 0.07$   |
|                   | 25.45  | $-5.94 \pm 0.10$   |
| $2.10 < z < 3.00$ | 24.06  | $-5.30 \pm 0.06$   |
| $Med(z) = 2.56$   | 24.86  | $-5.64 \pm 0.08$   |
|                   | 25.66  | $-6.28 \pm 0.10$   |
|                   | 26.46  | $-6.70 \pm 0.21$   |
|                   | 27.26  | $-6.88 \pm 0.30$   |
| $3.00 < z < 6.10$ | 24.40  | $-5.60 \pm 0.10$   |
| $Med(z) = 3.38$   | 25.20  | $-6.31 \pm 0.04$   |
|                   | 26.00  | $-6.76 \pm 0.09$   |

To test the evolution of their RQ AGN, [Padovani et al.](#) split their sample in six redshift bins, up to a redshift 3.66, and within each bin calculated the 1.4 GHz luminosity functions. Their RQ AGN luminosity functions agree well with our total luminosity functions in each redshift bin, possibly due to similar classification criteria (for a detailed comparison between the classifications applied in this paper and the one used by [Padovani et al. \(2015\)](#) see [Delvecchio et al. 2017](#)). At the low luminosity end, their luminosity functions tend to be higher than our AGN luminosity functions. This is expected since the RQ luminosity functions by [Padovani et al.](#) are based on the total 1.4 GHz luminosity which contains both star-forming and AGN contributions, while we construct HLAGN luminosity functions using only the AGN contribution to the 1.4 GHz luminosity derived with a decomposition method.

In this following Sections I explain the reasoning behind adopting the analytic form of the local luminosity function by [Pracy et al. \(2016\)](#) as an appropriate form to fit to HLAGN data.

Then I describe how the evolution of radio AGN luminosity function out to  $z \sim 6$  is constrained.

### Local luminosity function

The  $2 \text{ deg}^2$  area of the COSMOS field does not sample a large enough volume at low redshift to constrain the local luminosity function over a wide range of radio luminosities below and above the break of the luminosity function ( $L^*$ ). Since an analytic representation of the local luminosity function over a broad luminosity range is required to constrain its cosmic evolution, in this work I have considered local luminosity functions derived on the basis of larger area surveys, such as FIRST/NVSS combined with SDSS, LARGESS and the Palomar Nearby Galaxy Survey (Becker et al. 1994, Condon et al. 1998, York et al. 2000, Ching et al. 2017, Ho et al. 1997). In these surveys, the luminosity functions were separately derived for spectroscopically selected HERGs (Filho et al. 2006, Best & Heckman 2012, Best et al. 2014, Pracy et al. 2016) which can be assumed to be the local analogs of our HLAGN (as detailed above). However, some significant disagreement exists between various local luminosity functions, being the strongest at the low luminosity end ( $L_{1.4 \text{ GHz}} < 10^{25} \text{ WHz}^{-1}$ ). This disagreement is mainly due to the difference in the treatment of SFGs among different studies. Best & Heckman (2012) took a conservative approach removing all SFGs from the sample, which resulted in the normalization of the low luminosity end being lower by an order of magnitude than that by Filho et al. (2006) and Pracy et al. (2016). To test if the lower luminosity end of the HERG luminosity function is biased by radio emission contribution from SFGs, I independently estimated the contribution of star formation to the radio luminosity of HERGs in the LARGESS sample, used by Pracy et al. (2016) for the derivation of their luminosity function.

To the LARGESS data, I added SFR estimates provided in the MPA-JHU DR7 catalog<sup>1</sup>. In this catalog SFRs for sources classified as SFGs were derived directly from optical emission lines, while SFRs for AGN, composite, and unclassified classes were estimated on the basis of the observed spectral break at 4000 ( $D_{4000}$ ) and the relation existing for normal SFGs between specific SFR and  $D_{4000}$  (see Brinchmann et al. 2004 for details). The given SFRs are corrected for the effect of finite SDSS spectroscopic fibers as described in Salim et al. (2007).

Fig. 4.4 shows the ratio of 1.4 GHz luminosity to SFR as a function of the 1.4 GHz luminosity. As seen in this figure, the radio luminosities of HERGs are systematically higher than those of SFGs and the ratio is systematically offset from that of SFGs. By subtracting this value from the fit to the median values for the HERG population, I estimate the correlation of AGN

<sup>1</sup><http://wwwmpa.mpa-garching.mpg.de/SDSS/DR7/sfrs.html>

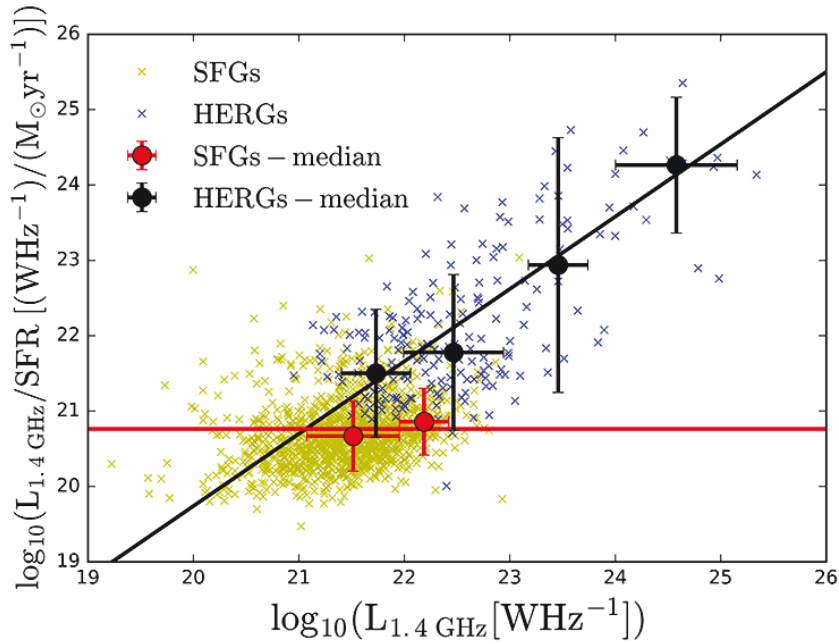


Figure 4.4: Distribution of the ratio of 1.4 GHz radio luminosity to SFR as a function of the 1.4 GHz radio luminosity for HERGs (blue symbols) and SFGs (yellow symbols) drawn from the LARGESS sample and cross-correlated with the MPA-JHU DR7 catalog. Median values of the ratio for HERGs and SFGs are shown by the filled black and red circles, respectively. The black solid line represents the linear fit to the median values for the HERG population. The red solid line represents the average value of the ratio of 1.4 GHz luminosity to SFR for star forming galaxies.

and total 1.4 GHz luminosity of HERGs (as identified in the LARGESS sample) to be:

$$L_{\text{AGN}} = L_{\text{TOT}}(1 - 10^{20.22} L_{\text{TOT}}^{-0.96}). \quad (4.1)$$

I used Relation (4.1) to statistically decompose the total radio luminosities of the HERG sample provided in Table 1 in Pracy et al. into the luminosity components originating from an AGN and star-forming processes and then I compute the luminosity function using these estimates for the AGN radio luminosities. The results are plotted in Fig. 4.5 where I compare them to the original luminosity functions by Pracy et al. (2016). The decomposed radio luminosity function, as derived here, is perfectly consistent with that presented by Pracy et al. (2016). From this I conclude that the total luminosity of sources in the HERG sample is dominated by the AGN emission. The analytic form of the local HERG luminosity function as derived by Pracy et al. can hence be further used to constrain the cosmic evolution of the HLAGN sample (which is selected to trace the high redshift analogs of HERGs).

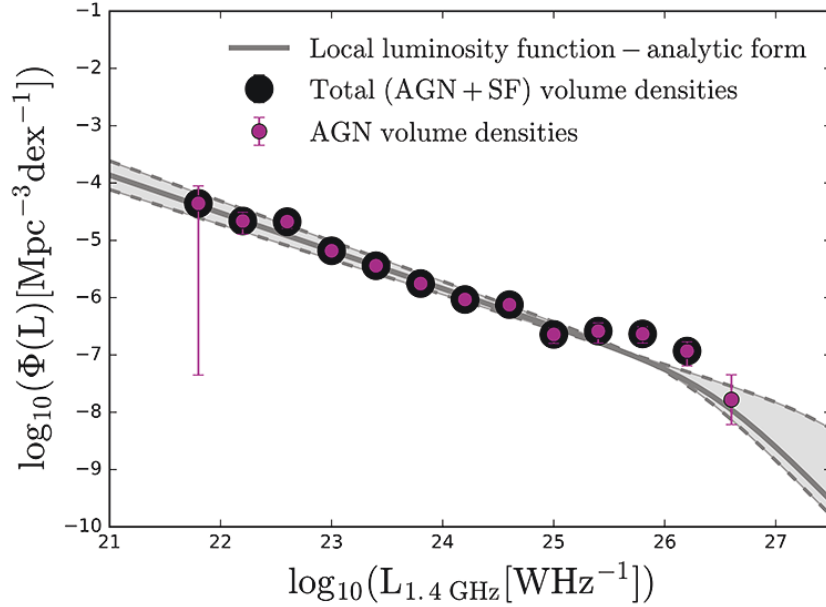


Figure 4.5: Local HERG luminosity function. Black circles show the total (AGN + SF) volume densities, while the gray line is the analytic fit to the data as done by Pracy et al. (2016). Magenta circles show the AGN luminosity functions derived by decomposing the total luminosity. The overlap between AGN and total volume densities confirms that the radio luminosity of sources in the HERG sample by Pracy et al. is dominated by the AGN emission.

### Cosmic evolution of the radio AGN luminosity function

As described in Section 3.3.3, the analytic form of local luminosity function  $\Phi_0$  can be used to constrain the cosmic evolution of the HLAGN sample. As discussed above, I found that the appropriate analytic form of local luminosity function is that defined by Pracy et al. (2016):

$$\Phi_0(L) = \frac{\Phi^*}{(L^*/L)^\alpha + (L^*/L)^\beta}, \quad (4.2)$$

where  $\Phi^* = 10^{-7.47} \text{ Mpc}^{-3} \text{ dex}^{-1}$  is the normalization,  $L^* = 10^{26.47} \text{ WHz}^{-1}$  is the knee of the luminosity function and  $\alpha = -0.66$  and  $\beta < 0$  are the faint and bright end slopes, respectively. This analytic form was constrained using the local ( $0.005 < z < 0.3$ ) sample of HERGs down to the optical apparent magnitude limit of their survey ( $m_i < 20.5$ ). As discussed by Pracy et al. (2016; see Sect. 3.6), due to the poor statistics they give only an upper limit for the parameter  $\beta$ . In our analysis, we set the bright end slope to the value of -2 as it well-matches the radiative-mode AGN luminosity functions derived by Best et al. (2014; see Fig.4.3). However, to properly constrain this parameter, better statistics of bright objects are needed.

To constrain the evolution of the HLAGN sample, I used the AGN luminosity function data

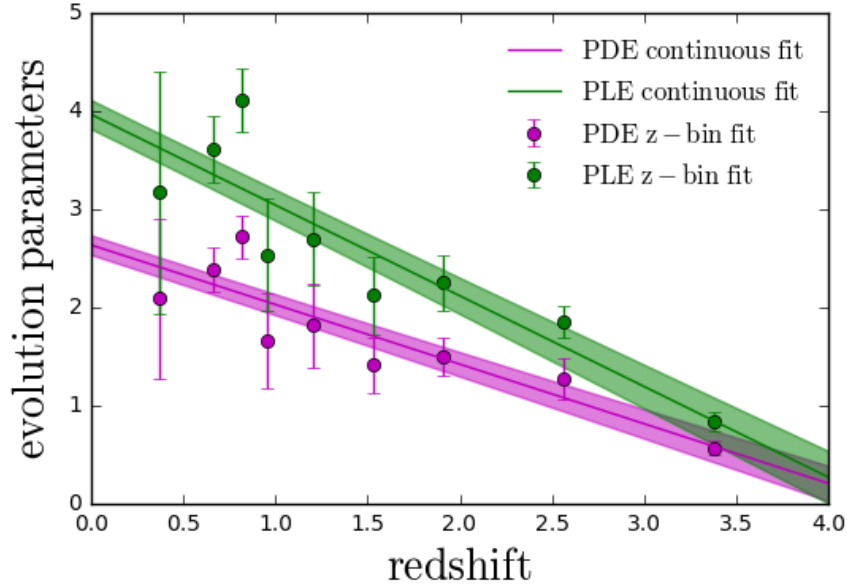


Figure 4.6: Parameters obtained from fitting two different redshift evolution models to the HLAGN luminosity functions. Green and magenta circles show the evolution parameters obtained from fitting the assumed analytic form of the luminosity function in nine redshift bins assuming pure luminosity and pure density evolution scenarios, respectively (see text for details). The same color lines show the results from the continuous fit assuming that the PLE and PDE parameters evolve linearly with redshift.

with luminosities above the  $5\sigma$  luminosity threshold of our survey at the minimum redshift of the bin ( $L(z_{\min})$ ). I make an exception in the first redshift bin ( $0.1 < z < 0.5$ ), where the lower luminosity data are not well constrained due to the small area of the COSMOS field. In this bin, I fit the analytic form of the local luminosity function by [Pracy et al.](#) only to the data which are above the luminosity threshold of our survey at the maximum redshift of the bin ( $L(z_{\max})$ ).

Firstly, the analytic form of the local luminosity function is fitted to the data in nine redshift bins. I tested the PDE and PLE models (see Eq. 3.10 in Sect. 3.3.3) by setting either  $\alpha_D = 0$  or  $\alpha_L = 0$  for the case of pure luminosity or density evolution, respectively. Evolution parameters for each redshift bin obtained with this procedure are presented in Table 4.2 and Fig. 4.6.

Secondly, I continuously modeled the redshift dependence of the evolution parameters following the procedure described by [Novak et al. \(2017\)](#). I fit a simple linear redshift-dependent evolution model to all AGN luminosity functions in all redshift bins simultaneously:

$$\Phi(L, z) = (1 + z)^{\alpha_d + z \cdot \beta_d} \times \Phi_0 \left[ \frac{L}{(1 + z)^{\alpha_l + z \cdot \beta_l}} \right], \quad (4.3)$$

where  $\alpha_d$ ,  $\alpha_l$ ,  $\beta_d$  and  $\beta_l$  are the various evolution parameters. I again tested pure density and pure luminosity evolutions separately via a  $\chi^2$  minimization procedure. The best-fit param-

Table 4.2: Best-fit evolution parameters obtained by the fitting local luminosity function to the redshift binned data assuming pure density ( $\alpha_D$ ) and pure luminosity ( $\alpha_L$ ) evolution.

| Med(z) | $\alpha_D$      | $\alpha_L$      |
|--------|-----------------|-----------------|
| 0.37   | $2.09 \pm 0.82$ | $3.17 \pm 1.23$ |
| 0.66   | $2.38 \pm 0.22$ | $3.61 \pm 0.33$ |
| 0.82   | $2.72 \pm 0.22$ | $4.11 \pm 0.32$ |
| 0.96   | $1.66 \pm 0.48$ | $2.54 \pm 0.57$ |
| 1.20   | $1.82 \pm 0.43$ | $2.70 \pm 0.48$ |
| 1.53   | $1.41 \pm 0.28$ | $2.12 \pm 0.39$ |
| 1.91   | $1.50 \pm 0.19$ | $2.26 \pm 0.28$ |
| 2.56   | $1.28 \pm 0.21$ | $1.86 \pm 0.16$ |
| 3.38   | $0.57 \pm 0.08$ | $0.83 \pm 0.10$ |

ters obtained in the case of pure luminosity evolution ( $\alpha_d = \beta_d = 0$ ) are  $\alpha_l = 3.97 \pm 0.15$  and  $\beta_l = -0.92 \pm 0.06$ . In the case of pure density evolution ( $\alpha_l = \beta_l = 0$ ) the best-fit parameters are  $\alpha_d = 2.64 \pm 0.10$  and  $\beta_d = -0.61 \pm 0.04$ . The values of these continuous evolution parameters and their uncertainties are shown with color lines in Fig. 4.6.

The results show a global decline of evolution parameters with redshift. The high parameters of evolution in the redshift bin  $0.7 < z < 0.9$ , significantly higher than those derived with the linear redshift dependent evolution model, are likely due to the presence of a very prominent large-scale structure in the COSMOS field at  $z \sim 0.73$  (Guzzo et al. 2007, Iovino et al. 2016). The presence of such a structure, enhancing the normalization of the luminosity function, produces higher than expected parameters of evolution.

To test if the chosen redshift binning has a significant effect on the obtained results, I repeated the entire analysis using the binning designed to contain roughly the same number of sources with  $S_{3 \text{ GHz, AGN}} \geq S_{\text{lim}, 3 \text{ GHz}}$  per redshift bin. Results of the best-fit parameters of a simple linear redshift dependent evolution model obtained through this analysis are consistent within the confidence range ( $\pm 1\sigma$ ) with the results presented above.

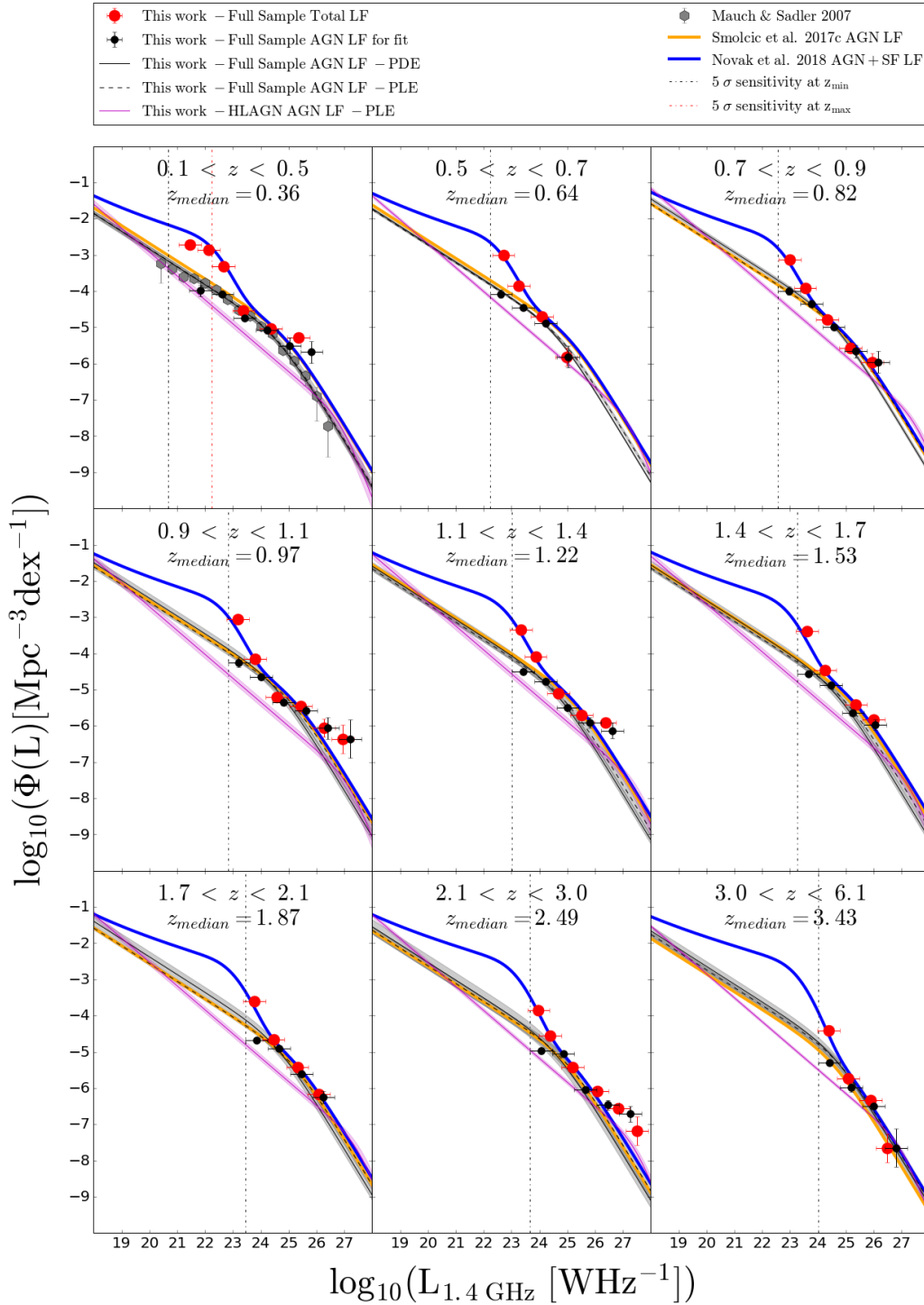


Figure 4.7: 1.4 GHz AGN luminosity function of the full VLA-COSMOS 3 GHz Large Project sample with COSMOS2015 counterparts out to  $z \sim 6$ . The AGN and total luminosity functions are shown with black and red circles, respectively. Solid and dashed black lines show the fit of analytic local AGN luminosity function in PDE and PLE models, respectively, with shaded areas indicating  $1\sigma$  confidence range. The black and red vertical dashed lines show the luminosity corresponding to the  $5\sigma$  sensitivity at  $z_{\text{min}}$  and  $z_{\text{max}}$  of the redshift bin, respectively. Results from the literature are also shown, as detailed in the legend.



### 4.2.2 Radio AGN luminosity functions and the cosmic evolution of AGN within the full 3 GHz sample

In this section I describe luminosity functions constructed using the same methods as described in Chapter 3. The total luminosity functions were constructed from the total 1.4 GHz luminosities of all sources within the full sample. The AGN luminosity functions were calculated using the AGN luminosities of sources from the full sample which would be observable by our survey ( $S_{3 \text{ GHz, AGN}} \geq S_{\text{lim}, 3 \text{ GHz}}$ ). Both the total and AGN luminosity functions of the full sample are shown in Fig. 4.7. The values of the AGN luminosity functions are listed in Table 4.3.

Following the same procedure as in Sect. 3.3.3, I used the analytic form of the local luminosity function to trace the cosmic evolution of this sample, which after decomposition contains the entire radio AGN population in the COSMOS field. I used the analytic form of the local luminosity function as derived by Mauch & Sadler (2007):

$$\Phi_0(L) = \frac{\Phi^*}{(L^*/L)^\alpha + (L^*/L)^\beta}, \quad (4.4)$$

with parameters  $\Phi^* = 10^{-5.1} \text{ Mpc}^{-3} \text{ dex}^{-1}$ ,  $L^* = 10^{24.59} \text{ WHz}^{-1}$ ,  $\alpha = -1.27$ ,  $\beta = -0.49$ . To constrain the shape of the luminosity function over six orders of magnitudes, Mauch & Sadler (2007) used a sample of 2,661 spectroscopically selected RL AGN from a local ( $z < \sim 0.073$ ) sample of the NVSS sources in the six-degree Field Galaxy Survey (6dFGS). I fit the Mauch & Sadler analytic form of the local luminosity function to the AGN luminosity functions of the full sample. Values of evolution parameters derived as described in Sect. 3.3.3 are shown in Table 4.4 and in Fig. 4.8. Best-fit parameters obtained with a continuous fit of the analytic form are  $\alpha_1 = 1.97 \pm 0.10$  and  $\beta_1 = -0.46 \pm 0.04$  in the case of pure luminosity evolution ( $\alpha_d = \beta_d = 0$ ). In the case of pure density evolution ( $\alpha_1 = \beta_1 = 0$ ) the best-fit parameters are  $\alpha_d = 1.24 \pm 0.08$  and  $\beta_d = -0.25 \pm 0.03$ .

#### Comparison with the literature

Smolčić et al. (2017c) constructed the 1.4 GHz luminosity functions of radio AGN selected by applying a redshift dependent ( $> 3\sigma$ ) threshold in the ratio of the radio luminosity and SFRs derived from IR luminosities. This selection yielded a sample of 1,814 sources in which over 80% of radio emission comes from an AGN activity. By fitting the analytical form of local luminosity function by Mauch & Sadler (2007), as done also here, they constrained the pure density and pure luminosity evolutions of the radio AGN luminosity function out to  $z \sim 5.5$ . I show their luminosity functions for the PLE model in Fig. 4.7. Their results agree well with



Table 4.3: AGN luminosity functions for the full VLA-COSMOS 3 GHz Large Project sample with COSMOS2015 multiwavelength counterparts.

| Redshift          | $\log\left(\frac{L_{1.4\text{GHz}}}{\text{WHz}^{-1}}\right)$ | $\log\left(\frac{\Phi}{\text{Mpc}^{-3} \text{dex}^{-1}}\right)$ |
|-------------------|--|---|
| $0.10 < z < 0.50$ | 21.82  | $-3.99 \pm 0.15$  |
| $Med(z) = 0.36$   | 22.62  | $-4.09 \pm 0.04$  |
|                   | 23.42  | $-4.74 \pm 0.06$  |
|                   | 24.22  | $-5.08 \pm 0.10$  |
|                   | 25.02  | $-5.50 \pm 0.22$  |
|                   | 25.82  | $-5.68 \pm 0.30$  |
| $0.50 < z < 0.70$ | 22.62  | $-4.07 \pm 0.11$  |
| $Med(z) = 0.64$   | 23.42  | $-4.45 \pm 0.05$  |
|                   | 24.22  | $-4.88 \pm 0.06$  |
|                   | 25.02  | $-5.81 \pm 0.30$  |
| $0.70 < z < 0.90$ | 22.96  | $-3.99 \pm 0.11$  |
| $Med(z) = 0.82$   | 23.76  | $-4.35 \pm 0.09$  |
|                   | 24.56  | $-4.98 \pm 0.06$  |
|                   | 25.36  | $-5.66 \pm 0.17$  |
|                   | 26.16  | $-5.96 \pm 0.30$  |
| $0.90 < z < 1.10$ | 23.21  | $-4.25 \pm 0.13$  |
| $Med(z) = 0.97$   | 24.01  | $-4.66 \pm 0.06$  |
|                   | 24.81  | $-5.35 \pm 0.08$  |
|                   | 25.61  | $-5.58 \pm 0.12$  |
|                   | 26.41  | $-6.06 \pm 0.30$  |
|                   | 27.21  | $-6.36 \pm 0.53$  |
| $1.10 < z < 1.40$ | 23.42  | $-4.51 \pm 0.05$  |
| $Med(z) = 1.22$   | 24.22  | $-4.78 \pm 0.04$  |
|                   | 25.02  | $-5.49 \pm 0.07$  |
|                   | 25.82  | $-5.91 \pm 0.14$  |
|                   | 26.62  | $-6.13 \pm 0.22$  |

Table 4.3: Continued.

| Redshift          | $\log\left(\frac{L_{1.4\text{GHz}}}{\text{WHz}^{-1}}\right)$ | $\log\left(\frac{\Phi}{\text{Mpc}^{-3}\text{dex}^{-1}}\right)$ |
|-------------------|--|--|
| $1.40 < z < 1.70$ | 23.66  | $-4.56 \pm 0.04$   |
| $Med(z) = 1.53$   | 24.46  | $-4.87 \pm 0.05$   |
|                   | 25.26  | $-5.64 \pm 0.08$   |
|                   | 26.06  | $-5.96 \pm 0.14$   |
| $1.70 < z < 2.10$ | 23.85  | $-4.67 \pm 0.06$   |
| $Med(z) = 1.87$   | 24.65  | $-4.90 \pm 0.09$   |
|                   | 25.45  | $-5.62 \pm 0.06$   |
|                   | 26.25  | $-6.25 \pm 0.16$   |
| $2.10 < z < 3.00$ | 24.06  | $-4.97 \pm 0.05$   |
| $Med(z) = 2.49$   | 24.86  | $-5.04 \pm 0.09$   |
|                   | 25.66  | $-6.03 \pm 0.08$   |
|                   | 26.46  | $-6.46 \pm 0.14$   |
|                   | 27.26  | $-6.71 \pm 0.22$   |
| $3.00 < z < 6.10$ | 24.40  | $-5.30 \pm 0.07$   |
| $Med(z) = 3.43$   | 25.20  | $-5.99 \pm 0.11$   |
|                   | 26.00  | $-6.49 \pm 0.06$   |
|                   | 26.80  | $-7.65 \pm 0.53$   |

AGN luminosity functions of the full sample. The modeling of the redshift evolution of their luminosity function is equivalent to the analysis described here. The differences found in the evolution parameters in the case of the discrete and continuous fitting of the radio luminosity function come from several factors. To ensure a complete sample, I first imposed an AGN flux density cut which reduces the number of sources used in the analysis. I calculated the maximum observable volume of each source using the AGN luminosity derived from the luminosity decomposition analysis, obtaining lower values for the volumes than would be the case if using the total luminosity of the source. Finally, to construct luminosity functions I used the AGN luminosities, which are the total luminosities scaled by AGN fraction. All of these factors result in slightly different values of evolution parameters obtained here and by [Smolčić et al. \(2017c\)](#).

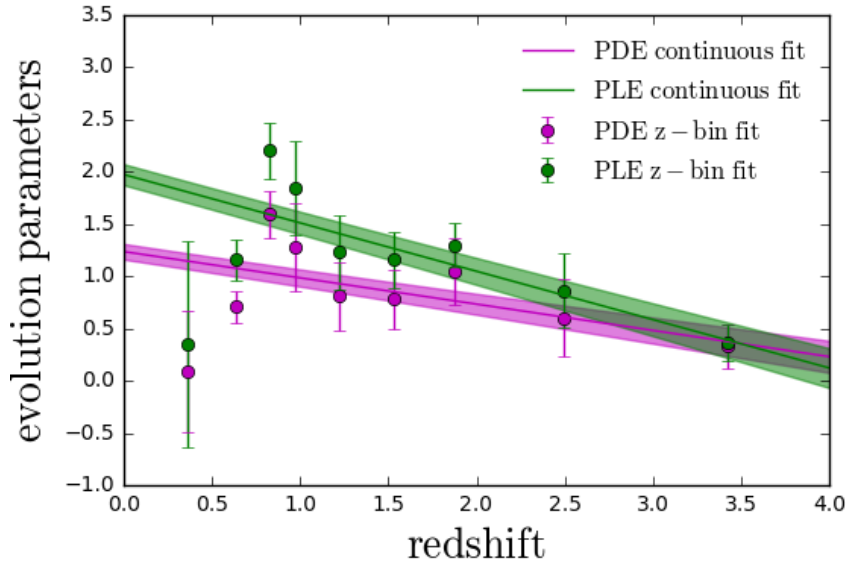


Figure 4.8: Fitting parameters obtained to model the redshift evolution of the full AGN sample. Green (magenta) circles and line show the pure luminosity (density) evolution parameter values and model, respectively.

However, the results are still consistent within  $2\sigma$ .

I also compare our results with the study done by [Novak et al. \(2018\)](#). Using a sample of 8,035 radio detected sources from the VLA-COSMOS 3 GHz Large Project with COSMOS2015 ([Laigle et al. 2016](#)) and i-band ([Capak et al. 2007](#)) multiwavelength counterparts they constrained the evolution of the total radio luminosity function. To construct the total radio luminosity function, they combine the local luminosity functions of SFGs and of AGN from the literature. The total (AGN+SF) luminosity functions shown in Fig. 4.7 are in excellent agreement with their results.

Agreement with the results by [Smolčić et al. \(2017c\)](#) and [Novak et al. \(2018\)](#) shows that the high luminosity end of AGN luminosity function as derived here is populated by sources which are predominantly dominated by AGN activity. Sources with lower AGN fractions are more common toward the lower luminosity end of AGN luminosity function, in a regime below the luminosity threshold of our survey. In this regime, the decomposition allows us to go further in determining the true shape of the AGN luminosity function.

### 4.3 Discussion

In this section I discuss the results in the context of galaxy evolution, also investigating the origin of the radio emission in HLAGN. I have estimated the evolution of number, luminosity,

Table 4.4: Best-fit evolution parameters obtained by fitting local luminosity function to redshift binned data assuming pure density ( $\alpha_D$ ) and pure luminosity ( $\alpha_L$ ) evolution.

| Med(z) | $\alpha_D$      | $\alpha_L$      |
|--------|-----------------|-----------------|
| 0.36   | $0.09 \pm 0.58$ | $0.35 \pm 0.99$ |
| 0.64   | $0.71 \pm 0.15$ | $1.16 \pm 0.19$ |
| 0.82   | $1.59 \pm 0.22$ | $2.20 \pm 0.27$ |
| 0.97   | $1.28 \pm 0.43$ | $1.84 \pm 0.45$ |
| 1.22   | $0.81 \pm 0.32$ | $1.23 \pm 0.36$ |
| 1.53   | $0.78 \pm 0.28$ | $1.16 \pm 0.27$ |
| 1.87   | $1.04 \pm 0.32$ | $1.30 \pm 0.21$ |
| 2.49   | $0.60 \pm 0.37$ | $0.86 \pm 0.36$ |
| 3.43   | $0.33 \pm 0.21$ | $0.37 \pm 0.17$ |

and kinetic luminosity density and compare our results to other studies of galaxy evolution.

### 4.3.1 Origin of radio emission in HLAGN

Previous studies conducted on radio samples of X-ray and mid-IR selected AGN suggest that AGN identified through these criteria are hosted mostly by star-forming systems in which the bulk of the radio emission originates from the host galaxy rather than SMBH activity (e.g., [Hickox et al. 2009](#), [Bonzini et al. 2013](#), [Goulding et al. 2014](#), [Padovani et al. 2015](#)). For instance, in a comprehensive analysis performed by [Delvecchio et al. \(2017\)](#) on the HLAGN sample they report that only  $\sim 30\%$  of them display significant radio excess due to non-thermal emission originating from AGN, while the radio emission of the rest is dominated by star formation. However, this behavior does not apply to the most luminous radio sources, which are found to mostly reside in massive and passive systems (e.g., [Dunlop et al. 2003](#)).

In this work I have separated the radio emission of HLAGN into radiation originating from star formation and AGN activity using a statistical decomposition technique. By deriving AGN fractions for all galaxies within our sample, I was able to estimate the extent to which the AGN component contributes to the total radio luminosity. Based on the estimates of AGN fractions I find that the majority,  $(68.0 \pm 1.5)\%$ , of the HLAGN are dominated by star-forming processes ( $0 \leq f_{\text{AGN}} \leq 0.5$ ), while in  $(32.0 \pm 1.5)\%$  of HLAGN AGN activity domi-

nates ( $0.5 < f_{\text{AGN}} \leq 1.0$ ) in the radio regime (see Sect. 3.2). No significant redshift evolution of the AGN fraction for HLAGN with AGN-related radio emission was found.

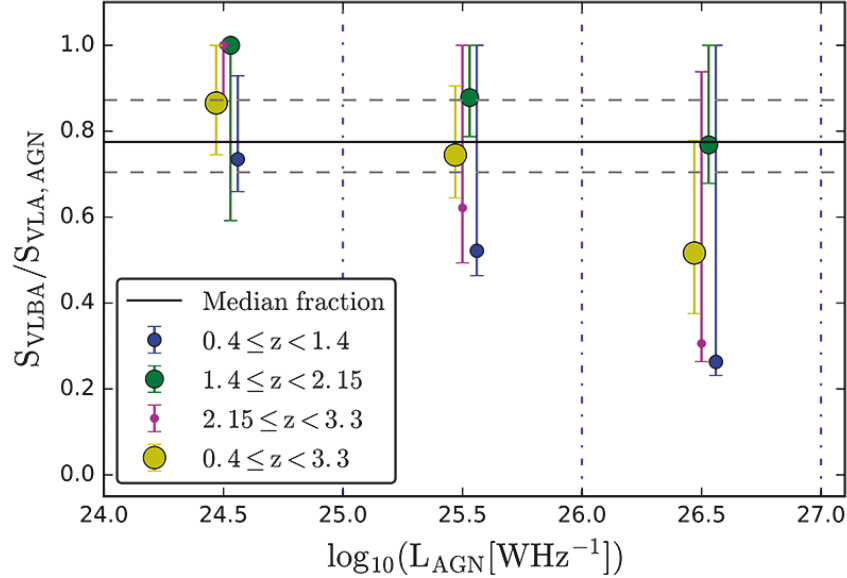


Figure 4.9: VLBA-to-VLA AGN flux density ratio vs. 1.4 GHz AGN luminosity. Yellow circles show the luminosity binned values of the ratio, while solid and dashed black lines show the median, 84th and 16th percentile values of the sample with  $L_{1.4 \text{ GHz, TOT}} \geq 10^{24.4} \text{ WHz}^{-1}$ . Blue, green, and magenta circles and error bars show the data in three redshift bins as indicated in the legend. For better visibility of error bars, I introduced a small shift along the luminosity axis.

The question that arises next is whether radio AGN emission is extended or confined to the galaxies' nuclear regions. To answer this question, I cross-matched the 3 GHz sample of 1604 HLAGN with the Very Long Baseline Array (VLBA) 1.4 GHz radio catalog by [Herrera Ruiz et al. \(2017\)](#). The authors identified a sample of 468 radio AGN detected by VLBA previously targeted with the VLA-COSMOS survey at 1.4 GHz ([Schinnerer et al. 2010](#)). They find that roughly  $\sim 70\%$  (237/344) of the faint sources ( $S_{\text{VLA}} \leq 1 \text{ mJy}$ ) are dominated by emission originating from a compact core, while this is true for only  $\sim 30\%$  (6/21) of the bright population ( $S_{\text{VLA}} > 10 \text{ mJy}$ ). They argue that the bulk of the radio emission of the bright population originates from structures larger than the VLBA scale. To check whether these conclusions also hold for HLAGN, I have limited our HLAGN sample to match the original VLBA selection.

To match the VLBA selection, I require a  $> 5.5\sigma$  VLA detection at 1.4 GHz<sup>2</sup>. Out of 619 HLAGN satisfying this condition, I find only 113 (18%) to have a VLBA counterpart within a 0.4" radius corresponding to about half a beam size of the 3 GHz VLA-COSMOS Large Project observations. The remaining 82% of HLAGN were not detected with the VLBA either because

<sup>2</sup>The average rms reported by [Schinnerer et al. \(2010\)](#) is  $12 \mu\text{Jy}/\text{beam}$ .

they were not detected within the VLA-COSMOS survey at 1.4 GHz (22%) or due to their radio emission being extended to scales larger than those probed with the VLBI method<sup>3</sup> (60%).

To study the properties of the VLBA detected HLAGN, I restricted our analysis to a luminosity-limited subsample of sources with 1.4 GHz luminosities  $L_{1.4 \text{ GHz}} \geq 10^{24.4} \text{ WHz}^{-1}$  (the lowest 1.4 GHz luminosity of the sources at redshifts  $z \geq 2$ ). This criterion yields 51 (8%) HLAGN, spanning redshifts of  $0.4 < z < 3.3$ . By scaling the 1.4 GHz VLA fluxes by AGN fractions, I estimate the flux expected to originate from the AGN component of these sources (see Sect. 3.2). Using these fluxes I further calculate the VLBA-to-VLA AGN flux density ratios. To find the median value and the corresponding  $1\sigma$  confidence range of the flux density ratios, I perform Monte Carlo simulations taking into account the measurement errors of the 1.4 GHz VLA and VLBA flux densities and AGN fractions.

For the sample of the VLBA detected HLAGN with  $L_{1.4 \text{ GHz}} \geq 10^{24.4} \text{ WHz}^{-1}$ , I find the median VLBA-to-VLA AGN flux density ratio to be  $0.78_{-0.07}^{+0.09}$ . By separating the sample in bins of the AGN luminosity ( $\Delta \log L_{\text{AGN}} = 1$ ), I find that the higher AGN luminosity sources tend to have lower VLBA-to-VLA AGN flux density ratios (see Fig. 4.9). These results suggest that the most powerful AGN are dominated by more extended radio emission. To test whether this trend changes with redshift, I separate the sample into three redshift intervals with equal number of sources (17 per bin). A trend of higher AGN luminosity sources having lower flux density ratios is present at all redshifts. Median flux density ratios of the sources with  $L_{1.4 \text{ GHz, AGN}} > 10^{26} \text{ WHz}^{-1}$  at redshifts  $z < 1.4$  and  $2.15 < z < 3.3$  hint that over 50% of the AGN related radio emission might arise from more extended structures (relative to scales probed by the VLBA). This is in agreement with the above-mentioned results by [Herrera Ruiz et al. \(2017\)](#).

The physical explanation for the variety of the observed radio AGN fractions in our HLAGN sample is most likely closely related to the intrinsic properties of individual AGN: the mass and spin of the central SMBH and accretion rate (e.g., [King 2008](#)). [Fanidakis et al. \(2011\)](#) used GALFORM, the semi-analytical simulation of formation and evolution of galaxies, to study the effect these properties might have on the appearance of an AGN. Their simulation shows that massive, rapidly spinning SMBHs are hosted by giant early-type galaxies, while lower-mass SMBHs with much lower spins are mostly found in late-type galaxies. On the basis of the Blandford-Znajek (BZ) mechanism ([Blandford & Znajek 1977](#)), the authors suggest radio-loudness to be determined by the spin of the SMBH as only a rotating SMBH can form radio jets. In this scenario, the range of AGN fractions in the HLAGN sample suggests they may have a range of spins, ranging from AGN with rapidly rotating SMBHs with prominent AGN

<sup>3</sup>Physical scales of VLBA sources range from 20 pc at  $z = 0.1$  to 80 pc at  $z \sim 3$

emission to SMBHs with low spin in which faint AGN emission might be diluted by the light of the host galaxy. This is supported by the results from [Falcke & Biermann \(1999\)](#) who derive equations for a scaled-down AGN jet model based on equipartition assumptions and applied it to observationally well defined samples of galactic and extragalactic sources. They find that the jet powers of their studied sources were comparable to their accretion disk luminosities providing evidence for a disk-jet coupling holding from stellar mass BHs to low-luminosity AGN.

[Merloni & Heinz \(2008\)](#) present a synthesis model for the AGN evolution where they studied how SMBHs grow and evolve through the age of the Universe. In this model, AGN with high Eddington ratios may display either only radiative feedback (high-radiative mode, HR) or both radiative and kinetic feedback (high-kinetic mode, HK). In this context, HLAGN with low radio AGN fractions ( $f_{\text{AGN}} < 0.5$ ) would be those which display mostly radiative feedback, while those with high radio AGN fractions ( $f_{\text{AGN}} \geq 0.5$ ) also produce kinetic feedback in the form of radio-detectable features, such as cores, jets and lobes.

Radiative feedback is expected to arise in galaxies hosting rapidly accreting SMBHs, where the energy released by the growth of the SMBH can influence the properties of the hosts (e.g., see a review by [Fabian 2012](#)). The models of galaxy evolution usually find the AGN bolometric luminosity density to increase from the local redshift out to a peak around  $z \sim 2 - 3$ , followed by a decrease toward higher redshifts (e.g., [Croton et al. 2006](#), [Merloni & Heinz 2008](#)). For the  $\sim 38\%$  of HLAGN, for which I estimated a radio luminosity arising from AGN emission (Sect. 3.2), I compare the radiative luminosity density to literature expectations (e.g., [Croton et al. 2006](#), [Merloni & Heinz 2008](#)). I binned the radiative luminosities derived from the SED-fitting decomposition (see [Delvecchio et al. 2017](#)) into nine redshift bins, finding typical values of bolometric luminosity density to be  $< 1\%$  of those found from the literature for all radiatively efficient AGN. This confirms that X-ray and MIR selected AGN detected in radio are not the dominant contribution to the total bolometric output expected for radiatively efficient AGN.

In the following sections, I describe how the number and luminosity densities of HLAGN and full samples change through cosmic time. By scaling the 1.4 GHz AGN luminosity into kinetic luminosity, I calculate the kinetic luminosity density and compare it to semi-analytic model predictions.

### 4.3.2 Cosmic evolution of radio AGN

To calculate the number and luminosity density, I use:

$$N = \int \Phi(L_{1.4 \text{ GHz}}) d(\log L_{1.4 \text{ GHz}}), \quad (4.5)$$

$$L = \int L_{1.4 \text{ GHz}} \times \Phi(L_{1.4 \text{ GHz}}) d(\log L_{1.4 \text{ GHz}}), \quad (4.6)$$

where  $\Phi(L_{1.4 \text{ GHz}})$  is the redshift evolved luminosity function, using both best-fit evolution parameters derived from the redshift binned and continuous fitting. Here I take the lower and upper limits of the integral to be  $L_{1.4 \text{ GHz}} = 10^{22} \text{ WHz}^{-1}$  and  $L_{1.4 \text{ GHz}} = 10^{28} \text{ WHz}^{-1}$ , respectively. The normalizations of the number and luminosity density evolution curves are affected by the chosen limits of integration. For example, a decrease of the lower limit to  $L_{1.4 \text{ GHz}} = 10^{21} \text{ WHz}^{-1}$  would produce a number density higher by a factor of approximately five, but it would have almost no effect on the luminosity density curve. However, a decrease of the upper limit to  $L_{1.4 \text{ GHz}} = 10^{27} \text{ WHz}^{-1}$  would lower the normalization of the luminosity density by a factor of approximately two, while the number density would remain unchanged.

The evolution of the number and luminosity densities is shown in Fig. 4.10. I find that the number density of HLAGN increased over time, reaching a maximum of  $\sim 9.5 \times 10^{-5} \text{ Mpc}^{-3}$  in the redshift range  $1 < z < 2.5$ , after which it decreased by a factor of approximately five toward the local ( $z = 0$ ) value. A similar trend is seen in the luminosity density evolution, with the peak at  $\sim 1.4 \times 10^{20} \text{ WHz}^{-1} \text{ Mpc}^{-3}$  occurring in the redshift range  $1 < z < 2.5$  followed by a decline of a factor  $\sim 10$  toward the local value. An outlier in redshift bin  $0.7 < z < 0.9$  seen in Fig. 4.10 most likely occurs due to a large scale structure known to exist in the COSMOS field at  $z \sim 0.73$ , as previously discussed in Sect. 4.2.1.

In Fig. 4.10 I also compare our results for the HLAGN sample with the results derived for all sources within the full sample which contain an AGN-related radio emission. The number and luminosity densities of the full sample flatten over the redshift range  $1 < z < 2.5$  at  $\sim 2.2 \times 10^{-4} \text{ Mpc}^{-3}$  and  $1.7 \times 10^{20} \text{ WHz}^{-1} \text{ Mpc}^{-3}$ , respectively. The more rapid decrease with redshift of the HLAGN number and luminosity density at  $z > 2$  when compared to the full sample may be in part explained by the incompleteness of X-ray data used to classify sources as HLAGN (see also Discussion in Smolčić et al. 2017c). I note that the Mauch & Sadler (2007) local luminosity function used to constrain the evolution of the full sample has a different shape than the one by Pracy et al. (2016) used to constrain the evolution of HLAGN. The difference between the two local luminosity functions results in a higher normalization of the number density curve for the full sample with respect to the HLAGN curve.

### 4.3.3 Kinetic feedback of radio AGN and comparison with semi-analytic models

To get an insight into how the kinetic feedback of AGN changes through cosmic time, one of many scaling relations available in the literature (e.g., Willott et al. 1999, Merloni & Heinz 2007,



Godfrey & Shabala 2016) can be used to estimate the kinetic luminosity (see, e.g., Appendix A in Smolčić et al. 2017c). Willott et al. (1999) used the minimum energy condition to estimate the energy stored in lobes from the observed monochromatic synchrotron emission, finding the relation

$$\log(L_{\text{kin}}) = 0.86 \log L_{1.4\text{GHz}} + 14.08 + 1.5 \log f_W, \quad (4.7)$$

where  $L_{\text{kin}}$  is the kinetic luminosity,  $L_{1.4\text{GHz}}$  is the 1.4 GHz radio luminosity and  $f_W$  is the factor into which all the uncertainties were combined. Using observational constraints,  $f_W$  is estimated

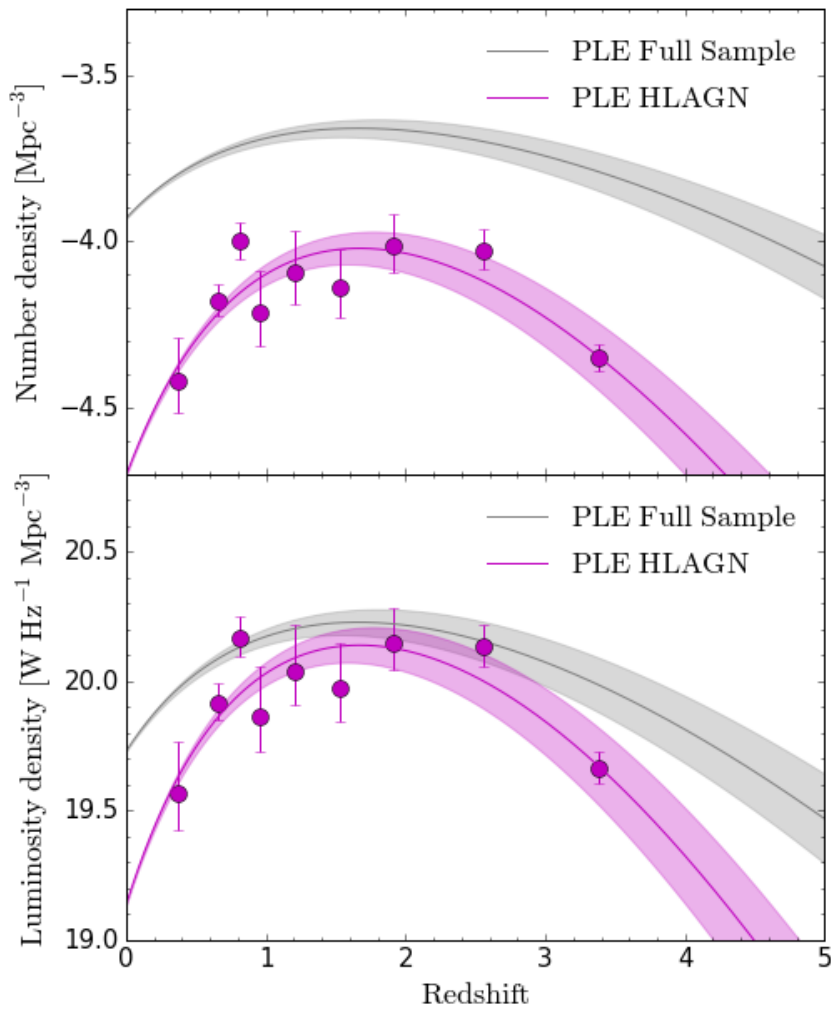


Figure 4.10: Redshift evolution of the number and luminosity density of AGN in COSMOS field for the PLE model are shown in the upper and lower panels, respectively. Magenta circles show the values of number and luminosity density for the HLAGN sample calculated from the redshift binned evolution parameters. Magenta and gray lines show the continuous redshift evolution and corresponding  $1\sigma$  confidence range of HLAGN and the full sample, respectively.

to be in the range of 1 – 20. In this work, the [Willott et al.](#) conversion is used to estimate the kinetic luminosity of HLAGN and the full radio detected samples. I assumed  $f_W = 15$  for which the [Willott et al.](#) relation agrees with results found from radio and X-ray observations of cavities in galaxy groups and clusters ([Bîrzan et al. 2004](#), [O’Sullivan et al. 2011](#)).

To calculate the kinetic luminosity density at a given redshift, I use the relation

$$\Omega_{\text{kin}}(z) = \int L_{\text{kin}}(L_{1.4 \text{ GHz}}) \times \Phi(L_{1.4 \text{ GHz}}) d(\log L_{1.4 \text{ GHz}}), \quad (4.8)$$

where  $\Phi(L_{1.4 \text{ GHz}})$  is the analytic form of the local luminosity function (see Eq. 4.2) and  $\Omega_{\text{kin}}$  is the kinetic luminosity density (KLD; see Fig. 4.11). The normalization of the KLD curve is highly affected by the [Willott et al. \(1999\)](#) uncertainty factor  $f_W$ , whose values can shift the curve both toward lower and higher values<sup>4</sup>. By assuming  $f_W = 15$ , the KLD curve of HLAGN peaks at the value  $2.1 \times 10^{32} \text{ WMpc}^{-3}$  at  $z \sim 1.5$ . The full sample KLD curve is relatively flat in the redshift range  $1 < z < 2.5$  at the value  $3.4 \times 10^{32} \text{ WMpc}^{-3}$ .

Using the calculations embedded in the GALFORM semi-analytic model of formation and evolution of galaxies ([Bower et al. 2006](#)), [Fanidakis et al. \(2012\)](#) studied the evolution of AGN across cosmic time. In their model, the buildup of BH mass occurs in two different modes: (i) starburst mode in which the accretion event is triggered by disk instabilities or galaxy mergers, and (ii) hot-halo mode in which the gas from a quasi-hydrostatic hot halo accretes onto the SMBH. They find that different accretion channels show different evolutionary trends, with starburst and hot-halo modes changing their dominance in the buildup of SMBH mass from higher to lower redshifts, respectively. An update of the [Fanidakis et al.](#) model, using a new version of GALFORM ([Lacey et al. 2016](#)), will be presented in [Griffin et al.](#) (in prep.). After the implementation of the Planck cosmology and using a higher resolution dark matter simulation, one of predictions by [Griffin et al.](#) is the cosmic evolution of kinetic luminosity density for the starburst and hot-halo modes of BH accretion (see Fig. 4.11). The kinetic luminosity density is expected to arise from AGN jets in both of these modes. In the hot halo mode gas from the hot halo slowly accretes onto the SMBH, forming an advection-dominated accretion flow (ADAF; [Narayan & Yi 1994](#)). On the other hand, in the starburst mode a merger or a disk instability causes stars to form from inflowing gas which may also accrete onto the SMBH, in the form of

<sup>4</sup>The kinetic luminosity density (KLD) can be scaled from factor  $f_W^1$  to  $f_W^2$  using the relation

$$\text{KLD}(f_W^2) = \text{KLD}(f_W^1) \left( \frac{f_W^2}{f_W^1} \right)^{3/2}. \quad (4.9)$$

The ratio of the KLD ( $f_W = 20$ ) and KLD ( $f_W = 1$ ) is  $\sim 90$ , that is, the maximum difference in estimates of the KLD using  $f_W$  factors is almost two orders of magnitude.

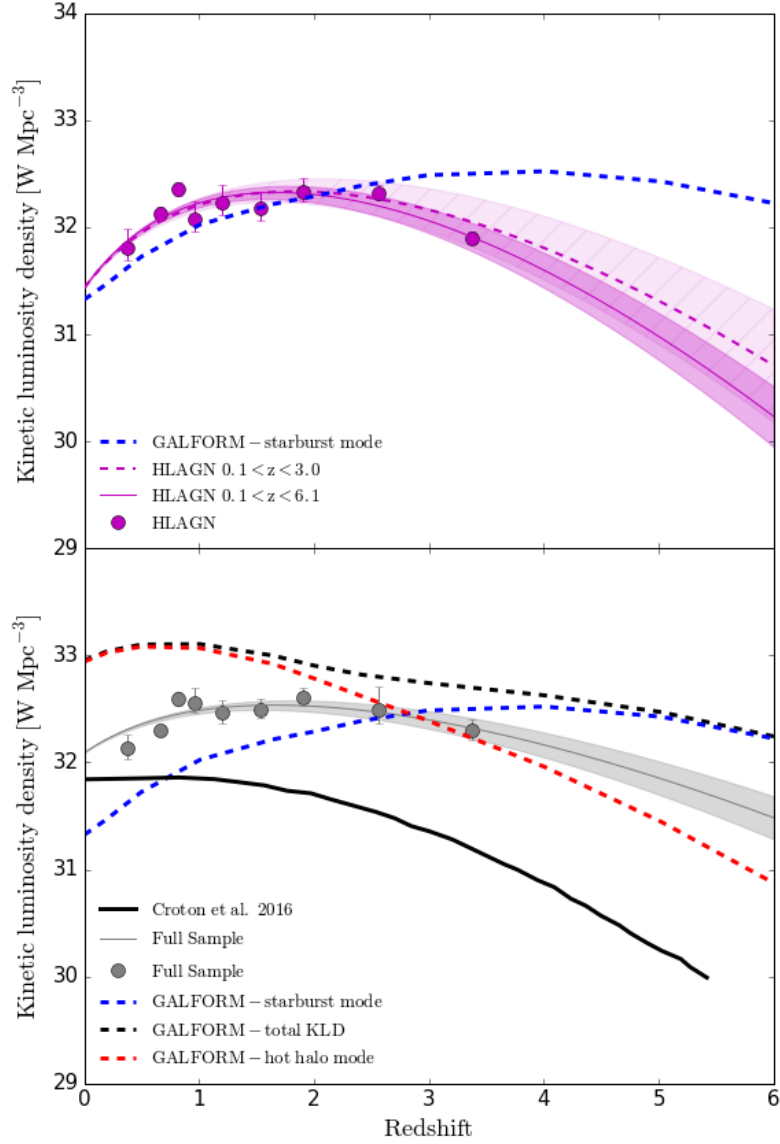


Figure 4.11: Cosmic evolution of the kinetic luminosity density. In the upper panel, the kinetic luminosity density derived using the Willott et al. (1999) conversion between radio and kinetic luminosity for the PLE continuous and redshift binned model of HLAGN is shown by a magenta line and circles, respectively, with the corresponding  $1\sigma$  uncertainties. The KLD estimate for the starburst mode of accretion based on the semi-analytic GALFORM model as calculated by Griffin et al. (in prep.) is shown by a blue dashed line. Lower panel shows the KLD for the PLE continuous and redshift binned models of the full sample (gray line and circles, respectively), with corresponding  $1\sigma$  uncertainties. The black solid line shows the prediction of the semi-analytical model for the radio mode of BH accretion by Croton et al. (2016). Estimates of the KLD based on the GALFORM model for the starburst and hot-halo modes of accretion and their sum are shown with blue, red and black dashed lines, respectively.

a standard thin disk accretion (Shakura & Sunyaev 1973).

The selection of the HLAGN sample based on X-ray and MIR criteria aims to trace the thin disk accreters and therefore should be compared to the starburst mode AGN from GALFORM. In the upper panel of Fig. 4.11, the HLAGN KLD curve shows a steep increasing trend similar to that predicted for the starburst mode of accretion out to a  $z \sim 2$ . At higher redshifts the HLAGN evolutionary curve disagrees with predictions for the starburst mode of accretion. A possible reason for the disagreement could be an overly simplistic conversion between the monochromatic and kinetic luminosity. A more complex conversion dependent on various parameters, such as synchrotron age and environments (Hardcastle & Krause 2014, Kapinska et al. 2015), could alter the overall shape of the KLD curve. Another reason could be the incompleteness of the HLAGN sample at high redshifts (Delvecchio et al. 2017). If I were to exclude the highest redshift measurement and fit the evolution to the data, our results would show agreement to GALFORM prediction for the starburst mode out to a  $z \sim 3$  (as shown in the upper panel of Fig. 4.11). However, the discrepancy still remains between our results and the GALFORM prediction present at higher redshift. I note that, as detailed below, various semi-analytic models tend to disagree in this regime as well.

The lower panel of Fig. 4.11 shows the comparison between the KLD curve derived for the full sample and the prediction from semi-analytic models. Despite the difference in normalizations, the KLD curve of the full sample interestingly shows a similar shape to the total KLD estimate from GALFORM, both of which contain kinetic luminosity contribution of all AGN, regardless of the assumed mode of accretion.

I also compare our results of the full sample with the semi-analytical simulation of cosmological galaxy formation by Croton et al. (2006). They examined two different modes of SMBH accretion, namely quasar and radio mode. They find that powerful outflows that occur in radio mode accretion can efficiently quench star formation in massive systems, thus offering a solution for the cooling flow problem. One of the predictions of their model is the BH accretion rate density evolution, estimated using the Bondi-Hoyle accretion model. An update to this work is presented in Croton et al. (2016) where the authors introduce the so-called radio mode efficiency factor to modulate the strength of the SMBH accretion. Using the accretion rate formula (see Eq. 16 in Croton et al. 2016), and adopting the suggested radio mode efficiency parameter value of 0.08, the SMBH luminosity can be calculated. Under the assumption that most of the accretion energy is ejected in the kinetic form, we can compare the Croton et al. SMBH luminosity to our estimate of KLD for the full sample which contains the contribution from all AGN that show evidence of AGN-related radio emission. At redshifts higher than  $z \sim 1.5$  the full sample KLD curve shows a decline similar to that expected from semi-analytic simulation

by Croton et al. for the radio mode AGN. The observed decline toward the local value at lower redshift instead is not in agreement with the predicted radio mode curve. As discussed, the normalization of KLD curves is affected by the uncertainty on the  $f_W$  factor. The normalization of the peak of the KLD curve of the full sample would agree with the Croton et al. expectations for  $f_W = 4$ .

From Fig. 4.11 it is clear that the two compared simulations disagree in their predictions of the KLD both in normalization and overall shape. This stresses the need for more in-depth studies of the conversion between monochromatic and kinetic luminosity.

In summary, I find that our data do not completely agree with any of the predictions from the available models. However, given the significant uncertainties present both in the data and in the models, it is interesting to note that each of the features shown by the data (i.e., approximately constant maximum of KLD in the redshift range  $1 < z < 2.5$ , with significant decreases at both lower and higher redshift), are predicted by at least one of the models. This suggests that, using somewhat different assumptions, it should be possible to generate new models of galaxy evolution which could better reproduce our data.

## 4.4 Chapter summary and conclusions

In this Chapter, I presented an analysis of a sample of 1604 X-ray and mid-IR selected AGN with moderate-to-high radiative luminosities (HLAGN) from the VLA-COSMOS 3 GHz Large Project, selected to trace analogs of local high-excitation radio galaxies (HERGs) out to  $z \sim 6$ . The findings are summarized as follows.

To study the origin of the radio emission in our HLAGN sample, I developed the method of statistical decomposition of the observed 3 GHz radio luminosities into contributions arising from star-forming processes and AGN activity. In agreement with other studies of X-ray and MIR selected AGN samples, I find that the majority,  $(68.0 \pm 1.5)\%$ , of HLAGN have radio emission dominated by star-forming processes ( $0 \leq f_{\text{AGN}} \leq 0.5$ ), while  $(32.0 \pm 1.5)\%$  of them are dominated by the AGN-related emission in the radio ( $0.5 < f_{\text{AGN}} \leq 1.0$ ).

For all sources with  $f_{\text{AGN}} > 0$  I calculated the AGN luminosity by scaling the total 1.4 GHz luminosity (converted from the observed 3 GHz radio luminosity) by the derived AGN fraction. Using a complete subsample ( $S_{3 \text{ GHz, AGN}} \geq S_{\text{lim}, 3 \text{ GHz}}$ ) of HLAGN I constructed the 1.4 GHz radio AGN luminosity function of HLAGN out to  $z \sim 6$ . By assuming pure luminosity and pure density evolution models I found  $L^*(z) \propto (1+z)^{(3.97 \pm 0.15) + (-0.92 \pm 0.06)z}$  and  $\Phi^*(z) \propto (1+z)^{(2.64 \pm 0.10) + (-0.61 \pm 0.04)z}$ , respectively.

I further studied the evolution of the number and luminosity densities of the HLAGN popu-

lation. I found an increasing trend from high redshifts up to a flattening at redshifts  $1 < z < 2.5$ , followed by a significant decrease down to the value in the local Universe.

I estimated the kinetic luminosity density and found an approximately constant maximum in the redshift range  $1 < z < 2.5$ . By comparing this behavior to expectations from semi-analytic models of galaxy formation and evolution, I find that such behavior is not entirely expected by any of the models tested here. However, given the significant uncertainties present both in the data and in the models, the similarities found show that by modifying assumptions of these models, it should be possible to better reproduce our data.

# Chapter 5

## The quasar radio loudness dichotomy exposed via radio luminosity functions by combining the COSMOS and XXL-S X-ray selected quasars

In this Chapter I present a study of a sample of 274 radio and X-ray selected quasars (XQSOs) detected in the COSMOS and XXL-S radio surveys at 3 GHz and 2.1 GHz, respectively. This sample was identified by adopting a conservative threshold in X-ray luminosity,  $L_X [2 - 10 \text{ keV}] \geq 10^{44} \text{ erg s}^{-1}$ , selecting only the most powerful quasars. Using this sample, I study the origin of the radio emission in this sample by constraining their radio luminosity functions, as proposed by [Kimball et al. \(2011\)](#) and [Condon et al. 2013](#). The presented work is currently under revision in A&A (Ceraj et al., A&A, submitted).

### 5.1 Chapter introduction

Quasars are among the most powerful AGN and usually they are very bright over most of the electromagnetic spectrum, from gamma to infrared frequencies. However, only 5 – 10% of quasars are associated with strong radio sources (e.g., [Condon et al. 1980](#), [Condon et al. 1981](#)). This observation triggered a long lasting search for the physical origin of the quasars' radio emission, especially for type-1 (unobscured) quasars (e.g., [Kellermann et al. 1989](#), [White et al. 2007](#), [Baloković et al. 2012](#), [Condon et al. 2013](#)). The most common approach is to separate the quasar population into so-called "radio-loud" (RL) and "radio-quiet" (RQ) categories with respect to some threshold (e.g., [Ivezić et al. 2002](#), [Cirasuolo et al. 2003](#), [Pierce et al. 2011](#)).

As described in Section 1.5.2, in search for the existence of two physically distinct populations, most authors have defined radio loudness as the radio-to-optical flux density or luminosity ratios (e.g., Kellermann et al. 1989, Ivezić et al. 2002, White et al. 2007, Baloković et al. 2012). Such definitions relate the two mechanisms associated with the accretion onto the supermassive black hole: (a) the optical luminosity (due to thermal emission from the accretion disk) and (b) the radio emission (due to synchrotron radiation from the core, jets or lobes). Despite the same or similar definition of radio loudness, the results differ widely: some report to have found a dichotomy (e.g., Ivezić et al. 2002, White et al. 2007), while others find no evidence of it (e.g., Cirasuolo et al. 2003). As discussed by Baloković et al. (2012), the disagreement can be explained by selection biases not fully accounted for in the various analysis and low number statistics.

Another approach to the problem of quasar radio loudness dichotomy is to study the quasar radio luminosity function (e.g., Kimball et al. 2011, Condon et al. 2013). In the local universe, the radio luminosity function above  $L_{1.4 \text{ GHz}} \geq 10^{23} \text{ WHz}^{-1}$  is dominated by AGN-related radio emission, while radio emission from star-forming processes in galaxies starts to dominate below that threshold (e.g., Condon et al. 2002). Condon et al. (2013) studied the 1.4 GHz RLF of color-selected quasars from the Sloan Digital Sky Survey (SDSS) Data Release 7 Quasar catalog (Schneider et al. 2010) at redshifts  $0.2 < z < 0.45$  detected at 1.4 GHz within NVSS (Condon et al. 1998). They argue that their RLF is most likely dominated by AGN-related radio emission due to the high radio luminosity ( $L_{1.4 \text{ GHz}} \geq 10^{24.2} \text{ WHz}^{-1}$ ) of the selected sources. To further study the origin of radio emission, they modelled the distribution of the peak flux densities of 179 color-selected quasars from the NVSS at redshifts  $0.2 < z < 0.3$  using flux densities below the NVSS detection limit ( $S_{1.4 \text{ GHz}} = 2.5 \text{ mJy}$ ; Condon et al. 1998). They argued that the observed distribution of peak fluxes for undetected sources should require the presence of a ‘bump’ in the 1.4 GHz RLF centered at the luminosity  $L_{1.4 \text{ GHz}} \approx 10^{22.7} \text{ WHz}^{-1}$ . This ‘bump’, due to highly star-forming galaxies in Condon’s model (see Fig. 6 in Condon et al. 2013), was confirmed by Kimball et al. (2011), who examined the same sample of color-selected quasars from SDSS, individually detected at 6 GHz using the Expanded VLA (EVLA; Perley et al. 2011). They constructed the 6 GHz quasar RLF, finding the sources above and below  $L_{6 \text{ GHz}} = 10^{23.5} \text{ WHz}^{-1}$  to be dominated by AGN-related emission and star-forming processes, respectively.

In this Chapter, I follow the approach of Kimball et al. (2011) and Condon et al. (2013) to study the origin of radio emission in radio and X-ray selected quasars (XQSOs) via RLFs. The used selection ( $L_X[2 - 10 \text{ keV}] \geq 10^{44} \text{ erg s}^{-1}$ ) is aimed at tracing the sources exhibiting quasar activity in the COSMOS and XXL-S fields. Selection of the XQSO sample is described



in Sect. 5.2, while in Sect. 5.3, I examine several definitions of radio loudness applied to the XQSOs. The shape and evolution of the XQSO RLF are described in Sect. 5.4, and discussed in Sect. 5.5 in the context of other studies of the origin of radio emission in quasars. The main conclusions are summarized in Sect. 5.6.

## 5.2 X-ray and radio selected quasars

In this section, I describe the selection of the XQSO sample. To construct a sample of quasars that span the wide range of 1.4 GHz radio luminosities needed to constrain the shape and evolution of the RLF, a combination of the available radio datasets with the multiwavelength (X-ray to infrared) coverage in the COSMOS and XXL-S fields, described in Sect. 2, is used.

### 5.2.1 Sample selection

From the catalogs of radio detected sources with multiwavelength counterparts described in Chapter 2, quasars are selected based on their hard X-ray luminosity. I applied a criterion of  $L_X[2 - 10 \text{ keV}] \geq 10^{44} \text{ erg s}^{-1}$  which broadly selects quasars (e.g., review by Padovani et al. 2017). Throughout this Thesis I refer to these X-ray and radio selected quasars as XQSOs.

The sample contains a total of 274 XQSOs, 191 from the COSMOS field and 83 from the XXL-S field. All COSMOS XQSOs were previously classified as moderate-to-high radiative luminosity AGN by Smolčić et al. (2017b) (see also Sect. 2.1.3), while all XXL-S XQSOs were classified as high-excitation radio galaxies by Butler et al. (2018a) (see also Sect. 2.2.2). For 60% of COSMOS XQSOs spectroscopic redshifts were available, while for the rest (40%) I use photometric redshifts. All of the XXL-S XQSOs have available spectroscopic redshifts. The redshift distribution of XQSOs is shown in the left panel of Fig. 5.1. With the selection based on the X-ray luminosities, our sample of COSMOS and XXL-S sources is complete out to  $z \sim 4$  (see Fig. 7 by Marchesi et al. 2016) and  $z \sim 2.2$  (see Fig. 7 in Butler et al. 2018a), respectively.

### 5.2.2 Infrared and B-band luminosities

For every source in the sample of XQSOs, the total infrared (IR; rest  $8 - 1000 \mu\text{m}$ ) luminosity arising from star formation within the host galaxy was estimated from the multi-component (star-forming galaxy and AGN) best-fit template from broad-band SED-fitting decomposition, as presented by Delvecchio et al. (2017) and Butler et al. (2018a). Using the same procedure, the intrinsic 4058 B-band AGN luminosity was estimated for all COSMOS sources and 81/83 XXL-S sources. Some of the B-band AGN luminosity estimates were calculated using SED

templates in which the model of AGN component is not well constrained by the data. This is true for 23/191 of COSMOS and 14/81 of XXL-S sources. These values of B-band AGN luminosity can be considered lower limits.

### 5.2.3 Radio spectral indices

The XQSO sample described above contains sources detected at 3 GHz (COSMOS) and 2.1 GHz (XXL-S). Spectral index estimates are available for 68 ( $\sim 36\%$ ) COSMOS and 75 ( $\sim 90\%$ ) XXL-S sources, as shown in the right panel of Fig. 5.1. The median value and the standard deviation of the derived spectral indices are  $-0.89 \pm 0.56$  and  $-0.47 \pm 0.62$  for the COSMOS and XXL-S XQSOs, respectively. For the sources without a spectral index estimate, I apply the median values obtained from the single-censored survival analysis. For the sources within the COSMOS field, this method finds a value of  $(-0.6 \pm 0.3)$ , while the estimated median spectral index value for the XXL-S sources is  $(-0.23 \pm 0.12)$ .

Spectral indices of COSMOS XQSOs are on average steeper than those of XXL-S sources due to flux limits of the radio surveys and the physical nature of the sources. As discussed by Novak et al. (2017), in order for a 3 GHz source close to the 3 GHz detection limit to be detected at 1.4 GHz, it needs to have a very steep radio spectrum ( $\alpha < -2$ ). The spectral indices of the

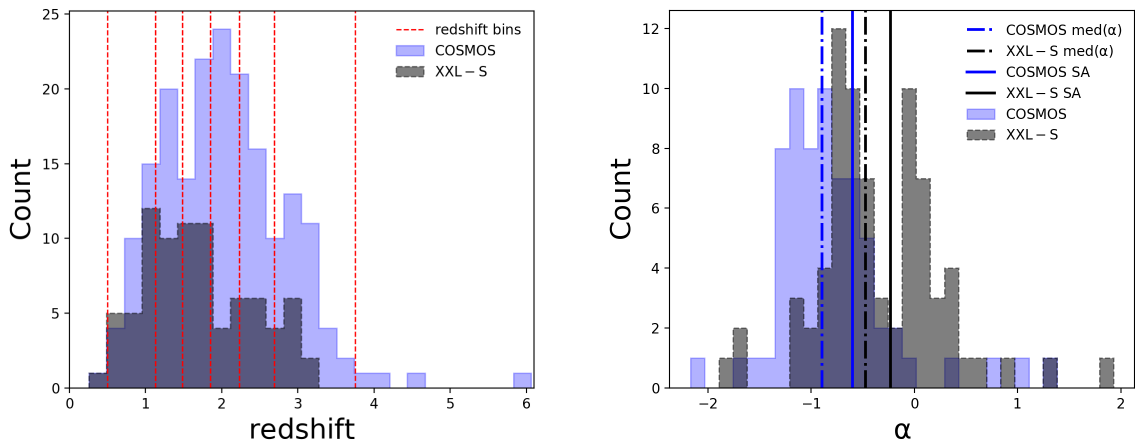


Figure 5.1: *Left:* Redshift distributions of COSMOS and XXL-S XQSOs are shown with blue and gray histograms, respectively. Red dashed lines show the edges of the redshift bins used in the radio luminosity function analysis in Ch. 5. *Right:* Spectral indices of XQSOs in the COSMOS (blue) and XXL-S (gray) fields for the subsample of objects detected in more than one frequency. Dashed-dotted blue and black lines show the median spectral index of COSMOS and XXL-S sources, respectively. Solid blue and black lines show the value of spectral index obtained from the single-censored survival analysis of COSMOS and XXL-S sources, respectively.

XXL-S sources were derived by splitting the observations at 2.1 GHz (bandwidth 2 GHz) into 3 sub-bands with bandwidths of 683 MHz centered at 1.417 GHz, 2.100 GHz and 2.783 GHz (Paper XXXI). Spectral indices derived in this way are less biased to the shape of the radio spectrum and a wide variety of spectral index values can be derived. As shown in the right panel of Fig. 5.1, the distribution of XXL-S spectral indices appears to be double-peaked. The bin width was set to  $3 \times \sigma_{\alpha, \text{XXL-S}}$ , where  $\sigma_{\alpha, \text{XXL-S}} = 0.08$  is the mean uncertainty on XXL-S spectral indices derived using sub-band analysis. I tested if there is dependence of spectral index on relevant physical parameters (such as radio flux densities and luminosities, X-ray luminosity and redshift) and found no statistically significant correlations. The apparently bimodal shape of the XXL-S XQSO spectral index distribution is most likely driven by a small number statistics.

For XQSOs in the COSMOS field, both the median value of derived spectral indices and the estimate from the survival analysis are consistent with the spectral index  $-0.7$  usually quoted in the literature. This value is consistent with spectral indices found in literature in studies of radio spectra of both star-forming galaxies and AGN (e.g., Condon 1992). On the other hand, roughly  $\sim 50\%$  of XXL-S XQSOs (and even more than 50% on the basis of the results from the survival analysis) have flat spectra ( $\alpha > -0.5$ ) typical of core-dominated AGN radio emission. Hence, I expect the radio emission of XXL-S XQSOs to be dominated by an AGN contribution to the radio emission, while a mixture of two contributions (star formation and AGN activity) may contribute to the total observed radio emission of COSMOS XQSOs.

## 5.3 Radio loudness

In this section I compare four different definitions of radio loudness and criteria used to select RL and RQ AGN. Each of these criteria relies on a different spectral window into AGN activity: (a) radio emission from the cores, jets or lobes, (b) excess of radio emission relative to that expected only from star-forming processes within the host galaxies, (c) AGN-related optical emission from the accretion disk and (d) X-ray emission from the hot corona.

### (a) 1.4 GHz radio luminosity ( $L_{1.4 \text{ GHz}}$ )

The simplest criterion is based solely on the radio luminosity of the source. Miller et al. (1990) and Goldschmidt et al. (1999) analyzed the distribution of the 5 GHz radio luminosity of optically-selected quasars. To test the thresholds they applied to radio luminosity, I convert the 5 GHz into 1.4 GHz luminosity thresholds with the cosmology used in this work. The RL quasars are then defined as those with 1.4 GHz luminosity above  $L_{1.4 \text{ GHz}} \approx 10^{24} \text{ W Hz}^{-1}$  (Goldschmidt et al. 1999) and  $L_{1.4 \text{ GHz}} \approx 10^{25} \text{ W Hz}^{-1}$  (Miller

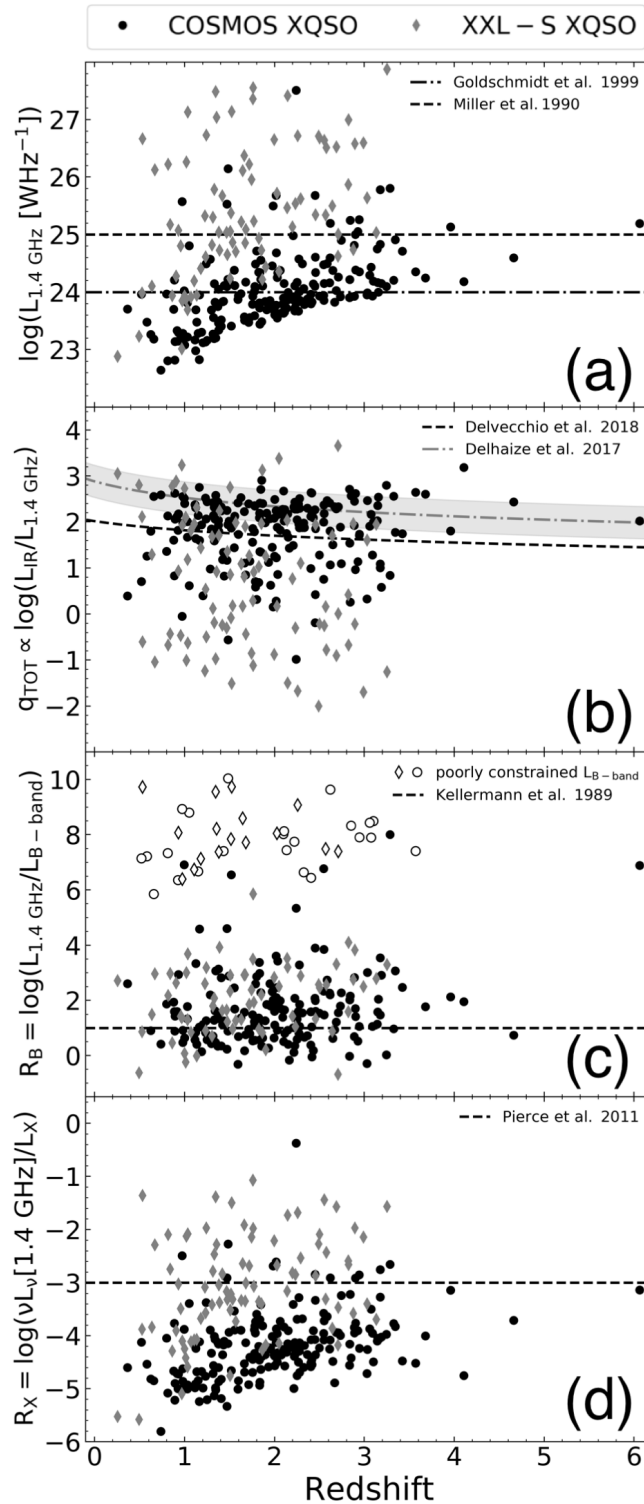


Figure 5.2: Radio loudness vs. redshift of XQSOs from COSMOS (circles) and XXL-S (diamonds). In different panels radio loudness is defined as: (a) 1.4 GHz radio luminosity, (b) IR-to-1.4 GHz luminosity ratio,  $q_{\text{TOT}}$ , (c) 1.4 GHz radio-to-optical luminosity ratio, (d) 1.4 GHz radio-to-X-ray luminosity ratio. Different thresholds from the literature, used to select sources as RL, are shown as indicated in the legends. The gray dot-dashed line and area show the  $q_{\text{TIR}}(z) \pm 0.35$  by Delhaize et al. (2017).

et al. 1990).

(b) **IR-to-radio luminosity ratio ( $q_{\text{TOT}}$ )**

The logarithmic value of the ratio of the IR-to-1.4 GHz luminosity,  $q_{\text{TOT}} \propto \log(L_{\text{IR}}/L_{1.4 \text{ GHz}})$ , can be used to select sources which display an excess of radio emission due to AGN activity in relation to that expected just from star-forming processes in the host galaxy (e.g., Delvecchio et al. 2017, Smolčić et al. 2017c, Ceraj et al. 2018). For example, a redshift-dependent radio excess threshold ( $q_{\text{REX}} = 24 - 21.984 \times (1+z)^{0.013}$ ) derived by Delvecchio et al. (2017) selects sources in which there is negligible ( $\sim 0.15\%$ ) contamination of radio emission due to star formation. I select sources that display significant radio excess ( $q_{\text{TOT}} \leq q_{\text{REX}}$ ) as RL.

(c) **Radio-to-optical luminosity ratio ( $R_{\text{B}}$ )**

The most widely used criterion to separate RL and RQ quasars is based on the radio-to-optical flux density or luminosity ratio (e.g., Kellermann et al. 1989, Ivezić et al. 2002, Baloković et al. 2012). RL quasars are defined as those having radio emission a factor of  $\sim 10$  stronger than the optical emission, i.e.  $R_{\text{B}} = \log(L_{1.4 \text{ GHz}}/L_{\text{B-band}}) = 1$ , where  $R_{\text{B}}$  is the logarithmic ratio of radio-to-B-band luminosity. In Fig. 5.2, empty symbols show the upper limits of  $R_{\text{B}}$  calculated using poorly constrained B-band AGN luminosities (see Sect. 5.2.2).

(d) **Radio-to-X-ray luminosity ratio ( $R_{\text{X}}$ )**

Radio loudness defined as the logarithm of radio-to-[2 – 10 keV] X-ray luminosity ratio,  $R_{\text{X}} = \log(\nu L_{\nu}(1.4 \text{ GHz})/L_{\text{X}}[2 - 10 \text{ keV}])$ , has proven to be successful in selecting RL AGN even in cases of heavily obscured nuclei (e.g., Terashima & Wilson 2003). Following Pierce et al. (2011), I adopt the threshold  $R_{\text{X}} \approx -3$  to separate RL ( $R_{\text{X}} > -3$ ) and RQ ( $R_{\text{X}} < -3$ ) quasars.

The radio loudness distributions described above are shown in Fig. 5.2 as a function of redshift. The number of RL and RQ XQSOs, as defined by different criteria, are listed in Table 5.1, and numbers of sources classified as RL using criteria (b)-(d) are shown using Venn diagrams in Fig. 5.3. It is important to note that, for the same sample of sources, these criteria select different numbers of RL XQSOs ranging from  $\sim 18\%$  to  $\sim 73\%$ . The origin of this discrepancy is the difference in definitions (a) and (b), which are related to different physical mechanisms than (c) and (d). The radio loudness defined via either monochromatic radio luminosity ( $L_{1.4 \text{ GHz}}$ ) or the IR-to-radio luminosity ratio ( $q_{\text{TOT}}$ ) traces the excess of radio emission, with RL sources

being those with high levels of radio emission and those in which there is more radio emission detected than expected from the star formation within the host galaxy, respectively. On the other hand, radio loudness defined as  $R_B$  and  $R_X$  compares radiative (traced via B-band or X-ray luminosities) and kinetic (traced via radio luminosity) AGN emission. By applying (a)-(b) definitions of radio loudness, I found that COSMOS XQSOs are predominantly RQ, while XXL-S XQSOs are mostly RL (see Table 5.1). This is a result of different flux density limits of COSMOS and XXL-S radio surveys.

As described in Sect. 5.2.3, the spectral indices of the COSMOS XQSOs are on average steeper than those of XXL-S XQSOs, which suggests a different origin of radio emission in these sources. The steep spectral indices of COSMOS XQSOs, which are mostly RQ, can originate from both star formation within the host galaxy and AGN. The logarithm of IR-to-1.4 GHz radio luminosity ratio,  $q_{TOT}$ , can be used to quantify radio excess, as was previously done in Chapter 4 for all COSMOS sources detected at 3 GHz that have multiwavelength coverage. By quantifying the radio excess due to an AGN contribution to the total radio emission, relative to that expected from the star forming-related IR luminosities, Ceraj et al. estimated the AGN fractions,  $f_{AGN}$ , defined as the AGN-related contribution to the total detected radio emission.

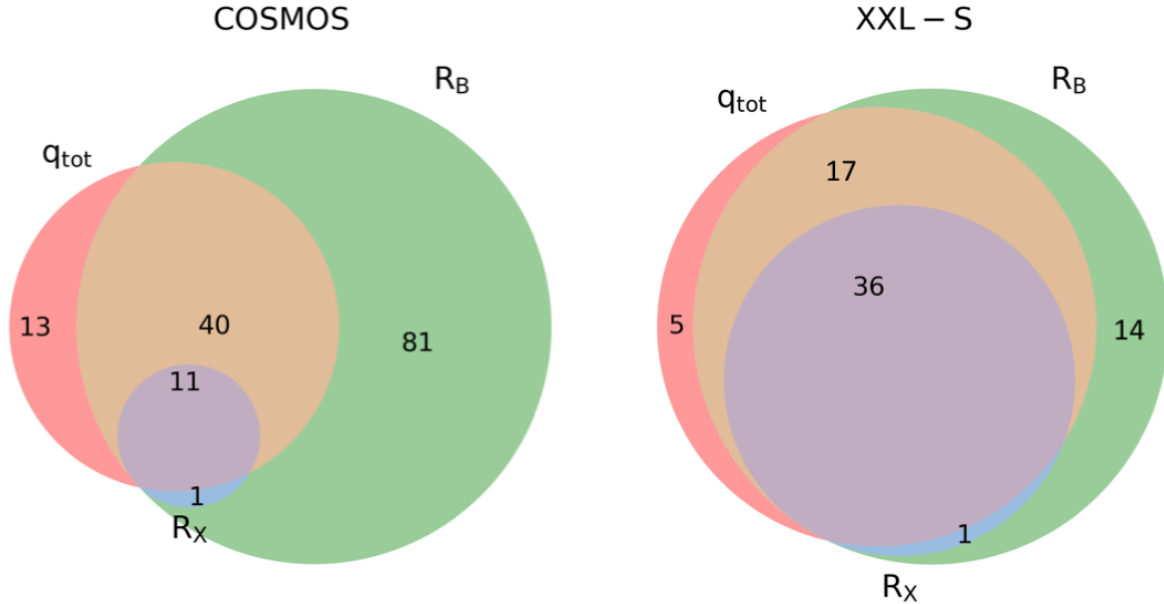


Figure 5.3: Venn diagram of COSMOS (left) and XXL-S (right) XQSOs classified as radio-loud based on three criteria: i) radio-excess threshold by Delvecchio et al. (2017) (pink circles), ii)  $R_B$  threshold by Kellermann et al. (1989) (green circles) and iii)  $R_X$  threshold by Terashima & Wilson (2003) (blue circles).

Table 5.1: Number of XQSOs defined as RL or RQ based on different criteria of radio loudness.

| Threshold  | COSMOS |       |                     | XXL-S |       |                     | Total               |
|--|--------|-------|---------------------|-------|-------|---------------------|---------------------|
|  | N(RL)  | N(RQ) | f <sub>RL</sub> (%) | N(RL) | N(RQ) | f <sub>RL</sub> (%) | f <sub>RL</sub> (%) |
| $L_{1.4 \text{ GHz}} = 10^{24} \text{ WHz}^{-1}$ | 86     | 105   | 45.0                | 72    | 11    | 86.7                | 57.7                |
| $L_{1.4 \text{ GHz}} = 10^{25} \text{ WHz}^{-1}$ | 16     | 175   | 8.4                 | 52    | 31    | 62.7                | 24.8                |
| $q_{\text{REX}} = 24 - 21.984(1+z)^{0.013}$      | 64     | 127   | 33.5                | 58    | 25    | 69.9                | 44.5                |
| $R_B = 1$  | 133    | 58    | 69.6                | 66    | 15    | 81.5                | 73.2                |
| $R_x = -3$                                       | 12     | 179   | 6.3                 | 37    | 46    | 44.6                | 17.9                |

Following the same approach to estimate  $f_{\text{AGN}}$  of XQSOs, I use the infrared-radio correlation derived by [Delhaize et al. \(2017\)](#); shown in Fig. 5.2.b) derived from a sample of  $\sim 9500$  star-forming galaxies (SFGs) in the COSMOS field. They found a redshift-dependent infrared-to-1.4 GHz radio luminosity ratio,  $q_{\text{TIR}}(z) = 2.88 \times (1+z)^{-0.19}$ , with a spread of 0.35 dex. Under the assumption that the host galaxies of XQSOs are regular SFGs (as supported by results by, e.g., [Stanley et al. 2015](#)), I can use  $q_{\text{TIR}}(z)$  to derive AGN fractions in XQSOs defined as  $f_{\text{AGN}} = 1 - 10^{q_{\text{TOT}} - q_{\text{TIR}}}$ .

Fig. 5.4 shows the logarithm of radio-to-[2 – 10 keV] X-ray luminosity ratio,  $R_x$ , as a function of  $L_{1.4 \text{ GHz}}$ , color-coded by the AGN fraction from both COSMOS and XXL-S sources. The radio loudness defined solely as the threshold in 1.4 GHz luminosity ([Miller et al. 1990](#)) mostly selects as RL sources which are dominated by the AGN-related radio emission. However, there are a few outliers (5/68) in which the AGN fraction is  $f_{\text{AGN}} < 0.5$ . For all sources with  $R_x$  above the threshold  $R_x = -3$  radio emission is dominated by AGN activity ( $f_{\text{AGN}} \geq 0.5$ ), with the exception of one XXL-S source. Below the thresholds adopted for both criteria, there are roughly  $\sim 50\%$  (102/206) of sources which are dominated by AGN-related radio emission ( $f_{\text{AGN}} \geq 0.5$ ). This shows that applying a simple radio loudness threshold yields only subsamples of AGN-dominated sources in the radio. In order to study the origin of radio emission in XQSOs, another approach is needed.

The radio luminosity function (RLF) has proven to be a highly useful tool for the study of the origin of radio emission in optically-selected quasars ([Kimball et al. 2011](#), [Condon et al. 2013](#)). In the next sections I follow the [Kimball et al.](#) approach in the study of the origin of the detected radio emission by constructing RLFs for all radio-detected XQSOs at  $0.5 < z < 3.75$ . For these sources I examine the cosmic evolution of the star-forming and AGN contributions to the radio emission via an analysis of the shape of their RLF.



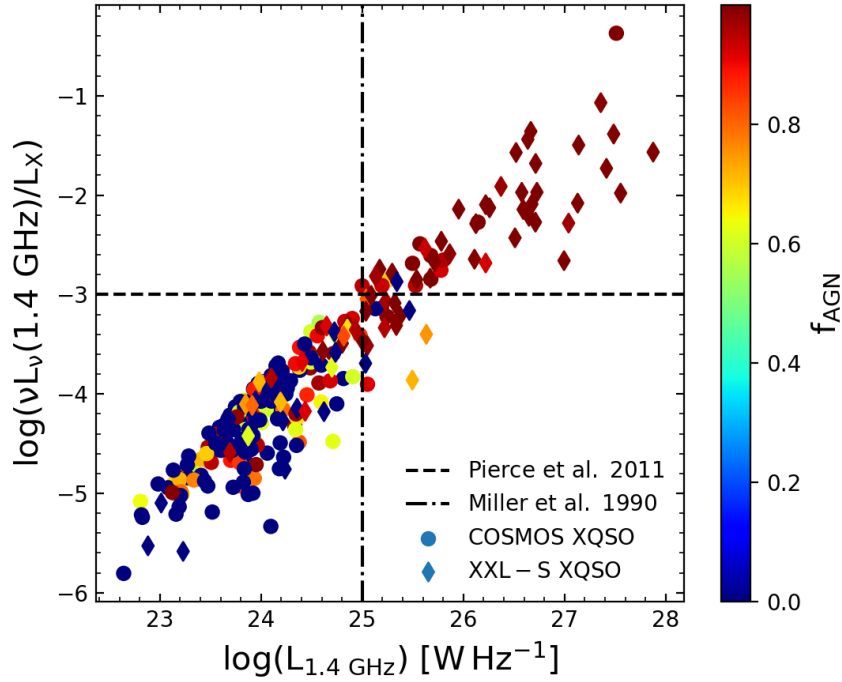


Figure 5.4:  $R_X$  vs. 1.4 GHz luminosity color-coded by the AGN fraction ( $f_{\text{AGN}}$ ) of COSMOS (circles) and XXL-S (diamonds) XQSOs. Radio loudness threshold in radio luminosity as defined by Miller et al. (1990) is shown with the black dash-dotted vertical line, while the radio-to-X-ray radio loudness threshold from Pierce et al. (2011) is shown with the black dashed horizontal line. It can be seen that both RL thresholds miss a significant fraction of sources where the AGN dominates the radio emission.

## 5.4 Cosmic evolution of XQSO RLFs

In this section, radio luminosity functions of XQSOs are calculated using the method described in Section 3.3. The sample of 267 XQSOs is split into six redshift bins (see the left panel of Fig. 5.1) with roughly the same number of sources ( $\sim 45$ ) in each bin over the range  $0.50 \leq z \leq 3.75$ . Briefly, construction of the RLF relies on the  $V_{\text{max}}$  procedure to estimate the maximum observable volume of each source within the sample. Taking into account the incompleteness of the COSMOS and XXL-S radio catalogs and the field areas, RLFs are constructed out to  $z \sim 3.75$ .

In the analysis I do not correct the RLFs for the fact that the X-ray data used to select XQSOs in the XXL-S field are incomplete at  $z > 2.2$  (see Sect. 5.2). The last two redshift bins are affected by this incompleteness and should be taken with caution. I note that the results remain valid even if I do not consider the last two redshift bins.

The choice of the local radio luminosity function used to constrain the evolution of the XQSO radio luminosity functions is described in the following section.



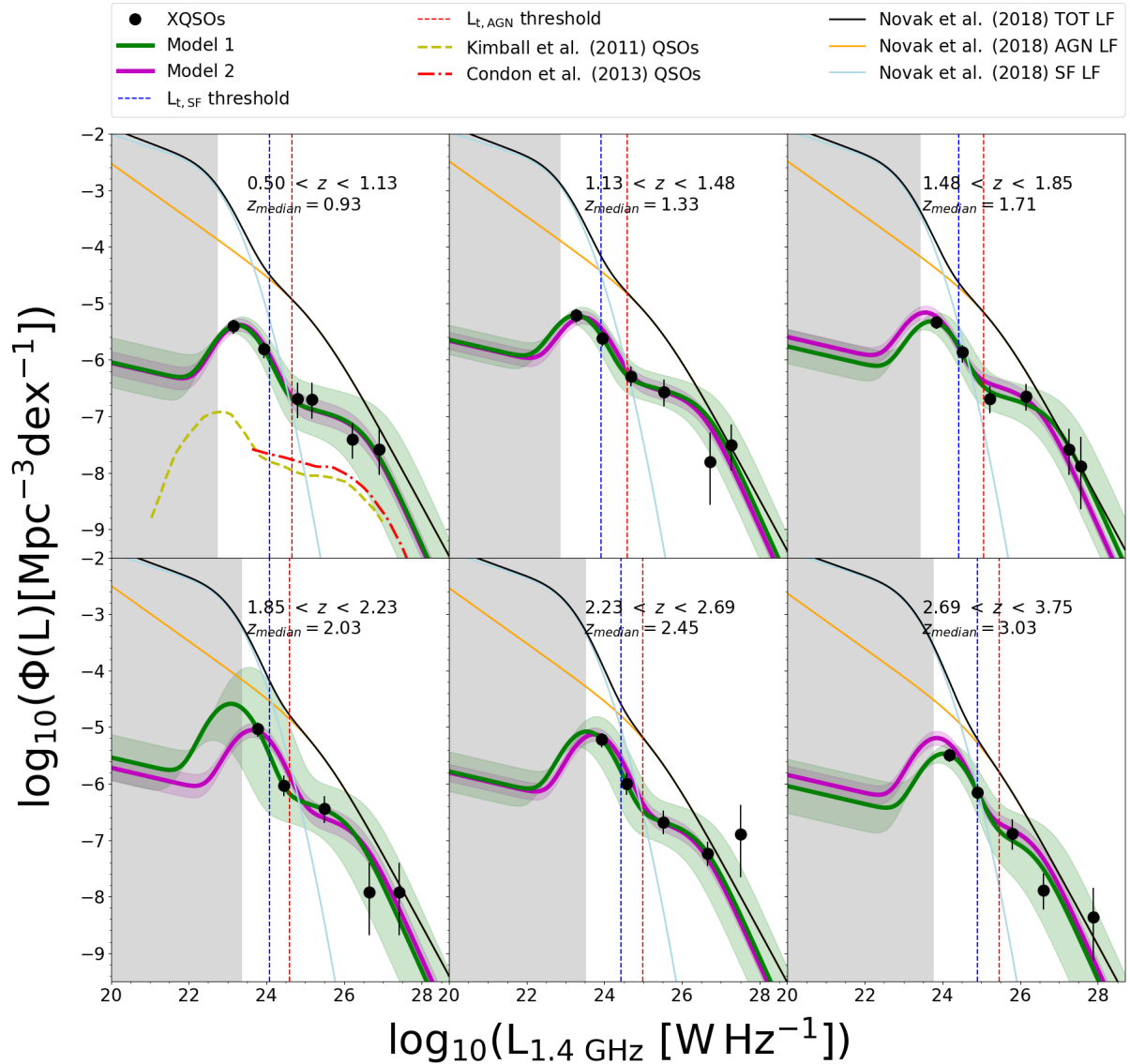


Figure 5.5: Radio luminosity function at 1.4 GHz of the radio and X-ray selected quasars at redshifts  $0.50 < z < 3.75$ . Solid green and magenta lines show the results of testing Model 1 and Model 2, respectively, with shaded areas showing  $1\sigma$  confidence range. Thin solid light blue, orange and black lines show the SFG, AGN and the total (SFG and AGN) RLFs by Novak et al. (2018). Thin blue and red vertical dashed lines show the threshold luminosities below and above which more than 80% of sources contributing to the RLF are dominated by SF and AGN-related processes, respectively. The gray shaded area shows the region unconstrained by our data where the RLF is just an extrapolation. Our results imply that the radio emission in a majority of lower radio luminosity XQSOs is powered by star formation.

Table 5.2: Radio luminosity functions of the radio and X-ray selected quasars.  $\log(L_{1.4 \text{ GHz}})$  is the logarithm of median value of  $L_{1.4 \text{ GHz}}$  of all sources within the luminosity bin and N is the number of sources per luminosity bin.

| Redshift          | $\log\left(\frac{L_{1.4\text{GHz}}}{\text{WHz}^{-1}}\right)$ | $\log\left(\frac{\Phi}{\text{Mpc}^{-3} \text{dex}^{-1}}\right)$ | N  |
|-------------------|--|---|----|
| $0.50 < z < 1.13$ | 23.16  | $-5.39^{+0.11}_{-0.15}$   | 16 |
| $Med(z) = 0.93$   | 23.93  | $-5.81^{+0.12}_{-0.17}$   | 17 |
|                   | 24.80  | $-6.70^{+0.30}_{-0.34}$   | 3  |
|                   | 25.17  | $-6.70^{+0.30}_{-0.34}$   | 3  |
|                   | 26.22  | $-7.41^{+0.30}_{-0.34}$   | 3  |
|                   | 26.90  | $-7.58^{+0.37}_{-0.45}$   | 2  |
| $1.13 < z < 1.48$ | 23.28  | $-5.21^{+0.10}_{-0.14}$   | 16 |
| $Med(z) = 1.33$   | 23.95  | $-5.62^{+0.11}_{-0.15}$   | 13 |
|                   | 24.69  | $-6.29^{+0.17}_{-0.18}$   | 8  |
|                   | 25.53  | $-6.57^{+0.22}_{-0.25}$   | 5  |
|                   | 26.73  | $-7.81^{+0.52}_{-0.76}$   | 1  |
|                   | 27.26  | $-7.51^{+0.37}_{-0.45}$   | 2  |
| $1.48 < z < 1.85$ | 23.84  | $-5.34^{+0.09}_{-0.11}$   | 20 |
| $Med(z) = 1.71$   | 24.52  | $-5.87^{+0.13}_{-0.19}$   | 12 |
|                   | 25.22  | $-6.69^{+0.22}_{-0.25}$   | 5  |
|                   | 26.15  | $-6.65^{+0.22}_{-0.25}$   | 5  |
|                   | 27.25  | $-7.59^{+0.37}_{-0.45}$   | 2  |
|                   | 27.55  | $-7.89^{+0.52}_{-0.76}$   | 1  |
| $1.85 < z < 2.23$ | 23.77  | $-5.03^{+0.11}_{-0.14}$   | 30 |
| $Med(z) = 2.03$   | 24.45  | $-6.03^{+0.17}_{-0.18}$   | 8  |
|                   | 25.50  | $-6.45^{+0.22}_{-0.25}$   | 5  |
|                   | 26.65  | $-7.92^{+0.52}_{-0.76}$   | 1  |
|                   | 27.41  | $-7.92^{+0.52}_{-0.76}$   | 1  |

Table 5.2.: Continued.

| Redshift          | $\log\left(\frac{L_{1.4\text{GHz}}}{\text{WHz}^{-1}}\right)$ | $\log\left(\frac{\Phi}{\text{Mpc}^{-3}\text{dex}^{-1}}\right)$ | N  |
|-------------------|--|--|----|
| $2.23 < z < 2.69$ | 23.93  | $-5.22^{+0.11}_{-0.14}$  | 25 |
| $Med(z) = 2.45$   | 24.58  | $-6.00^{+0.19}_{-0.20}$  | 7  |
|                   | 25.52  | $-6.68^{+0.20}_{-0.22}$  | 6  |
|                   | 26.66  | $-7.24^{+0.20}_{-0.22}$  | 6  |
|                   | 27.51  | $-6.89^{+0.52}_{-0.76}$  | 1  |
| $2.69 < z < 3.75$ | 24.18  | $-5.49^{+0.10}_{-0.13}$  | 22 |
| $Med(z) = 3.03$   | 24.91  | $-6.15^{+0.11}_{-0.15}$  | 13 |
|                   | 25.79  | $-6.89^{+0.25}_{-0.28}$  | 4  |
|                   | 26.59  | $-7.88^{+0.30}_{-0.34}$  | 3  |
|                   | 27.88  | $-8.36^{+0.52}_{-0.76}$  | 1  |

### 5.4.1 Local luminosity function

In order to constrain the XQSO RLF I need to adopt an analytic representation of the local RLF from the literature. Neither COSMOS nor XXL-S sample large enough volumes to detect a large number of local XQSOs in the radio band. To constrain the evolution of the XQSO RLF over the studied redshifts, I modify the local RLFs from the work by [Kimball et al. \(2011\)](#) and [Condon et al. \(2013\)](#).

As found by [Kimball et al. \(2011\)](#), the local ( $0.2 < z < 0.3$ ) RLF of optically selected QSOs is a superposition of contributions from star formation (SF) within the host galaxy (dominant at the low-luminosity end) and AGN-related radio emission (dominant at the high luminosity end). The radio emission from the host galaxies produces a ‘bump’ at the lower-luminosity end of the RLF which can be represented with a parabolic function:

$$\log \Phi_{\text{SF},0}(L) = \log \Phi_{\text{SF}}^* - (\log L - \log L^*)^2, \quad (5.1)$$

where  $\Phi_{\text{SF}}^* = 1.59 \times 10^{-7} \text{ Mpc}^{-3} \text{ dex}^{-1}$  and  $L_{\text{SF}}^* = 10^{22.84} \text{ WHz}^{-1}$  are the normalization and luminosity position of the vertex of parabola, respectively, converted to the units used in this paper.

To constrain the high luminosity end ( $L_{1.4 \text{ GHz}} > 10^{24} \text{ WHz}^{-1}$ ) of the RLF I modified the

analytic form of the RLF as described by [Condon et al. \(2013\)](#). [Condon et al.](#) examined the RLF of the color-selected quasars from the SDSS at  $0.2 < z < 0.45$  using the NVSS 1.4 GHz radio data. They found that their data constrain only the high luminosity end of the RLF where the radio emission is dominated by AGN activity. They fitted their data with an analytic function which is a combination of a power law function below  $L_{1.4 \text{ GHz}} = 10^{25.8} \text{ WHz}^{-1}$  and a quadratic function above it. Most of the analytic forms of RLFs in literature are some variation of the double power law function (e.g., [Condon et al. 1998](#), [Sadler et al. 2002](#), [Mauch & Sadler 2007](#), [Pracy et al. 2016](#)). To be consistent with the literature RLF, I adopted a double power law function. I constrained the parameters using the [Condon et al. \(2013\)](#) results for quasars in SDSS at  $0.2 < z < 0.45$  (de-evolved to  $z = 0.25$ ). This double power law function is:

$$\Phi_{\text{AGN},0}(L) = \frac{\Phi_{\text{AGN}}^*}{(L/L_{\text{AGN}}^*)^\alpha + (L/L_{\text{AGN}}^*)^\beta}, \quad (5.2)$$

where  $\Phi_{\text{AGN}}^* = 4.52 \times 10^{-9} \text{ Mpc}^{-3} \text{ dex}^{-1}$  is the normalization and  $L_{\text{AGN}}^* = 4.74 \times 10^{26} \text{ WHz}^{-1}$  is the knee of the luminosity function. The faint and bright end slopes of the RLF are  $\alpha = 0.16$  and  $\beta = 1.54$ , respectively.

## 5.4.2 Cosmic evolution of XQSOs

To test the redshift evolution of the RLF, I combined the analytic functions  $\Phi_{\text{SF},0}$  and  $\Phi_{\text{AGN},0}$  and assumed that both the SF and AGN components can evolve both in density and luminosity. The general analytic form of the function describing such evolution is:

$$\Phi_{\text{TOT}}(L, z) = (1+z)^{\alpha_{\text{D,SF}}} \Phi_{\text{SF},0} \left[ \frac{L}{(1+z)^{\alpha_{\text{L,SF}}}} \right] + (1+z)^{\alpha_{\text{D,AGN}}} \Phi_{\text{AGN},0} \left[ \frac{L}{(1+z)^{\alpha_{\text{L,AGN}}}} \right], \quad (5.3)$$

where  $\alpha_{\text{D,SF}}$ ,  $\alpha_{\text{L,SF}}$ ,  $\alpha_{\text{D,AGN}}$  and  $\alpha_{\text{L,AGN}}$  are parameters of the evolution of the SF and AGN components, respectively. The standard approach used in the literature (e.g., [Pracy et al. 2016](#), [Smolčić et al. 2017c](#), [Ceraj et al. 2018](#)) is to assume the simplest models of evolution: pure density ( $\alpha_{\text{L,SF}}, \alpha_{\text{L,AGN}} = 0$ ) or pure luminosity evolution ( $\alpha_{\text{D,SF}}, \alpha_{\text{D,AGN}} = 0$ ). However, due to significant variation in density and luminosity between different redshift bins, I found that such simplified models do not describe our data. In the following analysis, I use  $\chi^2$  minimization to test models in which both density and luminosity of both SF and AGN components change with redshift. An outlier at  $2.23 < z < 2.69$  with  $L_{1.4 \text{ GHz}} > 10^{27} \text{ WHz}^{-1}$  was excluded from the following analysis.

**Model 1 - Luminosity and density evolution of  $\Phi_{\text{TOT}}$ .** In this model I tested the evolution

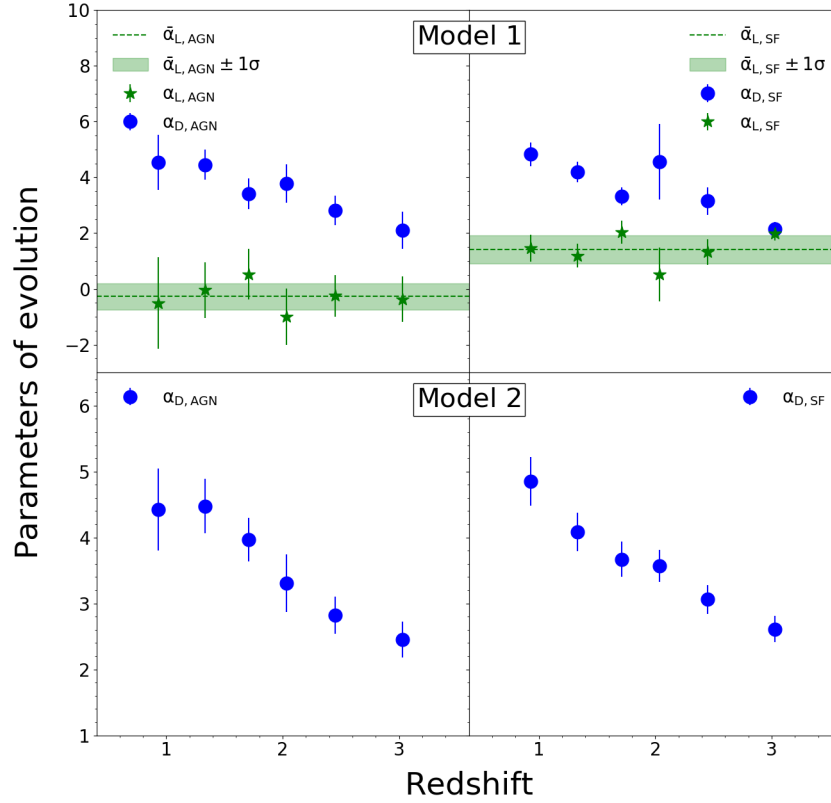


Figure 5.6: Parameters of evolution obtained from fitting Model 1 (upper panels) and Model 2 (lower panels). Left and right panels show the luminosity and density evolution parameters of  $\Phi_{\text{AGN}}$  and  $\Phi_{\text{SF}}$  components of  $\Phi_{\text{TOT}}$ .

of all four evolution parameters simultaneously. The results are shown in the upper panels of Fig. 5.6 and listed in Table 5.3. I found that both  $\alpha_{\text{D,SF}}$  and  $\alpha_{\text{D,AGN}}$  density evolution parameters show a decline with increasing redshift. The luminosity evolution parameter of the AGN component,  $\alpha_{\text{L,AGN}}$ , has a mean value of  $(-0.27 \pm 0.46)$  and is consistent with no redshift-dependent luminosity evolution. The luminosity evolution parameter of the SF component,  $\alpha_{\text{L,SF}}$ , is consistent with being constant with a mean value of  $(1.42 \pm 0.51)$ .

**Model 2 - Density evolution of  $\Phi_{\text{TOT}}$  with fixed  $\alpha_{\text{L,SF}}$  and  $\alpha_{\text{L,AGN}}$ .** In order to simplify the fitting procedure, in this model I set the luminosity evolution parameters to the mean values found from Model 1 ( $\alpha_{\text{L,SF}} = 1.42$ ,  $\alpha_{\text{L,AGN}} = -0.27$ ). With this model I found that the values of the density evolution parameters for both AGN and SF components of the RLF show a global decline with redshift, as shown in the lower panels of Fig. 5.6 and listed in Table 5.3.

I conclude that XQSOs evolve strongly with redshift in terms of the density parameters of

Table 5.3: Evolution parameters derived for the two evolution models: i) Model 1 in which both AGN and SF contributions to the  $\Phi_{\text{TOT}}$  can vary in luminosity and density over cosmic time and ii) Model 2 in which I fix the luminosity evolution parameters ( $\alpha_{\text{L,AGN}}$ ,  $\alpha_{\text{L,SF}}$ ) to the mean value obtained for Model 1 and test density evolution parameters of AGN and SF contributions to  $\Phi_{\text{TOT}}$ .

| Model 1           |                        |                         |                         |                         |          |
|-------------------|------------------------|-------------------------|-------------------------|-------------------------|----------|
| Redshift          | $\alpha_{\text{L,SF}}$ | $\alpha_{\text{D,SF}}$  | $\alpha_{\text{L,AGN}}$ | $\alpha_{\text{D,AGN}}$ | $\chi^2$ |
| $0.50 < z < 1.13$ | $1.46 \pm 0.49$        | $4.83 \pm 0.43$         | $-0.51 \pm 1.65$        | $4.53 \pm 0.99$         | 0.13     |
| $1.13 < z < 1.48$ | $1.19 \pm 0.43$        | $4.19 \pm 0.36$         | $-0.04 \pm 1.00$        | $4.45 \pm 0.55$         | 0.33     |
| $1.48 < z < 1.85$ | $2.03 \pm 0.41$        | $3.32 \pm 0.31$         | $0.52 \pm 0.91$         | $3.42 \pm 0.55$         | 0.07     |
| $1.85 < z < 2.23$ | $0.52 \pm 0.96$        | $4.56 \pm 1.36$         | $-0.99 \pm 1.01$        | $3.77 \pm 0.68$         | 0.04     |
| $2.23 < z < 2.69$ | $1.32 \pm 0.47$        | $3.16 \pm 0.49$         | $-0.24 \pm 0.75$        | $2.82 \pm 0.53$         | $< 0.01$ |
| $2.69 < z < 3.75$ | $1.98 \pm 0.24$        | $2.15 \pm 0.24$         | $-0.37 \pm 0.81$        | $2.10 \pm 0.66$         | 0.50     |
| Model 2           |                        |                         |                         |                         |          |
| Redshift          | $\alpha_{\text{D,SF}}$ | $\alpha_{\text{D,AGN}}$ | $\chi^2$                |                         |          |
| $0.50 < z < 1.13$ | $4.85 \pm 0.37$        | $4.43 \pm 0.62$         | 0.71                    |                         |          |
| $1.13 < z < 1.48$ | $4.08 \pm 0.29$        | $4.48 \pm 0.41$         | 1.43                    |                         |          |
| $1.48 < z < 1.85$ | $3.67 \pm 0.27$        | $3.97 \pm 0.33$         | 1.60                    |                         |          |
| $1.85 < z < 2.23$ | $3.57 \pm 0.24$        | $3.31 \pm 0.44$         | 2.08                    |                         |          |
| $2.23 < z < 2.69$ | $3.06 \pm 0.22$        | $2.82 \pm 0.28$         | 0.03                    |                         |          |
| $2.69 < z < 3.75$ | $2.61 \pm 0.20$        | $2.45 \pm 0.27$         | 4.37                    |                         |          |

both SF and AGN components of the RLF. In terms of luminosity evolution, both the SF and AGN components are consistent with being constant with redshift.

## 5.5 Discussion

In this Section, I discuss the possible contributions to the detected radio emission: star-forming processes within the host galaxy in Sect. 5.5.1 and AGN activity in Sect. 5.5.2. In Sect. 5.5.3, thresholds in 1.4 GHz radio luminosity are defined below and above which more than 80% of the XQSOs are dominated by the star formation and AGN-related radio emission, respectively. This enables us to disclose the true composite nature of the XQSOs in which both star formation and AGN activity make a significant contribution to the radio luminosity.

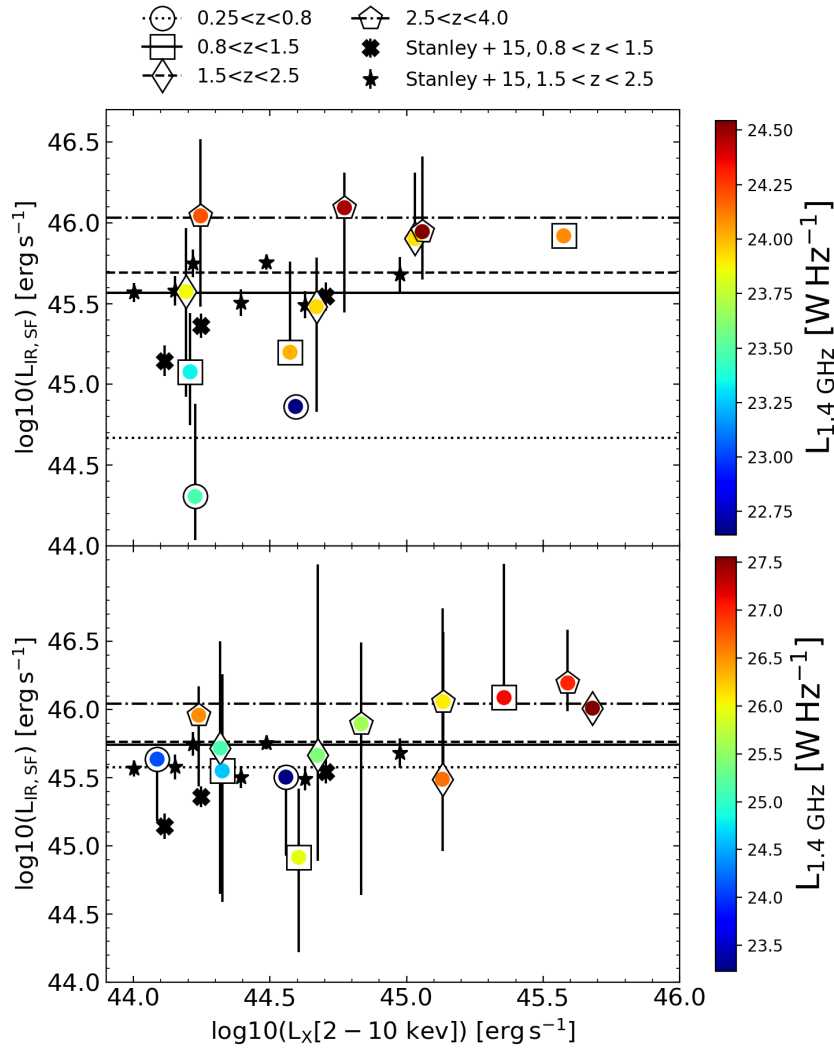


Figure 5.7:  $L_{\text{IR,SF}}$  vs.  $L_X[2-10 \text{ keV}]$  of the XQSOs separated in four redshift bins, color-coded by their median 1.4 GHz radio luminosity. The upper and lower panels show XQSOs from the COSMOS and XXL-S fields, respectively. Lines show the mean value of  $L_{\text{IR,SF}}$  in different redshift bins, as indicated in legend. I note that the two color-coded bars correspond to very different ranges in  $L_{1.4 \text{ GHz}}$  in COSMOS and XXL-S.

### 5.5.1 Host galaxies of XQSOs

The sample of XQSOs studied in this work was drawn from the moderate-to-high radiative luminosity AGN sample in COSMOS and high-excitation radio galaxy sample of AGN in XXL-S (see Chapter 2). Host galaxy properties of these AGN have been studied by [Delvecchio et al. \(2017; COSMOS\)](#) and [Butler et al. \(2018a; XXL-S\)](#). Both studies found that the host galaxies of these AGN have SFRs and stellar masses consistent with typical main-sequence galaxies.

The same conclusion was reached by [Stanley et al. \(2015\)](#) from an analysis of a sample

of  $\sim 2000$  X-ray selected AGN ( $10^{42} \text{ erg s}^{-1} < L_{2-8 \text{ keV}} < 10^{45.5} \text{ erg s}^{-1}$ ) detected in the Chandra Deep Field North and South and the COSMOS field. They studied the distribution of star formation-related IR luminosity and X-ray luminosity over  $0.2 < z < 2.5$ , as proxies of SFRs and AGN activity, respectively. They found a strong evolution of their average  $L_{\text{IR,SF}}$  with redshift, similar to that observed for the main-sequence galaxies. These results were confirmed by multiple other studies of quasar and AGN host galaxy properties (e.g., Rosario et al. 2012, Rosario et al. 2013, Lanzuisi et al. 2017, Stanley et al. 2017, Suh et al. 2017, Suh et al. 2019). However, the relationship between the  $L_{\text{IR,SF}}$  and  $L_X[2-8 \text{ keV}]$  appears flat as a result of different timescales of star-forming processes and AGN activity.

Fig. 5.7 shows the  $\log_{10}(L_{\text{IR,SF}})$  as a function of  $\log_{10}(L_X[2-10 \text{ keV}])$  of our XQSOs for both COSMOS (upper panel) and XXL-S (lower panel) sources, binned by X-ray luminosity (0.5 dex bin width). The dashed lines show the mean  $L_{\text{IR,SF}}$  for all the sources per redshift bin. I compare the results with those for X-ray selected AGN by Stanley et al. (2015), by converting their  $[2-8 \text{ keV}]$  X-ray luminosities into  $[2-10 \text{ keV}]$  X-ray luminosities, assuming photon index value of 1.9. Fig. 5.7 shows only the results by Stanley et al. in matching redshift ranges ( $0.8 < z < 1.5$  and  $1.5 < z < 2.5$ ) and above the X-ray threshold applied to define our sample of XQSOs ( $L_X[2-10 \text{ keV}] = 10^{44} \text{ erg s}^{-1}$ ).

For the COSMOS XQSOs, a rapid redshift evolution of the mean  $L_{\text{IR,SF}}$  (lines in the upper panel of Fig. 5.7) is found, with an average increase of IR luminosities by a factor  $\sim 3.8$  from one redshift bin to the next one, in rough agreement with results by Stanley et al. (2015). However, XXL-S XQSOs show a slower evolution of the  $L_{\text{IR,SF}}$  with an average increase by a factor of  $\sim 1.5$ . XXL-S XQSOs have higher mean values of  $L_{\text{IR,SF}}$  in the first redshift bin ( $0.25 < z < 0.8$ ) than the COSMOS XQSOs. The observed difference most likely arises due to different sensitivities of the radio data in the COSMOS and XXL-S field, with the COSMOS data-set being more sensitive to fainter radio sources. XQSOs with  $L_X[2-10 \text{ keV}] > 10^{45} \text{ erg s}^{-1}$  tend to have higher  $L_{\text{IR,SF}}$  than the lower  $L_X[2-10 \text{ keV}]$  XQSOs. There is a hint that higher redshift bins contain sources with higher median values of 1.4 GHz radio luminosities, both in COSMOS and XXL-S.

The mean values of  $L_{\text{IR,SF}}$  can be used to make a rough qualitative estimate of the contribution of star formation to the total radio luminosity,  $L_{1.4 \text{ GHz,SF}}$ . The mean  $L_{\text{IR,SF}}$  values can be scaled to SFRs using Kennicutt (1998) relation, which can then be used to calculate the expected radio emission via the redshift dependent  $q_{\text{TIR}}$  parameter by Delhaize et al. (2017) (assuming a radio spectral index  $\alpha = -0.7$ ). Estimated values of  $L_{1.4 \text{ GHz,SF}}$  for the COSMOS XQSOs increase with redshift, ranging from  $\sim 3 \times 10^{22} \text{ WHz}^{-1}$  to  $\sim 2 \times 10^{24} \text{ WHz}^{-1}$ . Compared to the median total radio luminosity of COSMOS XQSOs per redshift bin, star formation



can make a significant contribution to the total radio luminosity and even be a dominant source of radio emission. The estimates of the XXL-S XQSO  $L_{1.4 \text{ GHz, SF}}$  are comparable to those found for COSMOS XQSOs and show an increasing trend, ranging from  $\sim 2 \times 10^{23} \text{ WHz}^{-1}$  to  $\sim 2 \times 10^{24} \text{ WHz}^{-1}$ . However, despite the similarity in the level of the star formation occurring

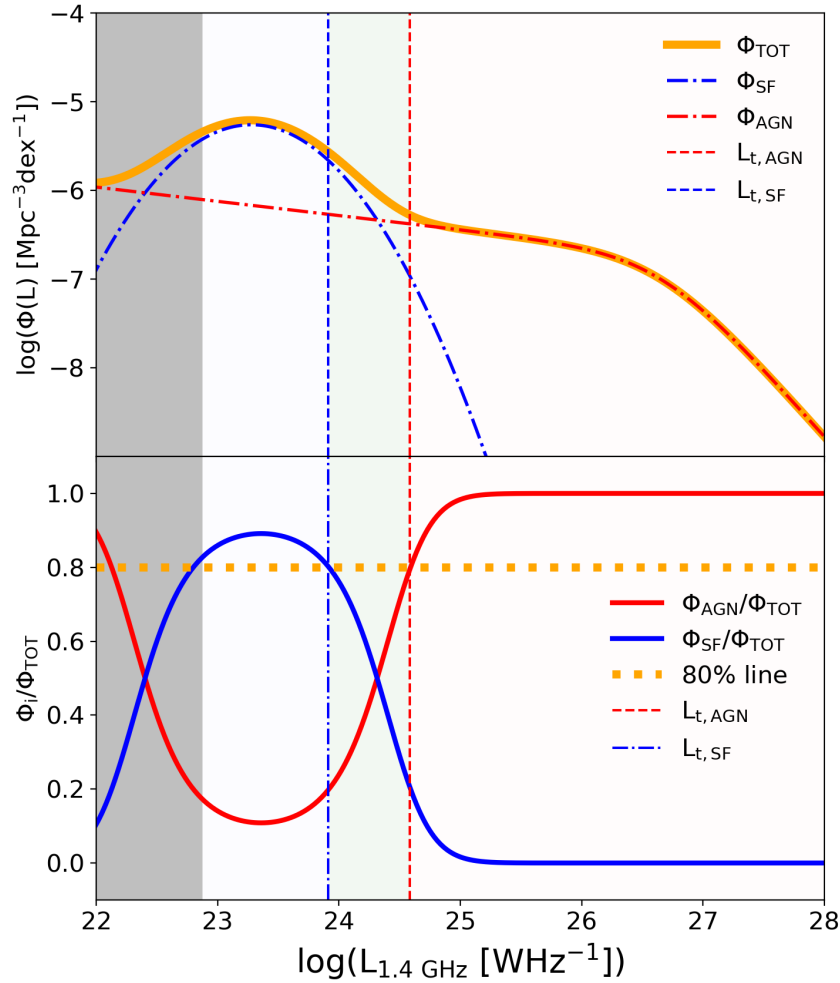


Figure 5.8: An example of how luminosity thresholds  $L_{t,SF}$  and  $L_{t,AGN}$  (blue and red dashed lines, respectively) were defined. *Top*: The radio luminosity function ( $\Phi_{TOT}$ ; orange line), constrained by the data at  $2.23 < z < 2.69$ , is separated into a lower-luminosity ‘bump’ ( $\Phi_{SF}$ ; dot-dashed blue line) and the higher-luminosity double power-law ( $\Phi_{AGN}$ ; dot-dashed red line). *Bottom*: Ratios of the SF ( $\Phi_{SF}$ ) and AGN ( $\Phi_{AGN}$ ) contributions to the total RLF ( $\Phi_{TOT}$ ) as a function of  $L_{1.4 \text{ GHz}}$  are shown by blue and red lines, respectively.  $L_{t,SF}$  and  $L_{t,AGN}$  are values of  $L_{1.4 \text{ GHz}}$  below and above which more than 80% of sources used to constrain the RLF are dominated by star formation and AGN-related radio emission, respectively. In both panels, the gray area shows the region of the plot in which the curves are just an extrapolation of the analytic forms of RLFs below the detection limits of radio data used to constrain them.

within the host galaxies, the relative contribution of the star formation to the total luminosity of the XXL-S XQSOs is significantly smaller than the observed radio luminosity.

### 5.5.2 AGN-related radio emission in XQSOs

The extent to which AGN-related radio emission can contribute to the total observed radio emission in AGN and quasars has been a subject of several recent studies. [White et al. \(2015\)](#) studied the properties of 74 RQ quasars (RQQs) selected in optical and NIR bands within a  $1 \text{ deg}^2$  area covered with the VIDEO Survey. They used the stacking technique to extract the information below the detection limit of the VLA-VIRMOS Deep Field survey ([Bondi et al. 2003](#)) at 1.4 GHz, finding evidence of radio emission in their quasar sample. By comparing the radio-based SFRs ([Yun et al. 2001](#)) and those based on the assumption that quasar host galaxies lie on the main sequence of SFGs ([Whitaker et al. 2012](#)), they found a mismatch in distributions which they attributed to a significant amount of AGN-related contribution to the total radio flux in these sources. They argued that the primary origin of the radio emission in sources at  $S_{1.4 \text{ GHz}} < 1 \text{ mJy}$  are BH accretion processes. The same conclusion was reached by [White et al. \(2017\)](#) who studied a sample of 70 RQQs from *Spitzer-Herschel* Active Galaxy Survey at  $0.9 < z < 1.1$ . They performed targeted observations of RQQs with the VLA at 1.5 GHz, detecting 35/70 of sources within their sample above  $2\sigma$ . For the sources with both radio and FIR detections (26/70), comparing the rest-frame  $125 \mu\text{m}$  luminosity (as a tracer of the level of star formation within the host galaxy) and the 1.5 GHz radio luminosity with FIR-to-radio correlation by [Smith et al. \(2014\)](#), they found that 92% of them are dominated by AGN-related radio emission.

The above results were obtained by extracting signal below the radio detection limit and for a relatively small sample of optically very bright RQQs at  $z \sim 1$  with targeted radio observations. As I show in the next section, by combining deep radio data within the COSMOS field with shallower radio data gathered over the larger XXL-S field, a study of the origin of radio emission in XQSOs is possible via the shape of the radio luminosity function over  $\sim 5$  orders of magnitude in  $L_{1.4 \text{ GHz}}$ . This enables me to capture the true composite nature of quasars in which both an AGN and star formation can make a noticeable contribution to the observed radio emission.

### 5.5.3 Origin of XQSO radio emission

From the RLF analysis I have found evidence of star-forming processes operating in galaxies hosting XQSOs. This means that star formation-related radio emission is expected to contribute to the total radio emission detected in the XQSOs below  $L_{1.4 \text{ GHz}} \sim 10^{24} \text{ W Hz}^{-1}$ .

Table 5.4: Number of COSMOS and XXL-S XQSOs divided in ranges of  $L_{1.4 \text{ GHz}}$  defined on the basis of the thresholds  $L_{t,\text{SF}}$  and  $L_{t,\text{AGN}}$ . Numbers in parentheses show the number of sources within each  $L_{1.4 \text{ GHz}}$  interval that would be defined as radio-excess with respect to criterion defined by [Delvecchio et al. \(2017\)](#).

|  | COSMOS   | XXL-S   |
|--|----------|---------|
| $L_{1.4 \text{ GHz}} \leq L_{t,\text{SF}}$                 | 143 (34) | 11 (1)  |
| $L_{t,\text{SF}} < L_{1.4 \text{ GHz}} < L_{t,\text{AGN}}$ | 30 (16)  | 15 (7)  |
| $L_{1.4 \text{ GHz}} \geq L_{t,\text{AGN}}$                | 13 (13)  | 55 (50) |

To define redshift-dependent thresholds in  $L_{1.4 \text{ GHz}}$  below and above which the dominant contribution to the RLF arises from the star formation and AGN activity, I calculated ratios of  $\Phi_{\text{SF-to-TOT}}$  and  $\Phi_{\text{AGN-to-TOT}}$  as a function of 1.4 GHz luminosity, as shown in Fig. 5.8. Luminosity dependent values of  $\Phi_{\text{SF}}$ ,  $\Phi_{\text{AGN}}$  and  $\Phi_{\text{TOT}}$  (see Sect. 5.4.2) were calculated at the median redshift in six redshift bins using the evolution parameters calculated for the luminosity and density evolution model of  $\Phi_{\text{TOT}}$  (see Model 1 in Table 5.3). For each redshift bin, I defined two threshold luminosities,  $L_{t,\text{SF}}$  and  $L_{t,\text{AGN}}$ , where  $L_{t,\text{SF}}$  is the luminosity below which I expect  $\geq 80\%$  of sources contributing to the RLF to be dominated by star formation-related radio emission and  $L_{t,\text{AGN}}$  is the luminosity above which  $\geq 80\%$  of sources are expected to have radio emission dominated by AGN activity. Sources with luminosities  $L_{t,\text{SF}} \leq L_{1.4 \text{ GHz}} \leq L_{t,\text{AGN}}$  are expected to be those in which both star formation and AGN activity have a significant contribution to the total radio emission. The numbers of COSMOS and XXL-S sources within each radio luminosity range are listed in Table 5.4.

Fig. 5.9 shows the XQSOs in  $q_{\text{TOT}}$  vs.  $z$  plane. The infrared-radio correlation found for the sample of SFGs, expressed via the  $q_{\text{TIR}}$  parameter, is a valuable tool for quantifying the amount of radio emission arising from star formation within the host galaxy ([Delhaize et al. 2017](#), [Ceraj et al. 2018](#)). If the radio luminosity of the source is dominated by the star formation-related emission, it would populate the so-called ‘SFG locus’ of the  $q_{\text{TOT}}$  vs.  $z$  plane. In Fig. 5.9 I show this locus using the redshift-evolving  $q_{\text{TIR}} \pm 0.35$  by [Delhaize et al. \(2017\)](#). Below this locus, the radio excess due to the AGN-related radio emission increases with decreasing  $q_{\text{TOT}}$ . Most COSMOS XQSOs are located within or near the ‘SFG locus’, while the XXL-S XQSOs mostly show significant radio excess. This indicates that a large fraction of COSMOS XQSOs have their emission dominated by star formation, while most of the XXL-S XQSOs radio emission comes from AGN activity.

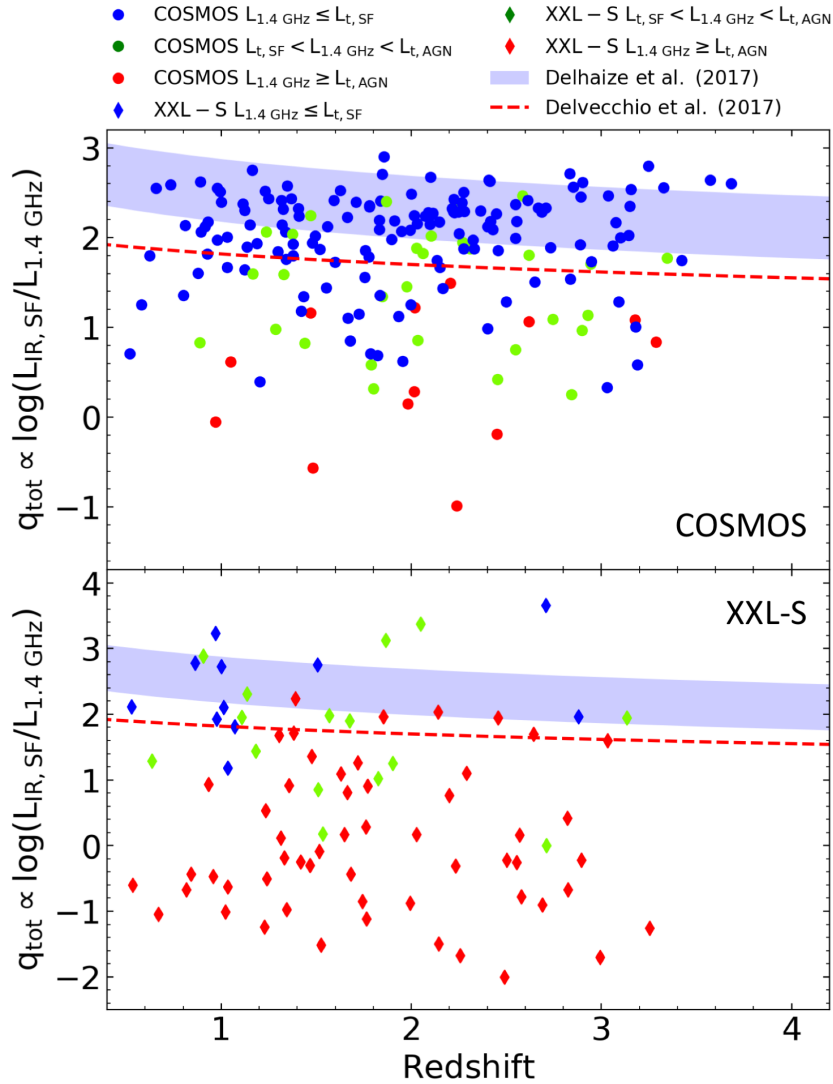


Figure 5.9:  $q_{\text{TOT}}$  vs. redshift of COSMOS (upper panel) and XXL-S (lower panel) XQSOs. Sources with  $L_{1.4 \text{ GHz}} \leq L_{t,\text{SF}}$ ,  $L_{t,\text{SF}} < L_{1.4 \text{ GHz}} < L_{t,\text{AGN}}$  and  $L_{1.4 \text{ GHz}} \geq L_{t,\text{AGN}}$  are shown with blue, green and red symbols respectively. The red dashed line shows the radio-excess threshold defined by [Delvecchio et al. \(2017\)](#). The blue shaded area shows the ‘SFG locus’ by [Delhaize et al. \(2017\)](#).

I further separated COSMOS and XXL-S XQSOs with respect to the radio luminosity thresholds  $L_{t,\text{SF}}$  and  $L_{t,\text{AGN}}$  in the  $q_{\text{TOT}}$  vs.  $z$  plane. The number of XQSOs which are below the radio excess threshold by [Delvecchio et al. 2017](#),  $q_{\text{REX}} = 24 - 21.984 \times (1+z)^{0.013}$ , are shown in parentheses in Table 5.4. The results show that the majority of sources contribution to the RLF ‘bump’ have their radio luminosity dominated by star formation-related emission, while the XQSOs at the higher-luminosity end of RLF are dominated by the AGN radio emission.

## 5.6 Chapter summary and conclusions

I studied the origin of the radio emission of a sample of 274 radio and X-ray selected quasars (XQSOs) at  $0.25 < z < 6.1$  detected at 3 GHz and 2.1 GHz in the COSMOS and XXL-S fields, respectively. Using the multiwavelength data available for these sources, I examined four different criteria of radio loudness and found that 18 – 73% of XQSOs are selected as radio-loud. This disagreement arises both from different flux density thresholds of COSMOS and XXL-S radio surveys and from the fact that the four radio loudness criteria capture different physical processes related to the AGN activity (radio luminosity, B-band luminosity, hard X-ray luminosity) and star-forming processes within the AGN host galaxies (star formation-related infrared luminosity). These different fractions of XQSOs selected as radio-loud and radio-quiet indicate that another approach is needed to disclose the true origin of radio emission in XQSOs.

The 1.4 GHz radio luminosity functions (RLFs) were constructed for a subsample of 267 XQSOs in six redshift bins between  $0.5 < z < 3.75$ . The lower-luminosity end of the RLF at all redshifts has a higher normalization than expected just from AGN-related radio emission and manifests as a ‘bump’ in the RLF. To constrain the shape and the evolution of the XQSOs, I used the analytic representation of the local radio luminosity function from the literature. The RLF employed is a combination of parabolic and double power-law functions constraining the lower and higher-luminosity end of RLF, respectively. The lower- and higher-luminosity ends were found to evolve significantly with redshift in terms of density. The luminosity evolution parameters of both the lower- and higher-luminosity end are consistent with being constant with redshift.

I used the RLF in different redshift bins to define thresholds in 1.4 GHz radio luminosity below and above which more than 80% of sources contributing to the RLF are expected to be dominated by star formation and AGN activity, respectively. To test this, the so-called  $q_{\text{TOT}}$  parameter was exploited, which is proportional to the logarithm of the ratio of IR luminosity due to star formation and 1.4 GHz luminosity. I confirmed that the majority of sources contributing to the ‘bump’ of the RLF are dominated by star formation-related radio emission, while the sources contributing to higher-luminosity end of RLF are dominated by AGN-related radio emission. These result expose the dichotomy of the processes behind the XQSO radio emission: star formation dominating the radio emission of the lower radio luminosity and AGN activity dominating the higher radio luminosity.

# Chapter 6

## Environments of radio-detected AGN within the COSMOS field

In this Chapter, I study the environments of radio detected AGN within the COSMOS field to test the role environment plays on the presence of AGN-related radio emission. I use the sample of moderate-to-high radiatively efficient AGN (HLAGN) and low-to-moderate radiatively efficient AGN (MLAGN) within the COSMOS field ([Smolčić et al. 2017b](#)), the selection of which was described in Chapter 2. To study the environments of these AGN, I select all the radio detected AGN found to reside in X-ray groups identified by [Gozaliasl et al. \(2019\)](#) within the COSMOS field.

### 6.1 Chapter introduction

The tight correlation between the SMBH mass and the bulge properties of the galaxy hosting SMBH points toward co-evolution of the two components through cosmic time (e.g., [Magorrian et al. 1998](#), [Ferrarese & Merritt 2000](#)). In some cases, the AGN, powered by the accretion of the gas onto the SMBH, is present.

It is now widely accepted that there are two different types of AGN found in the universe: radiatively efficient and radiatively inefficient AGN, although a variety of different nomenclatures are present in the literature. Most likely the origin of the different modes of accretion is the different supply of the gas available for the accretion onto the SMBH. While the cold gas from within the host galaxy creates signatures expected from the radiatively efficient accretion, the hot gas from the halo of the host galaxy slowly accretes onto the SMBH, creating signatures of radiatively inefficient accretion. Many studies have found that the different types of AGN reside in different host galaxies: radiatively efficient AGN tend to live in galaxies with bluer colors,

while the radiatively inefficient AGN are more likely to be found in the early-type red galaxies (e.g., [Smolčić et al. 2009](#), [Smolčić et al. 2017b](#), [Delvecchio et al. 2017](#)). The most likely reason that drives this is a common gas supply needed for the fueling of star formation and radiatively efficient accretion (i.e., cold gas). A similar trend has been found between the host galaxies and the radio detected radiatively efficient and inefficient AGN, with radiatively efficient AGN being found in hosts with significant ongoing star formation (e.g., [Best & Heckman 2012](#), [Delvecchio et al. 2017](#), [Ching et al. 2017](#)).

Galaxy properties have been previously found to correlate with the galaxy's morphology: galaxies residing in a local environment of higher density are more likely to have early-type morphologies and lower levels of ongoing star formation (e.g., [Blanton & Moustakas 2009](#), [Conselice 2014](#)). On the other hand, the level of star formation increases from dense regions towards the field. A similar trend is followed by AGN in the local universe: while the radiatively inefficient AGN are preferentially found in the centers of groups and clusters (e.g., [Best et al. 2005b](#)), radiatively efficient AGN are found to be more common in the field (e.g., [Heckman & Best 2014](#)). Depending on the presence of the strong radio emission, radiatively efficient AGN that are found in denser environments are more likely to be radio-loud, which likely reflects the trend that these sources are hosted by more massive galaxies relative to the radio-quiet ones ([Shen et al. 2009](#)).

In a statistical sense, the radiatively inefficient AGN are hosted by quiescent red galaxies in which there is little or no ongoing star formation (e.g., [Ching et al. 2017](#)). Their radio emission is dominated by the synchrotron emission from AGN activity. However, the origin of the radio emission in radiatively efficient AGN and quasars has been long debated (e.g., [Miller et al. 1990](#), [Kimball et al. 2011](#), [Baloković et al. 2012](#)). The results presented in Chapter 4 suggest that the radio emission in radiatively efficient AGN detected at 3 GHz within the COSMOS field, referred to as HLAGN, originates both from star formation or AGN activity. The fraction of radio emission due to AGN activity (AGN fraction) of radio detected HLAGN ranges from 0 to 1, indicating that, while some sources are dominated by AGN emission, others exhibit no evidence of it. The reason for this is still unclear, but most likely it reflects a combination of both internal and external processes which influence the evolution of the host galaxy and AGN within it.

In the following text, I describe the selection of radio detected AGN found within X-ray groups in the COSMOS field. In Section 6.3, I describe the results of the analysis of environments in which those AGN are found.

## 6.2 Radio-detected AGN in X-ray groups

In this Section, I use the multiwavelength dataset (radio-to-X-ray) available within the COSMOS field used to select HLAGN and MLAGN (see Sect. 2.1). I use the COSMOS X-ray group catalog (see Sect. 2.1.4) to select all radio-detected AGN that belong to these groups. The origin of the radio emission of the HLAGN sample has been previously studied in Chapter 4. There, the AGN fractions,  $f_{\text{AGN}}$ , defined as the fraction of the radio luminosity that originates from the AGN-related radio emission, were derived for all radio sources within HLAGN and MLAGN samples. These fractions are used in Sect. 6.3 and 6.4 to test if the presence of AGN-related radio emission changes with the distance from the center of X-ray groups.

To determine how many of the radio-detected AGN are found within the X-ray groups, I restrict the AGN samples onto those found at redshifts  $0.08 < z < 1.53$ , to match the selection of the X-ray group catalog presented by Gozaliasl et al. (2019). Using the X-ray group positions (RA, Dec,  $z_{\text{group}}$ ) and group radius ( $R_{200}$ ) provided in the X-ray group catalog, I searched for all the AGN within the  $|z_{\text{source}} - z_{\text{group}}| \leq \sigma_{z,\text{group}}$ , where  $\sigma_{z,\text{group}}$  is 0.0029 at  $z \leq 0.5$  and 0.0045 at  $z > 0.5$  (Gozaliasl et al. 2019) with positions within the  $R_{200}$  radius from the center of the X-ray group. There are 43 HLAGN and 72 MLAGN found within 40 and 57 different X-ray groups, respectively. These HLAGN and MLAGN have redshifts  $0.22 < z < 1.3$ . I also tested a different sample selection, choosing  $|z_{\text{source}} - z_{\text{group}}| \leq 3 \times \sigma_{z,\text{group}}$ , increasing the number of sources within both samples. However, results obtained using such selected samples are consistent with those derived using  $1\sigma$  cut.

In Fig. 6.1 I show the distributions of  $f_{\text{AGN}}$  of HLAGN/MLAGN within X-ray groups, compared to the distributions of parent HLAGN/MLAGN samples at redshifts  $0.2 < z < 1.3$ . Both HLAGN and MLAGN found in X-ray groups have distributions similar to those of their parent populations.

## 6.3 Results

To test if there is a correlation between the presence of AGN-related radio emission and the environment within the X-ray groups, I calculated the distance of HLAGN and MLAGN from the X-ray group center. Out of 43 HLAGN and 72 MLAGN found in X-ray groups, 24 and 65 have  $f_{\text{AGN}} > 0$ , respectively. Those sources were split into bins of distance from the center of the group to which they belong so that each bin contains a roughly equal number of sources. The results are shown in Fig. 6.2. In both samples, a decreasing trend between the  $f_{\text{AGN}}$  and the distance from the center is observed, suggesting that the radio-detected AGN, which are



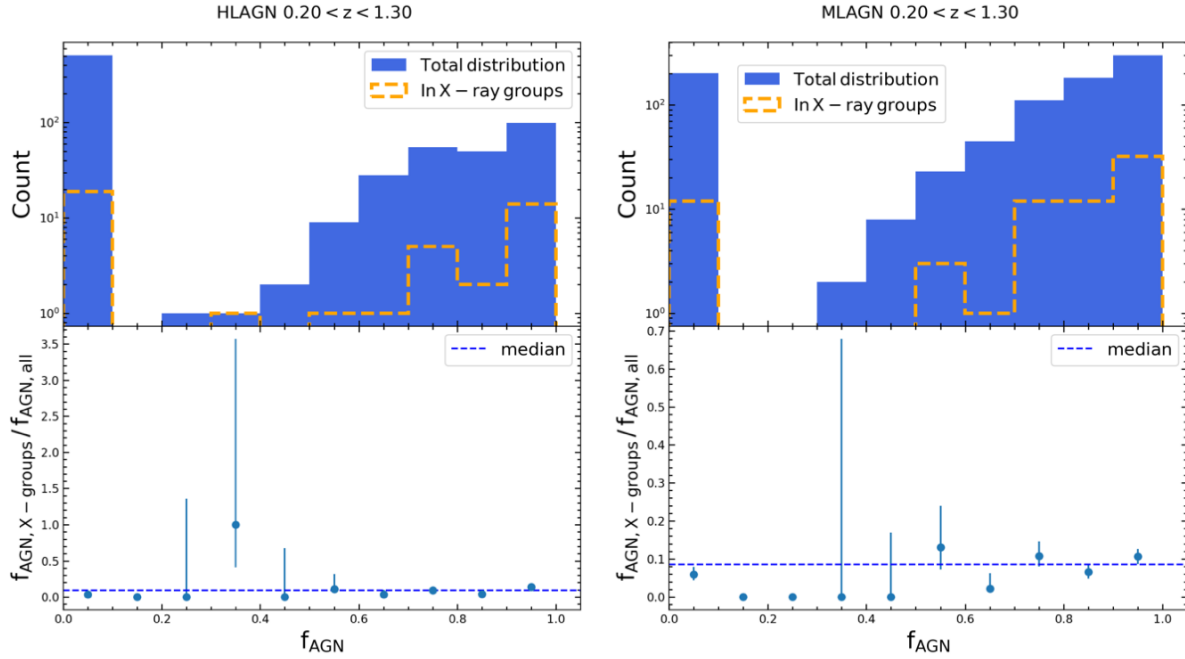


Figure 6.1: *Upper panel:* AGN fractions of the parent distributions of all AGN (blue distribution) and those within X-ray groups (orange dashed distribution). *Lower panel:* Ratio of AGN fractions of the AGN within X-ray groups and of the parent population per bin of AGN fraction. Left and right panels show the results for HLAGN and MLAGN, respectively.

closer to the X-ray group center, are more likely to have the radio emission dominated by the AGN-related activity.

### XQSO environments

The origin of radio emission in X-ray selected quasars (XQSOs) has been previously studied in Chapter 5, where I selected those sources using hard band X-ray luminosity  $L_X \geq 10^{44} \text{ erg s}^{-1}$ . There are 2 XQSOs found within the X-ray groups. Both of these XQSOs are found very close to the centers ( $R < 0.01 \text{ Mpc}$ ) of corresponding X-ray groups and have high AGN fractions ( $f_{\text{AGN}} > 0.75$ ).

## 6.4 Discussion

Using photometry of the two rich and centrally concentrated galaxy clusters at  $z = 0.39$  and  $z = 0.46$ , [Butcher & Oemler \(1978\)](#) found that these clusters contain more blue galaxies in their cores than was observed to be the case in the local clusters of similar richness and morphology.

This, so-called, Butcher-Oemler effect was confirmed by multiple photometric and spectrometric observations of rich clusters at  $0.2 < z < 0.9$  (e.g., Couch et al. 1994, Dressler et al. 1994). Possible scenarios for the blue galaxies found in centers of intermediate redshift clusters are thought to be episodes of star formation triggered either by galaxy encounters or hierarchical merging of clusters (e.g., Dressler et al. 1994, Mansheim et al. 2017).

As shown by Delvecchio et al. (2017), HLAGN host galaxies have high levels of star-forming activity and are similar to the typical star-forming galaxies at the considered redshift. To test if the number of HLAGN within centers of X-ray groups increases with increasing redshift, I split our sample into three redshift bins, as shown in the left panel of Fig. 6.3. A decreasing trend is found between the number of sources and the dimensionless radius ( $R/R_{200}$ ) for the overall HLAGN sample, and this trend is present at all redshifts considered. Even though the number of sources in the highest redshift bin closest to the center of the X-ray groups is larger than for the lower redshift bins, no clear redshift trend emerges in our analysis that would confirm Butcher-Oemler effect is valid for HLAGN within X-ray groups.

Similar to the HLAGN, a declining trend is found for an overall MLAGN number with the distance from the group centers (see right panel of Fig. 6.3). This trend is not so evident in all redshift bins, which may be affected by the small-number statistics of our sample.

However, these results may be biased by the selection based solely on the positions of the sources with respect to the X-ray group centers. A more detailed analysis is needed to confirm

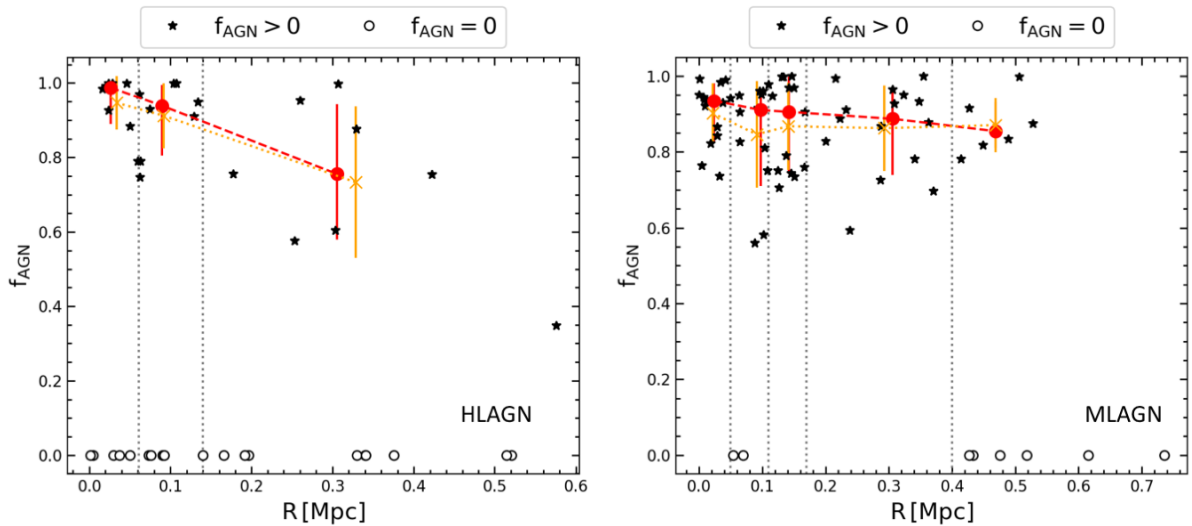


Figure 6.2: AGN fractions vs. the distances from the centers of the X-ray groups of HLAGN (left) and MLAGN (right). Black stars and empty circles show AGN with  $f_{\text{AGN}} > 0$  and  $f_{\text{AGN}} = 0$ , respectively. For the AGN with  $f_{\text{AGN}} > 0$ , median values and  $1\sigma$  confidence range are shown with red circles, while the orange symbols show the mean value and the standard deviation.

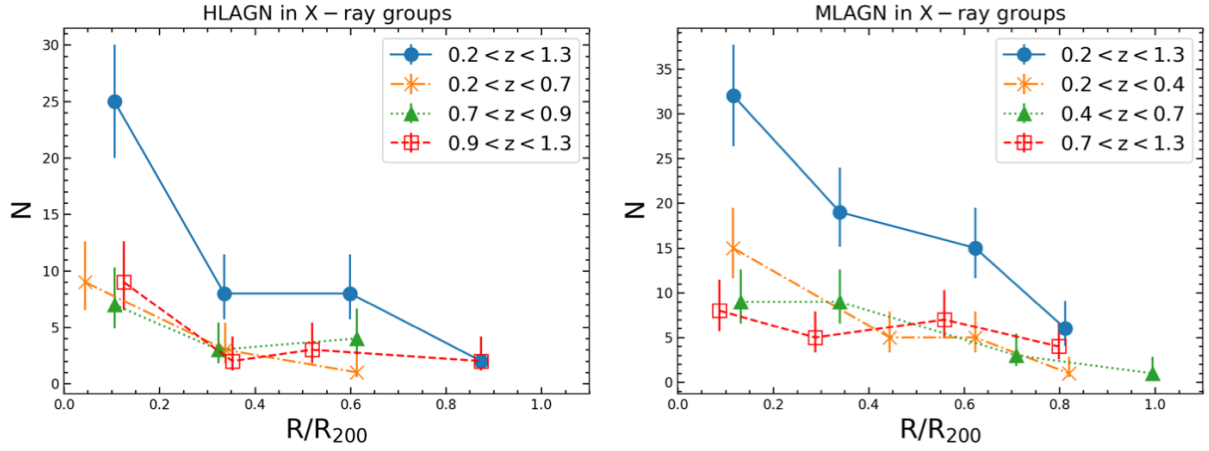


Figure 6.3: The number of sources (*left*: HLAGN, *right*: MLAGN) at different distances from the X-ray group center, quantified via dimensionless  $R/R_{200}$ . Error bars show the Poissonian uncertainties which were, for small number statistics ( $N \leq 20$ ), corrected using tabular values given by [Gehrels \(1986\)](#). The decreasing trend with the increasing radius is seen for both samples, both for the total samples and the subsamples split in redshift, as indicated in legends of the left and right panels.

these results, using a method such as Voronoi tessalation ([Ramella et al. 2001](#)), and taking into account the position of the radio-detected AGN within the different components of the cosmic web - field, filaments and clusters.

In Fig. 6.4, I separated both HLAGN and MLAGN sources according to their AGN fractions into those with  $f_{\text{AGN}} > 0$  and  $f_{\text{AGN}} = 0$ . Both the numbers of HLAGN and MLAGN with  $f_{\text{AGN}} > 0$  appear to increase closer to the centers of the groups. This trend is present for the overall samples and the redshift binned subsamples. On the other hand, the number of HLAGN with  $f_{\text{AGN}} = 0$  also seems to increase toward the centers of the groups, while the opposite trend is seen in MLAGN.

The results for the MLAGN sample are consistent with previous studies of radiatively inefficient AGN (e.g., [Best et al. 2005a](#), [Conselice 2014](#)), which are hosted mostly by early-type quiescent galaxies known to reside in denser environments. However, the increased number of HLAGN in the centers of X-ray groups may indicate that both the AGN and star formation-related radio activity in HLAGN favor denser environments.

## 6.5 Chapter summary and conclusions

In this Chapter, I cross-correlated the radio detected AGN within the COSMOS field with the X-ray group catalog by [Gozaliasl et al. \(2019\)](#). By using the environment data available

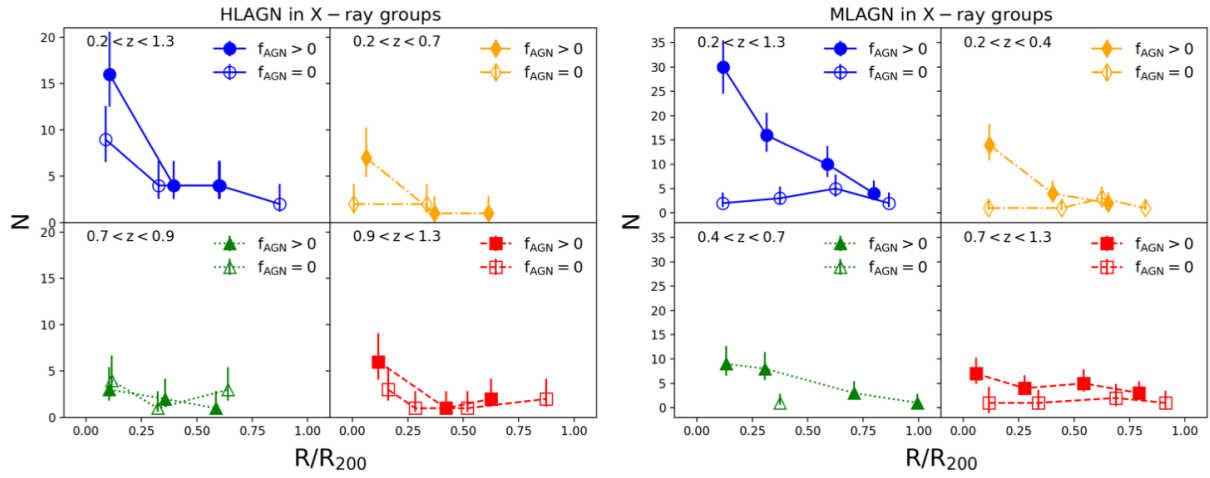


Figure 6.4: The number of sources vs. the distance from the center of the X-ray groups. Sources were split into four redshift bins and separated onto those with  $f_{\text{AGN}} > 0$  (filled symbols) and  $f_{\text{AGN}} = 0$  (empty symbols). Results for the HLAGN and MLAGN samples are shown in the left and right panels, respectively.

within the COSMOS field, I selected 43 HLAGN and 72 MLAGN located in X-ray groups at  $0.2 < z < 1.3$ . The analysis yielded that the fraction of AGN-related radio emission of both HLAGN and MLAGN decreases with the increasing distance from the group center. Also, the number of HLAGN and MLAGN with AGN fraction  $f_{\text{AGN}} > 0$  decreases with increasing distance from the center of groups. A possible explanation for the found trend is that the radio-AGN activity is increased in denser environments. This trend is present for both HLAGN and MLAGN in all cosmic epoch considered.

# Chapter 7

## Thesis summary and outlook

### 7.1 Summary of this Thesis

The origin of radio emission in radiatively efficient AGN and their cosmic evolution were studied in this Thesis. In order to do so, I used high-quality 3 GHz and 2.1 GHz radio data of extragalactic sources observed within the COSMOS and XXL-S fields, respectively (see Chapter 2 for details). These data were previously combined with the wealth of multiwavelength data within those two sky fields (e.g., [Laigle et al. 2016](#), [Civano et al. 2016](#), [Marchesi et al. 2016](#), [Fotopoulou et al. 2016](#)). The multiwavelength approach enabled me to focus on a special type of radio-detected AGN - the radio-detected radiatively efficient AGN. These were identified based on their strong X-ray and MIR emissions, expected to arise from the radiatively efficient accretion of matter onto the central supermassive black hole in their centers. Based on studies of the local universe, radio emission in extragalactic sources at GHz frequencies is expected to originate from the synchrotron processes within galaxies (e.g., [Condon 1992](#)). These processes can occur due to the activity of the SMBH and star-forming processes within the AGN host galaxy (e.g., [Klein & Emerson 1981](#), [Condon 1992](#)).

#### **The statistical method of radio luminosity decomposition**

The radio emission of the majority of sources detected within the VLA-COSMOS 3 GHz Large Project is unresolved and the morphological decomposition of the radio emission into the AGN and star-forming contributions is not possible. For this reason, I developed a statistical method of radio luminosity decomposition.

A sample of 1,604 X-ray and MIR selected AGN with moderate-to-high radiative luminosities (HLAGN) detected within the VLA-COSMOS 3 GHz Large Project was used to study the

origin of radio emission in radio-detected radiatively efficient AGN out to  $z \sim 6$ . These were selected to trace high-redshift analogs of the high-excitation radio galaxies detected in the local universe. As demonstrated by [Delvecchio et al. \(2017\)](#), HLAGN are hosted by galaxies with levels of star formation comparable to those of star-forming galaxies. The so-called infrared-radio correlation has been found to exist for star-forming galaxies from the local universe out to high redshifts (e.g., [Yun et al. 2001](#), [Bell 2003](#), [Magnelli et al. 2015](#), [Delhaize et al. 2017](#)). Under the assumption that HLAGN host galaxies are similar to the star-forming galaxy population at the same redshift, a well-calibrated infrared-radio correlation can be used to infer the amount of the radio emission expected based on the observed infrared emission. Also, in case there is an excess of radio emission due to AGN activity present in a given source, it will deviate (in some cases significantly) from the IRRC.

In Chapter 4, I have used the IRRC of the full 3 GHz sample to decompose the radio luminosity of HLAGN and all sources within the full 3 GHz sample. For these sources, I calculated the AGN fraction,  $f_{\text{AGN}}$ , defined as the fractional contribution of AGN-related radio emission to the total observed radio luminosity ( $0 \leq f_{\text{AGN}} \leq 0.5$ ). However,  $(32.0 \pm 1.5)\%$  of HLAGN are dominated by the AGN-related radio emission ( $0.5 < f_{\text{AGN}} \leq 1.0$ ). The significant differences found between AGN fractions of HLAGN are most likely related to the intrinsic properties of individual AGN (such as the mass, spin, and accretion rate of the central SMBH) and environment.

### Radio AGN luminosity functions and cosmic evolution of HLAGN

For all sources with AGN-related radio emission present ( $f_{\text{AGN}} > 0$ ), I calculated the 1.4 GHz AGN luminosity and 3 GHz AGN flux density by scaling the total 1.4 GHz luminosity (converted from the observed 3 GHz radio luminosity) and the total 3 GHz flux density by the derived AGN fraction. To construct radio AGN luminosity functions, I used 1.4 GHz AGN luminosities of a complete subsample of HLAGN with  $S_{3 \text{ GHz, AGN}} \geq S_{\text{lim}, 3 \text{ GHz}}$ , where  $S_{3 \text{ GHz, AGN}}$  is the AGN-related 3 GHz flux density after decomposition and  $S_{\text{lim}, 3 \text{ GHz}}$  detection limit of the VLA-COSMOS 3 GHz Large Project. Using the AGN radio luminosity functions of this HLAGN subsample, I have constrained the evolution out to  $z \sim 6$ , assuming pure luminosity and pure density evolution models, and found  $L^*(z) \propto (1+z)^{(3.97 \pm 0.15) + (-0.92 \pm 0.06)z}$  and  $\Phi^*(z) \propto (1+z)^{(2.64 \pm 0.10) + (-0.61 \pm 0.04)z}$ , respectively.

I used the constrained radio luminosity function to study the number and luminosity density evolution of the HLAGN. Both the number and luminosity density show an increasing trend from the local universe to a flattening at redshifts  $1 < z < 2.5$ , followed by a decline toward high redshifts.

If the AGN-related radio emission originates from AGN jets in HLAGN, these could exert kinetic feedback onto the HLAGN host galaxy and its surroundings. The kinetic luminosity, or the energy deposited into the environment by an AGN jet, can be estimated from the radio luminosity using one of many scaling relations available in the literature. I have used the scaling relation by Willott et al. (1999) to estimate the kinetic luminosity density of HLAGN and found an approximately constant maximum in the redshift range  $1 < z < 2.5$ . By comparing this trend to expectations from semi-analytic models by Croton et al. (2016) and Griffin et al. (2019) I do not find a total agreement. This indicates that the derived results, taking into account the uncertainties present in their calculation, could be used in the future to better constrain the models of galaxy formation and evolution.

### Radio and X-ray selected quasars

Quasars are among the most extreme AGN detected out to high redshifts due to their extreme brightness across almost the entire electromagnetic spectrum (e.g., Padovani et al. 2017). However, while some quasars do exhibit high levels of radio emission, the majority of them are quiet in the radio regime. The observation of the difference in levels of the observed radio emission within unobscured Type 1 quasars brought the question of the origin of radio emission in these sources, in which the spectrum is dominated by the AGN-related emission otherwise (e.g., Kellermann et al. 1989, Ivezić et al. 2002, Cirasuolo et al. 2003, Pierce et al. 2011, Baloković et al. 2012).

To address the question of the origin of radio emission in quasars, I used a combination of the COSMOS and XXL-S radio-to-X-ray data-sets. Exploiting these data, as described in Chapter 5, I studied a sample of 274 X-ray and radio selected quasars, referred to as XQSOs, which were detected at  $0.25 < z < 6.1$  at 3 GHz and 2.1 GHz in the COSMOS and XXL-S fields, respectively. These were selected using a hard X-ray luminosity criterion  $L_X[2 - 10 \text{ keV}] \geq 10^{44} \text{ erg s}^{-1}$ , which broadly selects quasars.

Most of the previous analyses were designed to study the question of the origin of radio emission based on the radio loudness distribution (e.g., Goldschmidt et al. 1999, Kellermann et al. 1989, Miller et al. 1990, Pierce et al. 2011). Radio loudness is typically defined as the ratio of the radio and optical flux density or luminosity, although many other definitions are present in the literature (e.g., Baloković et al. 2012, Hao et al. 2014). Within these distributions, a threshold is usually chosen to divide quasars into those which are radio-quiet and radio-loud. By examining four different criteria of radio loudness, I found that these select 18 – 73% of XQSOs as radio-loud. This significant disagreement between different criteria most likely arises from a combination of two factors: (i) different flux density thresholds of COSMOS and XXL-



S radio surveys, and (ii) different criteria capturing different physical processes related both to the AGN and star-forming activity. The disagreement of different criteria is the reason why we need another approach to study the origin of radio emission in XQSOs.

A different approach was suggested by [Kimball et al. \(2011\)](#) and [Condon et al. \(2013\)](#), where they used the shape of the radio luminosity functions of optically-selected quasars to infer the origin of radio emission in these sources. The results by [Kimball et al.](#) indicate that the higher normalization of quasar RLF (the so-called ‘bump’), when compared to that expected from AGN-related RLF only, reflects the presence of active processes of star formation in quasar host galaxies. Following their approach, I constructed 1.4 GHz radio luminosity functions for a subsample of 267 XQSOs in six redshift bins at redshifts  $0.5 < z < 3.75$ . To constrain the shape and the evolution of the XQSOs, I used [Kimball et al. \(2011\)](#) and [Condon et al. 2013](#) analytic representations of RLF to constrain the lower- and higher-luminosity ends of XQSO RLF in six redshift bins. Both the lower- and higher-luminosity ends evolve significantly in density, while their luminosity evolution parameters are consistent with being constant. The lower-luminosity end evolves both in density and luminosity, while the higher-luminosity end evolves significantly only in density.

Using the RLFs at different redshifts, I defined thresholds in 1.4 GHz luminosity below and above which more than 80% of sources that contribute to the RLFs are dominated by star-forming and AGN activities, respectively. By comparing these results with the  $q_{\text{TOT}}$  parameter, I confirm that most of the sources contributing to the ‘bump’ of the lower-luminosity end of XQSO RLF are dominated by star formation-related radio emission. The sources at the higher-luminosity end of XQSO RLF are dominated by AGN-related radio emission. These results confirm the dichotomy in processes behind the observed radio emission in XQSOs.

## Environments

The environment of radio-detected AGN (HLAGN and MLAGN) within the COSMOS field are studied in Chapter 6. By cross-correlating this AGN sample with the X-ray group catalog by [Gozaliasl et al. \(2019\)](#), I selected 43 HLAGN and 72 MLAGN located in X-ray groups at  $0.2 < z < 1.3$ . The results show that the AGN fractions of both HLAGN and MLAGN associated with X-ray groups decrease with the distance from the group center.



## 7.2 Future work

### Radio luminosity functions

As demonstrated in Chapter 5, combining the data from different radio surveys observed over different sky areas and cosmic volumes can be used to better constrain the evolution of rare extragalactic objects such as quasars. A so-called wedding cake approach can be used to combine the wide-area shallow surveys, which sample rare objects, with the narrow area deep surveys, which detect faint and distant objects (e.g., [Condon 2015](#)). Using such an approach, the (radio) luminosity functions of different galaxy populations (both AGN and SFGs) can be better constrained from the local volumes out to the earliest universe.

By combining the data from the radio surveys such as wide NVSS/FIRST combined with the SDSS, LARGESS, with observations of XXL South and North field, as well as deeper radio data over narrower fields such as those of the COSMOS field, the radio luminosity function of different galaxy populations can be studied in more detail ([Condon et al. 1998](#), [White et al. 1997](#), [Kimball & Ivezić 2008](#), [Pierre et al. 2016](#), [Ching et al. 2017](#), [Smolčić et al. 2017a](#), [Butler et al. 2018a](#), [Šlaus et al. 2020](#), *A&A*, in press). Exploiting the wealth of multiwavelength observations within those fields, combined with the radio data, an appropriate unified classification could be applied to separate sources into SFGs and two types of AGN from the local universe out to high redshifts. In the context of the continuation of the work presented in this Thesis, it would be interesting to see how a local radio luminosity function of the radio detected radiatively efficient AGN constrained by such a data-set would vary from those assumed to be appropriate in Chapters 4 and 5, as well as how it would influence the evolutionary trends found for HLAGN and XQSO populations.

### Environments of radio-detected galaxy populations

In Chapter 6, preliminary results of the analysis of environments of radio-detected AGN are presented. This analysis relies on the selection of radio-detected AGN based on their position with respect to positions of X-ray groups identified by [Gozaliasl et al. \(2019\)](#) within the COSMOS field. However, this selection provides information for only a small percentage (3 – 4%) of the total radio-detected AGN.

A more detailed analysis could be performed by using the method as described by [Smolčić et al. \(2017\)](#). [Smolčić et al.](#) studied environments of a sample of 23 submillimeter galaxies within the COSMOS field with well-defined multiwavelength counterparts and redshifts. They applied the Voronoi tessellation analysis (see also [Ramella et al. 2001](#)), as well as several different tests to validate their results. Their approach can be applied to the total sample of 3 GHz

detected sources with multiwavelength counterparts to study the affect different environments have on their properties, with a focus on how the density of environment affects the presence of AGN-related radio emission in two types of radio-detected AGN.

# References

- Abazajian K. N., et al., 2009, *ApJS*, **182**, 543, *The Seventh Data Release of the Sloan Digital Sky Survey*
- Abel T., Bryan G. L., Norman M. L., 2002, *Science*, **295**, 93, *The Formation of the First Star in the Universe*
- Abramowicz M. A., Chen X., Kato S., Lasota J.-P., Regev O., 1995, *ApJ*, **438**, L37, *Thermal Equilibria of Accretion Disks*
- Alexander D. M., Hickox R. C., 2012, *New A Rev.*, **56**, 93, *What drives the growth of black holes?*
- Antonucci R., 1993, *ARA&A*, **31**, 473, *Unified models for active galactic nuclei and quasars.*
- Antonucci R. R. J., Miller J. S., 1985, *ApJ*, **297**, 621, *Spectropolarimetry and the nature of NGC 1068.*
- Ashby M. L. N., et al., 2013, *ApJS*, **209**, 22, *The Spitzer South Pole Telescope Deep Field: Survey Design and Infrared Array Camera Catalogs*
- Baldry I. K., 2008, *Astronomy and Geophysics*, **49**, 5.25, *Hubble's galaxy nomenclature*
- Baloković M., Smolčić V., Ivezić Ž., Zamorani G., Schinnerer E., Kelly B. C., 2012, *ApJ*, **759**, 30, *Disclosing the Radio Loudness Distribution Dichotomy in Quasars: An Unbiased Monte Carlo Approach Applied to the SDSS-FIRST Quasar Sample*
- Baumann D., 2009, arXiv e-prints, p. [arXiv:0907.5424](https://arxiv.org/abs/0907.5424), *TASI Lectures on Inflation*
- Becker R. H., White R. L., Helfand D. J., 1994, in Crabtree D. R., Hanisch R. J., Barnes J., eds, *Astronomical Society of the Pacific Conference Series Vol. 61, Astronomical Data Analysis Software and Systems III*. p. 165
- Bell E. F., 2003, *ApJ*, **586**, 794, *Estimating Star Formation Rates from Infrared and Radio Luminosities: The Origin of the Radio-Infrared Correlation*
- Bell E. F., et al., 2004, *ApJ*, **608**, 752, *Nearly 5000 Distant Early-Type Galaxies in COMBO-17: A Red Sequence and Its Evolution since  $z \sim 1$*
- Best P. N., Heckman T. M., 2012, *MNRAS*, **421**, 1569, *On the fundamental dichotomy in the local radio-AGN population: accretion, evolution and host galaxy properties*
- Best P. N., Kauffmann G., Heckman T. M., Ivezić Ž., 2005a, *MNRAS*, **362**, 9, *A sample of radio-loud active galactic nuclei in the Sloan Digital Sky Survey*
- Best P. N., Kauffmann G., Heckman T. M., Brinchmann J., Charlot S., Ivezić Ž., White S. D. M., 2005b, *MNRAS*, **362**, 25, *The host galaxies of radio-loud active galactic nuclei: mass dependences, gas cooling and active galactic nuclei feedback*
- Best P. N., Ker L. M., Simpson C., Rigby E. E., Sabater J., 2014, *MNRAS*, **445**, 955, *The cosmic evolution of radio-AGN feedback to  $z = 1$*
- Binney J., Merrifield M., 1998, *Galactic Astronomy*
- Bîrzan L., Rafferty D. A., McNamara B. R., Wise M. W., Nulsen P. E. J., 2004, *ApJ*, **607**, 800, *A Systematic Study of Radio-induced X-Ray Cavities in Clusters, Groups, and Galaxies*
- Blandford R. D., Rees M. J., 1974, *MNRAS*, **169**, 395, *A "twin-exhaust" model for double radio sources.*
- Blandford R. D., Znajek R. L., 1977, *MNRAS*, **179**, 433, *Electromagnetic extraction of energy from Kerr black holes*
- Blanton M. R., Moustakas J., 2009, *ARA&A*, **47**, 159, *Physical Properties and Environments of Nearby Galaxies*
- Bond J. R., Kofman L., Pogosyan D., 1996, *Nature*, **380**, 603, *How filaments of galaxies are woven into the cosmic web*

- Bondi M., et al., 2003, *A&A*, **403**, 857, *The VLA-VIRMOS Deep Field. I. Radio observations probing the  $\mu$  Jy source population*
- Bonzini M., Padovani P., Mainieri V., Kellermann K. I., Miller N., Rosati P., Tozzi P., Vattakunnel S., 2013, *MNRAS*, **436**, 3759, *The sub-mJy radio sky in the Extended Chandra Deep Field-South: source population*
- Bower R. G., Benson A. J., Malbon R., Helly J. C., Frenk C. S., Baugh C. M., Cole S., Lacey C. G., 2006, *MNRAS*, **370**, 645, *Breaking the hierarchy of galaxy formation*
- Brinchmann J., Charlot S., White S. D. M., Tremonti C., Kauffmann G., Heckman T., Brinkmann J., 2004, *MNRAS*, **351**, 1151, *The physical properties of star-forming galaxies in the low-redshift Universe*
- Butcher H., Oemler A. J., 1978, *ApJ*, **219**, 18, *The evolution of galaxies in clusters. I. ISIT photometry of Cl 0024+1654 and 3C 295.*
- Butler A., et al., 2018a, *A&A*, **620**, A3, *The XXL Survey. XVIII. ATCA 2.1 GHz radio source catalogue and source counts for the XXL-South field*
- Butler A., et al., 2018b, *A&A*, **620**, A16, *The XXL Survey. XXXI. Classification and host galaxy properties of 2.1 GHz ATCA XXL-S radio sources*
- Butler A., Huynh M., Kapińska A., Delvecchio I., Smolčić V., Chiappetti L., Koulouridis E., Pierre M., 2019, *A&A*, **625**, A111, *The XXL Survey. XXXVI. Evolution and black hole feedback of high-excitation and low-excitation radio galaxies in XXL-S*
- Calistro Rivera G., et al., 2017, *MNRAS*, **469**, 3468, *The LOFAR window on star-forming galaxies and AGNs - curved radio SEDs and IR-radio correlation at  $0 < z < 2.5$*
- Capak P., et al., 2007, *ApJS*, **172**, 99, *The First Release COSMOS Optical and Near-IR Data and Catalog*
- Carroll B. W., Ostlie D. A., 2007, *An Introduction to Modern Astrophysics*, 2nd (international) edn
- Cavagnolo K. W., McNamara B. R., Nulsen P. E. J., Carilli C. L., Jones C., Bîrzan L., 2010, *ApJ*, **720**, 1066, *A Relationship Between AGN Jet Power and Radio Power*
- Ceraj L., et al., 2018, *A&A*, **620**, A192, *The VLA-COSMOS 3 GHz Large Project: Star formation properties and radio luminosity functions of AGN with moderate-to-high radiative luminosities out to  $z \sim 6$*
- Chabrier G., 2003, *PASP*, **115**, 763, *Galactic Stellar and Substellar Initial Mass Function*
- Ching J. H. Y., et al., 2017, *MNRAS*, **464**, 1306, *The Large Area Radio Galaxy Evolution Spectroscopic Survey (LARGESS): survey design, data catalogue and GAMA/WiggleZ spectroscopy*
- Ciliegli P., et al., 2018, *A&A*, **620**, A11, *The XXL Survey. XXVI. Optical and near-infrared identifications of the ATCA 2.1 GHz radio sources in the XXL-S Field*
- Cirasuolo M., Celotti A., Magliocchetti M., Danese L., 2003, *MNRAS*, **346**, 447, *Is there a dichotomy in the radio loudness distribution of quasars?*
- Civano F., et al., 2016, *ApJ*, **819**, 62, *The Chandra Cosmos Legacy Survey: Overview and Point Source Catalog*
- Condon J. J., 1992, *ARA&A*, **30**, 575, *Radio emission from normal galaxies*
- Condon J., 2015, in Proceedings of “The many facets of extragalactic radio surveys: towards new scientific challenges” (EXTRA-RADSUR2015). 20-23 October 2015. Bologna. p. 4
- Condon J. J., Odell S. L., Puschell J. J., Stein W. A., 1980, *Nature*, **283**, 357, *Radio emission from radio-quiet quasars*
- Condon J. J., Odell S. L., Puschell J. J., Stein W. A., 1981, *ApJ*, **246**, 624, *Radio emission from bright, optically selected quasars.*
- Condon J. J., Anderson M. L., Helou G., 1991, *ApJ*, **376**, 95, *Correlations between Far-Infrared, Radio, and Blue Luminosities of Spiral Galaxies*
- Condon J. J., Cotton W. D., Greisen E. W., Yin Q. F., Perley R. A., Taylor G. B., Broderick J. J., 1998, *AJ*, **115**, 1693, *The NRAO VLA Sky Survey*
- Condon J. J., Cotton W. D., Broderick J. J., 2002, *AJ*, **124**, 675, *Radio Sources and Star Formation in the Local Universe*
- Condon J. J., Kellermann K. I., Kimball A. E., Ivezić Ž., Perley R. A., 2013, *ApJ*, **768**, 37, *Active Galactic Nucleus and Starburst Radio Emission from Optically Selected Quasi-stellar Objects*

- Conselice C. J., 2014, *ARA&A*, **52**, 291, *The Evolution of Galaxy Structure Over Cosmic Time*
- Couch W. J., Ellis R. S., Sharples R. M., Smail I., 1994, *ApJ*, **430**, 121, *Morphological Studies of the Galaxy Populations in Distant “Butcher-Oemler” Clusters with HST. I. AC 114 at  $Z = 0.31$  and Abell 370 at  $Z = 0.37$*
- Crain R. A., et al., 2009, *MNRAS*, **399**, 1773, *Galaxies-intergalactic medium interaction calculation - I. Galaxy formation as a function of large-scale environment*
- Croton D. J., et al., 2006, *MNRAS*, **365**, 11, *The many lives of active galactic nuclei: cooling flows, black holes and the luminosities and colours of galaxies*
- Croton D. J., et al., 2016, *ApJS*, **222**, 22, *Semi-Analytic Galaxy Evolution (SAGE): Model Calibration and Basic Results*
- Delhaize J., et al., 2017, *A&A*, **602**, A4, *The VLA-COSMOS 3 GHz Large Project: The infrared-radio correlation of star-forming galaxies and AGN to  $z \lesssim 6$*
- Delvecchio I., et al., 2017, *A&A*, **602**, A3, *The VLA-COSMOS 3 GHz Large Project: AGN and host-galaxy properties out to  $z \lesssim 6$*
- Desai S., et al., 2012, *ApJ*, **757**, 83, *The Blanco Cosmology Survey: Data Acquisition, Processing, Calibration, Quality Diagnostics, and Data Release*
- Di Matteo T., Quataert E., Allen S. W., Narayan R., Fabian A. C., 2000, *MNRAS*, **311**, 507, *Low-radiative-efficiency accretion in the nuclei of elliptical galaxies*
- Donley J. L., et al., 2012, *ApJ*, **748**, 142, *Identifying Luminous Active Galactic Nuclei in Deep Surveys: Revised IRAC Selection Criteria*
- Dressler A., 1980, *ApJ*, **236**, 351, *Galaxy morphology in rich clusters: implications for the formation and evolution of galaxies.*
- Dressler A., Oemler Augustus J., Butcher H. R., Gunn J. E., 1994, *ApJ*, **430**, 107, *The Morphology of Distant Cluster Galaxies. I. HST Observations of CL 0939+4713*
- Dunlop J. S., McLure R. J., Kukula M. J., Baum S. A., O’Dea C. P., Hughes D. H., 2003, *MNRAS*, **340**, 1095, *Quasars, their host galaxies and their central black holes*
- Faber S. M., et al., 2007, *ApJ*, **665**, 265, *Galaxy Luminosity Functions to  $z \sim 1$  from DEEP2 and COMBO-17: Implications for Red Galaxy Formation*
- Fabian A. C., 2012, *ARA&A*, **50**, 455, *Observational Evidence of Active Galactic Nuclei Feedback*
- Falcke H., Biermann P. L., 1999, *A&A*, **342**, 49, *The jet/disk symbiosis. III. What the radio cores in GRS 1915+105, NGC 4258, M 81 and SGR A\* tell us about accreting black holes*
- Falcke H. D., et al., 2007, *Highlights of Astronomy*, **14**, 386, *A very brief description of LOFAR the Low Frequency Array*
- Fanidakis N., Baugh C. M., Benson A. J., Bower R. G., Cole S., Done C., Frenk C. S., 2011, *MNRAS*, **410**, 53, *Grand unification of AGN activity in the  $\Lambda$ CDM cosmology*
- Fanidakis N., et al., 2012, *MNRAS*, **419**, 2797, *The evolution of active galactic nuclei across cosmic time: what is downsizing?*
- Ferrarese L., Merritt D., 2000, *ApJ*, **539**, L9, *A Fundamental Relation between Supermassive Black Holes and Their Host Galaxies*
- Ferrarese L., et al., 2006, *ApJS*, **164**, 334, *The ACS Virgo Cluster Survey. VI. Isophotal Analysis and the Structure of Early-Type Galaxies*
- Filho M. E., Barthel P. D., Ho L. C., 2006, *A&A*, **451**, 71, *A radio census of nuclear activity in nearby galaxies*
- Finoguenov A., et al., 2009, *ApJ*, **704**, 564, *The Roadmap for Unification in Galaxy Group Selection. I. A Search for Extended X-ray Emission in the CNOC2 Survey*
- Fotopoulou S., et al., 2016, *A&A*, **592**, A5, *The XXL Survey. VI. The 1000 brightest X-ray point sources*
- Freedman D., Diaconis P., 1981, *Probability Theory and Related Fields*, **57**, 453, *On the histogram as a density estimator:  $L_2$  theory*
- Frenk C. S., White S. D. M., 2012, *Annalen der Physik*, **524**, 507, *Dark matter and cosmic structure*

- Frieman J. A., Turner M. S., Huterer D., 2008, *Annual Review of Astronomy and Astrophysics*, 46, 385–432, *Dark energy and the accelerating universe*
- Gehrels N., 1986, *ApJ*, 303, 336, *Confidence limits for small numbers of events in astrophysical data*
- Gendre M. A., Best P. N., Wall J. V., Ker L. M., 2013, *MNRAS*, 430, 3086, *The relation between morphology, accretion modes and environmental factors in local radio AGN*
- Goddi C., et al., 2019, *The Messenger*, 177, 25, *First M87 Event Horizon Telescope Results and the Role of ALMA*
- Godfrey L. E. H., Shabala S. S., 2016, *MNRAS*, 456, 1172, *Mutual distance dependence drives the observed jet-power-radio-luminosity scaling relations in radio galaxies*
- Goldschmidt P., Kukula M. J., Miller L., Dunlop J. S., 1999, *ApJ*, 511, 612, *A Comparison of the Optical Properties of Radio-loud and Radio-quiet Quasars*
- Goulding A. D., et al., 2014, *ApJ*, 783, 40, *Tracing the Evolution of Active Galactic Nuclei Host Galaxies over the Last 9 Gyr of Cosmic Time*
- Gozaliasl G., et al., 2019, *MNRAS*, 483, 3545, *Chandra centres for COSMOS X-ray galaxy groups: differences in stellar properties between central dominant and offset brightest group galaxies*
- Griffin M. J., et al., 2010, *A&A*, 518, L3, *The Herschel-SPIRE instrument and its in-flight performance*
- Griffin A. J., Lacey C. G., Gonzalez-Perez V., Lagos C. d. P., Baugh C. M., Fanidakis N., 2019, *MNRAS*, 487, 198, *The evolution of SMBH spin and AGN luminosities for  $z < 6$  within a semi-analytic model of galaxy formation*
- Guzzo L., et al., 2007, *ApJS*, 172, 254, *The Cosmic Evolution Survey (COSMOS): A Large-Scale Structure at  $z=0.73$  and the Relation of Galaxy Morphologies to Local Environment*
- Hao H., et al., 2014, arXiv e-prints, , *Inter-comparison of Radio-Loudness Criteria for Type 1 AGNs in the XMM-COSMOS Survey*
- Hardcastle M. J., Krause M. G. H., 2014, *MNRAS*, 443, 1482, *Numerical modelling of the lobes of radio galaxies in cluster environments - II. Magnetic field configuration and observability*
- Harrison C., 2014, PhD thesis, Durham University
- Hashimoto Y., Oemler Augustus J., Lin H., Tucker D. L., 1998, *ApJ*, 499, 589, *The Influence of Environment on the Star Formation Rates of Galaxies*
- Heckman T. M., Best P. N., 2014, *ARA&A*, 52, 589, *The Coevolution of Galaxies and Supermassive Black Holes: Insights from Surveys of the Contemporary Universe*
- Helou G., Soifer B. T., Rowan-Robinson M., 1985, *ApJ*, 298, L7, *Thermal infrared and nonthermal radio : remarkable correlation in disks of galaxies.*
- Herrera Ruiz N., et al., 2017, preprint, ([arXiv:1707.07512](https://arxiv.org/abs/1707.07512)), *The faint radio sky: VLBA observations of the COSMOS field*
- Hickox R. C., et al., 2009, *ApJ*, 696, 891, *Host Galaxies, Clustering, Eddington Ratios, and Evolution of Radio, X-Ray, and Infrared-Selected AGNs*
- Ho L. C., Filippenko A. V., Sargent W. L. W., 1997, *ApJS*, 112, 315, *A Search for “Dwarf” Seyfert Nuclei. III. Spectroscopic Parameters and Properties of the Host Galaxies*
- Hubble E., 1926, Contributions from the Mount Wilson Observatory / Carnegie Institution of Washington, 324, 1, No. 324. *Extra-galactic nebulae.*
- Hubble E. P., 1929, *ApJ*, 69, 103, *A spiral nebula as a stellar system, Messier 31.*
- Ilbert O., et al., 2010, *ApJ*, 709, 644, *Galaxy Stellar Mass Assembly Between  $0.2 < z < 2$  from the S-COSMOS Survey*
- Iovino A., et al., 2016, *A&A*, 592, A78, *A high definition view of the COSMOS Wall at  $z \sim 0.73$*
- Ivezić Ž., et al., 2002, *AJ*, 124, 2364, *Optical and Radio Properties of Extragalactic Sources Observed by the FIRST Survey and the Sloan Digital Sky Survey*
- Jansky K. G., 1933, Popular Astronomy, 41, 548, *Electrical phenomena that apparently are of interstellar origin*



- Kapinska A. D., Hardcastle M., Jackson C., An T., Baan W., Jarvis M., 2015, *Advancing Astrophysics with the Square Kilometre Array (AASKA14)*, p. 173, *Unravelling lifecycles and physics of radio-loud AGN in the SKA Era*
- Katz N., Hernquist L., Weinberg D. H., 1992, *ApJ*, **399**, L109, *Galaxies and Gas in a Cold Dark Matter Universe*
- Kauffmann G., et al., 2003, *MNRAS*, **346**, 1055, *The host galaxies of active galactic nuclei*
- Kellermann K. I., 2014, *Journal of Astronomical History and Heritage*, **17**, 267, *The discovery of quasars and its aftermath*
- Kellermann K. I., Sramek R., Schmidt M., Shaffer D. B., Green R., 1989, *AJ*, **98**, 1195, *VLA observations of objects in the Palomar Bright Quasar Survey*
- Kennicutt Jr. R. C., 1998, *ApJ*, **498**, 541, *The Global Schmidt Law in Star-forming Galaxies*
- Kerr R. P., 1963, *Phys. Rev. Lett.*, **11**, 237, *Gravitational Field of a Spinning Mass as an Example of Algebraically Special Metrics*
- Kimball A. E., Ivezić Ž., 2008, *AJ*, **136**, 684, *A Unified Catalog of Radio Objects Detected by NVSS, First, WENSS, GB6, and SDSS*
- Kimball A. E., Kellermann K. I., Condon J. J., Ivezić Ž., Perley R. A., 2011, *ApJ*, **739**, L29, *The Two-component Radio Luminosity Function of Quasi-stellar Objects: Star Formation and Active Galactic Nucleus*
- King A., 2008, *Mem. Soc. Astron. Italiana*, **79**, 1066, *Accretion in AGN: evolution of black hole mass and spin.*
- King A., 2014, *Space Sci. Rev.*, **183**, 427, *The Supermassive Black Hole—Galaxy Connection*
- Klein U., Emerson D. T., 1981, *A&A*, **94**, 29, *A survey of the distributions of 2.8 cm radio continuum in nearby galaxies.*
- Klypin A. A., Trujillo-Gomez S., Primack J., 2011, *ApJ*, **740**, 102, *Dark Matter Halos in the Standard Cosmological Model: Results from the Bolshoi Simulation*
- Lacey C. G., et al., 2016, *MNRAS*, **462**, 3854, *A unified multiwavelength model of galaxy formation*
- Laigle C., et al., 2016, *ApJS*, **224**, 24, *The COSMOS2015 Catalog: Exploring the  $1 < z < 6$  Universe with Half a Million Galaxies*
- Lanzuisi G., et al., 2017, *A&A*, **602**, A123, *Active galactic nuclei vs. host galaxy properties in the COSMOS field*
- Le Flocc'h E., et al., 2009, *ApJ*, **703**, 222, *Deep Spitzer 24  $\mu$ m COSMOS Imaging. I. The Evolution of Luminous Dusty Galaxies—Confronting the Models*
- Lintott C. J., et al., 2008, *MNRAS*, **389**, 1179, *Galaxy Zoo: morphologies derived from visual inspection of galaxies from the Sloan Digital Sky Survey*
- Lynden-Bell D., 1969, *Nature*, **223**, 690, *Galactic Nuclei as Collapsed Old Quasars*
- Madau P., Dickinson M., 2014, *ARA&A*, **52**, 415, *Cosmic Star-Formation History*
- Magnelli B., et al., 2015, *A&A*, **573**, A45, *The far-infrared/radio correlation and radio spectral index of galaxies in the SFR-M plane up to  $z \sim 2$*
- Magorrian J., et al., 1998, *AJ*, **115**, 2285, *The Demography of Massive Dark Objects in Galaxy Centers*
- Mansheim A. S., Lemaux B. C., Dawson W. A., Lubin L. M., Wittman D., Schmidt S., 2017, *ApJ*, **834**, 205, *Star Formation in the Cluster Merger DLSCL J0916.2+2953*
- Marchesi S., et al., 2016, *ApJ*, **817**, 34, *The Chandra COSMOS Legacy survey: optical/IR identifications*
- Marshall H. L., 1985, *ApJ*, **299**, 109, *The evolution of optically selected quasars with  $Z$  less than 2.2 and  $B$  less than 20*
- Mauch T., Sadler E. M., 2007, *MNRAS*, **375**, 931, *Radio sources in the 6dFGS: local luminosity functions at 1.4GHz for star-forming galaxies and radio-loud AGN*
- McCracken H. J., et al., 2010, *ApJ*, **708**, 202, *The COSMOS-WIRCAM Near-Infrared Imaging Survey. I. BzK-Selected Passive and Star-Forming Galaxy Candidates at  $z_{\text{gsim}} \sim 1.4$*
- McCracken H. J., et al., 2012, *A&A*, **544**, A156, *UltraVISTA: a new ultra-deep near-infrared survey in COSMOS*
- McDonald P., et al., 2005, *ApJ*, **635**, 761, *The Linear Theory Power Spectrum from the Ly $\alpha$  Forest in the Sloan Digital Sky Survey*

- McMahon R. G., Banerji M., Gonzalez E., Kuposov S. E., Bejar V. J., Lodieu N., Rebolo R., VHS Collaboration 2013, *The Messenger*, **154**, 35, *First Scientific Results from the VISTA Hemisphere Survey (VHS)*
- Merloni A., Heinz S., 2007, *MNRAS*, **381**, 589, *Measuring the kinetic power of active galactic nuclei in the radio mode*
- Merloni A., Heinz S., 2008, *MNRAS*, **388**, 1011, *A synthesis model for AGN evolution: supermassive black holes growth and feedback modes*
- Mickaelian A. M., 2015, *Iranian Journal of Astronomy and Astrophysics*, **2**, 1, *AGN Zoo and Classifications of Active Galaxies*
- Miller L., Peacock J. A., Mead A. R. G., 1990, *MNRAS*, **244**, 207, *The bimodal radio luminosity function of quasars*
- Miller P., Rawlings S., Saunders R., 1993, *MNRAS*, **263**, 425, *The Radio and Optical Properties of the  $Z < 0.5$  BQS Quasars*
- Miyazaki S., et al., 2012, *Hyper Suprime-Cam*. p. 84460Z, doi:10.1117/12.926844
- Morrissey P., et al., 2005, *ApJ*, **619**, L7, *The On-Orbit Performance of the Galaxy Evolution Explorer*
- Narayan R., Yi I., 1994, *ApJ*, **428**, L13, *Advection-dominated Accretion: A Self-similar Solution*
- Novak M., et al., 2017, *A&A*, **602**, A5, *The VLA-COSMOS 3 GHz Large Project: Cosmic star formation history since  $z = 5$*
- Novak M., Smolčić V., Schinnerer E., Zamorani G., Delvecchio I., Bondi M., Delhaize J., 2018, *A&A*, **614**, A47, *Constraints on submicrojansky radio number counts based on evolving VLA-COSMOS luminosity functions*
- O'Sullivan E., Giacintucci S., David L. P., Gitti M., Vrtilik J. M., Raychaudhury S., Ponman T. J., 2011, *ApJ*, **735**, 11, *Heating the Hot Atmospheres of Galaxy Groups and Clusters with Cavities: The Relationship between Jet Power and Low-frequency Radio Emission*
- Padovani P., Bonzini M., Kellermann K. I., Miller N., Mainieri V., Tozzi P., 2015, *MNRAS*, **452**, 1263, *Radio-faint AGN: a tale of two populations*
- Padovani P., et al., 2017, *A&A Rev.*, **25**, 2, *Active galactic nuclei: what's in a name?*
- Peebles P. J., Ratra B., 2003, *Reviews of Modern Physics*, **75**, 559, *The cosmological constant and dark energy*
- Peng Y.-j., et al., 2010, *ApJ*, **721**, 193, *Mass and Environment as Drivers of Galaxy Evolution in SDSS and  $z$ COSMOS and the Origin of the Schechter Function*
- Penzias A. A., Wilson R. W., 1965, *ApJ*, **142**, 419, *A Measurement of Excess Antenna Temperature at 4080 Mc/s.*
- Perley R. A., Chandler C. J., Butler B. J., Wrobel J. M., 2011, *ApJ*, **739**, L1, *The Expanded Very Large Array: A New Telescope for New Science*
- Pierce C. M., Ballantyne D. R., Ivison R. J., 2011, *ApJ*, **742**, 45, *Radio Stacking Reveals Evidence for Star Formation in the Host Galaxies of X-Ray-selected Active Galactic Nuclei at  $z < 1$*
- Pierre M., et al., 2016, *A&A*, **592**, A1, *The XXL Survey. I. Scientific motivations - XMM-Newton observing plan - Follow-up observations and simulation programme*
- Planck Collaboration et al., 2018, arXiv e-prints, p. arXiv:1807.06209, *Planck 2018 results. VI. Cosmological parameters*
- Poglitsch A., et al., 2010, *A&A*, **518**, L2, *The Photodetector Array Camera and Spectrometer (PACS) on the Herschel Space Observatory*
- Pracy M. B., et al., 2016, *MNRAS*, **460**, 2, *GAMA/WiggleZ: the 1.4 GHz radio luminosity functions of high- and low-excitation radio galaxies and their redshift evolution to  $z = 0.75$*
- Ramella M., Boschin W., Fadda D., Nonino M., 2001, *A&A*, **368**, 776, *Finding galaxy clusters using Voronoi tessellations*
- Rees M. J., 1984, *ARA&A*, **22**, 471, *Black Hole Models for Active Galactic Nuclei*
- Rosario D. J., et al., 2012, *A&A*, **545**, A45, *The mean star formation rate of X-ray selected active galaxies and its evolution from  $z \sim 2.5$ : results from PEP-Herschel*
- Rosario D. J., et al., 2013, *A&A*, **560**, A72, *The mean star-forming properties of QSO host galaxies*



- Sadler E. M., et al., 2002, *MNRAS*, **329**, 227, *Radio sources in the 2dF Galaxy Redshift Survey - II. Local radio luminosity functions for AGN and star-forming galaxies at 1.4 GHz*
- Salim S., et al., 2007, *ApJS*, **173**, 267, *UV Star Formation Rates in the Local Universe*
- Sanders D. B., et al., 2007, *ApJS*, **172**, 86, *S-COSMOS: The Spitzer Legacy Survey of the Hubble Space Telescope ACS 2 deg<sup>2</sup> COSMOS Field I: Survey Strategy and First Analysis*
- Sargent M. T., et al., 2010, *ApJS*, **186**, 341, *The VLA-COSMOS Perspective on the Infrared-Radio Relation. I. New Constraints on Selection Biases and the Non-Evolution of the Infrared/Radio Properties of Star-Forming and Active Galactic Nucleus Galaxies at Intermediate and High Redshift*
- Schawinski K., et al., 2014, *MNRAS*, **440**, 889, *The green valley is a red herring: Galaxy Zoo reveals two evolutionary pathways towards quenching of star formation in early- and late-type galaxies*
- Schinnerer E., et al., 2007, *ApJS*, **172**, 46, *The VLA-COSMOS Survey. II. Source Catalog of the Large Project*
- Schinnerer E., et al., 2010, *ApJS*, **188**, 384, *The VLA-COSMOS Survey. IV. Deep Data and Joint Catalog*
- Schmidt M., 1963, *Nature*, **197**, 1040, *3C 273 : A Star-Like Object with Large Red-Shift*
- Schmidt M., 1968, *ApJ*, **151**, 393, *Space Distribution and Luminosity Functions of Quasi-Stellar Radio Sources*
- Schneider D. P., et al., 2010, *AJ*, **139**, 2360, *The Sloan Digital Sky Survey Quasar Catalog. V. Seventh Data Release*
- Scoville N., 2007, *The Cosmic Evolution Survey: COSMOS*. p. 166
- Seyfert C. K., 1943, *ApJ*, **97**, 28, *Nuclear Emission in Spiral Nebulae.*
- Shakura N. I., Sunyaev R. A., 1973, *A&A*, **500**, 33, *Reprint of 1973A&A....24..337S. Black holes in binary systems. Observational appearance.*
- Shen Y., et al., 2009, *ApJ*, **697**, 1656, *Quasar Clustering from SDSS DR5: Dependences on Physical Properties*
- Silverman J. D., et al., 2008, *ApJ*, **675**, 1025, *The Evolution of AGN Host Galaxies: From Blue to Red and the Influence of Large-Scale Structures*
- Smith D. J. B., et al., 2014, *MNRAS*, **445**, 2232, *The temperature dependence of the far-infrared-radio correlation in the Herschel-ATLAS*
- Smolčić V., et al., 2009, *ApJ*, **696**, 24, *Cosmic Evolution of Radio Selected Active Galactic Nuclei in the Cosmos Field*
- Smolčić V., et al., 2017a, *A&A*, **602**, A1, *The VLA-COSMOS 3 GHz Large Project: Continuum data and source catalog release*
- Smolčić V., et al., 2017b, *A&A*, **602**, A2, *The VLA-COSMOS 3 GHz Large Project: Multiwavelength counterparts and the composition of the faint radio population*
- Smolčić V., et al., 2017c, *A&A*, **602**, A6, *The VLA-COSMOS 3 GHz Large Project: Cosmic evolution of radio AGN and implications for radio-mode feedback since  $z \approx 5$*
- Smolčić V., et al., 2017, *A&A*, **597**, A4, *(Sub)millimetre interferometric imaging of a sample of COSMOS/AzTEC submillimetre galaxies. III. Environments*
- Soltan A., 1982, *MNRAS*, **200**, 115, *Masses of quasars.*
- Springel V., Di Matteo T., Hernquist L., 2005a, *MNRAS*, **361**, 776, *Modelling feedback from stars and black holes in galaxy mergers*
- Springel V., et al., 2005b, *Nature*, **435**, 629, *Simulations of the formation, evolution and clustering of galaxies and quasars*
- Stanley F., Harrison C. M., Alexander D. M., Swinbank A. M., Aird J. A., Del Moro A., Hickox R. C., Mullaney J. R., 2015, *MNRAS*, **453**, 591, *A remarkably flat relationship between the average star formation rate and AGN luminosity for distant X-ray AGN*
- Stanley F., et al., 2017, *MNRAS*, **472**, 2221, *The mean star formation rates of unobscured QSOs: searching for evidence of suppressed or enhanced star formation*
- Steinhardt C. L., et al., 2014, *ApJ*, **791**, L25, *Star Formation at  $4 < z < 6$  from the Spitzer Large Area Survey with Hyper-Suprime-Cam (SPLASH)*
- Stoughton C., et al., 2002, *AJ*, **123**, 485, *Sloan Digital Sky Survey: Early Data Release*

- Strateva I., et al., 2001, *AJ*, **122**, 1861, *Color Separation of Galaxy Types in the Sloan Digital Sky Survey Imaging Data*
- Suh H., et al., 2017, *ApJ*, **841**, 102, *Type 2 AGN Host Galaxies in the Chandra-COSMOS Legacy Survey: No Evidence of AGN-driven Quenching*
- Suh H., et al., 2019, *ApJ*, **872**, 168, *Multi-wavelength Properties of Type 1 and Type 2 AGN Host Galaxies in the Chandra-COSMOS Legacy Survey*
- Taniguchi Y., et al., 2007, *ApJS*, **172**, 9, *The Cosmic Evolution Survey (COSMOS): Subaru Observations of the HST Cosmos Field*
- Taniguchi Y., et al., 2015, *PASJ*, **67**, 104, *The Subaru COSMOS 20: Subaru optical imaging of the HST COSMOS field with 20 filters\**
- Terashima Y., Wilson A. S., 2003, *ApJ*, **583**, 145, *Chandra Snapshot Observations of Low-Luminosity Active Galactic Nuclei with a Compact Radio Source*
- Thorne K. S., 1974, *ApJ*, **191**, 507, *Disk-Accretion onto a Black Hole. II. Evolution of the Hole*
- Tisanić K., et al., 2019, *A&A*, **621**, A139, *The VLA-COSMOS 3 GHz Large Project: Average radio spectral energy distribution of highly star-forming galaxies*
- Vogelsberger M., et al., 2014, *MNRAS*, **444**, 1518, *Introducing the Illustris Project: simulating the coevolution of dark and visible matter in the Universe*
- Weinberger R., et al., 2017, *MNRAS*, **465**, 3291, *Simulating galaxy formation with black hole driven thermal and kinetic feedback*
- Whitaker K. E., van Dokkum P. G., Brammer G., Franx M., 2012, *ApJ*, **754**, L29, *The Star Formation Mass Sequence Out to  $z = 2.5$*
- White S. D. M., Rees M. J., 1978, *MNRAS*, **183**, 341, *Core condensation in heavy halos: a two-stage theory for galaxy formation and clustering.*
- White R. L., Becker R. H., Helfand D. J., Gregg M. D., 1997, *ApJ*, **475**, 479, *A Catalog of 1.4 GHz Radio Sources from the FIRST Survey*
- White R. L., et al., 2000, *ApJS*, **126**, 133, *The FIRST Bright Quasar Survey. II. 60 Nights and 1200 Spectra Later*
- White R. L., Helfand D. J., Becker R. H., Glikman E., de Vries W., 2007, *ApJ*, **654**, 99, *Signals from the Noise: Image Stacking for Quasars in the FIRST Survey*
- White S. V., Jarvis M. J., Häußler B., Maddox N., 2015, *MNRAS*, **448**, 2665, *Radio-quiet quasars in the VIDEO survey: evidence for AGN-powered radio emission at  $S_{1.4\text{ GHz}} < 1\text{ mJy}$*
- White S. V., Jarvis M. J., Kalfountzou E., Hardcastle M. J., Verma A., Cao Orjales J. M., Stevens J., 2017, *MNRAS*, **468**, 217, *Evidence that the AGN dominates the radio emission in  $z \sim 1$  radio-quiet quasars*
- Willott C. J., Rawlings S., Blundell K. M., Lacy M., 1999, *MNRAS*, **309**, 1017, *The emission line-radio correlation for radio sources using the 7C Redshift Survey*
- Wright E. L., et al., 2010, *AJ*, **140**, 1868, *The Wide-field Infrared Survey Explorer (WISE): Mission Description and Initial On-orbit Performance*
- York D. G., et al., 2000, *AJ*, **120**, 1579, *The Sloan Digital Sky Survey: Technical Summary*
- Yun M. S., Reddy N. A., Condon J. J., 2001, *ApJ*, **554**, 803, *Radio Properties of Infrared-selected Galaxies in the IRAS 2 Jy Sample*
- Zamojski M. A., et al., 2007, *ApJS*, **172**, 468, *Deep GALEX Imaging of the COSMOS HST Field: A First Look at the Morphology of  $z \sim 0.7$  Star-forming Galaxies*
- van Moorsel G., 2014, in 2014 XXXIth URSI General Assembly and Scientific Symposium (URSI GASS). , doi:10.1109/URSIGASS.2014.6929995

# Curriculum vitae

Lana Ceraj was born in 1990 in Zagreb (Croatia). She completed "Voltino" primary school and "Ivan Supek" High School in Zagreb. In 2015 she obtained the title of Master of Physics at the Department of Physics, Faculty of Science at the University of Zagreb. The subject of her Master's thesis was "Studies of neutral hydrogen gas in distant galaxies using the spectral stacking technique", done under supervision of prof. dr. sc. Vernesa Smolčić and dr. sc. Jacinta Delhaize. In the fall of 2015 she enrolled at the PhD program in the field of atomic and molecular physics, module astrophysics, at the same faculty. In March 2016, she started working in the group led by prof. dr. sc. Vernesa Smolčić founded by the ERC project 337595: Constraining Stellar Mass and Supermassive Black Hole Growth through Cosmic Times: Paving the way for the next generation sky surveys. During her PhD studies she has presented her scientific work at ten international and two domestic conferences, and attended one astronomy winter school at which she presented a poster. She has actively participated in astronomy and science outreach events such as the public talks in museums, schools and faculties, the organization of The naked scientists in Croatia, making of the promo video and exhibition of the ERC project 337595, and the exhibition of Faculty of science at the European researchers' night event.

## Refereed publications

### Submitted

- 5 Tisanić, K., Smolčić, V., Imbrišak, M., Bondi, M., Zamorani, G., **Ceraj, L.**, et al., submitted to *A&A, The VLA-COSMOS 3 GHz Large Project: Average radio spectral energy distribution of active galactic nuclei*
- 4 **Ceraj, L.**, Smolčić, V., Delvecchio, I., et al., submitted to *A&A, The XXL Survey: XLIII. The quasar radio loudness dichotomy exposed via radio luminosity functions by combining the COSMOS and XXL-S X-ray selected quasars*
- 3 Šlaus, B., Smolčić, V., Novak, M., Fotopoulou, S., Ciliegi, P., Jurlin, N., **Ceraj, L.**, et al., accepted for publication in *A&A, The XXL Survey. XLI. Radio AGN luminosity functions based on the GMRT 610 MHz continuum observations*

## Published

- 2 **Ceraj, L.**, Smolčić, V., Delvecchio, I., et al., 2018, *A&A*, **620**, [A192](#), *The VLA-COSMOS 3 GHz Large Project: Star formation properties and radio luminosity functions of AGN with moderate-to-high radiative luminosities out to  $z\sim 6$*
- 1 Smolčić, V., Novak, M., Delvecchio, I., **Ceraj, L.**, et al., 2017, *A&A*, **602**, [A6](#), *The VLA-COSMOS 3 GHz Large Project: Cosmic evolution of radio AGN and implications for radio-mode feedback since  $z\sim 5$*

## Non-refereed publications

- 1 **Ceraj, L.**, Smolčić, V., Delvecchio, I., et al., 2018, proceeding of the IAU Symposium 333: "Peering towards Cosmic Dawn", [arXiv:1712.09838](#), *Cosmic evolution of AGN with moderate-to-high radiative luminosity in the COSMOS field*